The evolution of ocean fronts in the presence of mixed layer turbulence

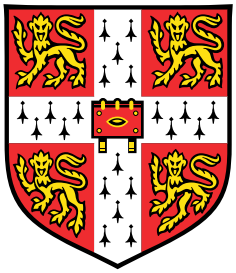

Matthew Neil Crowe

Supervisor: Dr. John R. Taylor

Department of Applied Mathematics and Theoretical Physics
University of Cambridge

This dissertation is submitted for the degree of
Doctor of Philosophy

Trinity College

15 May 2019

Declaration

This thesis is the result of my own work and includes nothing which is the outcome of work done in collaboration except as declared below. It is not substantially the same as any that I have submitted, or, is being concurrently submitted for a degree or diploma or other qualification at the University of Cambridge or any other University or similar institution. I further state that no substantial part of my thesis has already been submitted, or, is being concurrently submitted for any such degree, diploma or other qualification at the University of Cambridge or any other University or similar institution.

Much of the content of this thesis also appears in papers either published or currently in review with my PhD supervisor John R. Taylor as co-author. These papers are listed below along with the chapters to which they correspond:

Chapter 3 - Crowe, M., and J.R. Taylor, 2018, The evolution of a front in turbulent thermal wind balance. Part 1: Theory, J. Fluid Mech., 850, 179-211.

Chapter 4 - Crowe, M., and J.R. Taylor, 2019, The evolution of a front in turbulent thermal wind balance. Part 2: Numerics, J. Fluid Mech., 880, 326-352.

Chapter 5 - Crowe, M., and J.R. Taylor, 2019, The effects of surface wind stress and buoyancy flux on a front in turbulent thermal wind balance, J. Phys. Oceanogr., in completion.

Chapter 6 - Crowe, M., and J.R. Taylor, 2019, Baroclinic instability with a simple model for vertical mixing, J. Phys. Oceanogr., 10.1175/JPO-D-18-0270.1.

Matthew Neil Crowe
15 May 2019

The evolution of ocean fronts in the presence of mixed layer turbulence

Matthew Neil Crowe

Fronts, or regions with large horizontal density gradients, are common and important features of the upper ocean. On sufficiently large scales, the hydrostatic pressure gradient associated with the horizontal density gradient is often nearly balanced by a geostrophic (or thermal wind) vertically-sheared along-front flow. However, fronts in the ocean and atmosphere co-exist with small-scale turbulence which disrupts this balance. Analytic models of fronts (Eady, 1949; Eliassen, 1962; Hoskins & Bretherton, 1972; Blumen, 2000) have often neglected the effects of small-scale turbulence; however, more recent work has employed various simple parametrisations to describe the mixing properties of this turbulence and hence its effect on the frontal evolution (Garrett & Loder, 1981; Young, 1994; Thompson, 2000; Thomas & Lee, 2005; McWilliams, 2017).

Here, we use idealised models to examine the influence of this small-scale turbulence on the evolution of ocean fronts in the case of strong mixing. First we consider the evolution of an initially balanced density front subject to an imposed viscosity and diffusivity as a simple analogue for small-scale turbulence. At late times, the dominant balance is found to be the quasi-steady turbulent thermal wind balance with time-evolution due to an advection-diffusion balance in the buoyancy equation. In the absence of surface forcing this advection-diffusion equation admits similarity solutions describing a spreading front where the spreading results from shear dispersion associated with the cross-front flow and vertical diffusion of density. In response to shear dispersion, the front evolves towards a density profile that is nearly linear in the cross-front coordinate. At the edges of the frontal zone, the density field develops large curvature and these regions are associated with narrow bands of intense vertical velocity. The presence of surface wind stress and heat flux modifies the leading order velocity and buoyancy fields which, through the advection-diffusion balance, can lead to frontal gradients sharpening or reaching an equilibrium depending on the wind

stress direction and forcing magnitude. These predictions are tested using numerical simulations and found to be valid for a wide range of parameters.

Secondly we examine baroclinic instability in the presence of small-scale turbulence using a simple model for vertical mixing of momentum and buoyancy. The governing equations for buoyancy and vorticity are found to exhibit a normal mode linear instability which is studied using an analytical stability analysis and numerical simulations. The instability is found to be similar to the classical Eady instability however vertical mixing reduces the growth rate of the most unstable mode. Additionally, vertical mixing causes the wavenumber vector associated with the most unstable mode to point at an angle to the cross front direction with the angle being determined by the relaxation timescale. The most unstable modes grow by converting potential energy associated with the basic state into kinetic energy of the growing perturbations. However, unlike the inviscid Eady problem, the dominant energy balance is between the buoyancy flux and the energy dissipated by the modeled vertical mixing. We test our analytical predictions for the angle and growth rate of the most unstable mode using numerical simulations and generally find good agreement. In the absence of horizontal mixing, the most unstable mode has an infinite wavenumber. We discuss mechanisms providing a finite wavenumber cutoff including horizontal mixing and stratification.

Table of contents

List of figures

List of tables

Chapter 1

Introduction

1.1 Fronts in the ocean and atmosphere

Fronts, or regions with large horizontal density gradients, are common and important features in the atmosphere and ocean and appear on a wide range of scales. Fronts are highly anisotropic features where the cross-front width (in the direction of the density gradient) is small compared to the along-front length. The cross-front width can range from tens of kilometers for large fronts including the Gulf Stream (see Fig. 1.1), Kuroshio, and fronts associated with the Antarctic Circumpolar Current (ACC), to scales of meters for fronts associated with freshwater plumes and gravity currents. Atmospheric fronts are associated with weather patterns on both the local (Ostdiek & Blumen, 1997) and the continental (Hoskins, 1982) scale and coincide with strong winds and updrafts.

The term 'submesoscale' refers to structures on a scale of order 1-10km where the effects of rotation, velocity shear and turbulence all play an important role (Thomas *et al.*, 2008). Submesoscale fronts are commonly found in the surface mixed layer of the upper ocean where they can enhance the vertical transport of tracers such as heat, carbon and nutrients (Garrett & Loder, 1981; Ferrari, 2011). Fig. 1.2 shows two cross-front sections from surveys of the Azores Front, we can see regions of strong horizontal density gradients in the weakly stratified mixed layer with a horizontal lengthscale of around 10km. Density fronts can result from buoyancy differences due to both heat and salinity. Fig. 1.3 shows the sea surface temperature around the United Kingdom and a temperature front is shown by the red dashed line.

Fronts develop and intensify through a process known as frontogenesis (Hoskins, 1982). This phenomenon occurs in both the atmosphere and oceans and can be driven

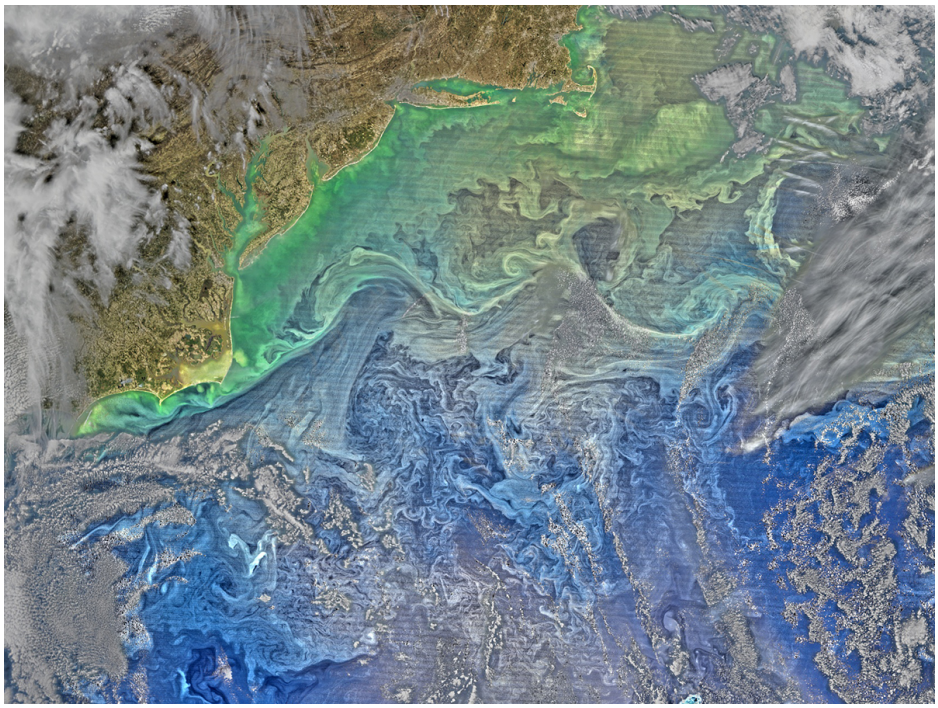

Fig. 1.1 Image of the western North Atlantic Ocean on March 9, 2016 collected by the Visible Infrared Imaging Radiometer Suite on NASA-NOAA's Suomi NPP satellite (NASA/Ocean Biology Processing Group, 2016). The small scale structures in the Gulf Stream are made visible by the presence of phytoplankton.

by a variety of processes including externally imposed strain, surface heat flux, wind stress and adjustment from an unbalanced initial state (Hoskins & Bretherton, 1972; Blumen, 2000). Large scale fronts in the ocean and atmosphere are often close to a state of thermal wind balance, i.e. the balance between a pressure gradient in hydrostatic balance with changes in density and the Coriolis force associated with an along-front 'thermal wind' jet (Holton & Hakim, 2012; Rudnick & Luyten, 1996). When a balanced front is disturbed (for example by turbulent mixing, large-scale flow, or surface stress), the dynamic response results in a secondary circulation with flow in the cross-front and vertical directions (Eliassen, 1962; Hoskins & Bretherton, 1972; Orlanski & Ross, 1977). The horizontal convergence associated with the secondary circulation further intensifies frontogenesis (Hoskins & Bretherton, 1972).

Externally imposed strain flows are often used to model the squeezing of fronts by large-scale currents and analytic work by Hoskins & Bretherton (1972) found that for an inviscid front, this external strain flow can lead to a finite-time discontinuity in the surface density. These infinitely sharp fronts are not observed physically, suggesting the existence of a process controlling frontal width. One candidate for

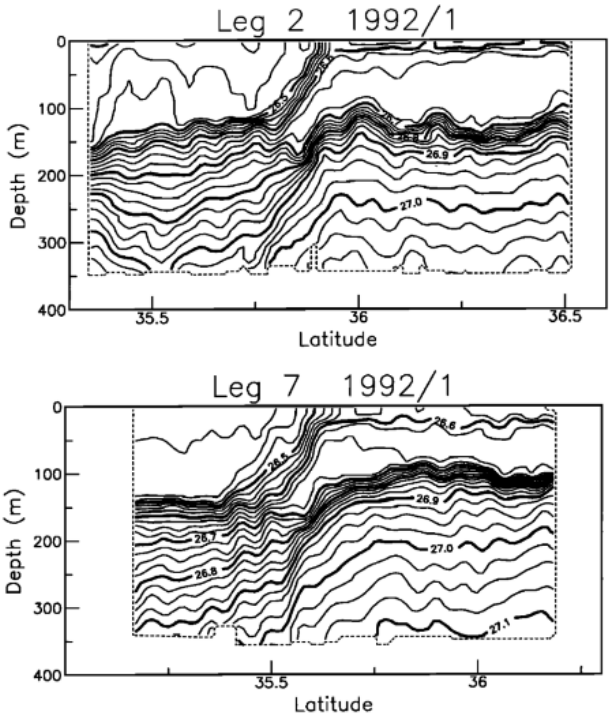

Fig. 1.2 Cross-front sections of potential density from surveys of the Azores Front done in May 1991 and March 1992 (Figure 5 of Rudnick & Luyten (1996)).

arresting frontogenesis is mixing of density and momentum by small scale turbulence (McWilliams, 2016; Sullivan & McWilliams, 2018).

The evolution of a front in response to frictional forcing was considered by Thompson (2000) who used a two-dimensional semi-geostrophic model modified to include vertical mixing. Constant diffusivity and viscosity were used to represent turbulent effects in the ocean surface mixed layer. A cross-front ageostrophic flow proportional to the horizontal buoyancy gradient led to a slumping of the frontal region and the formation of a sharp surface buoyancy gradient. In the case where vertical diffusion was small a buoyancy balance between time evolution and cross-front advection was considered giving an equation for the non-linear evolution of the surface buoyancy. The solution evolved towards a finite-time discontinuity as with the inviscid case and gave a good approximation to the frontal sharpening before the singularity was reached.

Early theoretical work by Garrett & Loder (1981) considered an idealised model of a front for two-layer and continuous stratification. For a continuously stratified front with small Ekman number it was assumed that the along-front velocity satisfies thermal wind balance allowing the cross-front velocity to be approximated using an eddy viscosity acting on the thermal wind flow. Using the equation for density advection

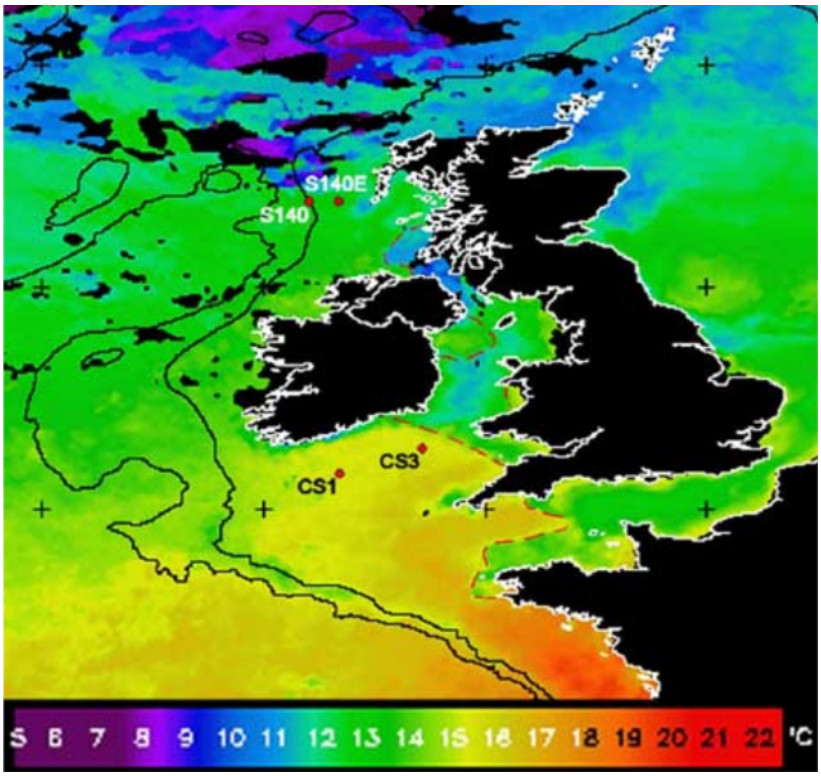

Fig. 1.3 A composite image of sea surface temperature (SST) for the northwest European continental shelf seas for 6–12th June 2004. In areas of the shelf where tidal mixing dominates over surface heat input, the water column remains mixed (cooler SST), whilst in deeper less turbulent regions surface heating dominates and the water column stratifies (warmer SST). The mixed and stratified areas are separated by fronts, indicated by red lines (Figure 1 of Rippeth *et al.* (2005)).

and neglecting eddy diffusivity, a diffusion equation with variable horizontal diffusivity was found for the depth of isopycnals outside of the surface Ekman layer.

Later, Young (1994) derived the subinertial mixed layer approximation to consider the effect of horizontal salinity and temperature gradients on shear and stratification in the mixed layer. He used a simple vertical mixing parametrisation which assumed that quantities evolve towards their depth averaged values at a rate linearly proportional to their departure from this depth average. Separate timescales for vertical mixing and inertia were considered and analytic solutions were given in terms of their ratio using an asymptotic expansion in small Rossby number. For a vertically-sheared flow in thermal wind balance, vertical mixing of momentum leads to an ageostrophic secondary circulation. The secondary circulation acts to restratify the mixed layer, a tendency which is balanced by vertical mixing of buoyancy to leading order. The vertically-sheared cross-front flow associated with the secondary circulation and vertical

mixing of buoyancy work together to spread the front via shear dispersion (Young *et al.*, 1982; Taylor, 1953). The shear dispersive spreading of fronts was examined in Ferrari & Young (1997) using an 'intermittent mixing' parametrisation where the tracers are advected freely until time $t = t_{mix}$ where the vertical tracer profile is instantaneously set to its vertical average and the process repeated.

In the limit of rapid mixing, the dominant balance in the subinertial mixed layer approximation is between the hydrostatic pressure gradient, the Coriolis force and the vertical mixing of momentum. This quasi-steady balance, recently termed the 'turbulent thermal wind' (TTW) or 'generalised Ekman' balance has been seen in models and observations of ocean fronts (Cronin & Kessler, 2009; Taylor & Ferrari, 2010; Gula *et al.*, 2014; McWilliams *et al.*, 2015; Wenegrat & McPhaden, 2016*b*) where the vertical momentum fluxes are associated with small-scale turbulence. As we show, TTW balance arises as the small-Ro and small-aspect-ratio limit of the momentum equations, corresponding to a shallow strongly rotating flow, as described earlier by Charney (1973).

McWilliams (2017) extended the previous analysis by combining the generalised nonlinear TTW equations with an Omega equation (ΩE) to construct a diagnostic framework to analyze the frontogenetic tendency and secondary circulation for fronts and filaments. For a given buoyancy field, the velocity fields were decomposed into TTW and ΩE components and an iterative procedure was used to numerically converge to the diagnostic secondary circulation. This procedure allowed the velocity field to be diagnosed for an imposed buoyancy field, boundary conditions and an externally imposed strain flow. By diagnosing the time-tendency, McWilliams (2017) showed that the ageostrophic secondary circulation associated with TTW balance could drive frontogenesis. While this analysis allowed the diagnosis of the instantaneous time tendency, it did not examine the temporal evolution of the front.

Other recent studies have examined the evolution of submesoscale filaments in TTW balance using numerical simulations with parametrised (McWilliams *et al.*, 2015) and partially-resolved (Sullivan & McWilliams, 2018) turbulence. These studies found that the TTW circulation is associated with convergent surface flow and downwelling along the centre of the filament. This induces frontogenesis which is eventually arrested by the enhancement of turbulence through small scale shear instabilities (Sullivan & McWilliams, 2018). The filament was subsequently seen to decay with the initial frontogenetic phase lasting less than a day.

Surface wind and buoyancy forcing can have a strong influence on the evolution of ocean fronts. For example, Thomas & Lee (2005) showed that when the surface wind stress is aligned with the thermal wind (in the along-front direction), the resulting Ekman flow destabilises the water column resulting in convection which, combined with Ekman pumping, drives a frontogenetic secondary circulation. This secondary circulation can spontaneously form very sharp fronts and also results in large vertical velocities. Thomas & Ferrari (2008) examined the relative influence of wind-driven circulation and a horizontal strain flow on the secondary circulation and stratification at ocean fronts and found that wind-driven circulation can dominate strain-driven frontogenesis for typical ocean conditions.

Surface buoyancy fluxes and wind stresses are the primary drivers of small scale instabilities and generators of mixed layer turbulence (Large *et al.*, 2011). However, observations by D'Asaro *et al.* (2011) and numerical work by Capet *et al.* (2008*b*) suggests that boundary layer turbulence can be significantly enhanced by the presence of fronts and is further increased by the intensification of surface buoyancy gradients during frontogenesis (Sullivan & McWilliams, 2018). Surface fluxes and wind stresses have been used to drive turbulent mixing in many large-eddy simulations (LES) of ocean fronts (Sullivan & McWilliams, 2018; Thomas *et al.*, 2013; Taylor & Ferrari, 2011) where the properties of sub-grid scale turbulence are parametrised in terms of an eddy viscosity.

1.2 Mixed layer instabilties

The ocean surface mixed layer (SML) is a weakly stratified region that forms the upper layer of the ocean. It is homogenised by intense small-scale turbulence generated by a wide variety of processes including convection, wind stress, breaking waves, evaporation and ice formation. This elevated level of turbulence leads to the nearly vertically uniform density field that characterises the mixed layer (Shay & Gregg, 1986; Kato & Phillips, 1969; Thorpe, 2005). The depth of the SML varies between around 10m and 500m due to variations in the strength of the turbulence with position and season and variation in the stratification controlling the depth to which turbulence can penetrate (Kato & Phillips, 1969; de Boyer Montégut *et al.*, 2004). The spatial and seasonal variation of the mixed layer depth is shown in Fig. 1.4 from de Boyer Montégut *et al.* (2004).

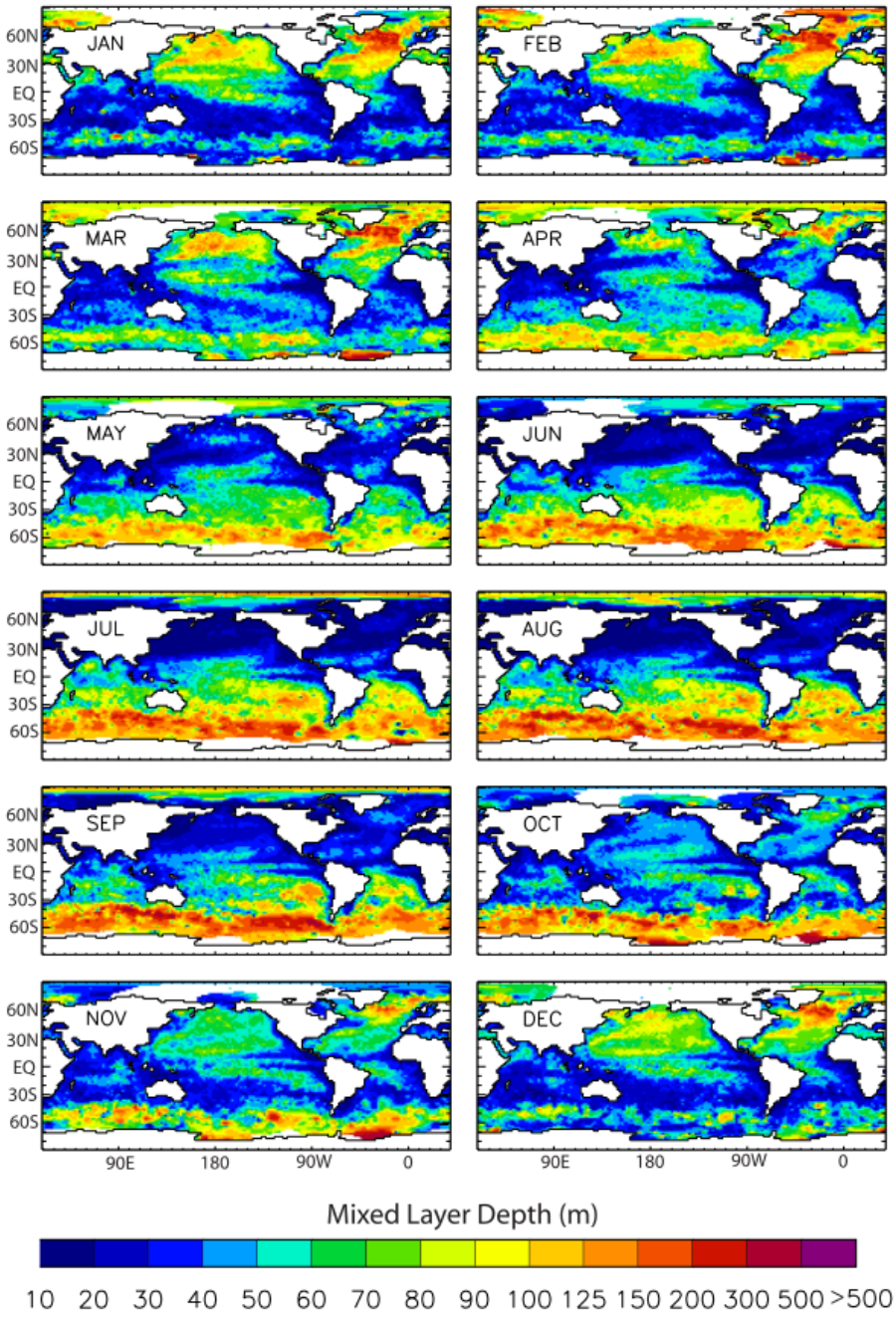

Fig. 1.4 Mixed layer depth (MLD) climatology estimated from observational profiles (Figure 5 of de Boyer Montégut *et al.* (2004)).

The SML plays a central role in the climate system by mediating transfers of heat, carbon, and other important tracers between the atmosphere and deep ocean and influencing the rate of primary production (Lorbacher *et al.*, 2006; Sverdrup, 1953).

The mixed layer also contains horizontal density gradients (e.g. Rudnick & Ferrari (1999)) in the form of fronts on a wide range of horizontal scales (e.g. Callies & Ferrari (2013)). The available potential energy associated with the horizontal density gradients fuels mixed layer baroclinic instability (or MLI) (Boccaletti *et al.*, 2007; Fox-Kemper *et al.*, 2008) which generates submesoscale eddies while re-stratifying the mixed layer. Although MLI develops in a highly turbulent environment, most previous theoretical studies of MLI have neglected the influence of small-scale turbulence.

Observations and numerical simulations have reported a strong seasonal cycle in submesoscale activity (Capet *et al.*, 2008*a*; Mensa *et al.*, 2013; Sasaki *et al.*, 2014; Callies *et al.*, 2015; Thompson *et al.*, 2016). Factors that could modulate submesoscale instabilities include the mixed layer depth, horizontal density gradients, and turbulent mixing. While the growth rate for MLI does not depend on the mixed layer depth (Fox-Kemper *et al.*, 2008), the potential energy available for release by MLI does (Callies *et al.*, 2015). It remains unclear whether MLI is less energetic and more difficult to detect in the summer, or whether it is arrested entirely.

Recently Callies *et al.* (2016) used a two layer Quasi-Geostrophic (QG) model to explore how baroclinic mixed layer instability energises submesoscale turbulence. Interestingly, their model results are consistent with available observations, despite using the QG limit of small Rossby number to describe structures with a Rossby number in the range of $0.1 - 1$. This suggests that QG dynamics may be useful to qualitatively describe submesoscale processes, although non-QG dynamics are still needed to describe phenomena such as submesoscale frontogenesis (Shakespeare & Taylor, 2013; McWilliams, 2017) and ageostrophic instabilities (e.g. symmetric instability (Taylor & Ferrari, 2010)).

Young & Chen (1995) used the sub-inertial mixed layer model from Young (1994) to study baroclinic instability associated with horizontal heat and salt gradients. For simplicity only cases of very strong and very weak mixing were considered, with the strong mixing corresponding to a 'slab' mixed layer model with no vertical variation and the weak mixing corresponding to a geostrophically balanced mixed layer. They speculated that the classical Eady model of baroclinic instability (Eady, 1949; Vallis, 2006) should be recovered in the limit of weak mixing. However, this connection was not explicitly made since there is no background vertical stratification in the sub-inertial

mixed layer model and the Richardson number is large (and hence the stratification is strong) in the limit of small Rossby numbers in the Eady model.

1.3 Overview and objectives

Our objective is to develop a theoretical description of the evolution of an isolated mixed layer front in TTW balance. We begin in Chapter 2 by introducing the analytic model used to describe a simple mixed layer front. We use two different parametrisations to model the effects of small scale turbulence. The first is a turbulent diffusivity parametrisation in which the effects of turbulence are modelled as a depth-dependent viscosity and diffusivity (Charney, 1973; Garrett & Loder, 1981; Thompson, 2000) while the second is a vertical relaxation parametrisation in which turbulence acts to relax the velocity and buoyancy profiles towards their depth-averaged value (Young, 1994; Young & Chen, 1995).

In Chapter 3 we use the turbulent diffusivity parametrisation to consider the effects of small-scale turbulence on the evolution of an initially balanced density front with no surface forcing. We aim to develop an asymptotically consistent model for the evolution of a front in the low Rossby number and leading order Ekman number regime. The predictions and validity of this model are examined in Chapter 4 using direct numerical simulations (DNS) of the full momentum and buoyancy equations. As well as determining the evolution of the background density field, we aim to examine dynamically important processes such as the up/down-welling that typically occurs at the edges of fronts (Mahadevan & Tandon, 2006; Capet *et al.*, 2008*a*) and the surface frontogenesis that can result from the adjustment towards a balanced state (Hoskins & Bretherton, 1972; Blumen, 2000; Shakespeare & Taylor, 2013).

In Chapter 5 we extend the analytic model from Chapter 3 to include the effects of surface forcing due to heat flux and wind stress. Our aim is to determine how these processes modify the frontal evolution and if they can act to maintain a front in equilibrium. Numerical simulations are used to test our predictions and typical ocean parameters are used to determine if the parameter regimes considered are relevant to the global oceans.

We also aim to examine the influence of turbulence on mixed layer instabilities in Chapter 6. Here, we use the linear relaxation model to examine baroclinic instability in the presence of vertical mixing. In the case of no turbulent mixing, we expect this instability to reduce to the classical Eady instability (Eady, 1949), and make this

link explicitly. Using direct numerical simulations (DNS) we test our predictions and examine the energetics of the system and the wavenumber cutoff of the instability. In order to connect our results to observations we determine growth rates for instability in various frontal systems and attempt to link this to the appearance of submesoscale activity.

Finally in Chapter 7 we summarise our results and discuss the potential applications and limitations of our work. We also comment on possible areas for future work.

Chapter 2

The Model

In this chapter we discuss the theoretical model of a front used in later chapters. We consider an idealised frontal geometry consisting of an incompressible fluid bounded from above and below by rigid horizontal surfaces in a reference frame rotating about the vertical (z) axis. The fluid density varies continuously across a front and we consider cases of both a single isolated front and a linear horizontal density gradient. This geometry is a canonical configuration for studies of frontal dynamics (e.g. Hoskins & Bretherton (1972); Blumen (2000)). For simplicity, we neglect the horizontal component of the rotation vector, the so-called 'traditional approximation' (Salmon, 1998).

We assume that density changes can be represented by a single scalar equation, invoking a linear equation of state, and that variations in density are small compared with a reference value, invoking the Boussinesq approximation. We let $b \equiv -g\rho'/\rho_0$ denote the fluid buoyancy, where ρ_0 is a constant reference density, ρ' denotes departures from ρ_0 and $\rho' << \rho_0$. The effects of turbulence will be parametrised in two different ways as described below.

We can non-dimensionalise the governing equations using a horizontal length scale L, vertical length scale H and buoyancy scale Δb, with the horizontal velocity scale $U = \Delta b H/(fL)$, vertical velocity scale $W = UH/L = \Delta b H^2/(fL^2)$, pressure scale $P = fUL = \Delta b H$ and timescale $T = L/U = fL^2/(H\Delta b)$ for Coriolis parameter f. We define the Rossby number, $\mathrm{Ro} = U/(fL)$, using the geostrophic shear, $U/H = \partial b/\partial x/f = \Delta b/(fL)$ and write the aspect ratio, H/L, as ϵ. We include a vertical background stratification, N^2, represented by the Burger number $\mathrm{Bu} = N^2H^2/(f^2L^2)$.

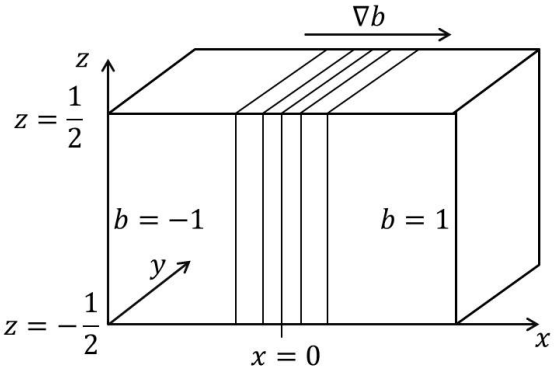

Fig. 2.1 Non-dimensional frontal geometry.

This gives the following non-dimensional equations (Charney, 1973):

$$\mathrm{Ro}\frac{Du}{Dt} - v = -\frac{\partial p}{\partial x} + \mathcal{L}_u u' + \epsilon^2 \mathrm{E}\,\nabla_H\cdot[\nu\nabla_H u], \tag{2.1a}$$

$$\mathrm{Ro}\frac{Dv}{Dt} + u = -\frac{\partial p}{\partial y} + \mathcal{L}_u v' + \epsilon^2 E\,\nabla_H\cdot[\nu\nabla_H v], \tag{2.1b}$$

$$\mathrm{Ro}\,\epsilon^2\frac{Dw}{Dt} = -\frac{\partial p}{\partial z} + b + \epsilon^2\mathcal{L}_u w' + \epsilon^4 E\,\nabla_H\cdot[\nu\nabla_H w], \tag{2.1c}$$

$$\mathrm{Ro}\frac{Db}{Dt} + \mathrm{Bu}\,w = \mathcal{L}_b b' + \frac{\epsilon^2\mathrm{E}}{\mathrm{Pr}}\,\nabla_H\cdot[\kappa\nabla_H b], \tag{2.1d}$$

$$\frac{\partial u}{\partial x} + \frac{\partial v}{\partial y} + \frac{\partial w}{\partial z} = 0, \tag{2.1e}$$

for material derivative

$$\frac{D}{Dt} = \frac{\partial}{\partial t} + u\frac{\partial}{\partial x} + v\frac{\partial}{\partial y} + w\frac{\partial}{\partial z}, \tag{2.2}$$

and horizontal gradient

$$\nabla_H = \left(\frac{\partial}{\partial x}, \frac{\partial}{\partial y}, 0\right), \tag{2.3}$$

and parameters given in Table 2.1. The depth-dependent component of a field is denoted by $\phi' = \phi - \overline{\phi}$ where

$$\overline{\phi} = \int_{-1/2}^{1/2} \phi\, dz, \tag{2.4}$$

denotes a depth average across the non-dimensional vertical domain $z \in [-1/2, 1/2]$. The vertical mixing terms are written in terms of the linear operators $\mathcal{L}_u$ and $\mathcal{L}_b$ which are assumed to depend only on z and be vertically symmetric. Note that the vertical mixing terms only act on the deviations from the depth averages. We use the vertical

Parameter	Rossby No.	Ekman No.	Prandtl No.	Aspect Ratio	Burger No.
Symbol	Ro	E	Pr	ϵ	Bu
Definition	$\epsilon\Delta b/f^2L$	$\overline{\nu}^*/fH^2$	$\overline{\nu}^*/\overline{\kappa}^*$	H/L	N^2H^2/f^2L^2

Table 2.1 Definitions of the dimensionless parameters and their values for buoyancy difference, Δb, Coriolis parameter, f, horizontal lengthscale, L, vertical lengthscale, H, background vertical stratification, N^2, and depth-averaged dimensional viscosity and diffusivity, $\overline{\nu}^*$ and $\overline{\kappa}^*$.

boundary condition that $w = 0$ at $z = \pm 1/2$. The vertical boundary conditions on (u, v, b) are chosen to be consistent with the vertical mixing parametrisation.

The last terms in the momentum and buoyancy equations describe horizontal viscosity and diffusion. The dimensionless viscosity, ν, and diffusivity, κ, are nondimensionalised by their dimensional depth-average values, $\overline{\nu}^*$ and $\overline{\kappa}^*$ respectively. The Ekman number, E, and Prandtl number, Pr, are given by $\mathrm{E} = \overline{\nu}^*/(fH^2)$ and $\mathrm{Pr} = \overline{\nu}^*/\overline{\kappa}^*$.

Some care is needed when interpreting the background stratification included through the Burger number. The parametrised vertical mixing terms are written in terms of b, the departure from the background stratification. Hence the mixing terms do not influence the background stratification, N^2.

While this system is three dimensional, we will occasionally consider the two dimensional $(x-z)$ case where the x-axis is aligned with the local density (or buoyancy) gradient. Motivated by the observation that variations aligned with the frontal axis are much smaller than cross-front variations, we will neglect along-front (y) derivatives, although we will retain all three components of the velocity vector. We then assume without loss of generality that the low-buoyancy region is on the left of the front while the high-buoyancy region is on the right (see Fig. 2.1).

We now describe the two different parametrisations used in later chapters.

2.1 Diffusive parametrisation

Here we describe the effects of turbulence using an imposed turbulent viscosity, ν, and diffusivity, κ, which we assume to depend only on the depth, z. It should be noted that, while ν and κ will be assumed to be constant in time and independent of both horizontal directions, our primary motivation is to study the influence of small-scale turbulence on the evolution of the front. By using a time-independent ν and κ, we are able to isolate the influence of a turbulent viscosity and diffusivity on the evolution of the front, without allowing the feedback associated with the front to alter the

properties of small-scale turbulence. This assumption is artificial but greatly simplifies the analysis. When considering constant ν and κ (as in Thompson (2000)), the setup can also be viewed as a laboratory-scale analogue with molecular ν and κ.

The effects of wind and surface heat fluxes are represented by a 2-dimensional wind stress vector, $\boldsymbol{\tau}$, and a surface heat flux Q. Note that we could take $\boldsymbol{\tau}$ and Q to depend on (x, y) and still obtain solutions, although here we take constant values for simplicity.

For this parametrisation we have

$$\mathcal{L}_u(*) = \mathrm{E}\,\frac{\partial}{\partial z}\left(\nu(z)\frac{\partial(*)}{\partial z}\right), \tag{2.5}$$

and

$$\mathcal{L}_b(*) = \frac{\mathrm{E}}{\mathrm{Pr}}\,\frac{\partial}{\partial z}\left(\kappa(z)\frac{\partial(*)}{\partial z}\right), \tag{2.6}$$

where we note that here ν and κ are normalised such that $\overline{\nu} = \overline{\kappa} = 1$. The magnitudes of the dimensional viscosity and diffusivity, $\overline{\nu}^*$ and $\overline{\kappa}^*$, are described by E and Pr as shown in Table 2.1. We use top and bottom boundary conditions

$$\mathrm{E}\nu\frac{\partial \mathbf{u}_H}{\partial z} = \boldsymbol{\tau}, \tag{2.7a}$$

$$\frac{\mathrm{E}\kappa}{Pr}\frac{\partial b}{\partial z} = Q, \tag{2.7b}$$

imposed at $z = 1/2$ and $z = -1/2$. The horizontal velocity, $\mathbf{u}_H$, is given by $(u, v, 0)$ and the stress is a 2D vector given by $\boldsymbol{\tau} = (\tau_x, \tau_y, 0)$. Note that we have applied the same wind stress and buoyancy flux to both surfaces. This is for mathematical convenience as it makes the problem vertically symmetric rather than to represent any physical processes.

2.2 Vertical relaxation parametrisation

For the vertical relaxation parametrisation we follow Young (1994) and parametrise vertical mixing by adding a forcing term to the RHS of the momentum and buoyancy equations which acts to relax the velocity and buoyancy to the local depth-average. The rates of relaxation for buoyancy and velocity are μ_b and μ_u, respectively. This parametrisation is chosen largely for mathematical convenience though it is not conspicuously less realistic than an eddy diffusivity parametrisation. We assume that the

buoyancy and velocity relaxation occur at rates of μ_b and μ_u respectively and write

$$\mathcal{L}_u(*) = -\alpha(*), \tag{2.8}$$

and

$$\mathcal{L}_b(*) = -\frac{\alpha}{\mathrm{Pr}_\alpha}(*), \tag{2.9}$$

for relaxation ratio, $\alpha = \mu_u/f$, and relaxation Prantl number, $\mathrm{Pr}_\alpha = \mu_u/\mu_b$. Due to the absence of higher order spatial derivatives we are unable to apply boundary conditions to the buoyancy or horizontal velocity but can apply the condition $w = 0$ at the top and bottom surfaces.

Our approach differs from Young (1994) where it was assumed that the ratio of the buoyancy mixing timescale to the advection timescale was small compared to one, but large compared to the Rossby number, such that

$$\frac{1/\mu_b}{T} = \frac{\mathrm{Ro}\,\mathrm{Pr}_\alpha}{\alpha} \gg \mathrm{Ro}. \tag{2.10}$$

Since Young makes no assumptions about the size of α, this results in the requirement that Pr_α is large unless α is small. Motivated by simulations and experiments of turbulent mixing in weakly stratified flows, we instead assume that $\mathrm{Pr}_\alpha = O(1)$ (Schumann & Gerz, 1995; Venayagamoorthy & Stretch, 2010). This choice of Pr_α allows us to consider the case where the mixing rates are similar for any value of α, although we are unable to solve the resulting equations to the same order in Ro as Young (1994).

Chapter 3

The evolution of a front in turbulent thermal wind balance: theory

3.1 Introduction

The objective of this chapter is to develop a theoretical description of the evolution of an unforced, isolated front in TTW balance. This can be viewed as an extension to the diagnostic analysis by McWilliams (2017), although we allow the front to evolve in time and restrict our analysis to small Rossby numbers where TTW balance holds. However, our analysis does extend to large Ekman numbers, and in this way our study can be viewed as a generalisation of the Garrett & Loder (1981) model. For simplicity, we represent small-scale turbulence through prescribed viscosity and diffusivity which are allowed to vary in depth but are assumed to be independent of time and both horizontal directions.

We find that frontogenesis, or intensification of the surface density gradient, occurs during a brief transient 'adjustment' period. After this transient period, we find that the front spreads through shear dispersion associated with the vertical diffusivity and the vertically-sheared cross-front velocity, as described by Young (1994). Here, our focus will be on the spreading regime, rather than the frontogenetic regime, conditions for which were examined in detail in McWilliams (2017). In a region of frontogenesis the cross front length scales can become small corresponding to an order-one Rossby number and advection by the secondary circulation contributes at leading order. We instead consider an unforced front with no sharp surface gradients in which the horizontal length scale can be taken as the frontal width and the resulting Rossby number is small.

We find that when the viscosity and diffusivity are sufficiently large, the front spreads through shear dispersion associated with the vertical diffusivity and the vertical shear of the cross-front velocity, a process also described by Young (1994) in the context of the SML equations. Further, we find that the density evolves towards a self-similar profile, with the density being an approximately piecewise linear function of the cross-front distance with a relatively constant density gradient inside the front and large curvature at the edges of the front. The vertical velocity is intensified in regions of large curvature in the cross-front density profile which occur at the edges of the front. This is consistent with the instantaneous TTW balance associated with the self-similar density profile.

In Section 3.3 we describe our approach to finding a solution using an expansion in Rossby number and a multiple time scale analysis. In Sections 3.3.1 to 3.3.3 we consider the balances at $O(1)$, $O(\mathrm{Ro})$ and $O(\mathrm{Ro}^2)$ which we find to be sufficient to determine a solution to leading order in velocity and first order in buoyancy. We find that the governing equation for the depth-averaged buoyancy can be solved using a similarity solution which we calculate in Section 3.3.5.

Analytic solutions for velocity and buoyancy are found in terms of vertical structure functions. These can be solved for analytically for simple viscosity and diffusivity profiles while numerical solutions are required in general. Finally in Section 3.4 we discuss our results.

3.2 Setup

In this chapter we use the diffusive parametrisation on a three-dimensional domain for an unforced front with no background stratification. Taking the buoyancy flux Q, wind stress $\boldsymbol{\tau}$ and Burger number Bu to be zero, we obtain governing equations:

$$\mathrm{Ro}\frac{Du}{Dt} - v = -\frac{\partial p}{\partial x} + \mathrm{E}\,\nabla_\epsilon \cdot (\nu \nabla_\epsilon u)\,, \tag{3.1a}$$

$$\mathrm{Ro}\frac{Dv}{Dt} + u = -\frac{\partial p}{\partial y} + \mathrm{E}\,\nabla_\epsilon \cdot (\nu \nabla_\epsilon v)\,, \tag{3.1b}$$

$$\mathrm{Ro}\,\epsilon^2\frac{Dw}{Dt} = -\frac{\partial p}{\partial z} + b + \epsilon^2 \mathrm{E}\,\nabla_\epsilon \cdot (\nu \nabla_\epsilon w)\,, \tag{3.1c}$$

$$\mathrm{Ro}\frac{Db}{Dt} = \frac{\mathrm{E}}{\mathrm{Pr}}\,\nabla_\epsilon \cdot (\kappa \nabla_\epsilon b)\,, \tag{3.1d}$$

$$\frac{\partial u}{\partial x} + \frac{\partial v}{\partial y} + \frac{\partial w}{\partial z} = 0, \tag{3.1e}$$

with boundary conditions of no stress and no buoyancy flux at $z = \pm 1/2$. The operator ∇_ϵ is given by

$$\nabla_\epsilon = \left(\epsilon \frac{\partial}{\partial x}, \epsilon \frac{\partial}{\partial y}, \frac{\partial}{\partial z} \right). \tag{3.2}$$

We allow arbitrary values of Pr, but will highlight the case where Pr = 1. For simplicity we later restrict to the case of a single isolated front on a two-dimensional $(x - z)$ domain. We then assume without loss of generality that the low-buoyancy region is on the left of the front while the high-buoyancy region is on the right.

3.3 Analytic Solution

Here, we analyze Eq. (3.1) using a multiple-time-scale asymptotic analysis with Ro as our small parameter and $\epsilon = O(\mathrm{Ro})$. Unlike the Rossby number, we do not assume that the Ekman number is small, and specifically consider $\mathrm{E} = O(1)$. Later, in Section 3.3.4 we will discuss the limit of $\mathrm{E} = O(\mathrm{Ro})$ and the connection with previous work by Garrett & Loder (1981).

After expanding $\mathbf{u}$ and b in powers of Ro, we find that there are two relevant timescales: a fast timescale, $\tau = t/\mathrm{Ro}$, representing vertical diffusion and initial adjustment, and a slow timescale, $T = \mathrm{Ro}\, t$, representing horizontal shear dispersion and spreading. The intermediate timescale, t, does not appear in the analysis.

We can use these new timescales to expand the time derivative as

$$\frac{\partial}{\partial t} = \frac{1}{\mathrm{Ro}} \frac{\partial}{\partial \tau} + \mathrm{Ro} \frac{\partial}{\partial T}. \tag{3.3}$$

The velocity and buoyancy are also expanded in powers of Ro,

$$\mathbf{u} = \mathbf{u}_0 + \mathrm{Ro}\, \mathbf{u}_1 + \ldots, \quad \text{and} \quad b = b_0 + \mathrm{Ro}\, b_1 + \ldots. \tag{3.4}$$

For simplicity, we restrict our attention to initial conditions where the buoyancy is independent of depth, i.e. $b|_{t=0} = f(x, y)$, although the initial velocity can have arbitrary depth dependence. After using the expansions introduced above, we collect terms in the governing equations (Eq. (3.1)) of like order in Ro. The sections below describe solutions of the resulting equations for the leading-order contributions to velocity and buoyancy.

3.3.1 The O(1) balance

We now consider the leading order buoyancy and momentum balances with $O(1)$ terms. The steady version of this balance is the TTW balanced described by Gula *et al.* (2014) and McWilliams (2017). The analysis in this section extends their work by including time dependence and unbalanced initial conditions. We find that the time dependence occurs on the fast timescale, τ, and that as $\tau \to \infty$, the steady TTW balance is recovered.

Buoyancy

The $O(1)$ terms in the buoyancy conservation equation (Eq. (3.1d)) are

$$\frac{\partial b_0}{\partial \tau} = \frac{\mathrm{E}}{\mathrm{Pr}} \frac{\partial}{\partial z} \left(\kappa \frac{\partial b_0}{\partial z} \right). \tag{3.5}$$

This is a diffusion equation and since the initial state is depth-independent the solution is of the form

$$b_0 = b_0(x, y, T) \quad \text{where} \quad b_0(x, y, 0) = f(x, y), \tag{3.6}$$

which is vertically homogeneous and hence not affected by vertical diffusion. We note that a z-dependent initial buoyancy field will result in diffusion towards a vertically homogeneous state on the fast timescale τ; hence, the leading order buoyancy will be depth-independent after some fast initial adjustment. Taking a depth-dependent initial b_0 will not change the long term behaviour of the system and will just add additional transients to the velocity fields and higher-order buoyancy terms.

Velocity

The $O(1)$ terms in the momentum and continuity equations (Eqs. (3.1a) to (3.1c) and (3.1e)) are

$$\frac{\partial u_0}{\partial \tau} - v_0 = -\frac{\partial p_0}{\partial x} + \mathrm{E} \frac{\partial}{\partial z} \left(\nu \frac{\partial u_0}{\partial z} \right), \tag{3.7a}$$

$$\frac{\partial v_0}{\partial \tau} + u_0 = -\frac{\partial p_0}{\partial y} + \mathrm{E} \frac{\partial}{\partial z} \left(\nu \frac{\partial v_0}{\partial z} \right), \tag{3.7b}$$

$$-\frac{\partial p_0}{\partial z} + b_0 = 0, \tag{3.7c}$$

$$\frac{\partial u_0}{\partial x} + \frac{\partial v_0}{\partial y} + \frac{\partial w_0}{\partial z} = 0. \tag{3.7d}$$

Eq. (3.7c) is hydrostatic balance, and since b_0 is independent of z, this gives

$$p_0 = b_0 z, \tag{3.8}$$

using $z = 0$ as the reference level. It can be shown (see Section 5.4) that a nonzero p_0 at $z = 0$ describes advection by a depth-independent background flow. It should be noted that the $O(1)$ momentum equations are linear in the horizontal velocity, $\mathbf{u}_{H0} = (u_0, v_0, 0)$. Through the hydrostatic relation, the horizontal pressure gradient is a linear function of the horizontal buoyancy gradient. Therefore, the horizontal velocity is a linear function of the horizontal buoyancy gradient, i.e.

$$\begin{pmatrix} u_0 \\ v_0 \end{pmatrix} = -\sqrt{\mathrm{E}} \begin{pmatrix} A_1(\zeta,\tau) & A_2(\zeta,\tau) \\ B_1(\zeta,\tau) & B_2(\zeta,\tau) \end{pmatrix} \begin{pmatrix} \frac{\partial b_0}{\partial x} \\ \frac{\partial b_0}{\partial y} \end{pmatrix}, \tag{3.9}$$

where $\zeta = z/\sqrt{\mathrm{E}}$. By splitting Eqs. (3.7a) and (3.7b) into parts linear in $\partial b_0/\partial x$ and $\partial b_0/\partial y$, we obtain the system of equations

$$L_\nu A_1 = B_1 + \zeta, \tag{3.10a}$$
$$L_\nu A_2 = B_2, \tag{3.10b}$$
$$L_\nu B_1 = -A_1, \tag{3.10c}$$
$$L_\nu B_2 = -A_2 + \zeta, \tag{3.10d}$$

where

$$L_\nu = \frac{\partial}{\partial \tau} - \frac{\partial}{\partial \zeta}\left(\nu \frac{\partial}{\partial \zeta}\right), \tag{3.11}$$

is a diffusion operator. These equations can be combined to give

$$-L_\nu^2 K(\zeta,\tau) = K(\zeta,\tau) + \zeta, \tag{3.12}$$

where $B_1 = -A_2 = K$ and $A_1 = B_2 = -L_\nu K$ and $K(\zeta,\tau)$ is a function to be determined by applying stress-free boundary conditions at $z = \pm 1/2$ (see Section A.1). The $O(1)$ horizontal velocity can then be written as

$$\mathbf{u}_{H0} = -\sqrt{\mathrm{E}}\,\mathbf{K}(\zeta,\tau) \cdot \nabla_H b_0, \tag{3.13}$$

where

$$\mathbf{K} = \begin{pmatrix} -L_\nu K & -K \\ K & -L_\nu K \end{pmatrix}, \tag{3.14}$$

and ∇_H is the horizontal gradient operator. It is instructive to re-write Eq. (3.13) as

$$\mathbf{u}_{H0} = -\sqrt{\mathrm{E}}\,\left[-L_\nu K\,\nabla_H b_0 + K\,\hat{\mathbf{z}}\times\nabla_H b_0\right], \tag{3.15}$$

hence, $-L_\nu K$ describes the velocity component that is locally perpendicular to the front while K describes the velocity that is locally orientated along the front.

From mass conservation we can solve for w_0 in terms of $K(\zeta,\tau)$,

$$\frac{\partial w_0}{\partial z} = -\nabla_H\cdot\mathbf{u}_{H0} = -\sqrt{\mathrm{E}}\,L_\nu K(z',\tau)\,\nabla_H^2 b_0, \tag{3.16}$$

which can be integrated to obtain

$$w_0 = -\sqrt{\mathrm{E}}\left(\int_{-1/2}^{z} L_\nu K(z',\tau)\,dz'\right)\nabla_H^2 b_0. \tag{3.17}$$

To complete the solution for the $O(1)$ velocity, we need to solve for $K(\zeta,\tau)$. We begin by considering the steady-state solution obtained by neglecting the time derivatives in Eqs. (3.7a) and (3.7b) and denoting the steady-state solution $K_0(\zeta)$. Eq. (3.12) becomes

$$-\frac{\partial}{\partial\zeta}\left(\nu\frac{\partial^2}{\partial\zeta^2}\left(\nu\frac{\partial}{\partial\zeta}K_0\right)\right) = K_0+\zeta. \tag{3.18}$$

For a general $\nu(\zeta)$ we can solve this equation numerically, subject to boundary conditions $K_0'=0$ and $(\nu K_0')''=0$ at $z=\pm 0.5$. The steady-state vertical velocity is given by

$$w_0 = \mathrm{E}\,\nu(z)\,K_0'\left(z/\sqrt{\mathrm{E}}\right)\nabla_H^2 b_0. \tag{3.19}$$

Since $K_0'<0$ in the interior of the domain, w_0 describes upwelling for negative buoyancy curvature and downwelling for positive curvature.

We now return to the general time-dependent case described by Eq. (3.12) and let $K(\zeta,t)=K_1(\zeta,t)+K_0(\zeta)$ for steady-state solution K_0. Eq. (3.12) becomes

$$-\frac{\partial}{\partial\zeta}\left(\nu\frac{\partial^2}{\partial\zeta^2}\left(\nu\frac{\partial}{\partial\zeta}K_0\right)\right) - L_\nu^2 K_1 = K_0+K_1+\zeta, \tag{3.20}$$

hence,

$$-L_\nu^2 K_1 = K_1, \tag{3.21}$$

with boundary conditions $K_1' = (L_\nu K_1)' = 0$ at $z = \pm 0.5$. On substituting for L_ν, we obtain

$$\left(\frac{\partial}{\partial\tau} - \mathrm{E}\frac{\partial}{\partial z}\nu\frac{\partial}{\partial z}\right)^2 K_1 = -K_1, \tag{3.22}$$

which we solve using separation of variables. Seeking solutions of the form $K_1 = \mathcal{T}(\tau)\mathcal{Z}(z)$, we find

$$K_1 = \sum_{n=0}^{\infty} B_n e^{-\mathrm{E}\lambda_n\tau}\left[\cos\tau + \mathrm{E}\lambda_n \sin\tau\right]\mathcal{Z}_n(z), \tag{3.23}$$

where $\mathcal{Z}_n$ is an eigenfunction of the linear system

$$\frac{\partial}{\partial z}\left(\nu\frac{\partial\mathcal{Z}_n}{\partial z}\right) = -\lambda_n\mathcal{Z}_n, \tag{3.24}$$

with eigenvalue λ_n. The boundary conditions discretise the modes and lead to an orthogonality relation

$$\int_{-1/2}^{1/2}\mathcal{Z}_n\mathcal{Z}_m dz = z_n^2\delta_{nm}. \tag{3.25}$$

We now consider initial conditions for $K = K_0 + K_1$ and use Eq. (3.25) to determine the coefficients B_n for each case. We denote the initial conditions $K(z,0) = \mathcal{K}(z)$. Using Eq. (3.23), we have

$$K_1(z,0) = \sum_{n=0}^{\infty} B_n\mathcal{Z}_n(z), \tag{3.26}$$

and using (Eq. (3.25)), we have

$$B_n = \frac{1}{z_n^2}\int_{-1/2}^{1/2} K_1(z,0)\mathcal{Z}(z)dz = \frac{1}{z_n^2}\int_{-1/2}^{1/2}\left[\mathcal{K}(z) - K_0(z/\sqrt{\mathrm{E}})\right]\mathcal{Z}(z)dz. \tag{3.27}$$

Combining the results given above, we can now write out the solution for $K(\zeta,\tau)$,

$$K(z,\tau) = K_0\left(z/\sqrt{\mathrm{E}}\right) + \sum_{n=0}^{\infty} B_n e^{-\mathrm{E}\lambda_n\tau}\left[\cos\tau + \mathrm{E}\lambda_n\sin\tau\right]\mathcal{Z}_n(z), \tag{3.28}$$

and the solution for $-L_\nu K$,

$$-L_\nu K(z,\tau) = \mathrm{E}\frac{\partial}{\partial z}\left(\nu\frac{\partial K_0}{\partial z}\right) + \sum_{n=0}^{\infty} B_n e^{-\mathrm{E}\lambda_n\tau}\left[\sin\tau - \mathrm{E}\lambda_n\cos\tau\right]\mathcal{Z}_n(z). \tag{3.29}$$

Some important initial conditions include stationary flow ($\mathbf{u}=0$) which corresponds to $\mathcal{K}=0$, thermal wind balance which corresponds to $\mathcal{K}=-z/\sqrt{\mathrm{E}}$, and steady TTW balance which corresponds to $\mathcal{K}=K_0$ and hence $B_n=0$. In all cases, after an initial adjustment period, the solution for $\mathbf{u}_0$ approaches steady TTW balance. The transients decay exponentially on a timescale of $\tau=O(1/\mathrm{E})$ corresponding to $t=O(\mathrm{Ro}/\mathrm{E})$.

Summary of the O(1) solution

When expanded in the limit of small Rossby number, the buoyancy conservation equation at leading order ($O(1)$) reduces to a diffusion equation on the fast timescale, τ.

In summary, the $O(1)$ velocity is

$$u_0 = -\sqrt{\mathrm{E}}\left[-L_\nu K(z,\tau)\frac{\partial b_0}{\partial x} - K(z,\tau)\frac{\partial b_0}{\partial y}\right], \tag{3.30}$$

$$v_0 = -\sqrt{\mathrm{E}}\left[\,K(z,\tau)\frac{\partial b_0}{\partial x} - L_\nu K(z,\tau)\frac{\partial b_0}{\partial y}\right], \tag{3.31}$$

where K and $-L_\nu K$ are given by Eqs. (3.28) and (3.29) and

$$w_0 = \mathrm{E}\left[\nu\,K_0'\left(z/\sqrt{\mathrm{E}}\right) - \sum_{n=0}^{\infty}\frac{B_n}{\sqrt{\mathrm{E}}}e^{-\mathrm{E}\lambda_n\tau}[-\sin\tau + \mathrm{E}\lambda_n\cos\tau]\int_{-1/2}^{z}\mathcal{Z}_n(z')dz'\right]\nabla_H^2 b_0, \tag{3.32}$$

which reduces to steady TTW balance (Eq. (3.19)), for large τ. The $\cos\tau$ and $\sin\tau$ terms correspond to inertial waves generated by departures from steady TTW balance in the initial conditions. Analytic solutions can be obtained for constant ν (see Section A.1).

It is useful to consider two limiting cases of the $O(1)$ velocity in terms of the Ekman number, E. For small E the along front velocity approaches thermal wind balance and all other velocity components become small, while for large E all velocity components become small due to the damping of motion by the high viscosity. The dependence of K_0, and hence $\mathbf{u}_0$ and ψ_0, on the Ekman number for a constant ν is given in Section A.1.

Fig. 3.1 shows the steady-state $O(1)$ velocity field (i.e. TTW balance) expressed in terms of an $x-z$ streamfunction, ψ_0, for a y-independent buoyancy field

$$b_0 = \tanh(x), \tag{3.33}$$

and constant ν with $\mathrm{E} = 0.1$. The streamfunction is defined by $u = \partial\psi/\partial z$ and $w = -\partial\psi/\partial x$, and in this case is

$$\psi_0 = -\mathrm{E}\, K_0'\left(z/\sqrt{\mathrm{E}}\right)\frac{\partial b_0}{\partial x}. \tag{3.34}$$

The streamfunction corresponds to anticlockwise circulation in the $x-z$ plane and will lead to stable stratification inside the front. There is upwelling on the high-buoyancy side of the front and downwelling on the low-buoyancy side, in regions of negative and positive curvature in the buoyancy field respectively. The along-front velocity (v_0) consists of jets perpendicular to the buoyancy gradient and is in the same direction as the thermal wind velocity but with reduced shear near the top and bottom boundaries.

To demonstrate the time-dependence of the leading order velocity field, Fig. 3.2 shows $K(z,\tau)$ for $\mathrm{E} = 0.1$ and 0.01, $\nu = 1$ and initial condition $K(z,0) = 0$. This initial condition corresponds to no flow so the system will rapidly adjust to a balanced state. Inertial waves occur with a period of 2π, corresponding to a dimensional period of $2\pi/f$, and are damped by viscosity on a timescale of $\tau = O(1/\mathrm{E}\lambda_1)$, corresponding to a dimensional decay rate of $\lambda_1\overline{\nu}/H^2$, where λ_1 is the smallest non-zero eigenvalue. For constant ν, $\lambda_1 = \pi^2 \approx 10$, and inertial waves will be observed for $\mathrm{E} \ll 0.1$. Fig. 3.2 shows that damped inertial waves occur for $\mathrm{E} = 0.01$, while for $\mathrm{E} = 0.1$, no waves are apparent since the inertial period and damping timescale are nearly equal.

3.3.2 The O(Ro) buoyancy balance

As shown above, the leading order ($O(1)$) buoyancy, b_0, is independent of depth, z. However, the leading order cross-front velocity, u_0, does exhibit depth-dependence, and this shear causes the front to 'slump' over, leading to a stable stratification, a result consistent with the SML model of Young (1994). This can be seen by solving the $O(\mathrm{Ro})$ buoyancy conservation equation, which conveniently involves just the $O(1)$ contributions to the velocity field found above.

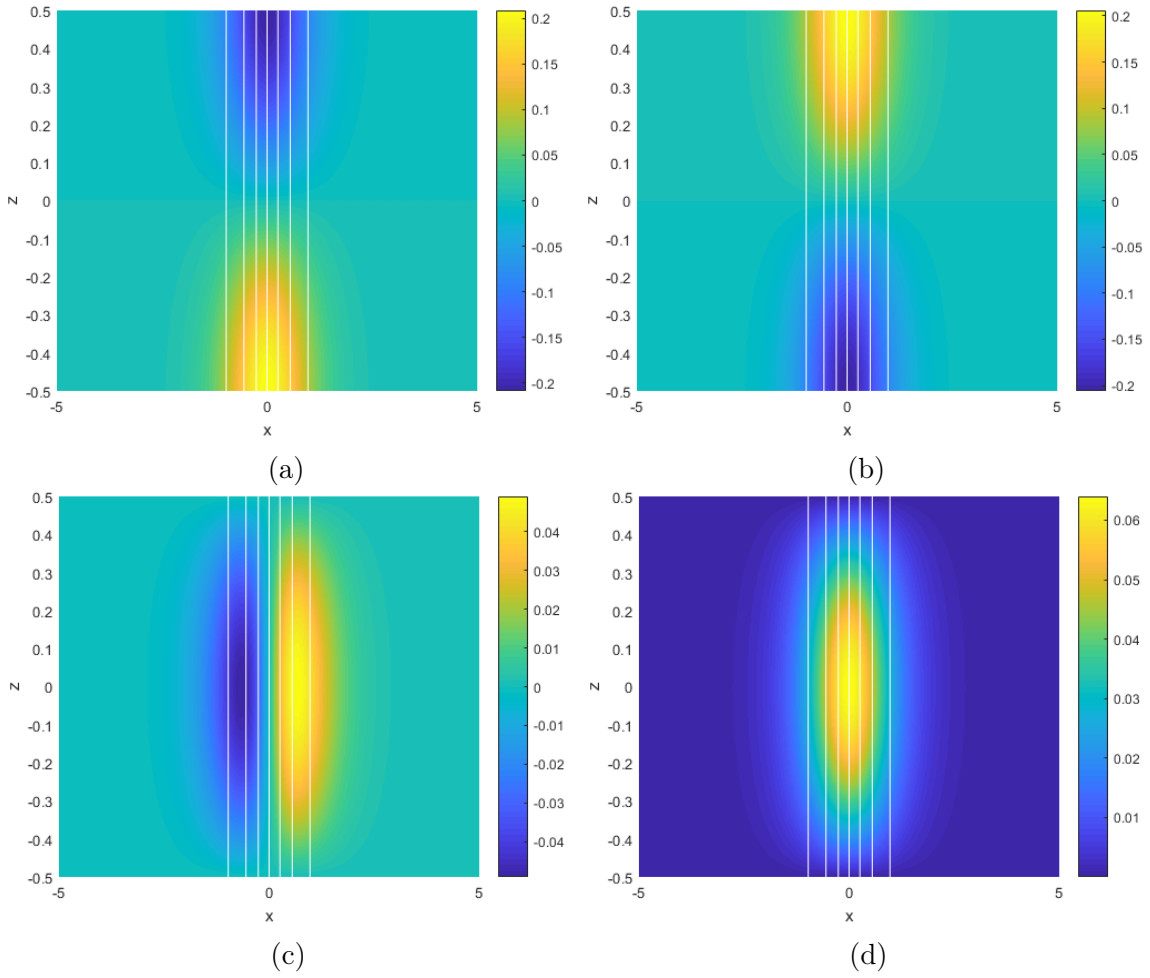

Fig. 3.1 Leading order steady (τ independent) velocity fields, u_0 (a), v_0 (b), w_0 (c) and streamfunction, ψ_0 (d), for $\mathrm{E} = 0.1$, $\nu = 1$ and $b_0 = \tanh x$.

The $O(\mathrm{Ro})$ terms in the buoyancy conservation equation are

$$\frac{\partial b_1}{\partial \tau} + u_0 \frac{\partial b_0}{\partial x} + v_0 \frac{\partial b_0}{\partial y} = \frac{\mathrm{E}}{\mathrm{Pr}} \frac{\partial}{\partial z} \left(\kappa \frac{\partial b_1}{\partial z} \right), \tag{3.35}$$

which can be re-written as the forced diffusion equation

$$\left[\frac{\partial}{\partial \tau} - \frac{\mathrm{E}}{\mathrm{Pr}} \frac{\partial}{\partial z} \left(\kappa \frac{\partial}{\partial z} \right) \right] b_1 = -\mathbf{u}_{H0} \cdot \nabla_H b_0, \tag{3.36}$$

where

$$-\mathbf{u}_{H0} \cdot \nabla_H b_0 = \sqrt{\mathrm{E}} \left(\nabla_H b_0 \cdot \mathbf{K} \cdot \nabla_H b_0 \right) = -\sqrt{\mathrm{E}} L_\nu K \left| \nabla_H b_0 \right|^2. \tag{3.37}$$

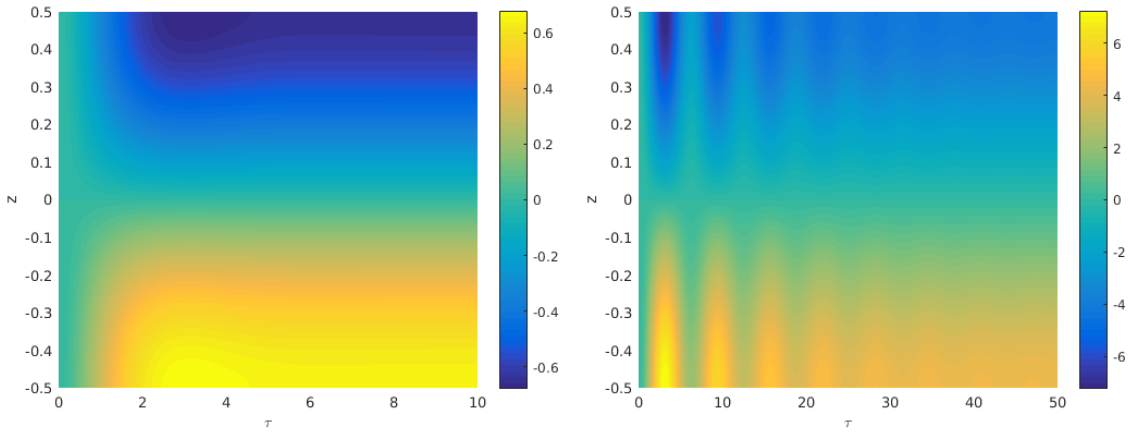

(a) (b)

Fig. 3.2 $K(z,\tau)$ for $\mathrm{E} = 0.1$ (a) and 0.01 (b), constant ν, and initial condition $K(z,0) = 0$ corresponding to no initial flow. Note that the along front velocity is proportional to K and the cross front velocity is proportional to $L_\nu K = [\partial/\partial\tau - \mathrm{E}\,\partial/\partial z(\nu\,\partial/\partial z)]\,K$.

It is convenient to define a function $M(z,\tau)$ such that

$$b_1 = -\sqrt{\mathrm{E}} M(z,\tau)\left|\nabla_H b_0\right|^2, \tag{3.38}$$

and, using the definition of L_ν, Eq. (3.36) becomes

$$\left[\frac{\partial}{\partial\tau} - \frac{\mathrm{E}}{\mathrm{Pr}}\frac{\partial}{\partial z}\left(\kappa\frac{\partial}{\partial z}\right)\right] M = \left[\frac{\partial}{\partial\tau} - \mathrm{E}\frac{\partial}{\partial z}\left(\nu\frac{\partial}{\partial z}\right)\right] K. \tag{3.39}$$

A general solution to Eq. (3.39) for $\nu \neq \kappa$ and arbitrary Pr is derived in Section A.2. We note that the steady-state solution for M, denoted M_0, is given by

$$M_0 = \mathrm{Pr}\int_{-1/2}^{z}\left[\frac{\nu}{\kappa}\frac{\partial}{\partial z'}K_0\left(z'/\sqrt{\mathrm{E}}\right)\right]dz', \tag{3.40}$$

which reduces to $M_0 = \mathrm{Pr}\,K_0$ for $\nu = \kappa$. For $\mathrm{Pr} = 1$ and $\nu = \kappa$ we can write Eq. (3.39) as

$$\left[\frac{\partial}{\partial\tau} - \mathrm{E}\frac{\partial}{\partial z}\left(\nu\frac{\partial}{\partial z}\right)\right](M - K) = 0, \tag{3.41}$$

so we write $M' = M - K$ with initial condition $M'|_{\tau=0} = \mathcal{M} - \mathcal{K}$ corresponding to $M|_{\tau=0} = \mathcal{M}$. We now use separation of variables to write

$$M' = \sum_{n=0}^{\infty} D_n e^{-\mathrm{E}\lambda_n\tau}\mathcal{Z}_n(z), \tag{3.42}$$

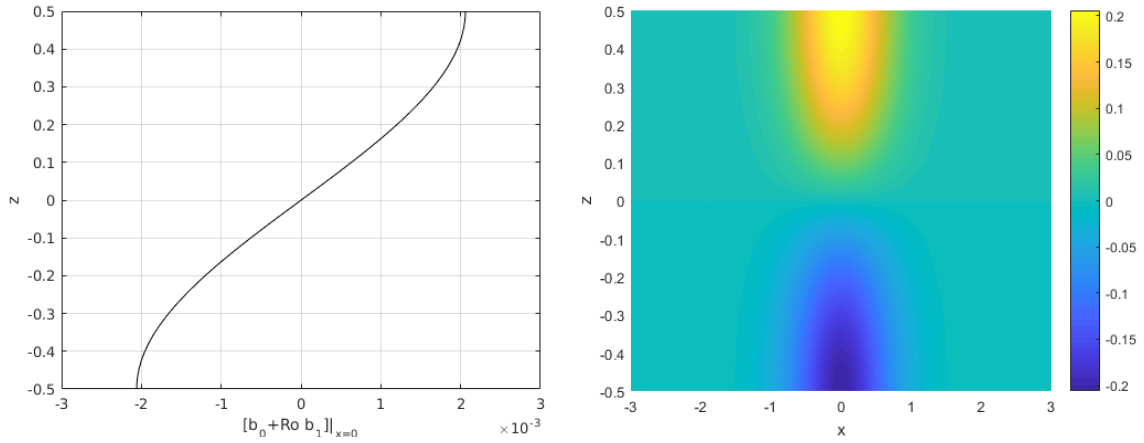

(a) (b)

Fig. 3.3 (a) The steady state buoyancy field to $O(\mathrm{Ro})$ at $x = 0$, $b(0, z) = b_0(0) + \mathrm{Ro}\, b_1(0, z)$, and (b) the $O(\mathrm{Ro})$ correction term, $b_1(x, z)$. Here $\mathrm{E} = 0.1$, $\mathrm{Ro} = 0.01$, $\mathrm{Pr} = 1$, $\nu = \kappa = 1$ and $b_0 = \tanh(x)$.

where

$$D_n = \frac{1}{z_n^2} \int_{-1/2}^{1/2} [\mathcal{M} - \mathcal{K}] \mathcal{Z}_n dz, \tag{3.43}$$

hence,

$$M = K_0 + \sum_{n=0}^{\infty} \left[B_n (\cos\tau + \mathrm{E}\lambda_n \sin\tau) + D_n \right] e^{-\mathrm{E}\lambda_n \tau} \mathcal{Z}_n(z). \tag{3.44}$$

The balanced buoyancy solution for $\nu = \kappa$ and arbitrary Pr can be written

$$b = b_0(x, y, T) - \sqrt{\mathrm{E}}\, \mathrm{Ro}\, \mathrm{Pr}\, K_0 \left(z/\sqrt{\mathrm{E}} \right) |\nabla_H b_0|^2 + O\left(\mathrm{Ro}^2\right). \tag{3.45}$$

Fig. 3.3 shows the $O(1)$ and $O(\mathrm{Ro})$ contributions to the buoyancy for $\mathrm{E} = 0.1$, $\mathrm{Ro} = 0.01$ and $\mathrm{Pr} = 1$ and $b_0(x) = \tanh(x)$. The $O(\mathrm{Ro})$ contribution to the buoyancy results in a slumping of the front towards a stable stratification.

As the front slumps, the surface buoyancy gradient can increase corresponding to a sharpening of the front hence allowing for short periods of frontogenesis. The horizontal buoyancy gradient is given by

$$\nabla_H b = \nabla_H b_0(x, y, T) - \sqrt{\mathrm{E}}\, \mathrm{Ro}\, \mathrm{Pr}\, K_0 \left(z/\sqrt{\mathrm{E}} \right) \nabla_H |\nabla_H b_0|^2 + O\left(\mathrm{Ro}^2\right). \tag{3.46}$$

At the upper surface where $K_0 < 0$, the buoyancy gradient ($|\nabla_H b|$) is larger than its initial value ($|\nabla_H b_0|$) on the low-buoyancy side of the front, while the converse is true on the high-buoyancy side of the front. Along the mid-plane ($z = 0$) $K_0 = 0$ and hence

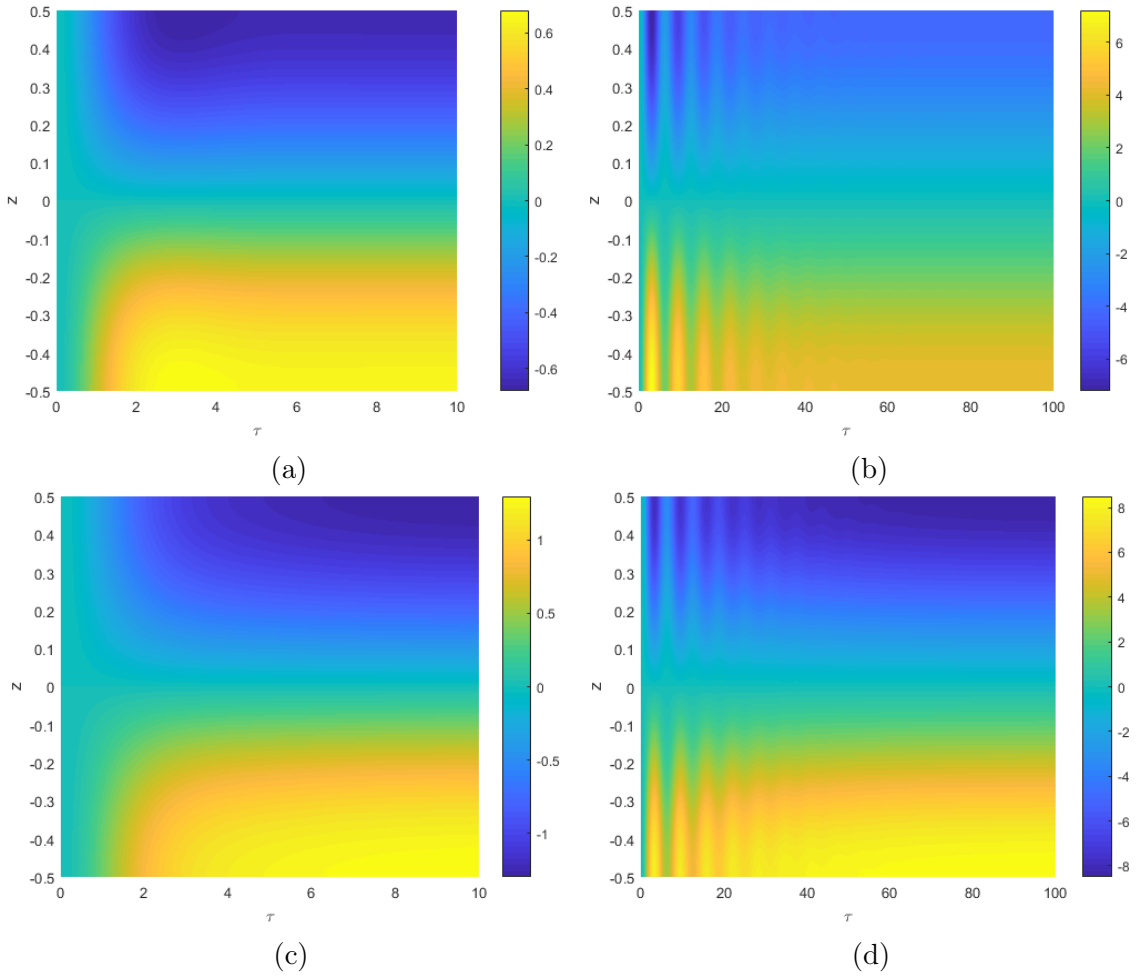

Fig. 3.4 $M(z,\tau)$ for $(\mathrm{E},\mathrm{Pr}) = (0.1,1)$ (a), $(0.01,1)$ (b), $(0.1,2)$ (c), and $(0.01,2)$ (d). We use $\nu = \kappa = 1$ and initial conditions $K(z,0) = 0$ corresponding to no initial flow and $M(z,0) = 0$ corresponding to an initially depth independent front. Note that $b_1 = -\sqrt{\mathrm{E}}\, M|\nabla_H b_0|^2$.

the buoyancy gradient is equal to $\nabla_H b_0$. It should be noted that the enhancement and reduction in the buoyancy gradient relative to $\nabla_H b_0$ is $O(\mathrm{Ro})$ and hence frontogenesis is a relatively weak effect for $\mathrm{Ro} \ll 1$.

Fig. 3.4 shows the time dependent $M(z,\tau)$ for four pairs of values of (E,Pr) and initial conditions of no flow and no depth dependence in the buoyancy field. We can see that the system rapidly adjusts to a balanced state with inertial waves for small E. Larger Pr results in a longer adjustment period and more stable stratification.

3.3.3 The O(Ro²) buoyancy balance and shear dispersion

We now consider the $O(\mathrm{Ro}^2)$ buoyancy balance. The depth-average of this balance allows us to determine the evolution of the leading order buoyancy field, b_0, over the slow timescale, T. The evolution is found to be due to both shear dispersion and horizontal diffusion, although horizontal diffusion is only important at late times.

Depth-Averaged Buoyancy

The previous two sections examined the leading order solutions to the time-dependent TTW equations. For initial conditions not in TTW balance, the leading order contributions consist of an adjustment phase with damped inertial oscillations. The evolution of $\mathbf{u}_0$ and b_1 during the adjustment phase involves the fast timescale, τ. After the end of the adjustment phase, the front will still evolve, but now on the slow timescale, T. In this section, we examine the slow evolution of $b_0(x, y, T)$ by depth-averaging the $O(\mathrm{Ro}^2)$ buoyancy conservation equation.

The $O(\mathrm{Ro}^2)$ buoyancy equation is

$$\frac{\partial b_0}{\partial T} + \frac{\partial b_2}{\partial \tau} + \mathbf{u}_1 \cdot \nabla_H b_0 + \mathbf{u}_0 \cdot \nabla b_1 = \frac{\mathrm{E}}{\mathrm{Pr}} \frac{\partial}{\partial z}\left(\kappa \frac{\partial b_2}{\partial z}\right) + \frac{\epsilon^2 \mathrm{E}}{\mathrm{Ro}^2 \mathrm{Pr}} \kappa \nabla_H^2 b_0, \tag{3.47}$$

where we note that $\epsilon = O(\mathrm{Ro})$. We define the depth average as

$$\overline{*} = \int_{-1/2}^{1/2} * \, dz, \tag{3.48}$$

and write a field f as $f = \overline{f} + f'$ where $\overline{f'} = 0$. We assume that the depth averages of the cross front components of $\mathbf{u}_{H0}$, $\mathbf{u}_{H1}$, ... and the depth averages of b_1, b_2, ... are zero. This assumption holds if the initial conditions, the viscosity, ν, and the diffusivity, κ, are symmetric in z about $z = 0$. We note that it is possible for depth-independent velocity components to develop, balanced by a depth-independent pressure term, but these lead to along front velocities which do not affect buoyancy advection across the front and hence can be ignored. With this assumption, the depth-averaged buoyancy is simply

$$\overline{b} = b_0(x, y, T). \tag{3.49}$$

We now take a depth average of Eq. (3.47) and note that $\overline{\kappa} = 1$ to get

$$\frac{\partial b_0}{\partial T} + \frac{\partial}{\partial x}\overline{u_0 b_1} + \frac{\partial}{\partial y}\overline{v_0 b_1} = \frac{\epsilon^2 \mathrm{E}}{\mathrm{Ro}^2 \mathrm{Pr}} \nabla_H^2 b_0, \tag{3.50}$$

where

$$\overline{\mathbf{u}_{H0} b_1} = \left(\overline{u_0 b_1}, \overline{v_0 b_1}\right) = \mathrm{E}\left[\overline{M\mathbf{K}} \cdot \nabla_H b_0\right] |\nabla_H b_0|^2, \tag{3.51}$$

so we can define a second-rank effective diffusivity tensor $\boldsymbol{\kappa}_{eff}$ by

$$-\overline{\mathbf{u}_{H0} b_1} = \boldsymbol{\kappa}_{eff} \cdot \nabla_H b_0, \tag{3.52}$$

such that

$$\boldsymbol{\kappa}_{eff} = -\mathrm{E}\,\overline{M\mathbf{K}}\,|\nabla_H b_0|^2, \tag{3.53}$$

and allowing us to write Eq. (3.50) as

$$\frac{\partial b_0}{\partial T} = \nabla_H \cdot \left[\boldsymbol{\kappa}_{eff} \cdot \nabla_H b_0 + \frac{\epsilon^2 \mathrm{E}}{\mathrm{Ro}^2 \mathrm{Pr}} \nabla_H b_0\right]. \tag{3.54}$$

Since b_0 does not evolve on the short timescale τ, we can describe its evolution using the steady-state effective diffusivity, $\boldsymbol{\kappa}_{eff}^{(0)}$, given by

$$\boldsymbol{\kappa}_{eff}^{(0)} = -\mathrm{E}\,\overline{M_0 \mathbf{K}_0}\,|\nabla_H b_0|^2, \tag{3.55}$$

where M_0 is given by Eq. (3.40) and

$$\mathbf{K}_0 = \begin{pmatrix} \mathrm{E}\frac{\partial}{\partial z}\left(\nu \frac{\partial K_0}{\partial z}\right) & -K_0 \\ K_0 & \mathrm{E}\frac{\partial}{\partial z}\left(\nu \frac{\partial K_0}{\partial z}\right) \end{pmatrix}. \tag{3.56}$$

We note that

$$\int_{-1/2}^{1/2} \mathrm{E}\frac{\partial}{\partial z}\left(\nu \frac{\partial K_0}{\partial z}\right)\left[\int_{-1/2}^{z} \frac{\nu}{\kappa}\frac{\partial K_0}{\partial z'}\, dz'\right] dz = -\int_{-1/2}^{1/2} \mathrm{E}\frac{\nu^2}{\kappa}\left(\frac{\partial K_0}{\partial z}\right)^2 dz < 0, \tag{3.57}$$

hence, the diagonal terms of $\overline{M_0 \mathbf{K}_0}$ are negative, the diagonal terms of $\boldsymbol{\kappa}_{eff}^{(0)}$ are positive and $\boldsymbol{\kappa}_{eff}^{(0)}$ is positive definite.

Using $\boldsymbol{\kappa}_{eff}^{(0)}$, we write Eq. (3.54) as

$$\frac{\partial b_0}{\partial T} = \nabla_H \cdot \left[-\mathrm{E}\,\overline{M_0 \mathbf{K}_0} \cdot \nabla_H b_0\,|\nabla_H b_0|^2 + \frac{\epsilon^2 \mathrm{E}}{\mathrm{Ro}^2 \mathrm{Pr}} \nabla_H b_0\right], \tag{3.58}$$

and define

$$\mathbf{Q}(\mathrm{E}) = -\mathrm{E}\,\overline{M_0\mathbf{K}_0}/\mathrm{Pr}, \tag{3.59}$$

for positive definite matrix $\mathbf{Q}$ that depends only on E. Hence we can write the non-linear diffusion equation, Eq. (3.58), as

$$\frac{\partial b_0}{\partial T} = \nabla_H \cdot \left[\mathrm{Pr}\,\mathbf{Q}\cdot\nabla_H b_0\,|\nabla_H b_0|^2 + \frac{\epsilon^2\mathrm{E}}{\mathrm{Ro}^2\mathrm{Pr}}\nabla_H b_0\right]. \tag{3.60}$$

In the case of a y independent front, $b_0 = b_0(x,T)$, Eq. (3.60) reduces to

$$\frac{\partial b_0}{\partial T} = \frac{\partial}{\partial x}\left[\mathrm{Pr}\,Q\left(\frac{\partial b_0}{\partial x}\right)^3 + \frac{\epsilon^2\mathrm{E}}{\mathrm{Ro}^2\mathrm{Pr}}\frac{\partial b_0}{\partial x}\right], \tag{3.61}$$

where

$$Q(\mathrm{E}) = \mathrm{E}^2\int_{-1/2}^{1/2}\frac{\nu^2}{\kappa}\left(\frac{\partial K_0}{\partial z}\right)^2 dz = \mathrm{E}\int_{-1/2}^{1/2}\frac{\nu^2}{\kappa}\left(K_0'\right)^2 dz > 0, \tag{3.62}$$

since $K_0 = K_0\left(z/\sqrt{\mathrm{E}}\right)$ and hence $\partial K_0/\partial z = \mathrm{E}^{-1/2}K_0'$. Eq. (3.61) is the Erdogan-Chatwin equation, first derived for longitudinal dispersion in pipe flow by Erdogan & Chatwin (1967). This equation arises in many non-rotating physical contexts where the dispersion rate is enhanced by buoyancy driven flow (Smith, 1982).

3.3.4 Shear dispersion in the limit of small Ekman number

Although the solution described in the previous sections is valid up to $\mathrm{E} = O(1)$, it is useful to examine the solution for small Ekman number, specifically $\mathrm{E} = O(\mathrm{Ro})$. In this limit, we recover a solution obtained previously by Garrett & Loder (1981).

We can write the buoyancy frequency, N^2, as

$$N^2 = \frac{\partial b}{\partial z} = \mathrm{Ro}\frac{\partial b_1}{\partial z} + O\left(\mathrm{Ro}^2\right), \tag{3.63}$$

so

$$N^2 = -\mathrm{Ro}\left(\sqrt{\mathrm{E}}\frac{\partial M}{\partial z}\right)|\nabla_H b_0|^2 + O\left(\mathrm{Ro}^2\right). \tag{3.64}$$

During the spreading regime, $\sqrt{\mathrm{E}}\,\partial M/\partial z = \sqrt{\mathrm{E}}\,\partial M_0/\partial z = (\mathrm{Pr}\,\nu/\kappa)K_0'$ so

$$N^2 = -\mathrm{Ro}\,\mathrm{Pr}\frac{\nu}{\kappa}K_0'\left(z/\sqrt{\mathrm{E}}\right)|\nabla_H b_0|^2 + O\left(\mathrm{Ro}^2\right). \tag{3.65}$$

In the case of $\mathrm{E} = O(\mathrm{Ro})$ the solution for velocity approaches that of thermal wind balance with $K_0(z/\sqrt{\mathrm{E}}) = -z/\sqrt{\mathrm{E}}$ outside of thin Ekman layers near the top and bottom surfaces. These Ekman layers generate a depth independent vertical velocity in the interior by Ekman pumping (Garrett & Loder, 1981). The vertical velocity is independent of z and the cross-front velocity is zero outside of the Ekman layers. Hence $K_0' \to -1$ so

$$N^2 \sim \mathrm{Ro}\,\mathrm{Pr}\frac{\nu}{\kappa}\left|\nabla_H b_0\right|^2 + O\left(\mathrm{Ro}^2\right). \tag{3.66}$$

In the 2d case, we have that

$$\kappa_{eff} = \mathrm{E}\,\mathrm{Pr}\left[\overline{\frac{\nu^2}{\kappa}\left(K_0'\right)^2}\right]\left|\frac{\partial b_0}{\partial x}\right|^2. \tag{3.67}$$

and from Eq. (3.65), to leading order

$$N^2 = -\mathrm{Ro}\,\mathrm{Pr}K_0'\frac{\nu}{\kappa}\left|\frac{\partial b_0}{\partial x}\right|^2, \tag{3.68}$$

and hence

$$\kappa_{eff} = \frac{\mathrm{E}[\overline{\nu^2 K_0'^2/\kappa}]N^2}{-\mathrm{Ro}\,\nu\,K_0'/\kappa}. \tag{3.69}$$

For small E we have $K_0' \to -1$ so $K_0'^2 \to 1$. If we assume that ν and κ are approximately constant and equal in the interior region, away from the Ekman layers, the effective diffusivity is

$$\kappa_{eff} \sim \frac{N^2}{\mathrm{Ro}}\mathrm{E}, \tag{3.70}$$

in the small-E and -Ro limit. We note that N^2 is approximately constant in the interior. Dimensionally this result corresponds to

$$\kappa_{eff} \sim \frac{\mathcal{N}^2}{f^2}\overline{\nu}_{dim}, \tag{3.71}$$

where $\overline{\nu}_{dim}$ is the depth-averaged turbulent viscosity and $\mathcal{N}$ is the dimensional buoyancy frequency. This result was obtained previously by Garrett & Loder (1981).

3.3.5 Self-similar solution

As the front spreads through shear dispersion on the slow timescale, T, it adopts a self-similar cross-front profile. The self-similar solution can be obtained from the Erdogan-Chatwin equation, Eq. (3.61). In this section we will consider a two-dimensional front with $b_0 = F(x, T)$. This assumption isn't necessary for the analysis but simplifies the notation. In this case, Eq. (3.61) can be written as

$$\frac{\partial F}{\partial T} = \frac{\partial}{\partial x}\left[\left(c_0 + c_2\left(\frac{\partial F}{\partial x}\right)^2\right)\frac{\partial F}{\partial x}\right], \tag{3.72}$$

where

$$c_0 = \frac{\epsilon^2 \mathrm{E}}{\mathrm{Ro}^2 \mathrm{Pr}} \quad \text{and} \quad c_2 = \mathrm{Pr}Q(\mathrm{E}), \tag{3.73}$$

subject to boundary and initial conditions

$$F \to \pm 1 \quad \text{as} \quad x \to \pm\infty \quad \text{and} \quad F(x, 0) = f(x). \tag{3.74}$$

We now consider the limit in which we can neglect horizontal diffusion, i.e. $c_0 \simeq 0$. This limit gives

$$\frac{\partial F}{\partial T} = c_2 \frac{\partial}{\partial x}\left(\frac{\partial F}{\partial x}\right)^3. \tag{3.75}$$

We now seek a similarity solution of the form

$$F(x, T) = F(\eta) \quad \text{for similarity variable} \quad \eta = \frac{x}{\gamma T^\alpha}. \tag{3.76}$$

We note that it will not in general be possible to satisfy the initial condition $F(x, 0) = f(x)$: however, Smith (1982) showed that, in the case where the non-linear diffusion dominates, the solutions to Eq. (3.72) will limit to this similarity solution for all nearby initial conditions. Using Eq. (3.75), we have

$$-\frac{\alpha\eta}{T}F' = \frac{c_2}{\gamma^4 T^{4\alpha}}\left(F'^3\right)'. \tag{3.77}$$

We let $\alpha = 1/4$ and $k_2 = 4c_2/\gamma^4$ so Eq. (3.77) becomes

$$\eta F' = -k_2\left(F'^3\right)', \tag{3.78}$$

which we can solve for F'; without loss of generality we assume that $F'(0) = 1$. The solution for F' is

$$F'(\eta) = \begin{cases} 0, & \eta < -\sqrt{3k_2} \\ \sqrt{1 - \frac{\eta^2}{3k_2}}, & \eta \in \left[-\sqrt{3k_2}, \sqrt{3k_2}\right] \\ 0, & \eta > \sqrt{3k_2} \end{cases}, \tag{3.79}$$

which we integrate to obtain the solution (Smith, 1982)

$$F(\eta) = \begin{cases} -1, & \eta < -\sqrt{3k_2} \\ \frac{1}{2}\left[\eta\sqrt{1 - \frac{\eta^2}{3k_2}} + \sqrt{3k_2}\arcsin\left(\frac{\eta}{\sqrt{3k_2}}\right)\right], & \eta \in \left[-\sqrt{3k_2}, \sqrt{3k_2}\right] \\ 1, & \eta > \sqrt{3k_2} \end{cases}. \tag{3.80}$$

By matching $F\left(\pm\sqrt{3k_2}\right) = \pm 1$ we obtain $\sqrt{3k_2} = 4/\pi$; hence,

$$k_2 = \frac{16}{3\pi^2}, \tag{3.81}$$

and

$$\gamma = \left(\frac{3\pi^2 c_2}{4}\right)^{1/4}. \tag{3.82}$$

As k_2 is independent of E and Pr we can see that the form of the solution is the same for all parameter ranges with the parameters entering only through the spreading parameter γ which describes the frontal width.

We note that F and F' are continuous while F'' diverges at the edge of the front, i.e. as $\eta \to \pm\sqrt{3k_2}$, as

$$F''(\eta) = \begin{cases} 0, & \eta < -\sqrt{3k_2} \\ -\frac{\eta}{3k_2\sqrt{1-\eta^2/3k_2}}, & \eta \in \left(-\sqrt{3k_2}, \sqrt{3k_2}\right) \\ 0, & \eta > \sqrt{3k_2} \end{cases}. \tag{3.83}$$

When horizontal diffusion is included as in Eq. (3.72), this singularity is smoothed.

Fig. 3.5.a shows the similarity solution, $F(\eta)$, and its first and second derivatives. The function $F(\eta)$ is approximately linear inside the front with regions of large curvature at the edges. Fig. 3.5.b shows the numerical solution to Eq. (3.72) for $c_0 = 1.6 \times 10^{-4}$ and $c_2 = 0.0208$ at $T = T_0$, $T = T_0 + 25$, $T = T_0 + 75$ and $T = T_0 + 100$. The initial

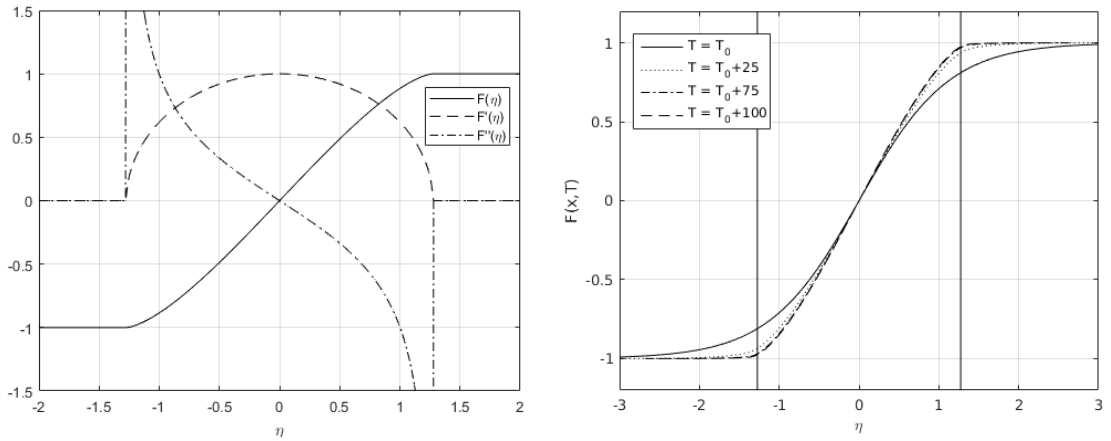

(a) (b)

Fig. 3.5 (a) Plots of the analytic similarity solution, $F(\eta)$, to Eq. (3.75) and derivatives $F'(\eta)$ and $F''(\eta)$. Note that $b_0 \propto F$, $(u_0, v_0) \propto F'$ and $w_0 \propto F''$. (b) The numerical solution to Eq. (3.72), $F(x,T)$, with initial condition $b(x,T_0) = \tanh(x)$ for $T_0 = 4$, $\mathrm{E} = 0.1$, $\nu = \kappa = 1$, $\mathrm{Ro} = 0.05$, $\epsilon = 0.002$ and $\mathrm{Pr} = 1$ corresponding to $c_0 = 1.6 \times 10^{-4}$ and $c_2 = 0.0208$. The initial condition in the numerical solution is imposed at $T = T_0$ to avoid the singularity in η at $T = 0$. The vertical lines in (b) show the predicted frontal edges, $\eta = \pm 4/\pi$.

profile is given by $b(x,T_0) = \tanh(x)$ for $T_0 = 4$ and we see that this profile has evolved towards the similarity solution, $F(\eta)$, by time $T = T_0 + 75$ before spreading out in a self similar manner for larger T.

By considering the relative magnitudes of the shear dispersion and horizontal diffusion terms, we find that our similarity solution is valid for

$$t \ll \frac{\mathrm{Ro}^3 \mathrm{Pr}^3 Q(\mathrm{E})}{\epsilon^4 \mathrm{E}^2}. \tag{3.84}$$

Fig. 3.6 shows logarithmic plots of Q and $\gamma/\mathrm{Pr}^{1/4}$ as functions of the Ekman number for constant ν. It should be noted that from Eqs. (3.72) and (3.73) that the effective diffusivity is proportional to $\mathrm{Pr}Q$, while the frontal width is given by

$$l_f(T) = 8\gamma T^{1/4}/\pi, \tag{3.85}$$

since the edges of the front correspond to $\eta = \pm\sqrt{3k_2}$. As described in Section 3.3.3 the effective diffusivity depends on the departure from the depth-averaged buoyancy, $b_1 = -\sqrt{\mathrm{E}}\mathrm{Pr}K_0|\partial b_0/\partial x|^2$, and the cross-front velocity, $u_0 = -\sqrt{\mathrm{E}}K_0''\partial b_0/\partial x$.

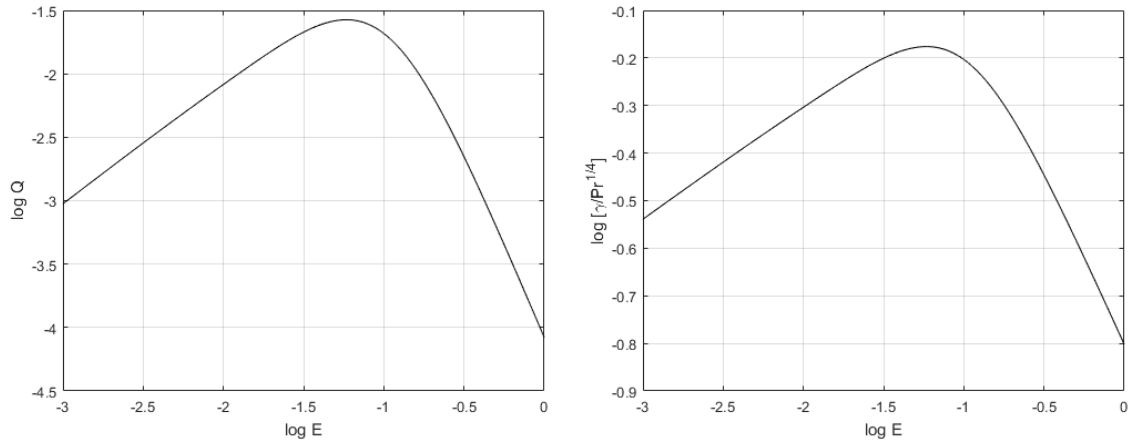

(a) (b)

Fig. 3.6 Logarithmic plots of Q(E) (a) and $\gamma/\mathrm{Pr}^{1/4}$ (b) as functions of E for constant ν. Note that $\gamma/\mathrm{Pr}^{1/4}$ depends only on E and the frontal width is proportional to $\gamma T^{1/4}$.

In the limit of small E, the cross-front velocity becomes small as the system is approximately in thermal wind balance. As discussed in Section 3.3.4 this leads to a small effective diffusivity, consistent with the result that $Q \sim \mathrm{E}$ and $\gamma \sim \mathrm{E}^{1/4}$ in this limit (see Fig. 3.6). In the limit of large E, strong vertical mixing causes the stratification and the cross-front velocity to decrease with increasing E resulting in a smaller effective diffusivity and slower spreading. In the limit of large E, $Q \sim \mathrm{E}^{-3}$ and $\gamma \sim \mathrm{E}^{-3/4}$, consistent with this description. The effective diffusivity and spreading rate are maximum for an intermediate value of $\mathrm{E} \approx 0.06$. See Section A.1 for a more complete description of the dependence of u_0 and b_1 on E.

Ferrari & Young (1997) consider a frontal problem using an 'intermittent mixing' parametrisation where the tracers are advected freely until time $t = t_{mix}$ where the vertical tracer profile is instantaneously set to its vertical average and the process repeated. The governing equation for the depth independent buoyancy profile is of the same form as Eq. (3.75) with a different value of c_2; hence it admits the same similarity solution. This will be true for any parametrised model in which the leading order velocity is linear in the buoyancy gradient, $u \approx c(z)\bar{b}_x$, and the leading order buoyancy flux scales as $F_b = \overline{ub} \sim \overline{uD_z u}\,\bar{b}_x \sim {\bar{b}_x}^3$ for some linear, z-dependent operator, D_z, which is determined by the parametrisation. We note that the vertical profiles of velocity and buoyancy differ between models, although the leading order depth-averaged tracer profiles have the same form over long times.

Fig. 3.7 shows the long-term evolution of the background buoyancy, buoyancy gradients and cross front velocity using the similarity solution. We can see that as the

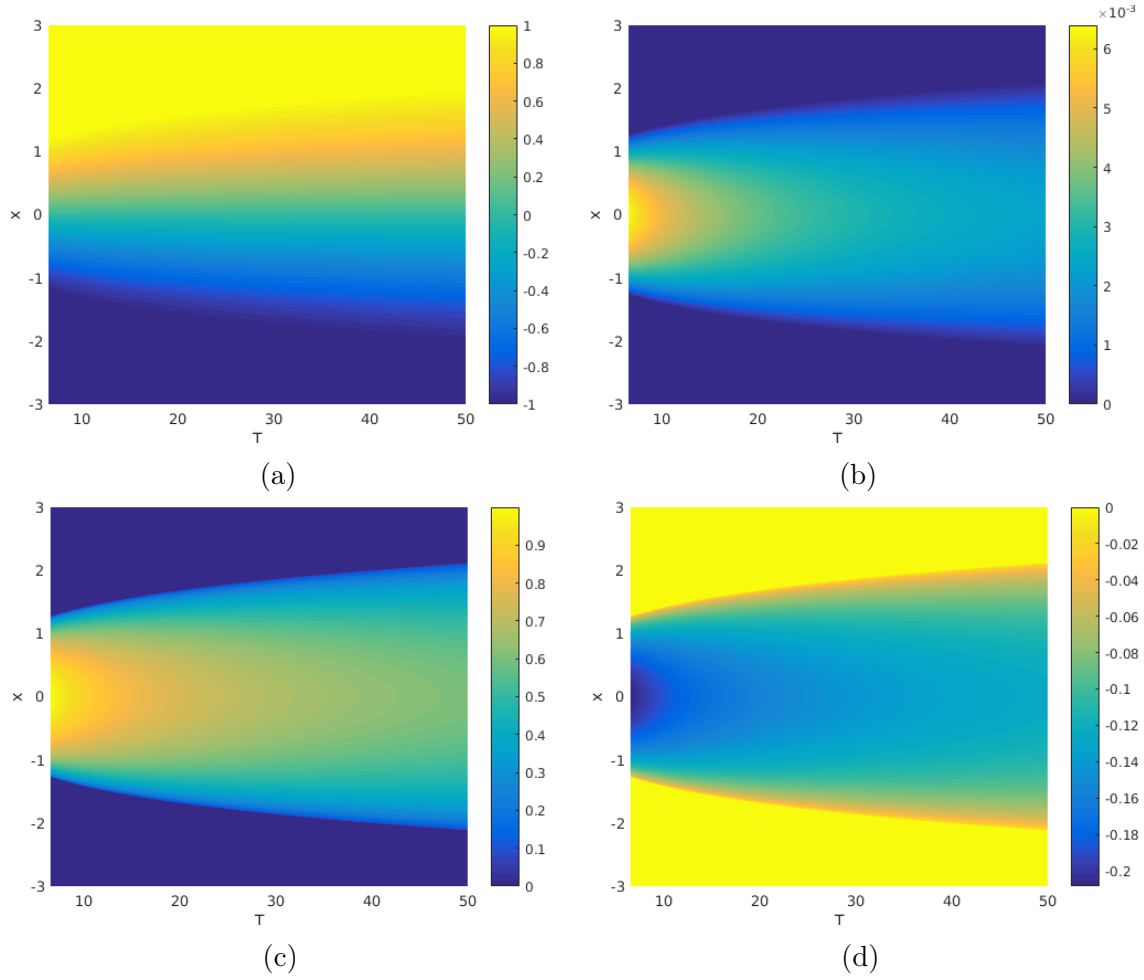

Fig. 3.7 Plots of $b_0(x,T)$ (a), $N_0^2(x,z,T) = \mathrm{Ro}\,\partial b_1/\partial z$ at $z=0$ (b), $M_0^2(x,T) = \partial b_0/\partial x$ (c) and $u_0(x,z,T)$ at $z=1/2$ (d) for $\mathrm{E}=0.1$, $\mathrm{Ro}=0.01$ and $\mathrm{Pr}=1$. We use the similarity solution for b_0 and assume that all transients have decayed. Note that $b_0 \sim F$, $N_0^2 \sim F'^2$ and $M_0^2, u_0 \sim F'$.

front spreads, both the vertical and the horizontal buoyancy gradients decrease and the cross front velocity decelerates. Since the vertical buoyancy stratification formed by the initial slumping is maintained by the cross front velocity shear, this stratification weakens as expected when the cross front velocity decelerates. The along front velocity, v_0, and vertical velocity, w_0, also decrease as the front spreads.

It should be noted that the vertical structure of the buoyancy perturbation, b_1, and the velocities, (u_0, v_0, w_0), are independent of the long timescale, T, and assuming that any transients have decayed, only depend on the depth z and Ekman number.

3.3.6 Summary of the analytic solution

Combining our results from the $O(1)$, $O(\mathrm{Ro})$ and $O(\mathrm{Ro}^2)$ balances, we can write our analytic solution as

$$\mathbf{u}_H(x,y,z,\tau,T) = -\sqrt{\mathrm{E}}\,\mathbf{K}(z,\tau)\cdot\nabla_H b_0(x,y,T) + O(\mathrm{Ro}), \tag{3.86a}$$

$$w(x,y,z,\tau,T) = \mathrm{E}\left[\int_{-1/2}^{z}\frac{-L_\nu K(z',\tau)}{\sqrt{\mathrm{E}}}dz'\right]\nabla_H^2 b_0(x,y,T) + O(\mathrm{Ro}), \tag{3.86b}$$

$$b(x,y,z,\tau,T) = b_0(x,y,T) - \mathrm{Ro}\sqrt{\mathrm{E}}\,M(z,\tau)\,|\nabla_H b_0(x,y,T)|^2 + O(\mathrm{Ro}^2), \tag{3.86c}$$

where b_0 satisfies

$$\frac{\partial b_0}{\partial T} = \nabla_H\cdot\left[\mathrm{Pr}\,\mathbf{Q}\cdot\nabla_H b_0\,|\nabla_H b_0|^2 + \frac{\epsilon^2\mathrm{E}}{\mathrm{Ro}^2\mathrm{Pr}}\nabla_H b_0\right]. \tag{3.87}$$

3.4 Discussion

Here, we have examined the influence of small-scale turbulence on the adjustment and spreading of density fronts in a rotating reference frame using a multiple-time-scale analysis and asymptotic analysis. After a short initial adjustment period, a self-similar spreading regime develops in which an effective horizontal diffusion results from the coupling of a vertically-sheared cross-front flow and vertical diffusion. During the initial adjustment period, weak frontogenesis is possible due to the slumping of the front while the long-term spreading is always frontolytic.

The time dependence and similarity solutions during the spreading phase have been calculated analytically using an expansion in small Rossby number, and allow us to predict the rate of spreading for a wide range of Ekman and Rossby numbers. The dominant balance in the buoyancy equation is between vertical diffusion and cross-front advection, resulting in a buoyancy field consisting of both spreading and slumping components in a dynamic equilibrium. The dominant balance in the momentum equations is the TTW balance between Coriolis forces, vertical momentum mixing and horizontal pressure gradients for which analytic and numerical solutions have been presented. This balance holds until the effects of horizontal diffusion become significant at late times.

Horizontal spreading of the depth-averaged buoyancy results from shear dispersion, which dominates the horizontal turbulent diffusion in the frontal region until late times (Eq. (3.84)). The spreading is described by the non-linear Erdogan-Chatwin (Erdogan

& Chatwin, 1967) equation, which arises in many contexts and has solutions that tend to a similarity solution in the region where shear dispersion dominates. Shear dispersion leads to a cross-front density profile that is nearly linear inside the front, with high curvature at the edges of the frontal zone. High curvature is associated with large vertical velocity through the TTW balance, which results in up/down-welling confined to thin bands at the edges of the front. Qualitatively, this result is similar to the velocity confinement effect observed by Shakespeare & Taylor (2013) for inviscid strain-driven fronts, although it arises from a different mechanism.

Dimensionally, we can write the frontal width as

$$L_f(t) = \left(\frac{3072}{\pi^2}\right)^{1/4} \left[\frac{Q(\mathrm{E})H^2\Delta b^2 \mathrm{Pr}}{f^3}\right]^{1/4} t^{1/4}, \tag{3.88}$$

using Eq. (3.85) and hence the spreading rate is given by

$$\frac{dL_f}{dt} = \frac{768}{\pi^2}\left[\frac{Q(\mathrm{E})H^2\Delta b^2 \mathrm{Pr}}{f^3}\right] L_f^{-3}, \tag{3.89}$$

where $Q(\mathrm{E})$ is defined in Eq. (3.62). For a typical ocean front with $H \sim 100\mathrm{m}$, $L_f \sim 10\mathrm{km}$, $f \sim 10^{-4}\mathrm{s}^{-1}$ and $\Delta\rho \sim 0.1\mathrm{kg\,m}^{-3}$, the observed frontal spreading would occur at a rate of order 1km per day for an Ekman number of $\mathrm{E} = 0.1$ (corresponding to a turbulent viscosity of $\nu \sim 0.1\mathrm{m}^2\mathrm{s}^{-1}$). By comparison, spreading due to horizontal diffusion would just be of the order of 1m per day for the same parameters.

Using scaling arguments, we can relate the Ekman number to the turbulent viscosity associated with convection driven by a surface heat flux, J_0, or a surface wind stress, τ_w. In the case of convection, the turbulent Ekman number scales according to (Taylor & Ferrari, 2011)

$$\mathrm{E} \simeq \frac{C}{f}\left(\frac{J_0\alpha g}{c_p\rho_0 H^2}\right)^{1/3},$$

where H is the depth of the convective layer, ρ_0 is the water density, c_p is the heat capacity, α is the thermal expansion coefficient, C is an empirical scaling constant and g is gravitational acceleration. Using typical values for the ocean including a convective layer depth of 100m and $f = 10^{-4}\mathrm{s}^{-1}$, typical heat flux values in the range $Q_0 = 1 - 1000\mathrm{W/m}^2$ correspond to Ekman numbers in the range $\mathrm{E} \simeq 0.1 - 1$. Similarly,

the Ekman number can be related to the wind stress using (Enriquez & Taylor, 2015)

$$\mathrm{E} \simeq \frac{C}{fH}\left(\frac{\tau_w}{\rho_0}\right)^{1/2},$$

and a wind stress of $\tau_w = 1\mathrm{Nm}^{-2}$ corresponds to $\mathrm{E} \simeq 0.1$.

In our analysis, the only mechanism driving frontogenesis is the coupling between the cross-front velocity and the along-front thermal wind through the turbulent mixing. For less idealised flows, the tendency for fronts to sharpen or spread is governed by a competition between the classical frontogenesis function and the effects of turbulent mixing. Interestingly we observe that turbulent mixing can both sharpen and spread fronts with sharpening associated with frontogenesis during an initial adjustment phase and spreading associated with shear dispersion.

In the ocean and atmosphere, deformation of fronts by larger-scale circulation can generate cross-front circulation that can drive further frontogenesis (Hoskins & Bretherton, 1972). Shear dispersion through vertical mixing might provide a mechanism to arrest deformation-driven frontogenesis, which can lead to finite-time singularities (Hoskins & Bretherton, 1972). Future work could include externally imposed large-scale strain to examine frontal arrest, which would provide insight into the properties of equilibrated fronts.

To simplify our analysis, we have kept the viscosity and diffusivity independent of time. Recent observations and numerical simulations have found that turbulence can be significantly enhanced at strong fronts including the Kuroshio (D'Asaro *et al.*, 2011), the Gulf Stream (Thomas *et al.*, 2013) and the California Current (Johnston *et al.*, 2011). On the other hand, the stable stratification that develops as a front slumps has been implicated in the suppression of turbulent mixing (Taylor, 2016; Taylor & Ferrari, 2010). It remains unclear how small-scale turbulence depends on the large-scale properties of the front and the surface wind and buoyancy forcing. In either case, the turbulent viscosity and diffusivity probably vary with position across the front and in time, effects that are neglected here. Varying levels of small-scale turbulence could lead to a feedback between the evolution of the front through TTW balance and turbulent mixing. The coupled response of turbulence and frontal dynamics will be the topic of future work.

Chapter 4

The evolution of a front in turbulent thermal wind balance: numerics

4.1 Introduction

In Chapter 3 we used a simple analytic model of an ocean front in the surface mixed layer to examine the dominant Turbulent Thermal Wind (TTW) flow and its effects on the background buoyancy field. We used an asymptotic expansion in small Rossby number and introduced fast and slow timescales. The $O(1)$ velocity fields consist of a thermal wind component and a cross-front flow resulting from the coupling of the along-front and cross-front velocities through vertical mixing. The vertical shear associated with the cross-velocity drives a slumping of the buoyancy field at $O(\mathrm{Ro})$ towards a balance between advection and vertical diffusion. Initial transients occur on the fast timescale as this balanced state is approached.

Using the leading order velocity fields and $O(\mathrm{Ro})$ buoyancy we can express the depth averaged $O(\mathrm{Ro}^2)$ buoyancy equation purely in terms of the background $O(1)$ buoyancy, b_0. The resulting equation, known as the Erdogan-Chatwin equation (Erdogan & Chatwin, 1967; Smith, 1982), describes non-linear diffusion over the slow timescale and can be solved using a similarity solution. Physically this represents shear dispersion; the vertical diffusion is projected horizontally by the velocity shear resulting in a horizontal spreading that occurs much faster than could be predicted by horizontal diffusion alone. The similarity solution consists of an approximately linear cross-front density profile in the center of the front and regions of high curvature at the edges. These high curvature regions correspond to bands of strong vertical velocity.

In this chapter we consider an idealised model of an isolated front and focus mainly on the long time evolution. We use direct numerical simulation (DNS) to examine the validity of the asymptotic results in Chapter 3 for a range of Rossby numbers by comparing them with full nonlinear numerical simulations.

We observe that in each simulation the front spreads and we begin by comparing the spreading rate with our analytic predictions. We also compare the form of the buoyancy profiles and the streamfunctions for order 1 Rossby numbers in order to determine if our results are valid outside the small Rossby number limit of the theory. The largest deviations from our predictions are observed for small E, we examine these cases in detail and present a modified theory to explain these discrepancies.

Once the front reaches the balanced self-similar phase, the evolution is purely frontolytic. However, we seek to determine if the initial transients or evolution of b_0 towards the similarity solution are frontogenetic by considering the surface buoyancy gradient. Near the edges of the front, the curvature of the cross-front buoyancy profile becomes high and could not be determined analytically as the curvature of the similarity solution diverges in this region. In the numerical simulations, this discontinuity is smoothed by horizontal diffusion. In Section 4.6, we derive a scaling for the vertical velocity which we compare with the numerical simulations.

4.2 Setup

In this chapter we use the diffusive parametrisation model on a two-dimensional domain $(x - z)$ for simplicity. We use a depth-independent viscosity ν and diffusivity κ with a Prandtl number of 1. We consider a single isolated front and, as in Chapter 3, we assume that the surface buoyancy flux Q, wind stress $\boldsymbol{\tau}$ and Burger number Bu are zero. For this simplified setup, the governing equations become:

$$\mathrm{Ro}\frac{Du}{Dt} - v = -\frac{\partial p}{\partial x} + \mathrm{E}\,\nabla_\epsilon^2 u, \tag{4.1a}$$

$$\mathrm{Ro}\frac{Dv}{Dt} + u = \mathrm{E}\,\nabla_\epsilon^2 v, \tag{4.1b}$$

$$\mathrm{Ro}\,\epsilon^2\frac{Dw}{Dt} = -\frac{\partial p}{\partial z} + b + \epsilon^2\mathrm{E}\,\nabla_\epsilon^2 w, \tag{4.1c}$$

$$\mathrm{Ro}\frac{Db}{Dt} = \frac{\mathrm{E}}{\mathrm{Pr}}\,\nabla_\epsilon^2 b, \tag{4.1d}$$

$$\frac{\partial u}{\partial x} + \frac{\partial w}{\partial z} = 0, \tag{4.1e}$$

with no stress and no buoyancy boundary conditions at $z = \pm 1/2$. Numerically we consider $x \in [-L_x/2, L_x/2]$ and use periodic boundary conditions at the edges on the horizontal domain.

4.3 Numerical Simulations

We use numerical simulations to study the time evolution of an initially depth independent front, $b|_{t=0} = b(x)$. The numerical simulations are carried out using DIABLO. Time stepping is performed with a combination of explicit third-order Runge-Kutta and implicit Crank Nicolson schemes while finite differences are used for derivatives in the vertical direction and discrete Fourier transforms, using the pseudo-spectral method for non-linear terms, are used for derivatives in the horizontal direction (Taylor, 2008).

In order to use periodic boundary conditions in the horizontal direction we subtract a linear profile from the buoyancy and define

$$b' = b - \frac{2x}{L_x}, \tag{4.2}$$

and

$$p' = p - \frac{2xz}{L_x}, \tag{4.3}$$

where L_x is the horizontal domain width so at $x = \pm L_x/2$ we have $b' = 0$. Eq. (4.1) becomes

$$\mathrm{Ro}\frac{Du}{Dt} - v = -\frac{\partial p'}{\partial x} - \frac{2z}{L_x} + \mathrm{E}\,\nabla_\epsilon^2 u, \tag{4.4a}$$

$$\mathrm{Ro}\frac{Dv}{Dt} + u = \mathrm{E}\,\nabla_\epsilon^2 v, \tag{4.4b}$$

$$\mathrm{Ro}\,\epsilon^2\frac{Dw}{Dt} = -\frac{\partial p'}{\partial z} + b' + \epsilon^2 \mathrm{E}\,\nabla_\epsilon^2 w, \tag{4.4c}$$

$$\mathrm{Ro}\frac{Db'}{Dt} + \frac{2\mathrm{Ro}\,u}{L_x} = \frac{\mathrm{E}}{\mathrm{Pr}}\,\nabla_\epsilon^2 b', \tag{4.4d}$$

$$\frac{\partial u}{\partial x} + \frac{\partial w}{\partial z} = 0, \tag{4.4e}$$

which we then solve for (u, v, w, b', p') with horizontally periodic boundary conditions.

Due to the large Ekman numbers used, the maximum timestep is set by the condition that the diffusive lengthscale per timestep is less than the horizontal grid

scale. Therefore, the timestep, Δt is chosen to be

$$\Delta t = C\frac{\mathrm{Ro}}{\mathrm{E}}, \tag{4.5}$$

where C is a constant determined by the grid scale, $\Delta x = L_x/N_x$. From Chapter 3 we expect the depth-averaged buoyancy field to evolve on the slow timescale

$$T = \mathrm{Ro}\, t, \tag{4.6}$$

so we run each simulation until $t_{end} = 10^3/\mathrm{Ro}$. The required number of timesteps is therefore

$$N_t = \frac{10^3\mathrm{E}}{C\,\mathrm{Ro}^2}. \tag{4.7}$$

We use a grid resolution of $N_x = 256$ and a domain width of $L_x = 10$ which requires a value of $C = 10^{-3}$ for accuracy.

Finally we impose the initial condition

$$b(x) = \tanh x, \tag{4.8}$$

and set the initial velocity using the leading order 'turbulent thermal wind' (TTW) solution from Eqs. (3.15) and (3.19):

$$u = -\sqrt{E}\,K_0''\left(z/\sqrt{E}\,;\zeta_0\right)\frac{\partial b}{\partial x}, \tag{4.9a}$$

$$v = -\sqrt{E}\,K_0\left(z/\sqrt{E}\,;\zeta_0\right)\frac{\partial b}{\partial x}, \tag{4.9b}$$

$$w = \quad E\,K_0'\left(z/\sqrt{E}\,;\zeta_0\right)\frac{\partial^2 b}{\partial x^2}, \tag{4.9c}$$

where

$$K_0(\zeta;\zeta_0) = -\zeta + C_+(\zeta_0)\,\mathrm{cs}(\zeta) + C_-(\zeta_0)\,\mathrm{sc}(\zeta), \tag{4.10}$$

for the functions

$$\begin{aligned}
\mathrm{cc}(\zeta) &= \cosh\left(\zeta/\sqrt{2}\right)\cos\left(\zeta/\sqrt{2}\right),\\
\mathrm{cs}(\zeta) &= \cosh\left(\zeta/\sqrt{2}\right)\sin\left(\zeta/\sqrt{2}\right),\\
\mathrm{ss}(\zeta) &= \sinh\left(\zeta/\sqrt{2}\right)\sin\left(\zeta/\sqrt{2}\right),\\
\mathrm{sc}(\zeta) &= \sinh\left(\zeta/\sqrt{2}\right)\cos\left(\zeta/\sqrt{2}\right),
\end{aligned} \tag{4.11}$$

and constants

$$C_\pm(\zeta_0) = \frac{1}{\sqrt{2}}\frac{\mathrm{cc}(\zeta_0) \pm \mathrm{ss}(\zeta_0)}{\mathrm{cc}^2(\zeta_0) + \mathrm{ss}^2(\zeta_0)}, \tag{4.12}$$

and $\zeta_0 = 1/\sqrt{4E}$. See Section A.1 for details. Note that the velocity reduces to the linear 'thermal wind' velocity profile, $K_0(\zeta) \sim -\zeta$, in the limit of small Ekman number. We expect some initial adjustment as the front slumps and b develops a small, order Ro, depth-dependence. However, we do not expect significant inertial oscillations since the velocity field is in TTW balance at $t = 0$. We perform simulations for 20 different Ekman numbers between E = 0.01 and E = 1 and 9 different Rossby numbers between Ro = 0.1 and Ro = 1 for a total of 180 simulations. An aspect ratio of $\epsilon = 0.02$ is used for all simulations.

4.4 Results

We now compare the results of our numerical simulations with our theoretical predictions. We begin by examining the spreading rate of the front and the accuracy of the theory for $O(1)$ Rossby numbers. We will then examine frontogenesis during the transient adjustment. Finally, we will derive and test a scaling for the maximum vertical velocity.

4.4.1 Spreading Rate

In Chapter 3 we found that over long times the leading order buoyancy profile, b_0, becomes self-similar with a form given by

$$b_0 = F\left(\frac{x}{\gamma(T+T_0)^{1/4}}\right), \tag{4.13}$$

where

$$F(\eta) = \begin{cases} -1, & \eta < -4/\pi \\ \frac{1}{2}\left[\eta\sqrt{1-\frac{\pi^2\eta^2}{16}} + \frac{4}{\pi}\arcsin\left(\frac{\pi\eta}{4}\right)\right], & \eta \in [-4/\pi, 4/\pi], \\ 1, & \eta > 4/\pi \end{cases} \tag{4.14}$$

γ is the spreading parameter and T_0 describes the time taken for the solution to reach a self-similar state. The spreading parameter can be linked to the frontal width by

$$l_f(T) = \frac{8\gamma(T+T_0)^{1/4}}{\pi}. \tag{4.15}$$

We now compare the numerically observed spreading with this theoretical prediction. In some simulations fast spreading results in the front reaching the edges of the horizontal domain so we choose a time interval of $T \in [100, 350]$ for the analysis, during which

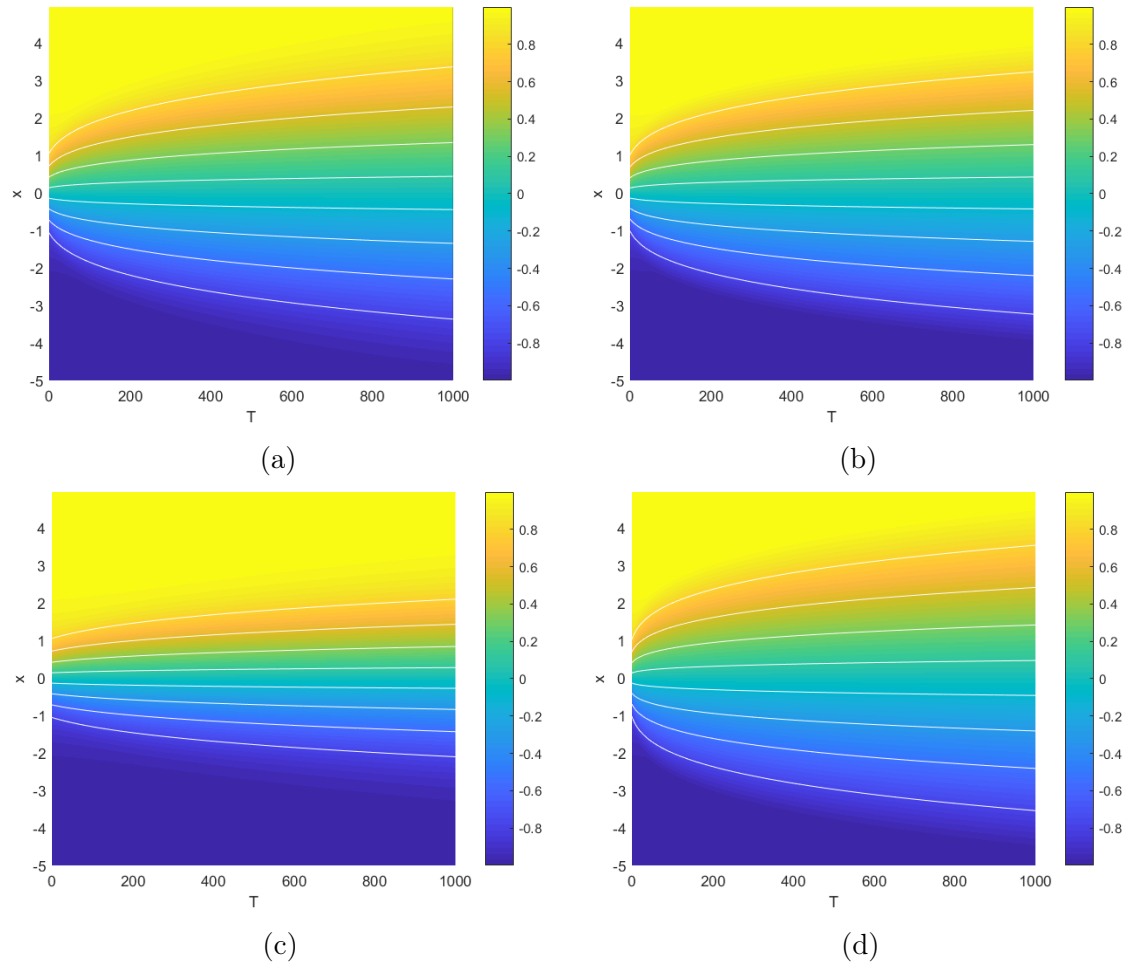

Fig. 4.1 Plots of $b(x, z, T)$ at $z = 0$ for (a) $\mathrm{Ro} = 0.1, \mathrm{E} = 0.02$, (b) $\mathrm{Ro} = 0.5, \mathrm{E} = 0.02$, (c) $\mathrm{Ro} = 0.5, \mathrm{E} = 0.3$, and (d) $\mathrm{Ro} = 1, \mathrm{E} = 0.06$. The white contours show the theoretical predictions using the numerical values of $(\gamma_n, T_{0n}, \alpha_n)$.

time the transients have decayed and, for most simulations, the front has not reached the edges of the domain. For this time interval we assume that the front is self-similar with a centerline ($z = 0$) buoyancy of the form

$$b = F\left(\frac{x}{f(T)}\right). \tag{4.16}$$

We now fit this prediction to the numerical centerline buoyancy field to determine $f(T)$ and finally fit $f(T)$ to the curve

$$f(T) = \gamma_n (T + T_{0n})^{\alpha_n}, \tag{4.17}$$

to determine the values of $(\gamma_n, T_{0n}, \alpha_n)$ for each pair of parameters, $(\mathrm{Ro}, \mathrm{E})$. All fitting is done using a least squares method. From Chapter 3 we expect that the predicted spreading rate is valid for

$$T \ll T_{max} = \frac{\mathrm{Ro}^4 \mathrm{Pr}^3 Q(\mathrm{E})}{\epsilon^4 \mathrm{E}^2}, \tag{4.18}$$

where

$$Q(\mathrm{E}) = \mathrm{E} \int_{-1/2}^{1/2} \frac{\nu^2}{\kappa} \left(K_0'\right)^2 dz, \tag{4.19}$$

and

$$\mathrm{Pr}\, Q(\mathrm{E}) = \frac{4\gamma^4}{3\pi^2} \tag{4.20}$$

is proportional to the effective horizontal diffusivity resulting from shear dispersion. This condition comes from the requirement that shear dispersion dominates horizontal diffusion. Note that horizontal diffusion becomes important sooner when Ro is small or E is large. When both E is large and Ro is small, the horizontal diffusion is fast and the front quickly spreads to fill the domain, therefore we do not expect the predicted spreading rate to be accurate in this region.

Fig. 4.1 shows the centerline ($z = 0$) buoyancy fields as functions of x and T for a variety of Rossby and Ekman numbers. The theoretical predictions are given by the white contours. In each case the long term behaviour exhibits frontal spreading. This spreading is well described by the predictions, even for the case of larger Rossby numbers where the theoretical predictions are not asymptotically valid. Fig. 4.1(a) and Fig. 4.1(b) show the centerline buoyancy for $\mathrm{E} = 0.02$ and two different Rossby numbers. The long term spreading is similar in each case when plotted as a function of the slow timescale, $T = \mathrm{Ro}t$. This is consistent with the theoretical similarity solution which depends on Ro only through T. Note that the edges of the front appear more diffuse for smaller Rossby numbers; this is expected since horizontal diffusion becomes important at earlier times for smaller Rossby numbers.

Fig. 4.2 shows the values of γ_n and α_n calculated over the time interval $[100, 350]$ and the ratio of these numerical values with the theoretical predictions for γ and α. We expect our theory to be valid for $T < T_{max}/10$ and plot the curve $T_{max} = 3500$ in white. The region below this curve is where the theory should be valid. The values of γ_n and α_n match the theoretical predictions within $10 - 20\%$. In the region where we expect horizontal diffusion to dominate, $\alpha_n \approx 1/2$, which is consistent with diffusive spreading. The front has filled the computational domain in the cases with large E

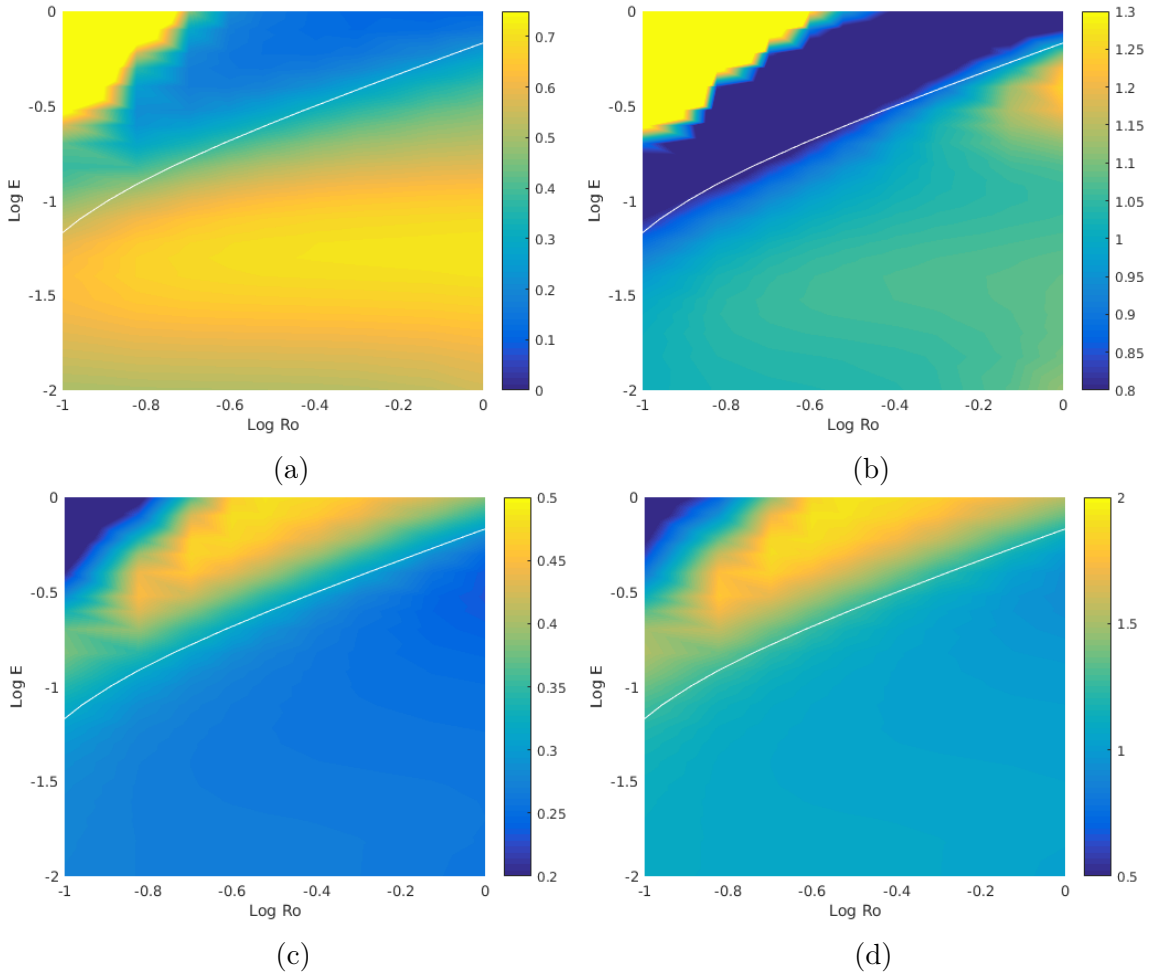

Fig. 4.2 Plots of (a) γ_n, (b) γ_n/γ, (c) α_n, (d) α_n/α as functions of E and Ro. We use a time interval of $[100, 350]$ and also plot the curve $T_{max} = 3500$ in white.

and small Ro so the results in the top left regions of each figure are not reflective of the true spreading rate.

From Fig. 4.2(a) we can see that the spreading rate, γ_n, is approximately independent of Ro below the curve $T_{max} = 3500$. This matches our theoretical prediction where γ depends only on E and Pr though interestingly the prediction is still valid for $\mathrm{Ro} = O(1)$. Similarly the prediction of $\alpha = 1/4$ is accurate for the case of $\mathrm{Ro} = O(1)$ which suggests that spreading via shear dispersion is still the dominant mechanism and the theory is valid for order 1 Rossby numbers despite being derived in the small Ro limit. We now consider the $\mathrm{Ro} = O(1)$ simulations in more detail to see how accurately the theory predicts the form of the velocity and buoyancy fields.

4.4.2 Accuracy of Theory for O(1) Rossby Numbers

Since the theoretical predictions in Chapter 3 were made in the limit of small Ro, these predictions do not necessarily hold in the case of $\mathrm{Ro} = O(1)$ where the nonlinear advection terms in the momentum and buoyancy equations are no longer small. Despite this, we have seen above that the spreading rate of the front when $\mathrm{Ro} = 1$ is still accurately captured by the theoretical predictions. We now examine the velocity and buoyancy fields for the $\mathrm{Ro} = 1$ case in more detail to determine how accurately they are described by the linear TTW solution in Chapter 3.

The 2D streamfunction, $\psi(x, z, t)$, describing the circulation around the front is defined by $u = \partial\psi/\partial z$ and $w = -\partial\psi/\partial x$. We define

$$\psi_n = \int_{-0.5}^{z} u(x, z', t)\, dz', \tag{4.21}$$

and calculate ψ_n by numerically integrating the velocity fields from the simulations. We compare ψ_n to the leading order analytic prediction

$$\psi_0 = -\mathrm{E}\, K_0'\left(z/\sqrt{\mathrm{E}}\right) \frac{\partial b}{\partial x}, \tag{4.22}$$

and define the difference between the analytic and numerical values of the streamfunction by

$$\Delta\psi = \psi_n - \psi_0. \tag{4.23}$$

Fig. 4.3 shows ψ_n, ψ_0 and $\Delta\psi$ for $\mathrm{Ro} = 1$ and $\mathrm{E} = 0.1$ at $T = 300$. We can see that the leading order analytic prediction is fairly accurate, with a maximum magnitude within 20% of the numerical value. The main difference is the shape of the contours with the contours of ψ_n being more circular than those of ψ_0.

Fig. 4.4(a) shows the normalised maximum difference between ψ_0 and ψ_n, defined as $\max[\Delta\psi]/\max[\psi_n]$. Interestingly, we can see that the deviation of ψ is more strongly dependent on Ekman number than on Rossby number and the predictions for $\mathrm{Ro} = 1$ are not significantly less accurate than for smaller Rossby numbers while the predictions for large E are much more accurate than for small E. It is notable that the theoretical prediction performs nearly as well for $\mathrm{Ro} = 1$ compared to smaller Rossby numbers, despite the fact that the theory was derived using an asymptotic expansion valid for $\mathrm{Ro} << 1$. The relatively poor performance of the theory for small E will be examined later.

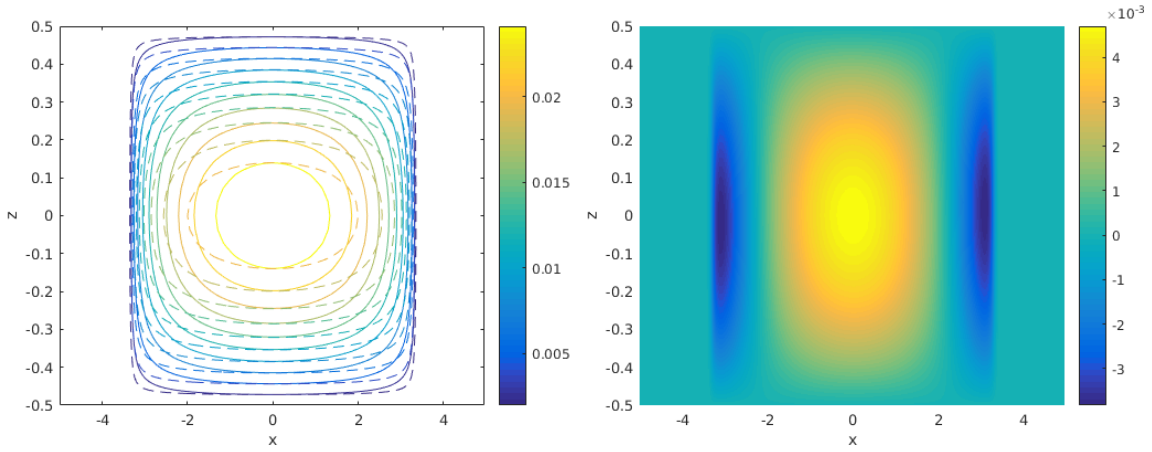

(a) (b)

Fig. 4.3 Plots of (a) ψ_n (solid) and ψ_0 (dashed) (b) $\Delta\psi$. Results are given for Ro $= 1$, E $= 0.1$ and $T = 300$.

The maximum cross-front velocity, $U(t)$, is given by

$$U(t) = |\max_{x,z}[u]|, \tag{4.24}$$

and using the leading order analytic solution, our prediction for the maximum cross front velocity is

$$U_0 = u_0(0, 1/2, t) = \sqrt{\mathrm{E}}\, K_0''\left(1/2\sqrt{\mathrm{E}}\right) \left.\frac{\partial b}{\partial x}\right|_{x,z=0}. \tag{4.25}$$

From the numerical simulations we define $U_n(t)$ to be the maximum value of u at each time and $\Delta U = |U_n - U_0|$ to be the difference between the numerical data and the theoretical prediction. Fig. 4.4(b)–(d) shows the error in the prediction of the maximum cross-front velocity, given by $\Delta U/U_n$, for E $= 0.02$, E $= 0.1$ and E $= 0.4$. We can see that the error is largest for small E and is not strongly affected by increasing the Rossby number from Ro $= 0.1$ to Ro $= 1$. We might anticipate that over long times the error will decrease as the neglected higher order terms of u should decay faster than the leading order term u_0 since they depend on higher powers and derivatives of $\partial b_0/\partial x$ and hence they depend on higher powers of $1/(T + T_0)^\alpha$. This interpretation is supported by the numerical data as shown in Fig. 4.4(b)–(d) where the error appears to gradually decrease over long times after an initial increase. Note that the duration of the initial increase may exceed the time window for some parameter ranges. This is

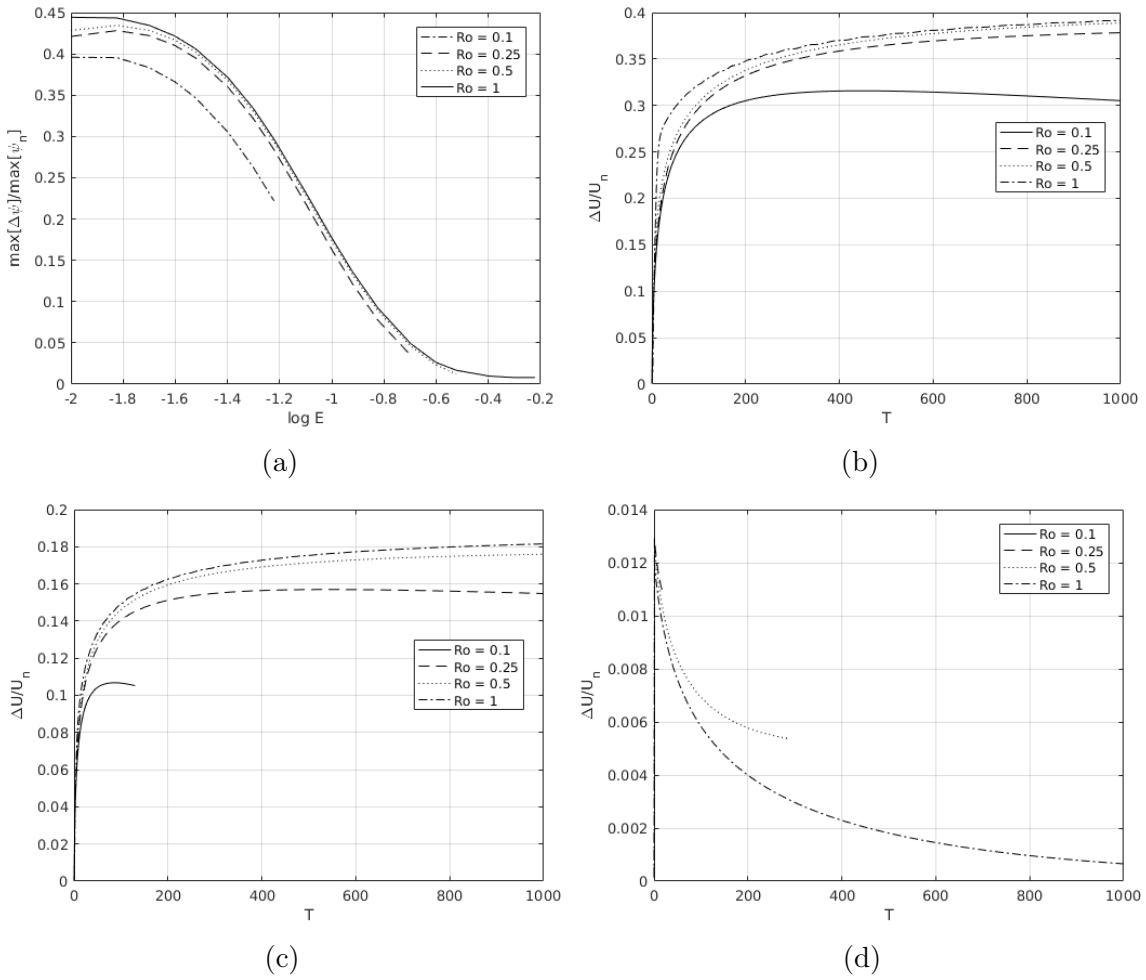

Fig. 4.4 (a) $\max[\Delta\psi]/\max[\psi_n]$ as a function of E for $T = 300$. Results are shown where $T_{max} < 3000$ for a range of Ro. (b)–(d) $\Delta U/U_n$ as a function of T for (b) E = 0.02, (c) E = 0.1, and (d) E = 0.4 and a range of Ro. Results are shown up to $T = T_{max}/10$.

most apparent for the cases of lowest Ro and highest E suggesting that this timescale scales as $\mathrm{Ro}^a/\mathrm{E}^b$ for positive a and b. We examine the case of small E in detail in Section 4.5.

From Chapter 3 the theoretical prediction of the centerline, $(z = 0)$, buoyancy is

$$b|_{z=0} = b_0 + O(\mathrm{Ro}^2), \tag{4.26}$$

where b_0 is given by Eq. (4.13). Note that the order Ro contribution has odd vertical symmetry and hence is zero along the centerline. We now compare this prediction with the numerical results by examining the shape of the cross front buoyancy profiles from the numerical simulations.

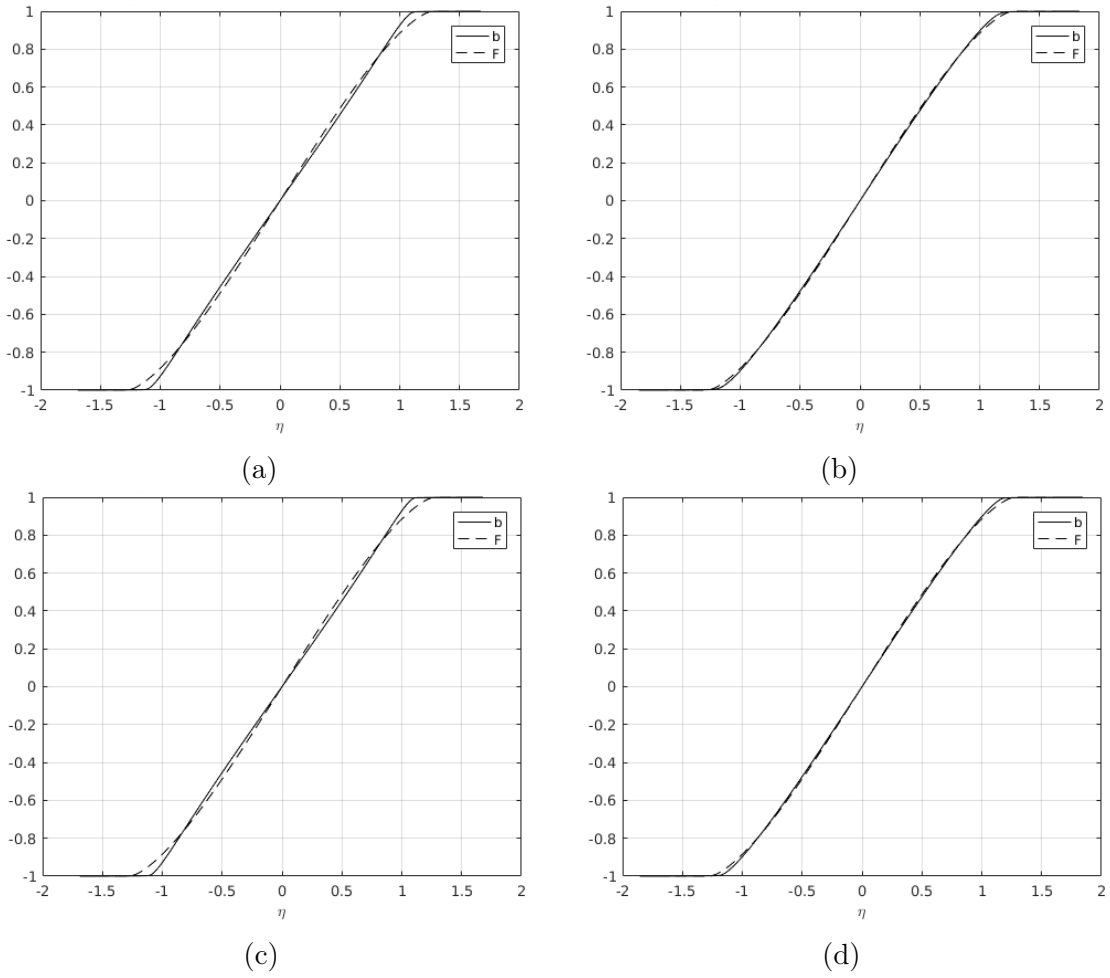

Fig. 4.5 Comparison of the centerline buoyancy at $T = 250$ as a function of $\eta = x/\gamma(T + T_0)^{1/4}$ with the similarity solution, $F(\eta)$ for (a) Ro = 0.5, E = 0.04, (b) Ro = 0.5, E = 0.1, (c) Ro = 1, E = 0.04, and (d) Ro = 1, E = 0.1.

Fig. 4.5 shows the centerline buoyancy profiles as a function of the normalised cross-front distance at $T = 250$ for a range of Rossby and Ekman numbers. We can see that the profiles are approximately linear in the center of the horizontal domain and more closely match the similarity solution for larger Ekman numbers. The size of the Rossby number has very little effect on the profile, even when Ro = 1. For all parameters shown in Fig. 4.5 we have that $T \ll T_{max}$. Therefore we predict that horizontal diffusion does not significantly affect the shape of these profiles and any discrepancies are due to small Ekman number effects which we will examine in Section 4.5.

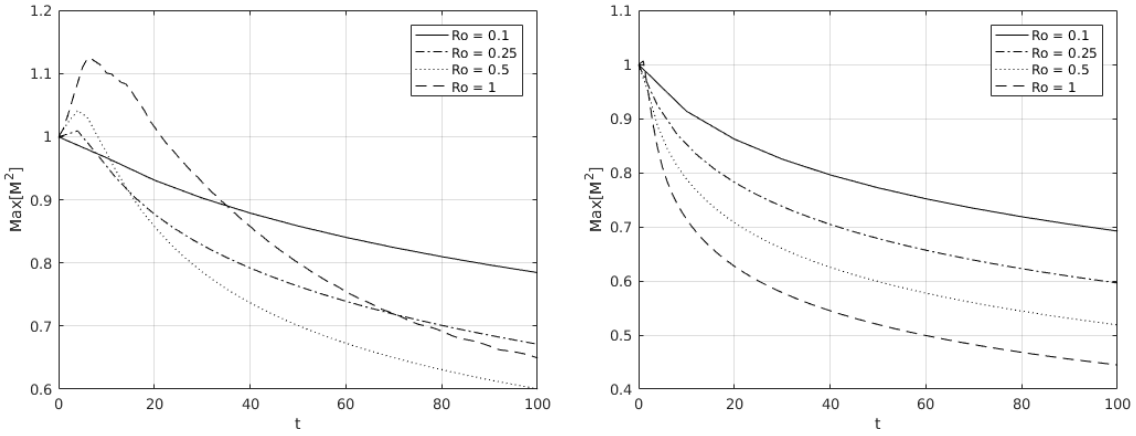

Fig. 4.6 Plots of the maximum surface horizontal buoyancy gradient, $\max_x[M^2(x, 1/2, t)]$ as a function of time, t, for a range of Rossby numbers and (a) $\mathrm{E} = 0.01$ and (b) $\mathrm{E} = 0.1$.

4.4.3 Initial Frontogenesis

In Chapter 3 we did not observe strong frontogenesis resulting from the evolution of an initially depth-independent front towards a balanced state. We found time-dependent solutions for this evolution, and saw that it was possible for surface gradients to sharpen during the initial adjustment even though the front was spreading in a depth-averaged sense, however this sharpening is an order Ro effect. We now consider the numerical simulations where $\mathrm{Ro} = O(1)$ to determine if these cases exhibit significant frontogenesis.

In Chapter 3 we found that the order Ro buoyancy component, b_1, is given by

$$b_1 = -\sqrt{\mathrm{E}}\left[K_0 + \sum_{n=0}^{\infty} D_n \mathcal{Z}_n(z) e^{-\mathrm{E}\lambda_n t/\mathrm{Ro}}\right] |\nabla_H b_0|^2 , \tag{4.27}$$

using the initial condition $b_1 = 0$. The D_n are given by

$$D_n = -\frac{1}{z_n^2}\int_{-1/2}^{1/2} K_0 \mathcal{Z}_n \, dz, \tag{4.28}$$

where the $\mathcal{Z}_n$ are vertical structure functions, the λ_n are their corresponding eigenvalues, and the z_n are normalisation constants, see Section A.1 for details. The cross-front

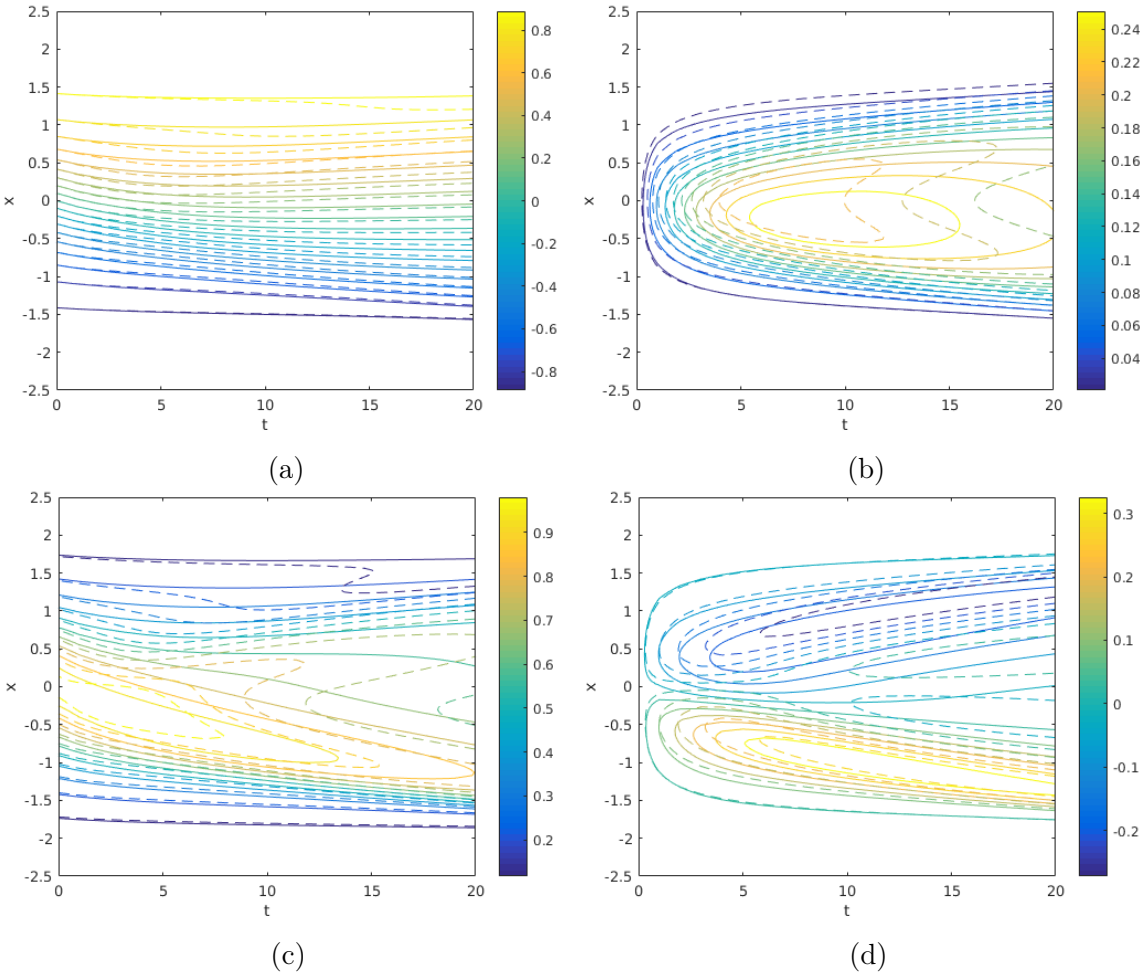

Fig. 4.7 (a) $b_0(x, 1/2, t)$, (b) $b_0(x, 1/2, t) - b_0(x, 0, t)$, (c) $M^2(x, 1/2, t)$, and (d) $M^2(x, 1/2, t) - M^2(x, 0, t)$ for Ro $= 1$ and E $= 0.02$. The solid contours show the numerical results and the dashed contours show the analytic predictions to order $O(\mathrm{Ro})$.

buoyancy gradient can now be calculated as

$$M^2 = \frac{\partial b_0}{\partial x} + \mathrm{Ro}\frac{\partial b_1}{\partial x} + O(\mathrm{Ro}^2), \tag{4.29}$$

and since we have seen that b_0 only spreads throughout the evolution, any sharpening must appear though the $O(\mathrm{Ro})$ term assuming that the $O(\mathrm{Ro}^2)$ term is small. This analysis is not asymptotically valid for Ro $= O(1)$ so we now seek to determine if significant surface frontogenesis occurs for larger Rossby numbers and how closely the behaviour is described by the analytic predictions.

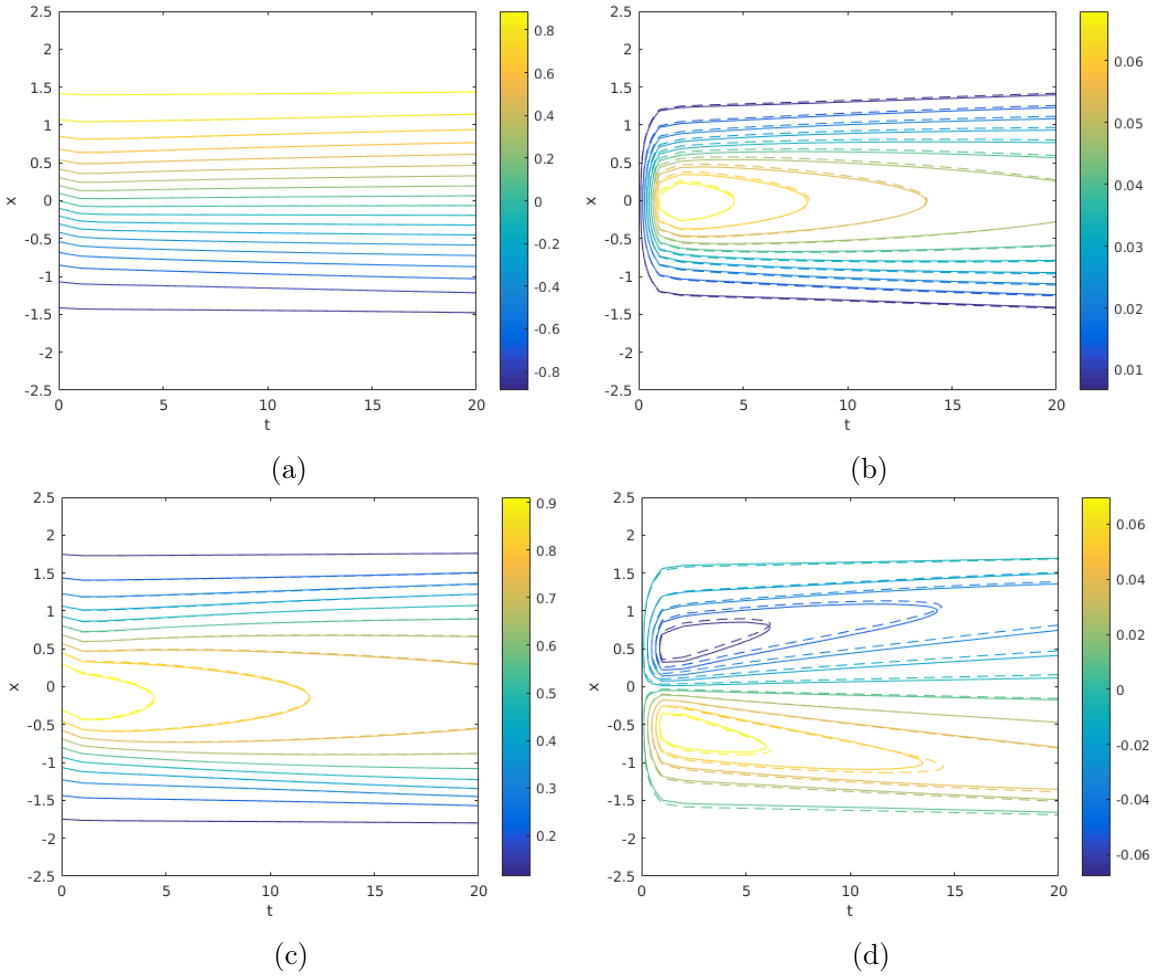

Fig. 4.8 (a) $b_0(x, 1/2, t)$, (b) $b_0(x, 1/2, t) - b_0(x, 0, t)$, (c) $M^2(x, 1/2, t)$, and (d) $M^2(x, 1/2, t) - M^2(x, 0, t)$ for Ro $= 1$ and E $= 0.2$. The solid contours show the numerical results and the dashed contours show the analytic predictions to order $O(\mathrm{Ro})$.

Fig. 4.6 shows the maximum horizontal buoyancy gradient on the top surface for a range of Rossby numbers. We can see that there is some surface sharpening of the front for small Ekman numbers however this effect is relatively small and short-lived as once a self-similar state is reached the front will only spread. There is no evidence of frontal sharpening leading to a surface discontinuity as observed for the evolution of an inviscid unbalanced front or a front in an imposed strain flow (Hoskins & Bretherton, 1972; Blumen, 2000; Shakespeare & Taylor, 2013; McWilliams, 2017).

Fig. 4.7 and Fig. 4.8 show the initial evolution of the surface buoyancy, $b(x, 1/2, t)$, and the surface buoyancy gradient, $M^2(x, 1/2, t)$ for Ro $= 1$ and E $= 0.02, 0.2$. We also show the difference between the surface and centerline values of b_0 and M^2 since

to leading order these corresponds to $\mathrm{Ro}\, b_1$ and $\mathrm{Ro}\, \partial b_1/\partial x$ respectively. The analytic predictions to order $O(\mathrm{Ro})$ are shown by the dashed contours. We can see that the analytic predictions are fairly accurate for $\mathrm{E} = 0.02$ with a maximum error of around 25% and very accurate for $\mathrm{E} = 0.2$ with a maximum error of around 2%. In both cases the theory accurately predicts the time taken for the depth-dependence to develop as well as both the position and the value of the maximum buoyancy gradient despite the Rossby number not being small and only using a prediction correct to first order in Ro. If there are additional frontogentic mechanisms, such as an imposed strain flow, the increase in the surface buoyancy gradient can be large and the theory based on the assumption of small Rossby model will likely no longer be valid. In this case a more general model will be required (Shakespeare & Taylor, 2013; McWilliams, 2017; Sullivan & McWilliams, 2018).

4.5 Theory for $O(1)$ Rossby number and small Ekman number

As noted above, the largest differences between the theoretical predictions and numerical simulations occur for large Ro and small E. In this section we analyse the momentum budget to identify the source of these discrepancies. We then propose a modification to TTW balance that includes the influence of a depth-independent geostrophic flow. We use this to extend the theory in Chapter 3 to $O(1)$ Rossby numbers and small Ekman numbers and find that it leads to excellent agreement with the numerical simulations.

Fig. 4.9 shows the balances in the horizontal momentum equations for $E = 0.01$ and $Ro = (1, 0.1)$ at $t = 100$ and $x = 0$. We can see that the cross-front (x) momentum equations in both cases are very close to TTW balance, even for $Ro = 1$. However, there are significant deviations in the y momentum equation due to a large advection term. We find that Dv/Dt is dominated by $u\,\partial v/\partial x$ with the along-front velocity, v, developing a large depth-independent component corresponding to two jets of opposite direction as shown in Fig. 4.10.

In order to understand the formation of these jets, we can examine the depth-averaged along-front momentum equation. First, define the depth-average as

$$\overline{\phi} = \int_{-1/2}^{1/2} \phi \, dz, \tag{4.30}$$

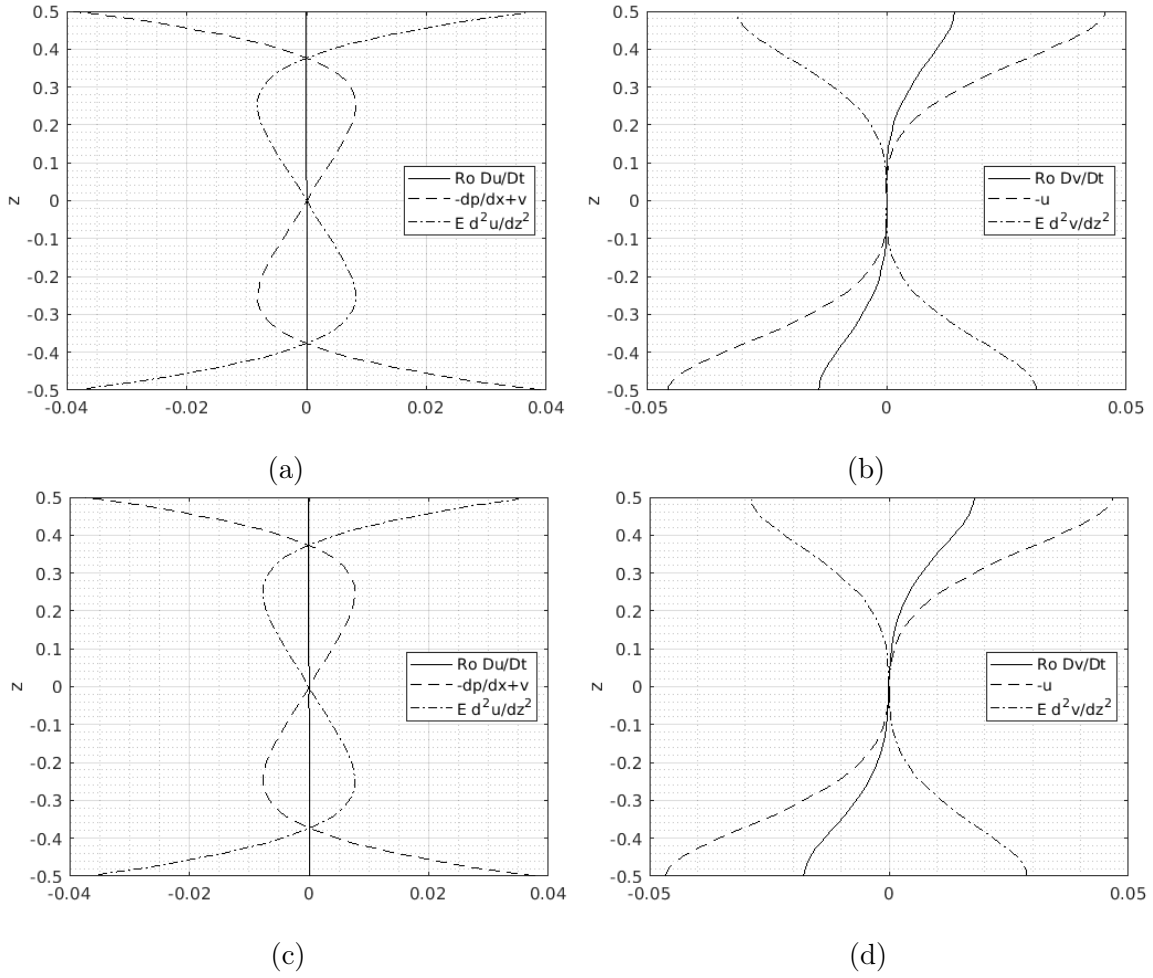

Fig. 4.9 Plots of the terms in the horizontal momentum balances for E = 0.01 and Ro = 0.1 ((a), (b)) and Ro = 1 ((c), (d)). Calculations use the data from our numerical simulations at $t = 100$ and $x = 0$.

and write $\phi' = \phi - \overline{\phi}$ to denote the deviation from this average. Depth-averaging the y momentum equation gives

$$\mathrm{Ro}\left(\frac{\partial \overline{v}}{\partial t} + \frac{\partial}{\partial x}\overline{u'v'}\right) = \epsilon^2 \mathrm{E}\,\nabla_H^2 \overline{v}, \tag{4.31}$$

where we have assumed that $\overline{u} = 0$ by symmetry (and hence $u' = u$). For $\epsilon^2\mathrm{E} \ll \mathrm{Ro}$ we can write

$$\frac{\partial \overline{v}}{\partial t} = -\frac{\partial}{\partial x}\overline{uv'}, \tag{4.32}$$

hence a depth-independent jet forms due to the correlation between the along-front and cross-front velocity fields. In the initial condition considered here, the depth average of

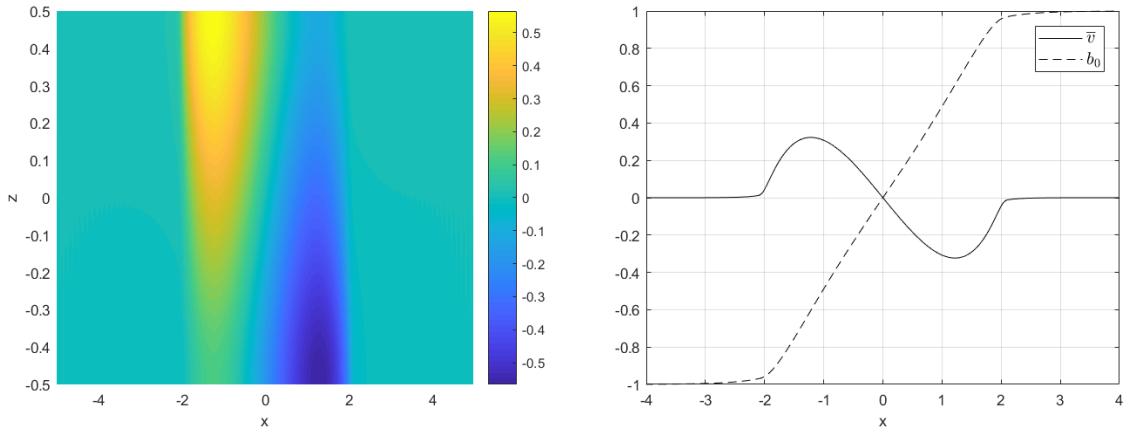

(a) (b)

Fig. 4.10 (a) plot of $v(x,z)$ at $t = 100$. (b) plot of $\overline{v}$ showing the structure of the depth-independent jet, b_0 is included for comparison.

the along-front velocity is exactly zero. However, as the front evolves, the cross-front velocity displaces the along-front thermal wind jets in the cross-front direction. The displaced along-front flow is then mixed vertically, leading to the formation of a depth-independent flow. This depth-independent flow can become large and acts to disrupt the TTW balance.

Splitting the along-front velocity into depth-average and deviation quantities, we can write the horizontal momentum equations as

$$\mathrm{Ro}\frac{Du}{Dt} - v' - \overline{v} = -\frac{\partial p}{\partial x} + \mathrm{E}\nabla_\epsilon^2 u, \tag{4.33}$$

and

$$\mathrm{Ro}\left(\frac{Dv'}{Dt} + \frac{\partial \overline{v}}{\partial t} + u\frac{\partial \overline{v}}{\partial x}\right) + u = \mathrm{E}\nabla_\epsilon^2 v. \tag{4.34}$$

If we depth-average Eq. (4.33) we find that the Coriolis term $-\overline{v}$ is balanced by the depth-independent component of the pressure gradient, $-\partial\overline{p}/\partial x$ hence

$$\mathrm{Ro}\frac{Du}{Dt} - v' = -\frac{\partial p'}{\partial x} + \mathrm{E}\nabla_\epsilon^2 u. \tag{4.35}$$

Assuming that u and v' remain order 1 fields, we have that $\partial\overline{v}/\partial t = O(1)$ by Eq. (4.32). However, we note that over the long timescale, $T = \mathrm{Ro}\,t$, we can have $\overline{v} = O(1/\mathrm{Ro})$. Therefore the term $\mathrm{Ro}\,u\,\partial\overline{v}/\partial x$ in Eq. (4.34) may appear in the leading order balance.

If we now assume that Ro is small, we obtain the leading order velocity balance

$$-v_0' = -\frac{\partial p_0'}{\partial x} + \mathrm{E}\frac{\partial^2 u_0}{\partial z^2}, \tag{4.36}$$

and

$$\left(\mathrm{Ro}\frac{\partial \overline{v}}{\partial x} + 1\right) u_0 = \mathrm{E}\frac{\partial^2 v_0'}{\partial z^2}, \tag{4.37}$$

hence $\overline{v}$ is a background geostrophic flow which modifies the absolute vorticity of the system. We note that $\overline{v}$ will form spontaneously and evolve throughout time in contrast to the imposed geostrophic flow often used in frontal problems (Thomas & Lee, 2005). Eq. (4.36) and Eq. (4.37) are only asymptotically valid in the limit of small Rossby number, however, examining the momentum balances we find that this approximation is accurate outside the region of initial frontogenesis for all parameter values tested.

Eq. (4.36) and Eq. (4.37) can be solved to obtain the modified TTW solution for the leading order velocity

$$u_0 = -\sqrt{\frac{\mathrm{E}_g}{\mathrm{Ro}\frac{\partial \overline{v}}{\partial x} + 1}}\, K_0''\left(\frac{z}{\sqrt{\mathrm{E}_g}}; \frac{1}{\sqrt{4\mathrm{E}_g}}\right)\frac{\partial b_0}{\partial x}, \tag{4.38a}$$

$$v_0' = \quad -\sqrt{\mathrm{E}_g}\;\; K_0\left(\frac{z}{\sqrt{\mathrm{E}_g}}; \frac{1}{\sqrt{4\mathrm{E}_g}}\right)\frac{\partial b_0}{\partial x}, \tag{4.38b}$$

where E_g is the Ekman number modified by the geostrophic flow

$$\mathrm{E}_g = \frac{\mathrm{E}}{\sqrt{\mathrm{Ro}\frac{\partial \overline{v}}{\partial x} + 1}}. \tag{4.39}$$

The $O(\mathrm{Ro})$ buoyancy correction can now be calculated as

$$b_1 = -\frac{\sqrt{\mathrm{E}_g}\,\mathrm{Pr}}{\mathrm{Ro}\frac{\partial \overline{v}}{\partial x} + 1} K_0\left(\frac{z}{\sqrt{\mathrm{E}_g}}; \frac{1}{\sqrt{4\mathrm{E}_g}}\right)\left[\frac{\partial b_0}{\partial x}\right]^2, \tag{4.40}$$

by the same steps described in Chapter 3. Combining our results, the background buoyancy field satisfies

$$\frac{\partial b_0}{\partial T} = \frac{\partial}{\partial x}\left[\frac{\mathrm{E}_g\,\mathrm{Pr}}{(g_0+1)^{3/2}}\overline{K_0'^2\left(\frac{z}{\sqrt{\mathrm{E}_g}}; \frac{1}{\sqrt{4\mathrm{E}_g}}\right)}\left(\frac{\partial b_0}{\partial x}\right)^3\right], \tag{4.41}$$

and from Eq. (4.32),

$$\frac{\partial g_0}{\partial T} = \frac{\partial^2}{\partial x^2}\left[\frac{\mathrm{E}_g}{(g_0+1)^{1/2}}\overline{K_0'^2\left(\frac{z}{\sqrt{\mathrm{E}_g}};\frac{1}{\sqrt{4\mathrm{E}_g}}\right)}\left(\frac{\partial b_0}{\partial x}\right)^2\right], \tag{4.42}$$

where

$$g_0 = \mathrm{Ro}\frac{\partial \overline{v}}{\partial x}, \tag{4.43}$$

is the vertical vorticity associated with the depth-independent geostrophic flow and $E_g = E/\sqrt{1+g_0}$. In the absence of a depth-independent flow ($\overline{v} = 0$), Eq. (4.38) reduces to TTW balance. The expressions in Eq. (4.42) and Eq. (4.41) can therefore be viewed as a generalization of the theory described in Chapter 3.

To test these predictions we compare the horizontal velocity fields from a range of simulations with both our original TTW predictions and our modified TTW solution from Eq. (4.38). Fig. 4.11 shows a comparison between the numerical cross-front velocity and our two analytic predictions; the TTW prediction and the modified TTW prediction. We can see that the modified TTW prediction very closely fits the numerical profiles with an error under 1% in all cases. Since the balance described in Eq. (4.36) and Eq. (4.37) is found to be accurate, we conclude that the accuracy of our spreading rate predictions depends on how large the geostrophic flow becomes for each pair of parameters, (Ro, E).

Fig. 4.12.(a) shows the magnitude of $g_0 = \mathrm{Ro}\,\partial\overline{v}/\partial x$ from our numerical simulations at $x = 0$ and $T = 100$ as a function of E and Ro. Fig. 4.12.(b) shows the maximum relative error between the TTW and modified TTW cross-front velocity (u) solutions as a function of E and g_0. From Fig. 4.12.(a) we can see that g_0 can become large for small values of E. Hence, from Fig. 4.12.(b), the magnitude of the cross-front velocity can change significantly; by around 30% for $\mathrm{E} < 0.05$. We note that even a large g_0 has very little effect on the cross-front velocity in the case of large E. For large E, the horizontal momentum balance is controlled by the dominant pressure gradient and vertical diffusion terms. Therefore the effect of changing the relative rotation is less significant than in the case of small E where the horizontal momentum balance is dominated by a thermal wind balance between the pressure gradient and rotation term. Interestingly we do not expect much variation with Ro since both g_0 and b_0 evolve on the slow timescale T and there remains no explicit Ro dependence in Eq. (4.41) and Eq. (4.42). This is consistent with Fig. 4.12.(a) where any weak Ro dependence likely arises through Ro dependent processes such as the time taken for the system

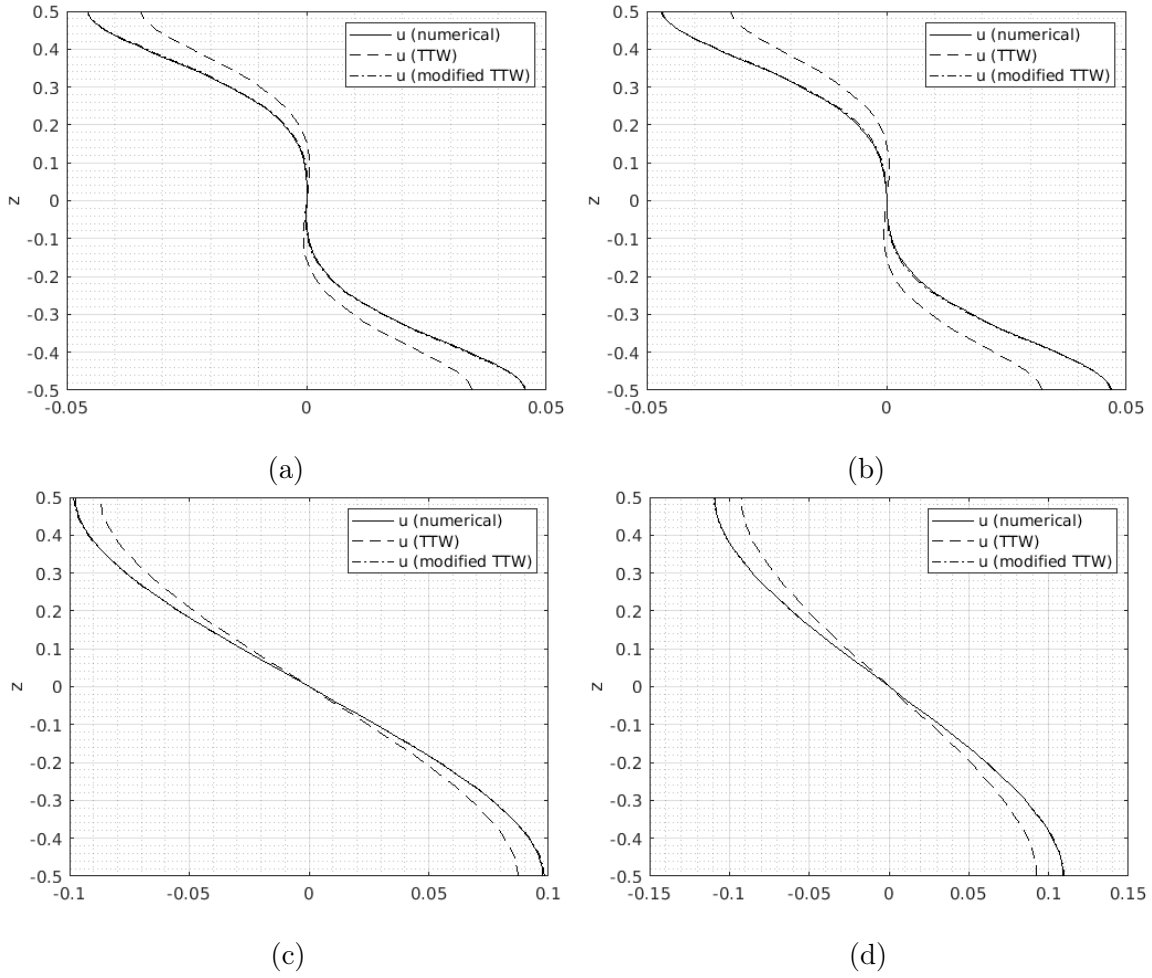

Fig. 4.11 Comparison of the cross front velocity field between numerical simulations, the TTW prediction and the modified TTW prediction for (a) $\mathrm{Ro} = 0.1, \mathrm{E} = 0.01$, (b) $\mathrm{Ro} = 1, \mathrm{E} = 0.01$, (c) $\mathrm{Ro} = 0.1, \mathrm{E} = 0.1$ and (d) $\mathrm{Ro} = 1, \mathrm{E} = 0.1$. The fields are evaluated at $x = 0$ and $T = 100$.

to equilibrate and begin spreading via shear dispersion and the effects of horizontal diffusion.

From Eq. (4.41) we can define a modified effective diffusivity function, Q_g, by

$$Q_g(x;\,\mathrm{E}) = \frac{\mathrm{E}_g}{(g_0+1)^{3/2}}\overline{K_0'^2\left(\frac{z}{\sqrt{\mathrm{E}_g}}\,;\frac{1}{\sqrt{4\mathrm{E}_g}}\right)}, \tag{4.44}$$

so Eq. (4.41) can be written as

$$\frac{\partial b_0}{\partial T} = \frac{\partial}{\partial x}\left[\mathrm{Pr}\,Q_g(x;\,\mathrm{E})\left(\frac{\partial b_0}{\partial x}\right)^3\right]. \tag{4.45}$$

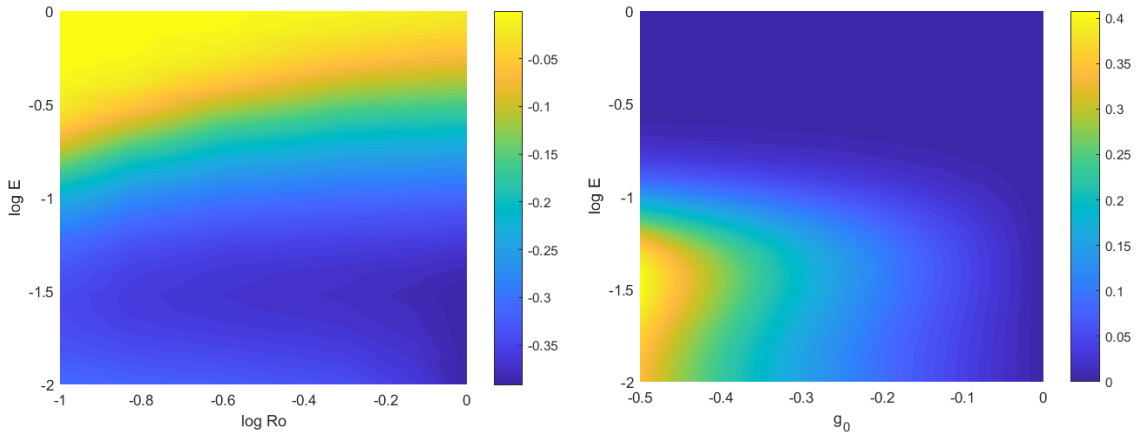

(a) (b)

Fig. 4.12 (a) Numerical value of g_0 at $T = 100$ and $x = 0$ as a function of E and Ro. (b) The maximum relative error between the TTW and modified TTW cross-front velocity fields (u) as a function of E and g_0.

We note that Q_g has a complex dependence on x and T so Eq. (4.45) cannot be solved using a similarity solution. Fig. 4.13 shows g_0 and Q_g calculated from our numerical simulation for E = 0.01 and Ro = 1. We can see that g_0 is negative throughout the middle of the frontal region corresponding to a higher effective diffusivity. At the frontal edges g_0 is strongly positive resulting in a decrease to the effective diffusivity.

In the case of $g_0 = 0$ we have that the frontal width scales as $x \sim \gamma T^{1/4}$ where $\gamma \sim Q^{1/4}$ due to the nonlinear nature of the spreading. If we assume here that the modified spreading parameter is $\gamma_g \sim Q_g^{1/4}$ we find that the spreading rate is less sensitive to the effects of a geostrophic flow than the velocity fields due to the 1/4 power dependence. Additionally, the spreading rate increases in the center of the domain and decreases at the edges, therefore averaging γ_g across the domain gives a value very similar to the original predicted value of γ. Therefore we do not expect significant change in the spreading rate which is consistent with the accuracy of our original predictions in Fig. 4.2.

4.6 Scaling for vertical velocity

A distinguishing feature of the circulation around the front is the appearance of large vertical velocities at the edges of the front. This is visible in the streamfunction associated with the simulations and the theory for the case plotted in Fig. 4.3 through

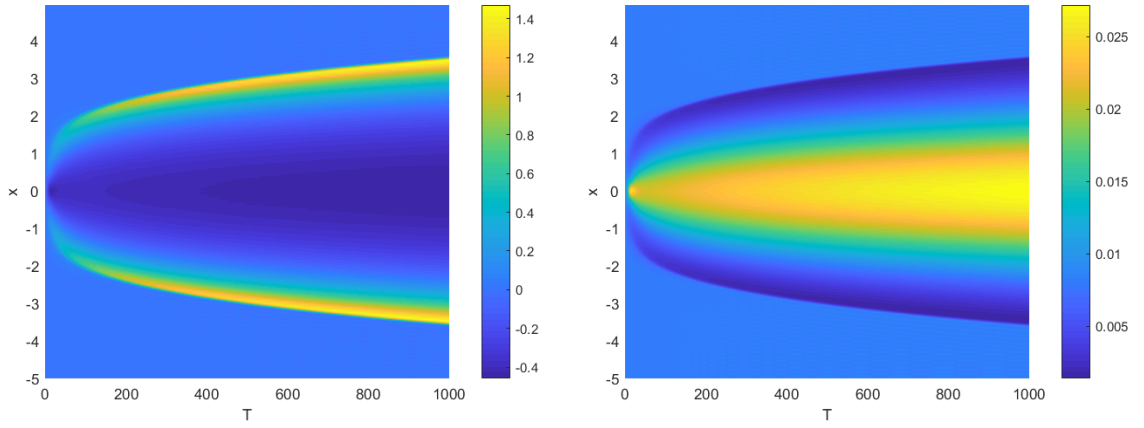

(a) (b)

Fig. 4.13 (a) Numerical value of g_0 as a function of x and T for $\mathrm{E} = 0.01$ and $\mathrm{Ro} = 1$. (b) $Q_g(x, \mathrm{E})$ as a function of x and T for $\mathrm{E} = 0.01$ and $\mathrm{Ro} = 1$.

a bunching of the streamlines near $x = \pm 3$. However, the theory described in Chapter 3 did not provide a prediction for the magnitude of the vertical velocity. In this section we will extend the theory to estimate the magnitude of the vertical velocity and the width of the regions of enhanced up/downwelling and test this prediction using the numerical simulations.

The theoretical prediction for the leading order vertical velocity is

$$w_0 = \mathrm{E}\, K_0' \left(z/\sqrt{\mathrm{E}} \right) \frac{\partial^2 b_0}{\partial x^2}. \tag{4.46}$$

However, since our similarity solution for b_0 (Eq. (4.14)) is piecewise with infinite curvature ($\partial^2 b_0/\partial x^2$) at the frontal edges, the theory is unable to predict the strength of the up/down-welling that occurs at the edges of the front. Fig. 4.14 shows the centerline values of the buoyancy and the vertical velocity for two different values of Rossby number. We can see than the maximum vertical velocity occurs at the edge of the front where the curvature is high and when the frontal edges are sharper (i.e. a greater curvature confined to a narrower region), the vertical velocity appears in thin bands of strong up/down-welling which correspond to the high curvature regions. We note that for $\mathrm{Ro} = 1$ these bands become very narrow and may be susceptible to numerical errors.

Though we cannot predict the functional form of $\partial^2 b_0/\partial x^2$ and hence w_0 near the edges of the front from our analytic solution, we can use the similarity solution to estimate a scaling for the maximum vertical velocity. From Chapter 3 the buoyancy

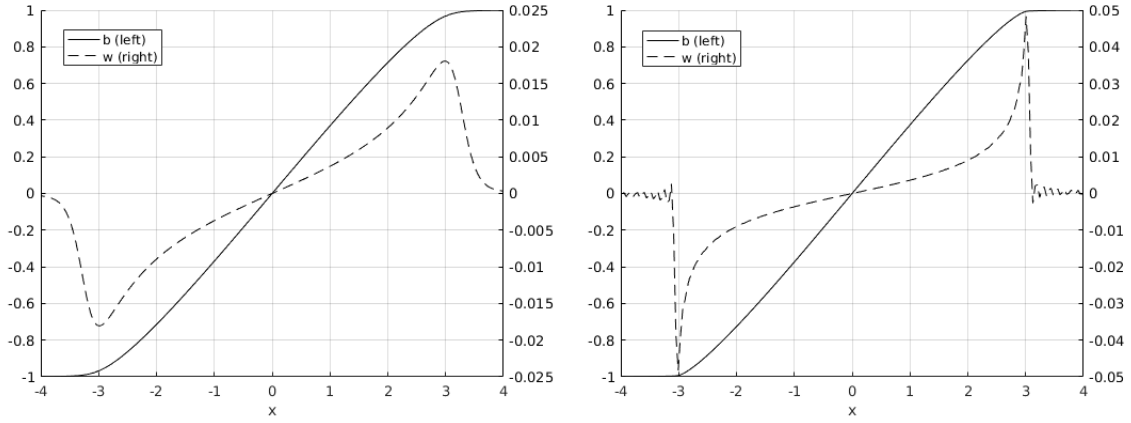

(a) (b)

Fig. 4.14 Plot of the centerline buoyancy (solid line) and centerline vertical velocity (dashed line) for E = 0.1 and (a) Ro = 0.25, (b) Ro = 1 at $T = 200$.

field, b_0, is determined by the equation

$$\frac{\partial b_0}{\partial T} = \frac{\partial}{\partial x}\left[\mathrm{Pr}\, Q\left(\frac{\partial b_0}{\partial x}\right)^3 + \frac{\epsilon^2 \mathrm{E}}{\mathrm{Ro}^2 \mathrm{Pr}}\frac{\partial b_0}{\partial x}\right], \tag{4.47}$$

where $Q(\mathrm{E})$ is defined in Eq. (4.20). The similarity solution arises as the solution of this equation when the second term in brackets is small, corresponding to an approximate balance between time evolution and shear dispersion. Near the edges of the front, where the curvature is high, the term describing horizontal diffusion becomes important and smooths out the singularity in F''.

We now assume that there are thin regions at the edges of the front where this smoothing occurs. In these regions we assume that the horizontal diffusion term is similar in magnitude to the other two terms and the curvature of the front, $\partial^2 b_0/\partial x^2$, is approximately constant. Using the similarity solution we have that

$$\mathrm{Pr}\, Q\,\frac{\partial}{\partial x}\left(\frac{\partial b_0}{\partial x}\right)^3 \sim -\frac{\eta}{4T}\sqrt{1-\frac{\pi^2\eta^2}{16}}, \tag{4.48}$$

and

$$\frac{\epsilon^2 \mathrm{E}}{\mathrm{Ro}^2 \mathrm{Pr}}\frac{\partial^2 b_0}{\partial x^2} \sim -\frac{\epsilon^2 \mathrm{E}}{\mathrm{Ro}^2 \mathrm{Pr}}\frac{\pi^2\eta}{16\gamma^2 T^{1/2}}\frac{1}{\sqrt{1-\frac{\pi^2\eta^2}{16}}}. \tag{4.49}$$

Balancing these two terms gives that

$$1 - \frac{\pi^2\eta^2}{16} \sim \frac{\epsilon^2 \mathrm{E}}{\mathrm{Ro}^2\mathrm{Pr}} \frac{\pi^2 T^{1/2}}{4\gamma^2}, \tag{4.50}$$

and allows us to estimate the width of the smoothing regions by writing

$$\eta = \pm\left(\frac{4}{\pi} - \chi\right), \tag{4.51}$$

for small region width χ to get

$$\chi \sim \frac{\epsilon^2 \mathrm{E}}{\mathrm{Ro}^2\mathrm{Pr}} \frac{\pi T^{1/2}}{2\gamma^2}. \tag{4.52}$$

When the edges spread to fill the whole domain we have $\chi \sim 1$ and recover the result from Eq. (4.18). We can now use Eq. (4.50) to estimate the magnitude of the curvature near the frontal edge ($\eta \approx \pm 4/\pi$) as

$$\frac{\partial^2 b_0}{\partial x^2} \sim \mp \frac{\mathrm{Ro}\sqrt{\mathrm{Pr}}}{2\epsilon\gamma\sqrt{\mathrm{E}}\, T^{3/4}}, \tag{4.53}$$

and since

$$w_0 = \mathrm{E}\, K_0' \frac{\partial^2 b_0}{\partial x^2}, \tag{4.54}$$

the maximum vertical velocity (occurring at $z = 0$) scales as

$$w_0 \sim \pm w_s, \tag{4.55}$$

where

$$w_s = \frac{\mathrm{Ro}\sqrt{\mathrm{Pr}}\, C(\mathrm{E})}{\epsilon\, T^{3/4}}, \tag{4.56}$$

and

$$C(\mathrm{E}) = \frac{\sqrt{\mathrm{E}}|K_0'(0)|}{(12\pi^2 Q)^{1/4}}. \tag{4.57}$$

We can also predict that the width of the bands of enhanced vertical velocity scales as

$$\gamma\, T^{1/4}\chi \sim \Delta x_w = \frac{\epsilon^2 \mathrm{E}}{\mathrm{Ro}^2\mathrm{Pr}} \frac{\pi T^{3/4}}{2\gamma}. \tag{4.58}$$

Note that $T = \mathrm{Ro}\, t$ so these results can also be written in terms of the time t with a different Rossby number scaling. Using the asymptotic behaviour of K_0' and Q shown

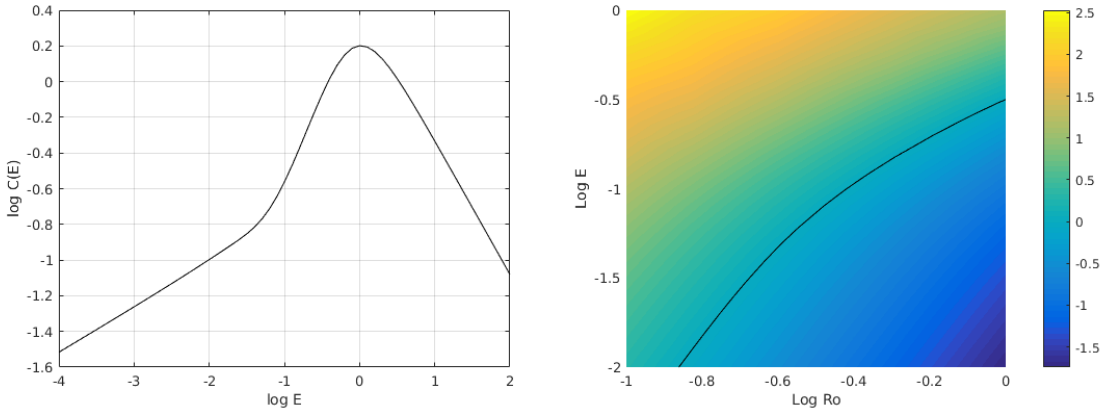

(a) (b)

Fig. 4.15 (a) $\log[C(\mathrm{E})]$ as a function of E, note that for small E, $C \sim \mathrm{E}^{1/4}$ and for large E, $C \sim \mathrm{E}^{-3/4}$ from Eq. (4.59). (b) $\log[\Delta x_w/\Delta x]$ as a function of E and Ro for $T = 200$. The black curve is the contour $\Delta x_w/\Delta x = 1$.

in Chapter 3 we find that

$$C(\mathrm{E}) \sim \begin{cases} \mathrm{E}^{1/4}, & \mathrm{E} \ll 1, \\ \mathrm{E}^{-3/4}, & \mathrm{E} \gg 1, \end{cases} \tag{4.59}$$

so we expect the vertical velocity to be small for both very small and very large values of E, assuming that the regions of high vertical velocity are still thin ($\chi \ll 1$).

We now use the numerical results to test these predictions. There are, however, some limitations to the numerical solution due to the resolution. For large Ro or small E the regions of enhanced vertical velocity can become very narrow and if they are of a scale similar or smaller than the grid size, Δx, the vertical velocity will likely not be accurate. We therefore consider the quantity $\Delta x_w/\Delta x$ when examining each simulation to see if the regions of strong vertical velocity are likely to be well resolved.

Fig. 4.15(a) shows $C(\mathrm{E})$ as a function of the Ekman number, E. The coefficient $C(\mathrm{E})$ and hence the vertical velocity are maximum for $\mathrm{E} \simeq 1$. Fig. 4.15(b) shows the ratio of the predicted width of the region with enhanced vertical velocity to the horizontal grid spacing used in the simulations, i.e. $\log[\Delta x_w/\Delta x]$. Here Δx_w is calculated at $T = 200$. The black contour indicates $\Delta x_w/\Delta x = 1$. For all cases below this line, the grid spacing will be insufficient to capture the maximum vertical velocity.

Fig. 4.16(a) shows the maximum vertical velocity at $T = 200$ as diagnosed from the numerical simulations as a function of E and Ro. The curves in white shows the region in which shear dispersion is dominant (the region below the curve) and the curves in

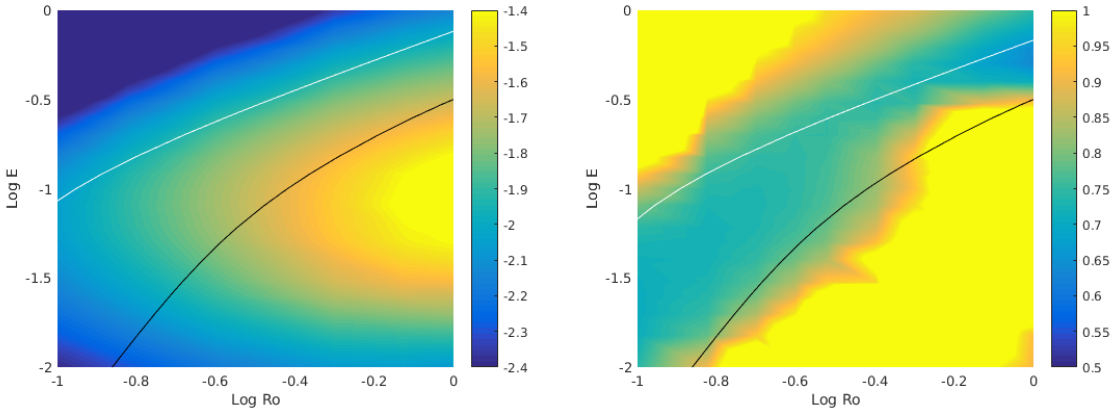

(a) (b)

Fig. 4.16 (a) $\log[\max w]$ diagnosed from the numerical solutions as a function of E and Ro at $T = 200$. (b) α_w as a function of E and Ro over the time interval $T \in [100, 350]$. The curves in white are (a) $T_{max} = 2000$ and (b) $T_{max} = 3500$ and the curves in black are contours of $\Delta x_w/\Delta x = 1$ at (a) $T = 200$ and (b) $T = 100$. We expect the theoretical predictions to be valid between the two curves.

black show the region where the regions of high curvature are smaller than the grid scale (the region below the curve). The theoretical prediction can be tested in the region between the white and black curves. The maximum vertical velocity increases with increasing E for small E and decreases with increasing E for large E. This is consistent with the predictions made in Eq. (4.56) since C also has this behaviour. However, the maximum vertical velocity in the simulations is seen at $\mathrm{E} \simeq 0.1$ while the theory predicts a maximum vertical velocity (and C) at $\mathrm{E} \simeq 1$. The maximum vertical velocity diagnosed from the simulations increases approximately linearly with increasing Ro, which is consistent with the theoretical prediction.

For larger Rossby numbers the effects of the $O(\mathrm{Ro})$ vertical velocity component may also become important and based on shape of the streamfunction from Fig. 4.3 we expect that the $O(\mathrm{Ro})$ vertical velocity will oppose the leading order component and hence reduce the maximum up/down-welling. Since the leading order streamfunction is still accurate for large E (see Fig. 4.4(a)), we can conclude that the effects of the $O(\mathrm{Ro})$ velocity component will be small for $\mathrm{E} \gtrsim 0.1$.

In order to determine the time dependence of the vertical velocity we fit $\max[w]$ to the curve

$$\max[w] = \frac{\gamma_w}{(T + T_0)^{\alpha_w}}, \tag{4.60}$$

to determine the value of the exponent, α_w. Fig. 4.16(b) shows the numerical values of the exponent calculated over a time interval of $T \in [100, 350]$, we can see that $\alpha_w \approx 3/4$ in the region between the two curves where we expect the theory to be valid; this is in agreement with the predictions made in Eq. (4.56).

4.7 Conclusions and Discussion

We have used fully nonlinear numerical simulations to consider the evolution of a front in the presence of strong vertical mixing. As predicted in Chapter 3, vertical mixing induces spreading of the front via shear dispersion and the spreading rate diagnosed from the simulations agrees with the theory. The simulated velocity and buoyancy fields generally compare well with the theoretical predictions with a better agreement between the theory and simulations for larger Ekman numbers.

The accuracy of the theory seems to depend only weakly on the Rossby number and the theory is accurate even for $O(1)$ Rossby numbers despite the fact that the theory was based on an asymptotic analysis which was valid in the limit of small Rossby numbers. This can be explained by the Rossby number entering primarily through the formation of geostrophic jets, the evolution of which do not explicitly depend on Rossby number. Interestingly, for $\mathrm{Ro} = 1, \mathrm{E} = 0.1$, the theoretical prediction for the streamfunction is accurate to within 20%, while the spreading rate is accurate to within about 5%. It is not immediately apparent why the spreading rate is less sensitive to the formation of geostrophic jets than the velocity field though this may be a consequence of the functional dependence.

Despite the theory being derived for the TTW limit where the Ekman number is assumed to be order 1 and much larger than the Rossby number, we find that it is valid for a much larger range of E with significant discrepancies only for $\mathrm{E} = O(0.01)$. For example we observe close (within 20%) agreement between the theory and numerics when Ro is one order of magnitude larger than E. We have presented a modified theory which, while again only asymptotically valid for small Ro and large E, accurately describes the evolution of the system and the formation of a depth-independent geostrophic jet for small E and order 1 Ro. For larger Rossby numbers or smaller Ekman numbers the solution is driven away from TTW balance by nonlinear effects such as surface frontogenesis (McWilliams, 2017) and nonlinear Ekman transport (Stern, 1965; Niiler, 1969; Thomas & Lee, 2005). We note that the formation of a geostrophic jet requires frontal edges so only occurs in finite width fronts. Therefore

our TTW solution is valid for the Garrett & Loder (1981) case of small E and Ro examined in Chapter 3.

For $O(1)$ Rossby numbers and small Ekman numbers the adjustment from an initially depth-independent front can cause surface frontogenesis, although for the parameters considered here the increase in the horizontal buoyancy gradient is modest. In the absence of frictional and diabatic effects, other factors such as a background strain or unbalanced flow have been shown to sharpen fronts towards a discontinuity (Hoskins & Bretherton, 1972; Blumen, 2000). It remains unclear whether a discontinuity could develop in response to TTW flow alone. For all Rossby numbers considered here, frontogenesis only occurs during a transient period and eventually gives way to frontal spreading as predicted by the theory.

Finally, we derived a new scaling for the vertical velocity. This scaling agrees with the numerical simulations as long as the dominant balance in the buoyancy equation is between time dependence and shear dispersion (the horizontal diffusion is small) and the region of enhanced vertical velocity is sufficiently resolved in the numerical simulation.

A dimensional vertical velocity can be obtained from the theoretical prediction ($W = \Delta b H^2/(fL^2)$) using typical parameters for upper ocean fronts. For example, with $\Delta b = 10^{-3}\mathrm{m\,s^{-2}}$, $H = 100\mathrm{m}$, $L = 3\mathrm{km}$ and $f = 10^{-4}\mathrm{s^{-1}}$ the vertical velocity scale is $W \approx 10^{-2}\mathrm{m\,s^{-1}}$. Numerically we find that $w \sim 10^{-2}$ corresponding to a dimensional vertical velocity of $w^* = Ww \sim 10^{-4}\mathrm{m\,s^{-1}}$ or 10m/day. This prediction is of the same order of magnitude as vertical velocity diagnosed from ocean models (e.g. Mahadevan & Tandon (2006); Capet *et al.* (2008*b*)), suggesting that the vertical circulation associated with turbulent thermal wind balance could contribute significantly to the vertical velocity at fronts.

Chapter 5

The evolution of a front in turbulent thermal wind balance: surface forcing

5.1 Introduction

In Chapter 3 we considered a simple analytic model of an unforced ocean front in the presence of strong vertical mixing. The dominant momentum balance was found to be between the Coriolis force, the horizontal pressure gradient and the vertical mixing of horizontal momentum; this balance is known as 'Turbulent thermal wind' (TTW) or 'generalised Ekman' and has been seen in models and observations of ocean fronts (Cronin & Kessler, 2009; Taylor & Ferrari, 2010; Gula *et al.*, 2014; McWilliams *et al.*, 2015; Wenegrat & McPhaden, 2016*b*) where the vertical momentum fluxes are associated with small-scale turbulence.

The effect of vertical mixing is to couple the along-front and cross-front velocities and drive a leading order circulation. The vertical shear associated with the cross-front velocity acts to spread the front by shear dispersion; the vertical diffusion is projected horizontally by the velocity shear resulting in a horizontal spreading (Young, 1994).

The central aim of this Chapter is to study the competition between frontal sharpening and frontal spreading induced by vertical mixing and surface forcing. This leads to the following question: for a prescribed level of mixing and surface forcing, does the front evolve towards an equilibrium state, and if so what controls the associated frontal width and the horizontal buoyancy gradient? An answer to this question could provide a basis for improving parametrisations of submesoscale processes where the horizontal buoyancy gradient is an important input parameter which is often under-resolved in ocean models (e.g. Fox-Kemper *et al.* (2011); Bachman *et al.* (2017)).

To address these questions we use the diffusive mixing parametrisation with a nonzero surface wind stress and buoyancy flux imposed as boundary conditions. This system is solved analytically in the limit of small Rossby number in Section 5.3 in terms of a background buoyancy field. The evolution of the background buoyancy field is examined in Section 5.4 for different values of wind stress and heat flux. We find that positive heat fluxes lead to a spreading of the front while wind stresses can cause either spreading or sharpening according to the strength and direction of the wind. These different cases are examined in Section 5.5 using numerical simulations of the buoyancy evolution equation. The focus here will be on relatively large scale fronts where the Rossby number is small and the frontal width is large compared to the mixed layer depth.

In Section 5.6 we use the mixing length arguments invoked by Taylor & Ferrari (2011) and Enriquez & Taylor (2015) to link the vertical diffusivity to the strength of the surface forcing and hence describe the frontal evolution in terms of the external forcing and buoyancy gradient. Finally, in Section 5.7 we use typical parameters to determine if equilibrium fronts are possible physically and on what scales they might occur.

5.2 Setup

In this chapter we use the three-dimensional diffusive parametrisation with non-zero buoyancy flux Q and wind stress $\boldsymbol{\tau}$. We write

$$\boldsymbol{\tau} = \tau(\cos\theta, \sin\theta, 0), \tag{5.1}$$

for wind stress magnitude τ and direction θ. Note that we could take $\boldsymbol{\tau}$ and Q to depend on (x, y) and still obtain solutions. However, we assume constant values for simplicity. Later, we consider a two-dimensional isolated front where $\theta = 0$ corresponds to the cross front direction.

For simplicity we take a depth-independent viscosity ν and diffusivity κ. However, we note that the analysis could be carried out similarly using the depth-dependent

profiles used in Chapter 3. With this simplification the governing equations are:

$$\mathrm{Ro}\frac{Du}{Dt} - v = -\frac{\partial p}{\partial x} + \mathrm{E}\,\nabla_\epsilon^2 u, \tag{5.2a}$$

$$\mathrm{Ro}\frac{Dv}{Dt} + u = -\frac{\partial p}{\partial y} + \mathrm{E}\,\nabla_\epsilon^2 v, \tag{5.2b}$$

$$\mathrm{Ro}\,\epsilon^2\frac{Dw}{Dt} = -\frac{\partial p}{\partial z} + b + \epsilon^2\mathrm{E}\,\nabla_\epsilon^2 w, \tag{5.2c}$$

$$\mathrm{Ro}\frac{Db}{Dt} = \frac{\mathrm{E}}{\mathrm{Pr}}\,\nabla_\epsilon^2 b, \tag{5.2d}$$

$$\frac{\partial u}{\partial x} + \frac{\partial v}{\partial y} + \frac{\partial w}{\partial z} = 0, \tag{5.2e}$$

with top and bottom boundary conditions

$$\mathrm{E}\frac{\partial \mathbf{u}_H}{\partial z} = \boldsymbol{\tau}, \tag{5.3a}$$

$$\frac{\mathrm{E}}{\mathrm{Pr}}\frac{\partial b}{\partial z} = Q, \tag{5.3b}$$

at $z = 1/2$ and $z = -1/2$.

5.3 Analytic Solution

We consider the limit of small Rossby number and aspect ratio, $\epsilon = O(\mathrm{Ro})$, and assume that the Ekman number and Prandtl number are order 1. We now expand the fields, $\mathbf{u}$ and b, in powers of Ro as

$$(\mathbf{u}, b) = (\mathbf{u}_0, b_0) + \mathrm{Ro}\,(\mathbf{u}_1, b_1) + \ldots, \tag{5.4}$$

and expand Eq. (3.1) and Eq. (2.7) in powers of Ro. We also use a multiple timescale approach to expand the time derivatives as

$$\frac{\partial}{\partial t} = \frac{1}{\mathrm{Ro}}\frac{\partial}{\partial \tau} + \frac{\partial}{\partial t} + \mathrm{Ro}\frac{\partial}{\partial T}, \tag{5.5}$$

for fast timescale, $\tau = t/\mathrm{Ro}$, intermediate timescale, t, and slow timescale, $T = \mathrm{Ro}\,t$. We can now consider the resulting equations at each order in Ro. Depth-averaged quantities are written as $\overline{\phi}$ and departures from the depth-average are defined as $\phi' = \phi - \overline{\phi}$. We consider a vertical domain $z \in [-0.5, 0.5]$ so the depth average is

defined as

$$\overline{\phi} = \int_{-1/2}^{1/2} \phi \, dz. \tag{5.6}$$

The dimensionless heat flux is given by

$$Q = \frac{\alpha g Q^*}{c_p \rho_0 f H L M^2}, \tag{5.7}$$

and the dimensionless wind stress magnitude by

$$\tau = \frac{\tau^*}{\rho_0 H^2 M^2}, \tag{5.8}$$

where Q^* and τ^* are the dimensional heat flux and wind stress magnitude respectively. Here α is the heat capacity, ρ_0 is a reference density, g is the gravitational acceleration, and c_p is the specific heat capacity. Using typical parameters of $H = 100\,\mathrm{m}$, $L = 5\,\mathrm{km}$, $M^2 = \Delta b/L = 10^{-8}\,\mathrm{s}^{-2}$, $\tau^* = 0.1\,\mathrm{Nm}^{-2}$, $Q^* = 100\,\mathrm{Wm}^{-2}$, and $f = 10^{-4}\,\mathrm{s}^{-1}$ we find that $Q \sim 0.01$ and $\tau \sim 1$ hence we let $Q = \mathrm{Ro}\, Q_1$ and $\boldsymbol{\tau} = \boldsymbol{\tau}_0$.

5.3.1 O(1) Balance

The leading order buoyancy equation is

$$\frac{\partial b_0}{\partial \tau} = \frac{\mathrm{E}}{\mathrm{Pr}} \frac{\partial^2 b_0}{\partial z^2}, \tag{5.9}$$

with boundary conditions

$$\frac{\mathrm{E}}{\mathrm{Pr}} \frac{\partial b_0}{\partial z} = 0, \tag{5.10}$$

at $z = \pm 1/2$. Assuming that any transients have decayed, the solution is

$$b_0 = b_0(x, y, t, T), \tag{5.11}$$

which is vertically homogeneous.

The leading order vertical momentum equation is just hydrostatic balance

$$\frac{\partial p_0}{\partial z} = b_0, \tag{5.12}$$

hence

$$p_0 = \overline{p}_0(x, y, t, T) + b_0(x, y, t, T)\, z. \tag{5.13}$$

The leading order horizontal momentum equation is

$$\frac{\partial \mathbf{u}_{H0}}{\partial \tau} + \mathbf{k} \times \mathbf{u}_{H0} = -\nabla_H p_0 + \mathrm{E}\frac{\partial^2 \mathbf{u}_{H0}}{\partial z^2}, \tag{5.14}$$

which, upon ignoring fast time transients and substituting for p_0, gives

$$\mathbf{k} \times \mathbf{u}_{H0} = -\nabla_H \overline{p}_0 - z\nabla_H b_0 + \mathrm{E}\frac{\partial^2 \mathbf{u}_{H0}}{\partial z^2}, \tag{5.15}$$

with boundary conditions

$$\mathrm{E}\frac{\partial \mathbf{u}_{H0}}{\partial z} = \boldsymbol{\tau}_0, \tag{5.16}$$

at $z = \pm 1/2$. This system can be solved (see Section B.1) to obtain the solution

$$\begin{aligned}\mathbf{u}_{H0} = -\nabla_H \times (\overline{p}_0 \mathbf{k}) + \frac{1}{\sqrt{\mathrm{E}}}\left[\left(K_0 + \frac{z}{\sqrt{\mathrm{E}}}\right)\boldsymbol{\tau}_0 - K_0''\,\mathbf{k} \times \boldsymbol{\tau}_0\right] \\ -\sqrt{\mathrm{E}}\left[K_0''\,\nabla_H b_0 + K_0\,\mathbf{k} \times \nabla_H b_0\right],\end{aligned} \tag{5.17}$$

where K_0 is defined in Eq. (A.2). Note that p_0 acts as a streamfunction for the depth-independent component of velocity, as in geostrophic balance. The first term in square brackets describes the stress-driven components of the velocity with components both parallel and perpendicular to the surface stress. The second term in square brackets describes the buoyancy driven velocity and also has components parallel and perpendicular to the direction of the buoyancy gradient. By mass conservation we can calculate the vertical velocity as

$$w_0 = \mathrm{E}\,K_0'\,\nabla_H^2 b_0, \tag{5.18}$$

in the case where $\boldsymbol{\tau}_0$ is homogeneous.

5.3.2 O(Ro) Balance

The $O(\mathrm{Ro})$ buoyancy equation is

$$\frac{\partial b_0}{\partial t} + \frac{\partial b_1}{\partial \tau} + \mathbf{u}_{H0} \cdot \nabla_H b_0 = \frac{\mathrm{E}}{\mathrm{Pr}}\frac{\partial^2 b_1}{\partial z^2}, \tag{5.19}$$

with boundary conditions

$$\frac{\mathrm{E}}{\mathrm{Pr}}\frac{\partial b_1}{\partial z} = Q_1, \tag{5.20}$$

at $z = \pm 1/2$. We begin by assuming that the fast time transients have decayed and depth-average Eq. (5.19) to get

$$\frac{\partial b_0}{\partial t} + \overline{\mathbf{u}}_{H0} \cdot \nabla_H b_0 = 0. \tag{5.21}$$

Subtracting Eq. (5.21) from Eq. (5.19) gives an equation for b_1',

$$\mathbf{u}_{H0}' \cdot \nabla_H b_0 = \frac{\mathrm{E}}{\mathrm{Pr}} \frac{\partial^2 b_1'}{\partial z^2}. \tag{5.22}$$

The depth-dependent horizontal velocity is

$$\mathbf{u}_{H0}' = \frac{1}{\sqrt{\mathrm{E}}} \left[\left(K_0 + \frac{z}{\sqrt{\mathrm{E}}} \right) \boldsymbol{\tau}_0 - K_0'' \, \mathbf{k} \times \boldsymbol{\tau}_0 \right] - \sqrt{\mathrm{E}} \left[K_0'' \, \nabla_H b_0 + K_0 \, \mathbf{k} \times \nabla_H b_0 \right], \tag{5.23}$$

and hence Eq. (5.22) becomes

$$\frac{\mathrm{E}}{\mathrm{Pr}} \frac{\partial^2 b_1'}{\partial z^2} = \frac{1}{\sqrt{\mathrm{E}}} \left[\left(K_0 + \frac{z}{\sqrt{\mathrm{E}}} \right) \boldsymbol{\tau}_0 - K_0'' \, \mathbf{k} \times \boldsymbol{\tau}_0 \right] \cdot \nabla_H b_0 - \sqrt{\mathrm{E}} \, K_0'' \, |\nabla_H b_0|^2, \tag{5.24}$$

which can be integrated to give

$$b_1' = \frac{\mathrm{Pr} \, Q_1}{\mathrm{E}} z - \frac{\mathrm{Pr}}{\sqrt{\mathrm{E}}} \left[K_0'' \, \boldsymbol{\tau}_0 + K_0 \, \mathbf{k} \times \boldsymbol{\tau}_0 \right] \cdot \nabla_H b_0 - \mathrm{Pr} \sqrt{\mathrm{E}} \, K_0 \, |\nabla_H b_0|^2. \tag{5.25}$$

The first term in b_1' describes the stratification induced by the surface buoyancy flux, the second term represents changes in buoyancy induced by wind forcing, and the third term represents re-stratification induced by the TTW circulation (see Chapter 3).

5.4 The evolution of the depth-averaged buoyancy

In order to determine the evolution of the horizontal buoyancy we now need to solve for the leading order component of the buoyancy field, b_0. Following Chapter 3 we derive an equation in terms of b_0 only by depth-averaging the buoyancy evolution equation and substituting for $\mathbf{u}_{H0}$ and b_1'. Depth-averaging the full buoyancy equation gives

$$\mathrm{Ro} \left[\frac{\partial \bar{b}}{\partial t} + \overline{\mathbf{u}}_H \cdot \nabla_H \bar{b} + \nabla_H \cdot \overline{\mathbf{u}_H' b'} \right] = \frac{\epsilon^2 \mathrm{E}}{\mathrm{Pr}} \nabla_H^2 \bar{b}, \tag{5.26}$$

which to leading order, $O(\mathrm{Ro})$, reduces to Eq. (5.21) and can be written using the depth-averaged velocity as

$$\frac{\partial b_0}{\partial t} + J\left(\overline{p}_0, b_0\right) = 0, \tag{5.27}$$

where the depth-averaged pressure acts as a stream function for the depth-averaged velocity. In order to determine the full evolution another equation is needed to determine $\overline{p}_0$. In Chapter 6 we will use a depth-averaged vorticity equation to close the system and obtain two coupled equations in $\overline{p}_0$ and b_0. Here we assume that the along front (y) scales are large. In this case we can neglect $J(\overline{p}_0, b_0)$ and find that b_0 does not depend on the intermediate timescale, t. As a result we must look to the $O(\mathrm{Ro}^2)$ evolution equation.

The $O(\mathrm{Ro}^2)$ depth-averaged buoyancy equation is

$$\frac{\partial \overline{b}_1}{\partial t} + \frac{\partial b_0}{\partial T} + J(\psi_1, b_0) + J(\overline{p}_0, \overline{b}_1) + \nabla_H \cdot \overline{\left[\mathbf{u}'_{H0} b'_1 + \mathbf{u}'_{H1} b'_0\right]} = \frac{\epsilon^2 \mathrm{E}}{\mathrm{Ro}^2 \mathrm{Pr}} \nabla_H^2 b_0, \tag{5.28}$$

where ψ_1 is a streamfunction for the depth-averaged flow $\overline{\mathbf{u}}_{H1}$. We note that $b'_0 = 0$ and by symmetry we can assume that the quantity $\overline{b}_1$ is zero to obtain an equation for the slow evolution of b_0

$$\frac{\partial b_0}{\partial T} + J(\psi_1, b_0) + \nabla_H \cdot \overline{\mathbf{u}'_{H0} b'_1} = \frac{\epsilon^2 \mathrm{E}}{\mathrm{Ro}^2 \mathrm{Pr}} \nabla_H^2 b_0. \tag{5.29}$$

Again we assume that the Jacobian term is small to obtain

$$\frac{\partial b_0}{\partial T} + \nabla_H \cdot \overline{\mathbf{u}'_{H0} b'_1} = \frac{\epsilon^2 \mathrm{E}}{\mathrm{Ro}^2 \mathrm{Pr}} \nabla_H^2 b_0. \tag{5.30}$$

We note that any dependence on $\mathbf{u}_{H1}$ disappears and Eq. (5.30) is just in terms of b_0 and known quantities. The term $\mathbf{u}'_{H0} b'_1$ can be written as

$$\begin{aligned}\mathbf{u}'_{H0} b'_1 = &\left(\frac{1}{\sqrt{\mathrm{E}}} \left[\left(K_0 + \frac{z}{\sqrt{\mathrm{E}}} \right) \boldsymbol{\tau}_0 - K_0'' \, \mathbf{k} \times \boldsymbol{\tau}_0 \right] - \sqrt{\mathrm{E}} \left[K_0'' \, \nabla_H b_0 + K_0 \, \mathbf{k} \times \nabla_H b_0 \right] \right) \\ &\times \left(\frac{\mathrm{Pr}\, Q_1}{\mathrm{E}} z - \frac{\mathrm{Pr}}{\sqrt{\mathrm{E}}} \left[K_0'' \, \boldsymbol{\tau}_0 + K_0 \, \mathbf{k} \times \boldsymbol{\tau}_0 \right] \cdot \nabla_H b_0 - \mathrm{Pr} \sqrt{\mathrm{E}} \, K_0 \left| \nabla_H b_0 \right|^2 \right),\end{aligned} \tag{5.31}$$

using the results for $\mathbf{u}'_{H0}$ and b'_1. Depth-averaging this result gives

$$\begin{aligned}\overline{\mathbf{u}'_{H0}b'_1} = -\mathrm{Pr}\big[&Q_1\,\mathbf{C}_{10}\cdot\boldsymbol{\tau}_0 + Q_1\,\mathbf{C}_{01}\cdot\nabla_H b_0 + \mathbf{C}_{21}\cdot[\boldsymbol{\tau}_0\boldsymbol{\tau}_0\nabla_H b_0]\\ &+\mathbf{C}_{12}\cdot[\boldsymbol{\tau}_0\nabla_H b_0\nabla_H b_0] + \mathbf{C}_{03}\cdot\nabla_H b_0|\nabla_H b_0|^2\big],\end{aligned} \tag{5.32}$$

where the tensors $\mathbf{C}_{10}$, $\mathbf{C}_{01}$, $\mathbf{C}_{21}$, $\mathbf{C}_{12}$ and $\mathbf{C}_{03}$ are defined in Section B.2 and are functions only of E. Note that $\mathbf{C}_{21}$ and $\mathbf{C}_{12}$ are fourth rank tensors so here we use $\cdot$ to denote the contraction $[\mathbf{A}\cdot[\mathbf{bcd}]]_i = A_{ijkl}b_jc_kd_l$. Substituting this result into Eq. (5.30) gives the evolution equation for the depth averaged buoyancy

$$\begin{aligned}\frac{\partial b_0}{\partial T} = \mathrm{Pr}\,\nabla_H\cdot\big(&Q_1\,\mathbf{C}_{10}\cdot\boldsymbol{\tau}_0 + Q_1\,\mathbf{C}_{01}\cdot\nabla_H b_0 + \mathbf{C}_{21}\cdot[\boldsymbol{\tau}_0\boldsymbol{\tau}_0\nabla_H b_0]\\ &+\mathbf{C}_{12}\cdot[\boldsymbol{\tau}_0\nabla_H b_0\nabla_H b_0] + \mathbf{C}_{03}\cdot\nabla_H b_0|\nabla_H b_0|^2\big) + \frac{\epsilon^2\mathrm{E}}{\mathrm{Ro}^2\mathrm{Pr}}\nabla_H^2 b_0.\end{aligned} \tag{5.33}$$

Note that Eq. (5.33) is valid for $\boldsymbol{\tau}_0 = \boldsymbol{\tau}_0(x,y)$ and $Q_1 = Q_1(x,y)$ but for constant $\boldsymbol{\tau}_0$ and Q_1 the term $Q_1\,\mathbf{C}_{10}\cdot\boldsymbol{\tau}_0$ is constant so can be neglected. Again we assume that along-front (y) variations are small so Eq. (5.33) simplifies to

$$\frac{\partial b_0}{\partial T} = \mathrm{Pr}\,\frac{\partial}{\partial x}\left[C_0(Q_1,\boldsymbol{\tau}_0) + C_1(Q_1,\boldsymbol{\tau}_0)\frac{\partial b_0}{\partial x} + C_2(\boldsymbol{\tau}_0)\frac{\partial b_0}{\partial x}^2 + C_3\frac{\partial b_0}{\partial x}^3\right] + D_H\frac{\partial^2 b_0}{\partial x^2}, \tag{5.34}$$

where

$$D_H = \frac{\epsilon^2\mathrm{E}}{\mathrm{Ro}^2\mathrm{Pr}}, \tag{5.35}$$

and the C_i are given in Section B.2. C_0 is linear in $\boldsymbol{\tau}_0$ and Q_1, C_1 consists of a part linear in Q_1 plus a part quadratic in $\boldsymbol{\tau}_0$ and C_2 is linear in $\boldsymbol{\tau}_0$. Note that C_3 does not depend on the wind stress or buoyancy flux and hence is the same as in the unforced case given in Chapter 3. Spatial variations in the wind stress and buoyancy flux can cause the buoyancy field to evolve from an initially constant buoyancy through the C_0 term which we predict can cause weak fronts to form. Note that when any one coefficient is dominant we can find an approximate solution to Eq. (5.34) using the similarity solutions in Section B.3. For illustration we start by considering the case with no wind stress.

5.4.1 Zero stress case

With $\boldsymbol{\tau}_0 = \mathbf{0}$ and $Q_1 = \text{const.}$ Eq. (5.34) reduces to

$$\frac{\partial b_0}{\partial T} = \Pr C_3 \frac{\partial}{\partial x}\left[\frac{\partial b_0}{\partial x}^3\right] + \left(D_H + \Pr C_1(Q_1, \mathbf{0})\right) \frac{\partial^2 b_0}{\partial x^2}. \tag{5.36}$$

We assume that the buoyancy flux is positive, $Q_1 > 0$, so all coefficients in Eq. (5.36) are positive and the linear stratification induced in b_1 is stable. We now write

$$D_Q = \Pr C_1(Q_1, \mathbf{0}) = \Pr Q_1 \left[\overline{K_0'^2} + \overline{K_0'''^2}\right], \tag{5.37}$$

where D_Q is a constant positive diffusivity. Eq. (5.36) is the nonlinear Erdogan-Chatwin equation (Erdogan & Chatwin, 1967; Smith, 1982) discussed in Chapter 3 with the horizontal diffusivity, D_H, replaced by the combined diffusivity, $D_H + D_Q$. The effect of the buoyancy flux is to increase the coefficient of the diffusion term and hence increase the spreading rate. This equation can be solved using similarity solutions and describes a spreading front. If D_Q is large compared with $Pr\, C_3$, Eq. (5.36) reduces to a diffusion equation with the similarity solution

$$b_0 = \text{erf}\left[\frac{x}{\sqrt{4(D_Q + D_H)(T + T_0)}}\right]. \tag{5.38}$$

Similarly over long times the diffusion terms in Eq. (5.36) dominate the nonlinear term and the front spreads as $T^{1/2}$ and approaches the similarity solution.

In the case of a negative buoyancy flux our analysis is no longer valid as an unstable linear stratification will not be maintained due to the onset of convective instabilities; we expect the interior of the domain to be vertically well-mixed with thin unstable layers near the boundaries. The lack of a background stratification results in Eq. (5.36) reducing to

$$\frac{\partial b_0}{\partial T} = \Pr C_3 \frac{\partial}{\partial x}\left[\frac{\partial b_0}{\partial x}^3\right] + D_H \frac{\partial^2 b_0}{\partial x^2}, \tag{5.39}$$

so we predict that surface cooling will not directly affect the frontal width. However, note that since turbulence driven by convection enhances vertical mixing, surface cooling may lead to an increased Ekman number and hence a larger C_3 resulting in faster spreading via shear dispersion as described in Chapter 3.

5.4.2 Non-Zero Stress Case

We now consider the more general case where the wind stress, $\boldsymbol{\tau}_0$, is constant and non-zero in addition to a constant, positive Q_1. Eq. (5.34) becomes

$$\frac{\partial b_0}{\partial T} = \mathrm{Pr}\frac{\partial}{\partial x}\left[C_1(Q_1,\boldsymbol{\tau}_0)\frac{\partial b_0}{\partial x} + C_2(\boldsymbol{\tau}_0)\frac{\partial b_0}{\partial x}^2 + C_3\frac{\partial b_0}{\partial x}^3\right] + D_H\frac{\partial^2 b_0}{\partial x^2}, \tag{5.40}$$

and we write

$$\boldsymbol{\tau}_0 = \tau_0(\cos\theta, \sin\theta, 0), \tag{5.41}$$

where $\tau_0 > 0$ describes the magnitude of the wind stress and θ describes the angle from the positive cross-front direction in the right-handed sense. The coefficients, C_1, C_2 and C_3 can now be written as

$$C_1 = Q_1\left[\overline{K_0'^2} + \overline{K_0''^2}\right] + \frac{1}{\mathrm{E}}\left[\overline{K_0''^2}\cos^2\theta + 2\overline{K_0''^2}\cos\theta\sin\theta + \overline{K_0'^2}\sin^2\theta\right]\tau_0^2, \tag{5.42}$$

$$C_2 = -2\left[\overline{K_0''^2}\cos\theta + \overline{K_0'^2}\sin\theta\right]\tau_0, \tag{5.43}$$

and

$$C_3 = \mathrm{E}\overline{K_0'^2}, \tag{5.44}$$

using the results from Section B.2. We note that C_1 and C_3 are positive, while C_2 may be negative. Since a positive buoyancy flux results in horizontal diffusion, we can group the term in Q_1 with D_H to write Eq. (5.40) as

$$\frac{\partial b_0}{\partial T} = \mathrm{Pr}\frac{\partial}{\partial x}\left[C_1'(E,\theta)\tau_0^2\frac{\partial b_0}{\partial x} + C_2'(E,\theta)\tau_0\frac{\partial b_0}{\partial x}^2 + C_3\frac{\partial b_0}{\partial x}^3\right] + D\frac{\partial^2 b_0}{\partial x^2}, \tag{5.45}$$

where

$$C_1'(E,\theta) = \frac{1}{\mathrm{E}}\left[\overline{K_0''^2}\cos^2\theta + 2\overline{K_0''^2}\cos\theta\sin\theta + \overline{K_0'^2}\sin^2\theta\right], \tag{5.46}$$

$$C_2'(E,\theta) = -2\left[\overline{K_0''^2}\cos\theta + \overline{K_0'^2}\sin\theta\right], \tag{5.47}$$

and

$$D = D_H + D_Q = \frac{\epsilon^2\mathrm{E}}{\mathrm{Ro}^2\mathrm{Pr}} + \mathrm{Pr}\,Q_1\left[\overline{K_0'^2} + \overline{K_0''^2}\right]. \tag{5.48}$$

Physically, the leading order velocity field consists of a TTW component plus a Ekman velocity driven by the wind stress. The leading order velocity maintains a buoyancy stratification through an advection-diffusion balance. The vertical buoyancy structure is therefore determined by the leading order velocity and the background

buoyancy gradient. The correlations between the leading order velocity and the buoyancy deviation give fluxes of buoyancy which are proportional to the velocity field squared multiplied by the buoyancy gradient. The buoyancy fluxes consist of three terms, the first comes from the advection of the stress-driven buoyancy deviation by the stress-driven flow and is quadratic in stress, the third is due to the advection of the TTW buoyancy deviation by the TTW flow and is cubic in buoyancy gradient while the second term results from the cross terms and is linear in stress and quadratic in buoyancy gradient.

We now write Eq. (5.45) as

$$\frac{\partial b_0}{\partial T} = \kappa_0 \frac{\partial^2 b_0}{\partial x^2}, \tag{5.49}$$

where

$$\kappa_0 = \mathrm{Pr}\left[C_1'(E,\theta)\tau_0^2 + 2C_2'(E,\theta)\tau_0\frac{\partial b_0}{\partial x} + 3C_3(E)\frac{\partial b_0}{\partial x}^2\right] + D, \tag{5.50}$$

is a non-constant diffusivity that depends on the buoyancy gradient. If $\kappa_0 > 0$ we can solve Eq. (5.50) numerically to obtain solutions where the frontal region spreads. If $\kappa_0 < 0$ then Eq. (5.50) describes 'backwards diffusion' which is an ill-posed problem, solutions exhibit sensitive dependence on initial conditions and rapidly form step discontinuities as the buoyancy gradients sharpen. If we assume that the front is oriented such that $\partial b_0/\partial x \geq 0$ and choose the horizontal length scale L such that

$$\left.\frac{\partial b_0}{\partial x}\right|_{x=0} = 1, \tag{5.51}$$

then κ_0 can only be negative if $C_2'\tau_0$ is negative and sufficiently large compared to the other coefficients. Physically this corresponds to the wind driving a cross-front Ekman flow that opposes the cross-front TTW flow in such a way that the overall buoyancy flux is reversed resulting in an up-gradient flux.

Fig. 5.1 shows C_1' and C_2' as functions of θ and E. We note that $C_1' \sim \mathrm{E}^{-1}$, $C_2' \sim 1$ and $C_3 \sim \mathrm{E}$ for small E hence for small Ekman number and $\tau_0 = O(1)$ we expect the front to spread through linear diffusion as the $C_1'\tau_0^2$ term is dominant. For intermediate values of E it may be possible for a negative $C_2'\tau_0$ to temporarily sharpen the frontal gradients and form steps. However as the front sharpens the cubic term in Eq. (5.45) will become large and, since $C_3 > 0$, the gradient will reach a maximum.

To formalise this argument we note that $\kappa_0 < 0$ between the two roots

$$\frac{\partial b_0}{\partial x} = B_c^{\pm}, \tag{5.52}$$

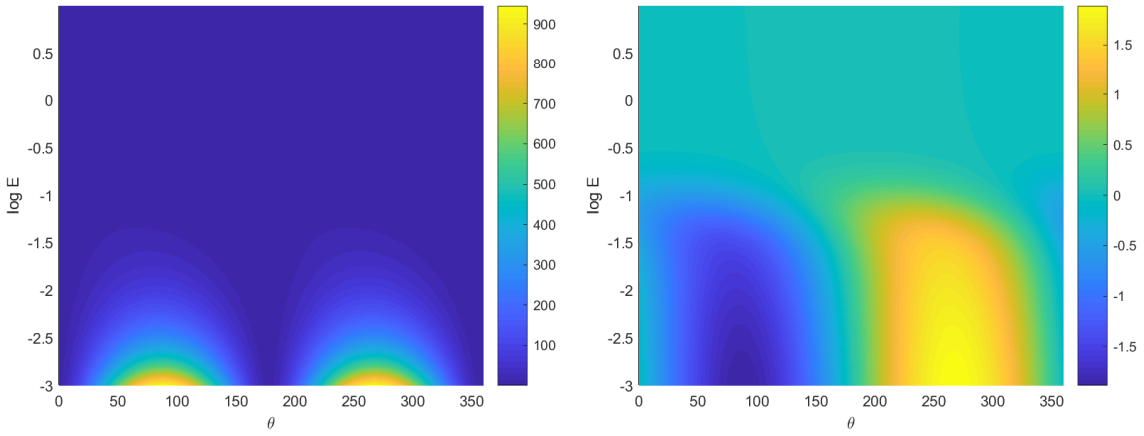

(a) (b)

Fig. 5.1 Plots of C_1' (a) and C_2' (b) as functions of θ and E.

where

$$B_c^{\pm} = \frac{-C_2'\tau_0 \pm \sqrt{C_2'^2\tau_0^2 - 3C_3(C_1'\tau_0^2 + D/\mathrm{Pr})}}{3C_3}, \tag{5.53}$$

assuming that these roots are real. Also if $\kappa_0 > 0$ then $\partial b_0/\partial x$ will decrease (and the front will spread) while if $\kappa_0 < 0$, $\partial b_0/\partial x$ will increase (and the front will sharpen). If there are no positive real roots then κ_0 is initially positive and remains positive throughout the evolution so the front spreads indefinitely.

If there are positive real roots then we have three possible cases. Firstly if $B_c^- > 1$ then κ_0 is initially positive and the front spreads indefinitely with κ_0 increasing throughout the evolution. Secondly if $B_c^- < 1 < B_c^+$ then κ_0 is initially negative and the front sharpens towards $\partial b_0/\partial x = B_c^+$; as this critical gradient is approached $\kappa_0 \to 0$ so the front will sharpen towards an equilibrium gradient. Finally if $B_c^+ < 1$ then initially $\kappa_0 > 0$ so the front will spread towards $\partial b_0/\partial x = B_c^+$ and again approach an equilibrium width. Note that due to the nature of backwards diffusion we expect the sharpening case to form small steps of equilibrium gradient rather than a significant narrowing of the frontal region.

Note that if $\kappa_0 < 0$ near the center of the front we will still have $\kappa_0 > 0$ towards the edges where the frontal gradient is smaller and if $B_c^+ < 1$ then we will have $\kappa_0 > 0$ near the center and edges of the front but $\kappa_0 < 0$ in some intermediate regions. Also κ_0 is always positive at the frontal edges since diffusion is dominant for small gradients. This will result in the edges of the front spreading as $T^{1/2}$ (Smith, 1982) as predicted by the classical similarity solution for diffusion.

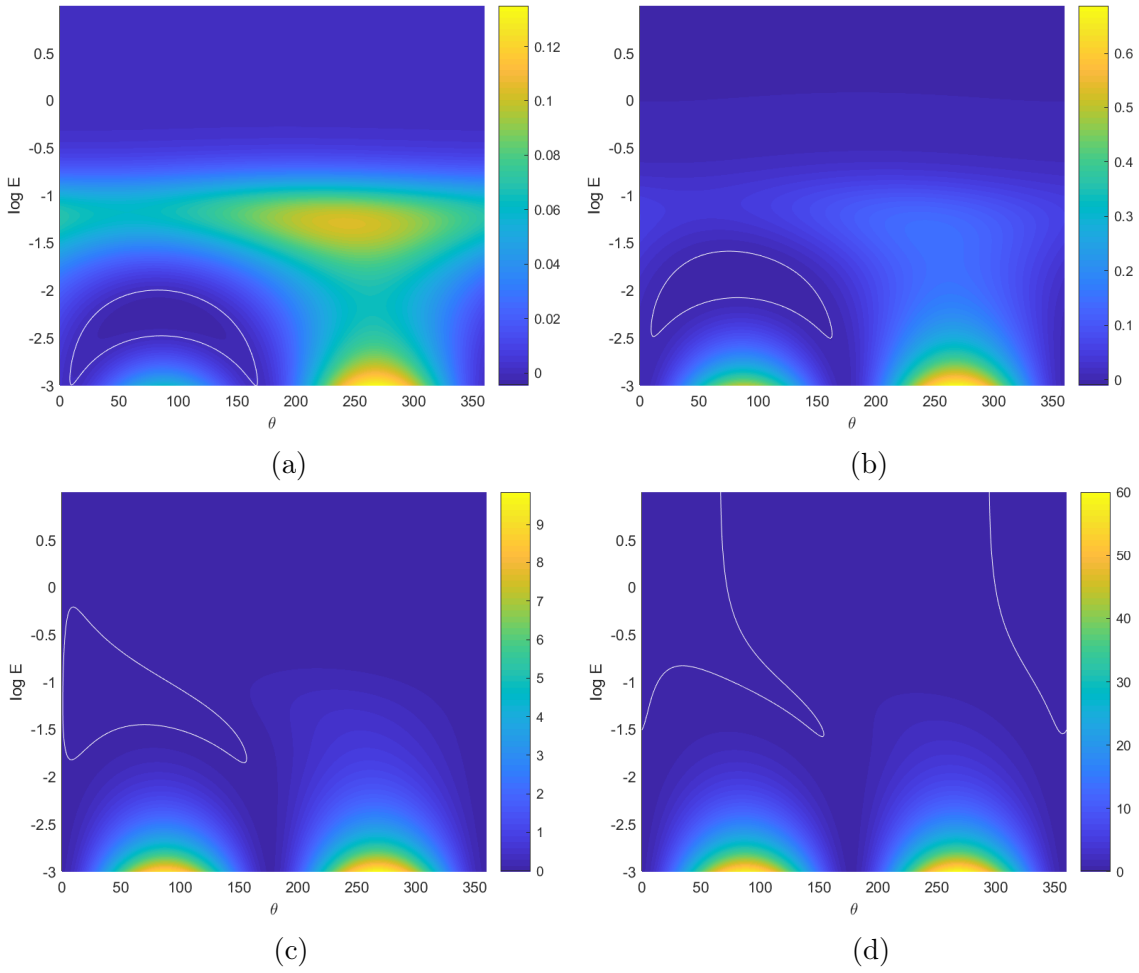

Fig. 5.2 κ_0 as a function of θ and $\log \mathrm{E}$ for $\partial b_0/\partial x = 1$, $Pr = 1$, $D = 0$ and (a) $\tau_0 = 0.01$, (b) $\tau_0 = 0.025$, (c) $\tau_0 = 0.1$ and (d) $\tau_0 = 0.25$. The white lines are the zero contours and enclose the region of negative κ_0.

Fig. 5.2 shows κ_0 as a function of θ and $\log \mathrm{E}$ for $\partial b_0/\partial x = 1$ and four different values of τ_0. We can see that the region in which the front will sharpen is strongly dependent on τ_0 and interestingly for some Ekman numbers the wind stress needs to be at a non-perpendicular angle to the front for sharpening to occur. This is a consequence of the coupling between the along front and cross front velocities through the vertical mixing and rotation terms; a wind angled to the perpendicular can drive a cross front flow both directly and by driving an along front flow which in turn drives a cross front flow through the coupling. Often an angled wind stress can drive a larger cross front flow than a completely perpendicular wind stress and hence the wind direction which drives the greatest sharpening is not necessarily perpendicular to the front.

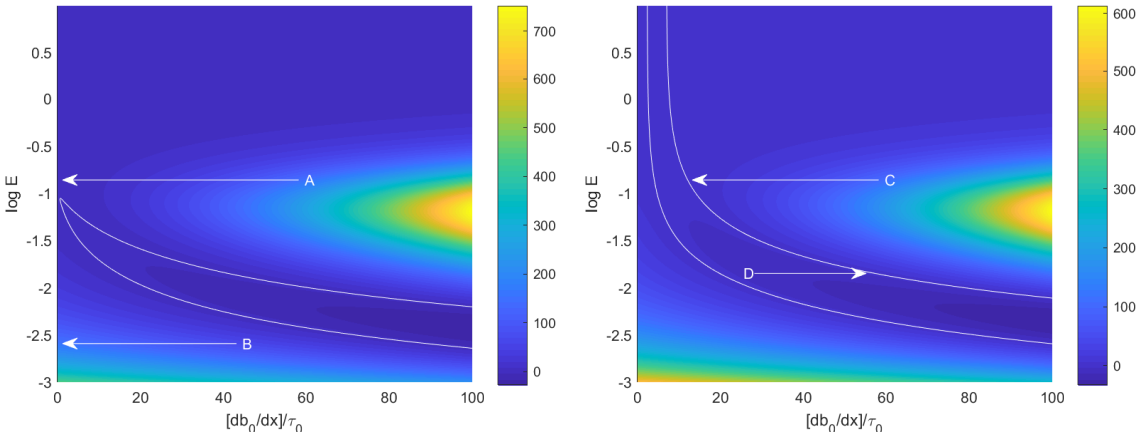

Fig. 5.3 Plots of $\kappa_0/[\mathrm{Pr}\tau_0^2]$ as a function of $[\partial b_0/\partial x]/\tau_0$ and $\log \mathrm{E}$ for $D = 0$ and (a) $\theta = 135^\circ$ and (b) $\theta = 45^\circ$. Points A-D correspond to initial frontal setups with the arrows showing the evolution of the buoyancy gradient, for example a front with initial conditions corresponding to point A will spread indefinitely with its buoyancy gradient decreasing towards 0. The points A and B correspond to indefinitely spreading fronts, point C corresponds to a front spreading towards an equilibrium width and point D corresponds to a front sharpening towards an equilibrium width.

In the case where D is small, The equilibrium gradient, B_c^+, and diffusivity, κ_0, can be written as

$$B_c^+ = \left[\frac{-C_2' + \sqrt{C_2'^2 - 3C_1'C_3}}{3C_3}\right]\tau_0, \tag{5.54}$$

and

$$\kappa_0 = Pr\,\tau_0^2\left[C_1' + 2C_2'\left[\frac{1}{\tau_0}\frac{\partial b_0}{\partial x}\right] + 3C_3\left[\frac{1}{\tau_0}\frac{\partial b_0}{\partial x}\right]^2\right]. \tag{5.55}$$

So the sign of κ_0 is a function only of three parameters; E, θ and $[\partial b_0/\partial x]/\tau_0$. We note that the equilibrium gradient is proportional to the wind stress so a stronger wind stress will sustain to a stronger equilibrium gradient.

Fig. 5.3 shows $\kappa_0/[\mathrm{Pr}\tau_0^2]$ as a function of $[\partial b_0/\partial x]/\tau_0$ for $D = 0$ and $\theta = 45^\circ, 135^\circ$. Points A-D correspond to initial frontal setups. Fronts A and B initially have positive κ_0 so will spread along the arrows, since κ_0 never becomes zero as these fronts spread they will spread indefinitely. Front C will initially spread as κ_0 is positive however as we approach the white line $\kappa_0 \to 0$ so the front approaches an equilibrium width. Finally front D has negative κ_0 so we expect regions of small scale sharpening to form as the gradients sharpen towards equilibrium. Fig. 5.4 shows $\log[B_c^+/\tau_0]$ as a function of θ and $\log \mathrm{E}$. The white region corresponds to the range of parameters where an

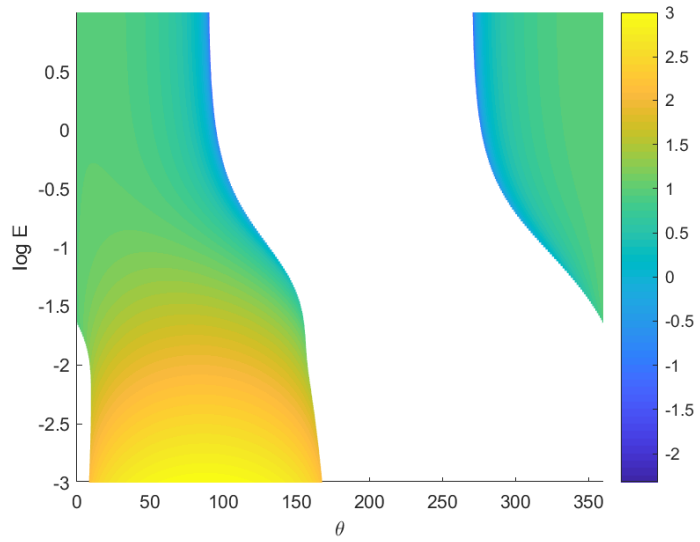

Fig. 5.4 $\log[B_c^+/\tau_0]$ as a function of θ and $\log \mathrm{E}$.

equilibrium gradient does not exist. We can see that the equilibrium gradient is weaker for stronger turbulent mixing.

5.5 Numerical simulations

We now use numerical simulations of Eq. (5.45) to examine the different cases of a spreading and a sharpening front. We use a pseudo-spectral method to evaluate the spatial derivatives and a fourth order Runge-Kutta scheme for the time stepping. We use a spatial grid with $N_x = 256$ grid points and choose the timestep for numerical stability.

We use a numerical domain of width $2L$ with $x \in [-L, L]$ and an initial buoyancy profile of

$$b_0(x, 0) = \mathrm{erf}\left(\frac{\sqrt{\pi}x}{2}\right), \tag{5.56}$$

so

$$\frac{\partial b_0}{\partial x}(0, 0) = 1. \tag{5.57}$$

In order to make the domain periodic and use a pseudo-spectral method we subtract a linear profile from b_0 and solve for $\tilde{b}_0$ where

$$\tilde{b}_0(x, T) = b_0(x, T) - \frac{x}{L}. \tag{5.58}$$

We now present three different cases of sharpening and spreading fronts that can arise from different choices of parameters. Fig. 5.2 is used to help select the parameters for the different cases.

For each simulation we plot b_0 as a function of x and T showing any spreading, b_0 as functions of x for several values of T showing the shape of the cross-front buoyancy profile, κ_0 as a function of x for several T values to show the cross-front variation in spreading rate, and κ_0 as a function of $\partial b_0/\partial x$ to see how the spreading rate changes as the front evolves and if there is a critical buoyancy gradient, B_c^+.

5.5.1 A spreading front - indefinite spreading

We begin by considering a case where there is no real positive equilibrium gradient, B_c^+, using parameters E $= 0.1$, $\tau_0 = 0.1$, $\theta = 225°$, Pr $= 1$, $Q_1 = 0$ and $D_H = 2.5 \times 10^{-4}$. The corresponding coefficients are $C_1'\tau_0^2 = 0.041$, $C_2'\tau_0 = 0.059$, $C_3 = 0.021$ and $D = 2.5 \times 10^{-4}$. The numerical solution is shown in Fig. 5.5. The spreading rate can be much different inside the front than it is towards the edges due to the dependence of κ_0 on $\partial b_0/\partial x$, in this case the spreading rate inside the front is larger than at the edges leading to an approximately linear region around $x = 0$. We note that it is possible to have cases with negative C_2' where the spreading rate is smaller inside the front than at the edges.

The case of no wind stress and a small or zero heat flux is the same as considered in Chapter 3 where the cubic nonlinear term is dominant inside the front and the solution resembles the similarity solution, F_3 (see Section B.3).

5.5.2 A spreading front - equilibrium width

We now consider the case where there exists a real, positive critical gradient, $B_c < 1$, using parameters E $= 0.1$, $\tau_0 = 0.1$, $\theta = 115°$, Pr $= 1$, $Q_1 = 0$ and $D_H = 2.5 \times 10^{-4}$. The corresponding coefficients are $C_1'\tau_0^2 = 0.0050$, $C_2'\tau_0 = -0.020$, $C_3 = 0.021$ and $D = 2.5 \times 10^{-4}$ and the numerical solution is shown in Fig. 5.6. We can see that near $x = 0$ the front spreads towards a constant gradient, while at the edges diffusion dominates. Initially there are regions in which κ_0 is negative. Here the gradient sharpens to match that of the interior region forming cusps between the spreading edges and the approximately linear interior profile. Once the interior profile reaches a gradient of B_c^+ we expect it to remain constant in time, the edges beyond the cusps will continue to spread.

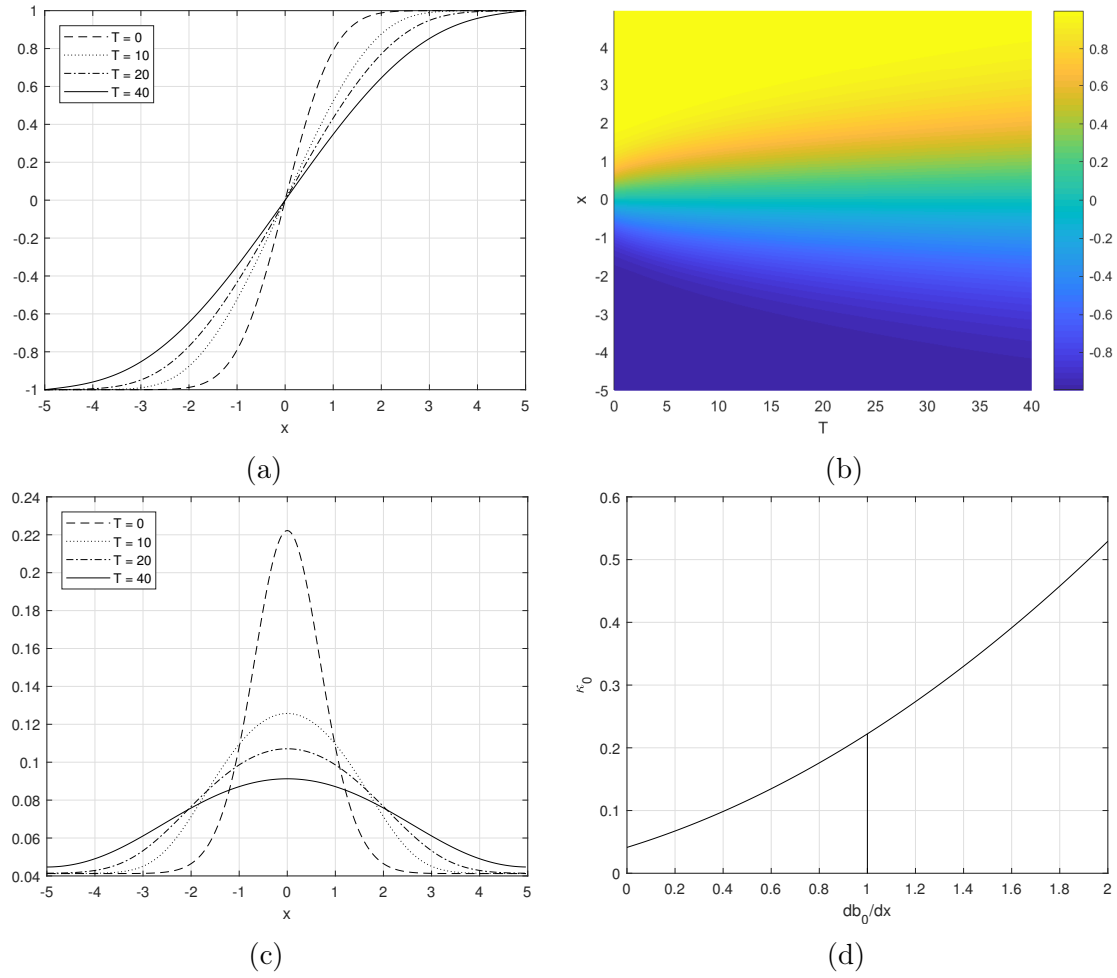

Fig. 5.5 Numerical solution for E = 0.1, $\tau_0 = 0.1$, $\theta = 225°$, Pr = 1, $Q_1 = 0$ and $D_H = 2.5 \times 10^{-4}$. (a) b_0 as a function of x, (b) b_0 as a function of (T, x), (c) κ_0 as a function of x, and (d) κ_0 as a function of $\partial b_0/\partial x$.

5.5.3 Sharpening front

Finally we consider the case of a real, positive critical gradient, $B_c^+ > 1$, using E = 0.1, $\tau_0 = 0.5$, $\theta = 124°$, Pr = 1, $Q_1 = 0$ and $D_H = 2.5 \times 10^{-4}$. The corresponding coefficients are $C_1'\tau_0^2 = 0.041$, $C_2'\tau_0 = -0.058$, $C_3 = 0.021$ and $D = 2.5 \times 10^{-4}$ and the numerical solution is shown in Fig. 5.7. We can see that the center of the front initially has a negative κ_0 so the gradients sharpen and small steps form, towards the edges of the front κ_0 is positive so spreading occurs.

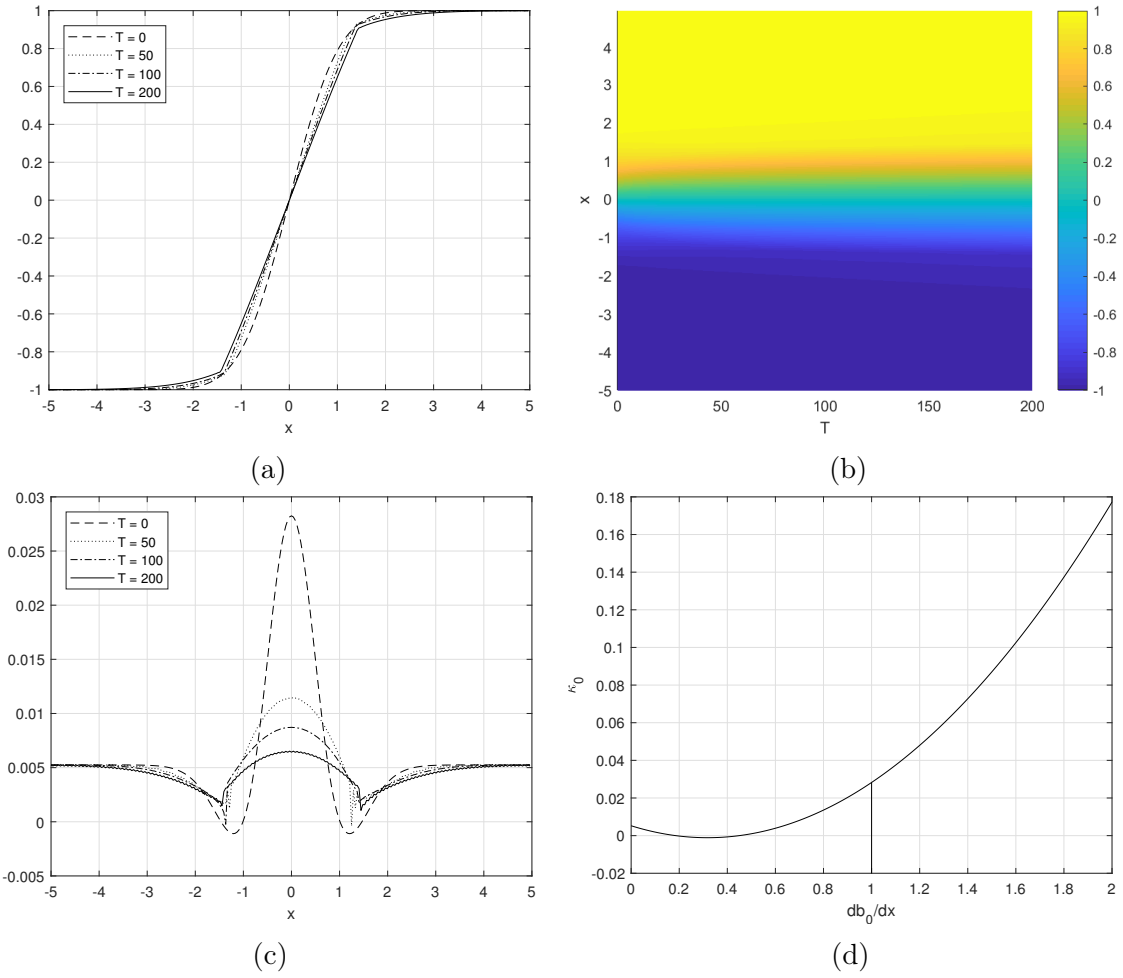

Fig. 5.6 Numerical solution for E = 0.1, $\tau_0 = 0.1$, $\theta = 115°$, Pr = 1, $Q_1 = 0$ and $D_H = 2.5 \times 10^{-4}$. (a) b_0 as a function of x, (b) b_0 as a function of (T, x), (c) κ_0 as a function of x, and (d) κ_0 as a function of $\partial b_0/\partial x$.

We note that due to the ill-posed nature of backwards diffusion, numerical solutions will not be accurate, particularly over long times where gradient discontinuities have started to form, and increasing the grid resolution will only result in more small scale oscillations. However we expect that the qualitative behaviour will be similar to observed here with a sharpened frontal region and spreading edges.

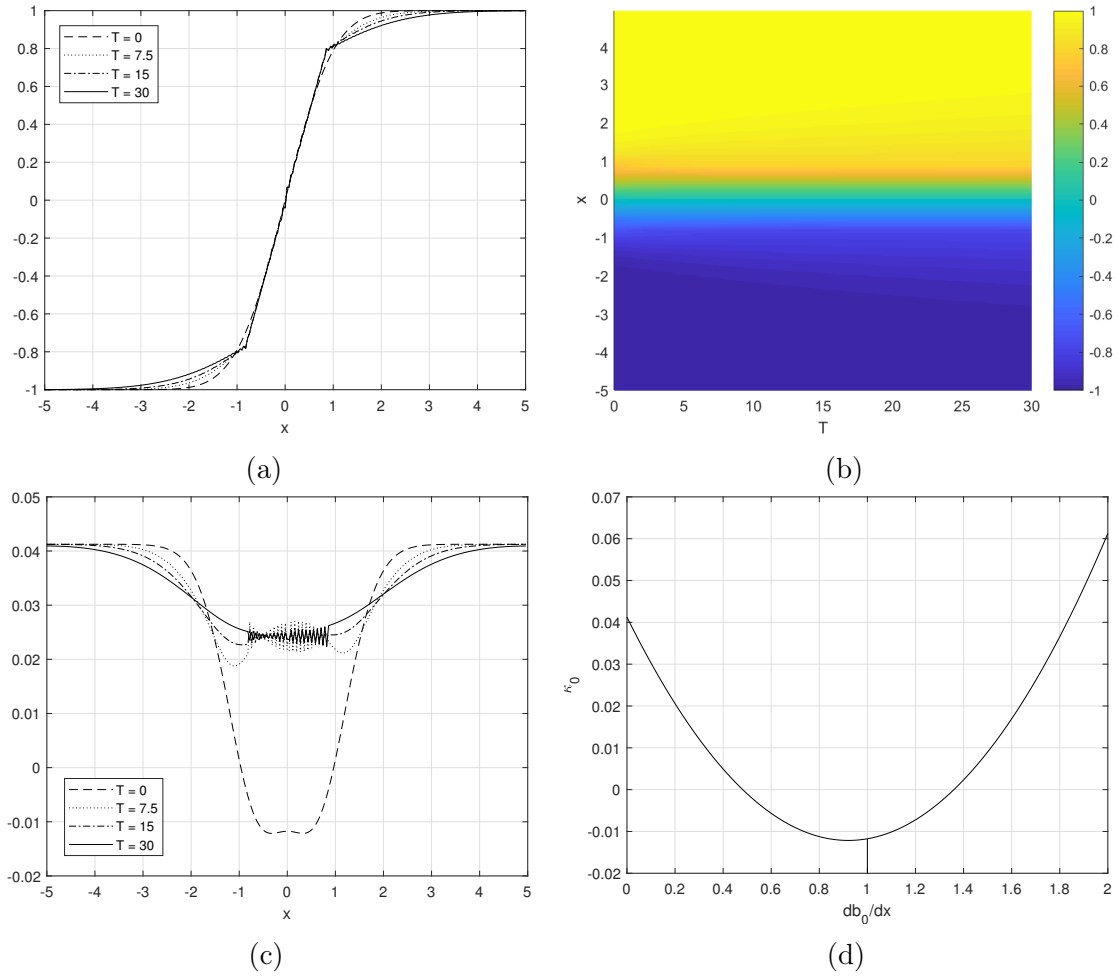

Fig. 5.7 Numerical solution for E = 0.1, $\tau_0 = 0.5$, $\theta = 124°$, Pr = 1, $Q_1 = 0$ and $D_H = 2.5 \times 10^{-4}$. (a) b_0 as a function of x, (b) b_0 as a function of (T, x), (c) κ_0 as a function of x, and (d) κ_0 as a function of $\partial b_0/\partial x$.

5.6 Wind stress and buoyancy flux driven turbulence

So far we have assumed that the Ekman number describing the strength of the turbulence is independent of the surface wind stress and buoyancy flux. In reality we expect the strength of boundary layer turbulence to be governed by surface processes such as wind stress and buoyancy flux (Enriquez & Taylor, 2015; Taylor & Ferrari, 2011) so the Ekman number will depend on $\boldsymbol{\tau}$ and Q. We now consider the cases where the turbulence is wind driven and heat flux driven and relate the Ekman number and spreading coefficients to the strength of the forcing.

Coefficient	(M, τ_0)
C_1	$M^{-1}\tau_0^{3/2}$
C_2	τ_0
C_3	$M\tau_0^{1/2}$

Table 5.1 The asymptotic behaviour of the coefficients C_1, C_2 and C_3 for small Ekman number, E, as functions of (M, τ_0) and (M, τ_w). Note that since $E \lesssim 0.1$ the large E limit is unlikely to be reached and most choices of parameters will fall within the small E limit or the intermediate range.

5.6.1 Wind Stress

Assuming the the wind stress is dominant, the Ekman number can be related to the wind stress using Enriquez & Taylor (2015)

$$\mathrm{E} \simeq \frac{C_\tau}{fH}\sqrt{\frac{\tau^*}{\rho_0}}, \tag{5.59}$$

for empirical scaling constant $C_\tau \approx 0.02$, layer depth H, Coriolis parameter f, dimensional stress τ^* and water density ρ_0. A typical maximum wind stress of $\tau^* = 0.1 - 1\,\mathrm{Nm}^{-2}$ corresponds to $\mathrm{E} \simeq 0.1$. From Eq. (5.8) we note that the non-dimensional wind stress, τ, depends on the horizontal buoyancy gradient, M^2, so using Eq. (5.59) we have

$$\mathrm{E} \simeq \frac{C_\tau M}{f}\sqrt{\tau_0}, \tag{5.60}$$

and we note that because of the choice of nondimensional variables both $C_\tau M/f$ and τ_0 depend on M^2 though E itself does not. In the absence of a buoyancy flux the coefficients C_1, C_2 and C_3 scale as shown in Table 5.1 for small E. We can see that for large τ_0, C_1 will be dominant and the front will spread indefinitely, similarly for very small τ_0 the coefficient C_3 will be dominant and the front will also spread. Therefore for frontal sharpening or spreading towards an equilibrium width we need an intermediate wind stress value.

5.6.2 Buoyancy Flux

Similarly to the wind stress we can relate the Ekman number to the convection driven turbulence caused by a surface heat flux, Q^*, in the case of surface cooling. The

turbulent Ekman number scales according to Taylor & Ferrari (2011)

$$\mathrm{E} \simeq \frac{C_Q}{f}\left(\frac{|Q^*|\alpha g}{c_p \rho_0 H^2}\right)^{1/3}, \tag{5.61}$$

where H is the depth of the convective layer, ρ_0 is the water density, c_p is the heat capacity, α is the thermal expansion coefficient, $C_Q = 0.1$ is an empirical scaling constant and g is gravitational acceleration. Using a typical heat flux in the range $|Q^*| = 1 - 100\,\mathrm{Wm}^{-2}$ we obtain an Ekman number of $E \sim 0.1$. Using Eq. (5.7) and $Q = \mathrm{Ro}\, Q_1$ the Ekman number can be written in terms of Q_1 as

$$\mathrm{E} \simeq C_Q\left(\frac{M^4|Q_1|}{f^4}\right)^{1/3}, \tag{5.62}$$

where again we note that M^4/f^4 and Q_1 both depend on M^2 though E does not. Since a positive heat flux does not generate convective overturning, we expect that in the case of positive Q^* the Ekman number will be primarily driven by the wind stress.

In the case of a positive buoyancy flux, the buoyancy flux driven diffusivity, D_Q, (Eq. (5.37)) scales as

$$D_Q = \mathrm{Pr}\, Q_1\left[\overline{K_0'^2} + \overline{k_0'''^2}\right] \sim Q_1 \sim \frac{\alpha g f Q^*}{c_p \rho_0 H^2 M^4}, \tag{5.63}$$

while the horizontal diffusivity due to horizontal mixing, D_H, (Eq. (5.35)) scales as

$$D_H = \frac{\epsilon^2 \mathrm{E}}{\mathrm{Ro}^2 \mathrm{Pr}} \sim \frac{f^4}{M^4}\mathrm{E}, \tag{5.64}$$

where E is driven by the wind stress, $\mathrm{Ro} = (HM^2)/(Lf^2)$ and $\mathrm{Pr} = 1$. Therefore the ratio D_Q/D_H can be written

$$\frac{D_Q}{D_H} \sim \frac{\alpha g Q^*}{c_p \rho_0 H^2 f^3 \mathrm{E}} \sim 10, \tag{5.65}$$

using $\mathrm{E} \sim 0.1$, $f = 10^{-4}\,\mathrm{s}^{-1}$, $c_p = 4.18 \times 10^3\,\mathrm{JKg}^{-1}\mathrm{K}^{-1}$, $\alpha = 1.67 \times 10^{-4}\,\mathrm{K}^{-1}$, $Q^* = 10\,\mathrm{Wm}^{-2}$ and $H = 100\,\mathrm{m}$. Therefore in the case of no wind stress and a positive heat flux, any horizontal spreading is primarily due to the vertical buoyancy flux caused by vertical advection acting on a buoyancy stratification rather than the horizontal mixing.

The ratio $C_1'\tau_0^2/D_Q$ is given by

$$\frac{C_1'\tau_0^2}{D_Q} \sim \frac{C_1' c_p \tau_0^{*2}}{\rho_0 H^2 \alpha g f Q^*} \sim C_1', \tag{5.66}$$

using $\tau^* = 0.1\,\mathrm{Nm}^{-2}$. In general $C_1' > 1$ for small E, so we predict that the wind stress is the dominant process controlling spreading and sharpening with the heat flux acting only to drive mixed layer turbulence or to spread a front when the wind stress is weak.

In the case of negative buoyancy flux we have no stable background stratification and hence $D_Q \approx 0$. Therefore a negative buoyancy flux will not lead directly to spreading however it will drive mixed layer turbulence and hence lead to an enhanced Ekman number through Eq. (5.61) and frontal spreading via shear dispersion.

5.7 Equilibrium width due to stress-Ekman balance

Using Eq. (5.54) we have that the dimensional equilibrium horizontal buoyancy gradient is

$$\frac{\partial b^*}{\partial x^*} = \mathcal{C}(\mathrm{E}, \theta, \mathcal{D}) \frac{\tau^*}{\rho_0 H^2}, \tag{5.67}$$

where

$$\mathcal{C}(\mathrm{E}, \theta, \mathcal{D}) = \frac{-C_2'(\mathrm{E}, \theta) + \sqrt{C_2(\mathrm{E}, \theta)^2 - 3\left(C_1'(\mathrm{E}, \theta) + \mathcal{D}\right) C_3(\mathrm{E})}}{3C_3(\mathrm{E})}, \tag{5.68}$$

and

$$\mathcal{D} = \frac{D_H + D_Q}{Pr\,\tau_0^2} = \left(\frac{\rho_0^2 H^4}{\tau^{*2}}\right)\left(\frac{f^4 \mathrm{E}}{Pr^2} + \frac{\alpha g f \max[Q^*, 0]}{c_p \rho_0 H^2}\left[\overline{K_0'^2} + \overline{K_0'''^2}\right]\right). \tag{5.69}$$

Here $\mathcal{D}/C_1'$ describes the strength of the combined horizontal diffusivity due to horizontal mixing and heat flux compared with the strength of the wind stress driven diffusivity. We expect this ratio to be small as explained in Section 5.6.2. The term $\max[Q^*, 0]$ appears since heat flux driven spreading occurs only when $Q^* > 0$.

For simplicity, we consider a simple case where $\mathcal{D} = 0$ and $\theta = 90^{\circ}$. In this case we have

$$(C_1', C_2', C_3) = (1/\mathrm{E}, -2, \mathrm{E})\ \overline{K_0'^2}, \tag{5.70}$$

so

$$\mathcal{C} = \frac{1}{\mathrm{E}}, \tag{5.71}$$

and

$$\frac{\partial b^*}{\partial x^*} = \frac{\tau^*}{\rho_0 H^2 \mathrm{E}} = \frac{f\tau^*}{\rho_0 \nu}, \tag{5.72}$$

since $\mathrm{E} = \nu/(fH^2)$ for turbulent diffusivity ν. For typical values of $H = 100\,\mathrm{m}$, $\mathrm{E} = 0.1$ and $\tau^* = 0.1\,\mathrm{Nm}^{-2}$ this gives an equilibrium gradient of

$$\partial b^*/\partial x^* = 10^{-7}\,\mathrm{s}^{-2}, \tag{5.73}$$

which corresponds to a Rossby number of

$$Ro = \frac{H}{f^2 L}\frac{\partial b^*}{\partial x^*} \approx 0.1, \tag{5.74}$$

using $H/L \approx 0.01$. Therefore it is possible to obtain an equilibrium frontal width at a scale where order 1 Rossby number effects can still be neglected. For weaker mixing or stronger wind stress, the sharpening effects of the wind stress dominate over the buoyancy driven spreading and the front sharpens towards an equilibrium state where high Rossby number effects such as frontogenesis (Hoskins & Bretherton, 1972; Shakespeare & Taylor, 2013) are important. We note that an equilibrium width will only exist if the Ekman flow opposes the cross-front TTW flow. If the TTW flow is initially stronger (i.e. the initial gradient is stronger than the equilibrium gradient) the front will spread towards an equilibrium whereas if the wind stress driven flow is stronger the front will sharpen towards an equilibrium. Note that sharpening may lead to regions with sharp buoyancy gradient resulting in a step-like pattern rather than a narrowing of the whole frontal region.

Observations of submesoscale fronts (Thomas *et al.*, 2013; Thompson *et al.*, 2016) reveal small scale structures with buoyancy gradients on the scale of $O(10^{-6} - 10^{-8}\,\mathrm{s}^{-2})$ that are not captured by global ocean models. Our predicted equilibrium gradient is on a similar scale to strong submesoscale fronts which suggests that the wind stress may play an important role in setting the scale of these structures. As global ocean models cannot resolve submesoscale structures - which play an important role in processes such as symmetric instability (Bachman *et al.*, 2017) and mixed layer eddies (Fox-Kemper *et al.*, 2008), a parametrisation is required. Understanding the balance between spreading and sharpening of fronts may allow for more accurate parametrisation of the frontal width.

5.8 Conclusions and Discussion

We have considered a simple analytic model of a mixed layer front forced by surface fluxes of buoyancy and momentum. Using an asymptotic expansion in Rossby number we determined the leading order velocity and buoyancy perturbations. By calculating the depth-averaged buoyancy fluxes, we then showed that the background buoyancy satisfies a nonlinear diffusion equation where the diffusivity depends on the surface forcing and the strength of the mixed layer turbulence.

Depending on the direction of alignment between the front and the wind stress we found that it is possible for the front to sharpen or to spread. Sharpening occurs when the wind stress drives a cross front flux that opposes and overcomes the TTW driven cross front flux and leads to a horizontal convergence in the buoyancy field. Spreading occurs when the stress driven flux either reinforces the TTW flux or opposes but does not exceed it, the cross-front flux then spreads the front via shear dispersion (Young & Jones, 1991).

We find analytically that surface heating also acts to spread a front due to the upward advection of less buoyant fluid by the vertical velocity. We could not consider the case of surface cooling analytically as we did not model the effects of gravitational instability or convective overturning however we predict that surface cooling will act only to enhance the mixed layer turbulence and will not directly spread or sharpen the front. We note that cooling may indirectly lead to an faster horizontal spreading via shear dispersion due to an increased Ekman number.

For the cases of sharpening fronts, we find that the front will only sharpen so far before the cross front wind driven flow is no longer able to overcome the cross front TTW velocity and the front approaches a balanced state with an equilibrium buoyancy gradient. Similarly fronts may spread towards an equilibrium width if initially the TTW flow dominates and the final balance will be the same as in the spreading case. Due to the nature of backwards diffusion, any sharpening will likely form small steps in the buoyancy profile rather than a significant narrowing of the frontal region.

Horizontal diffusion dominates in all cases over very long timescales however these scales will likely be too long to be observed physically. Therefore the process of fronts reaching an equilibrium width may provide a means of maintaining a constant frontal width over long periods of time. Additionally the spreading that can result from heat flux or wind stress may provide a means of balancing frontogenesis from frontogenetic

processes such as an external strain flow or the TTW secondary circulation (Hoskins & Bretherton, 1972; McWilliams, 2017) leading to an equilibrium frontal width.

Using typical parameters for ocean fronts we have estimated values for the equilibrium buoyancy gradient. We note that our prediction is of a similar magnitude to the gradients observed in strong submesoscale fronts and much stronger than the large-scale buoyancy gradients resolved by the global ocean model. Our predictions for the scaling of the equilibrium buoyancy gradient may be useful for parametrising the frontal strength in models which do not resolve these scales.

Chapter 6

Mixed layer baroclinic instability in the presence of vertical mixing

6.1 Introduction

In Chapter 3 we considered the evolution of an isolated front subject to a depth-dependent turbulent viscosity and diffusivity - a simple vertical mixing parametrisation intended to represent the effects of small-scale turbulence. The leading order momentum balance was found to be the so-called 'turbulent thermal wind' (TTW) balance (Gula *et al.*, 2014) between the Coriolis acceleration, the horizontal pressure gradient, and vertical mixing, with the resulting velocity depending linearly on the horizontal buoyancy gradient. As in the SML model (Young, 1994), vertically-sheared cross-front flow leads to a re-stratification of the mixed layer, while shear dispersion leads to spreading of the front.

Here, we take a different approach and use the vertical mixing scheme introduced by Young (1994) to consider mixed layer instabilities in the presence of vertical mixing. Unlike Young & Chen (1995) we use a single scalar, buoyancy, which simplifies the analysis for arbitrary mixing intensity. We also include a background vertical stratification to allow direct comparison with the Eady instability and add horizontal viscous terms to examine the high wavenumber cutoff. While similar to the SML model, our asymptotic approach differs slightly in that the buoyancy and momentum mixing timescales are assumed to be the same order, which leads to a slightly different parameter regime. The parameter regime we use is the same as that considered in Chapter 3, although here the turbulent mixing is represented by relaxation towards the local depth-averaged profile rather than diffusion.

In Section 6.2 we describe the governing equations and the asymptotic limit and discuss the differences between our approach and the approach of Young (1994). In Section 6.3 we give the asymptotic solution to the governing equations in terms of the background buoyancy field, b_0, and horizontal streamfunction, ψ_0. The governing equations for b_0 and ψ_0 are given in Section 6.4 and the instabilities of these equations are considered analytically in Section 6.5 and numerically in Section 6.6. In Section 6.7 we use a quasi-geostrophic model to examine a mechanism that can control the fastest growing mode. Finally in Section 6.8 we discuss our results and the limitations of our model.

6.2 Setup

Here we use the vertical relaxation parametrisation described in Chapter 2. A similar analysis could be carried out with the vertical relaxation scheme replaced with a vertical viscosity and diffusivity. Although this complicates the analysis, qualitatively similar results can be obtained (see Section C.3). For simplicity we initially neglect the horizontal diffusion terms those these are included later.

With the choices described above, the non-dimensional governing equations are:

$$\mathrm{Ro}\frac{Du}{Dt} - v = -\frac{\partial p}{\partial x} + \alpha\left(\overline{u} - u\right), \tag{6.1a}$$

$$\mathrm{Ro}\frac{Dv}{Dt} + u = -\frac{\partial p}{\partial y} + \alpha\left(\overline{v} - v\right), \tag{6.1b}$$

$$\mathrm{Ro}\,\epsilon^2\frac{Dw}{Dt} = -\frac{\partial p}{\partial z} + b, \tag{6.1c}$$

$$\mathrm{Ro}\frac{Db}{Dt} + \mathrm{Bu}\,w = \frac{\alpha}{\mathrm{Pr}_\alpha}\left(\overline{b} - b\right), \tag{6.1d}$$

$$\frac{\partial u}{\partial x} + \frac{\partial v}{\partial y} + \frac{\partial w}{\partial z} = 0, \tag{6.1e}$$

where $w = 0$ at $z = \pm 1/2$.

Before proceeding with the analysis, it is useful to relate our nondimensional parameters to physical quantities. We can relate the relaxation (mixing) rates, μ_u and μ_b, to a turbulent eddy turnover time by defining a characteristic turbulent velocity scale, u_*, and a characteristic length scale, l. The parametrised mixing rates, μ_u and μ_b, then scale with

$$\mu_u, \mu_b \sim \frac{u_*}{l}. \tag{6.2}$$

Therefore, the ratio of the mixing rate to the Coriolis frequency is

$$\alpha \sim \frac{u_*}{lf}. \tag{6.3}$$

For wind-driven turbulence, the friction velocity provides a characteristic velocity scale such that $u_* = \sqrt{\tau_w/\rho_0}$, where τ_w is the magnitude of the wind stress. In this case the turbulent lengthscale, l, characterising the largest turbulent eddies would be the smaller of the mixed layer depth or the Ekman layer depth. On the other hand for convection an appropriate characteristic velocity scale is instead $u_* = w_* = (B_0 l)^{1/3}$ where B_0 is the surface buoyancy flux and l is the mixed layer (or convective layer) depth. Note that the relaxation ratio can be related to the Ekman number, $E = \nu/(fl^2)$, by invoking a mixing length argument where the turbulent viscosity, $\nu \sim u_* l$. Hence

$$\alpha \sim \frac{u_*}{lf} \sim \frac{\nu}{fl^2} \sim E. \tag{6.4}$$

We can estimate some of the important parameters including the aspect ratio, Rossby number, and relaxation ratio from reported observations of fronts. We have selected three examples using observations reported in Mahadevan *et al.* (2012); Thompson *et al.* (2016); Thomas *et al.* (2013) which correspond to weak, moderate, and strong horizontal density gradients, respectively. Note that the values chosen from Mahadevan *et al.* (2012) correspond to the north/south density gradient characterising the North Atlantic as observed during the North Atlantic Bloom Experiment, rather than individual fronts. The estimated parameter values are given in Table 6.1 on page 135. Note that the values are roughly representative of the observations, but the structure of the fronts are complicated and cannot be fully represented with a simple set of parameters. Nevertheless, the relatively weak fronts observed during the North Atlantic Bloom experiment (Mahadevan *et al.*, 2012) and simulated by Mahadevan *et al.* (2012) and Taylor (2016) and the fronts reported in Thompson *et al.* (2016) have relatively small Rossby numbers using our definition. As we will show using comparisons with numerical simulations, aspects of our asymptotic theory are valid at these Rossby numbers. In contrast, the Rossby number associated with the Gulf Stream front is quite large and outside of the range of validity of our asymptotic theory. We note that it is possible to have $\alpha = O(1)$ for both strong and weak fronts and the aspect ratio, ϵ, is generally small for open ocean fronts.

Note that our definition of Rossby number uses a length scale characteristic of the horizontal density gradient and not necessarily the resulting eddies. As a result, the

Rossby number as defined here can be quite small in practice. If we instead define a Rossby number, Ro_s, using the length-scale of a baroclinic eddy, we have $\mathrm{Ro}_s = K\,\mathrm{Ro}$ for nondimensional wavenumber K. In the analysis that follows, we will show that K can be on the order of 100, and hence $\mathrm{Ro}_s = O(1)$ as typical of a submesoscale eddy. Therefore, even though the values of Ro used in our theory and simulations will be very small, our results are applicable to the formation of submesoscale structures where $\mathrm{Ro}_s \sim 1$.

6.3 Asymptotic Solution

In this section we will solve Eq. (6.1) using an asymptotic method valid for small Rossby numbers. We begin by assuming that the aspect ratio is small and expand all variables in powers of Ro, e.g. $b = b_0 + \mathrm{Ro}b_1 + \mathrm{Ro}^2 b_2 + \ldots$. We impose no conditions on the relaxation rate, α, and allow it to appear at leading order. We also assume that the stratification is weak with $\mathrm{Bu} = O(\mathrm{Ro})$, hence we write $\mathrm{Bu} = \mathrm{Ro}\,\mathcal{N}^2$ where

$$\mathcal{N}^2 = N^2 H/\Delta b, \tag{6.5}$$

is an $O(1)$ parameter describing the ratio of the vertical buoyancy difference ($N^2 H$) to the horizontal buoyancy difference (Δb). The time derivative is expanded into fast and slow timescales:

$$\frac{\partial}{\partial t} \to \frac{\partial}{\partial t} + \frac{1}{\mathrm{Ro}}\frac{\partial}{\partial \tau}, \tag{6.6}$$

for fast transient timescale, $\tau = t/\mathrm{Ro}$. The fast timescale, τ, represents the transient evolution from a general initial condition. In order to simplify the analysis we assume that all transients have decayed and hence neglect the τ derivatives. For completeness, the full solution including the transients is given in Section C.1.

6.3.1 Order 1 Equations

We now consider separately the $O(1)$ and $O(\mathrm{Ro})$ terms in the governing equations. With the assumption that $\mathrm{Bu} = O(\mathrm{Ro})$, the only term in the buoyancy equation that contributes to $O(1)$ is the parametrised vertical mixing term. Hence, the $O(1)$ buoyancy balance is

$$\frac{\alpha}{\mathrm{Pr}_\alpha} b_0' = 0, \tag{6.7}$$

where $(\cdot)'$ denotes a departure from the local depth-average. Eq. (6.7) implies that b_0 is independent of depth. This is consistent with the limit of strong mixing leading to a well-mixed layer as also found by Young (1994).

Similarly, the leading order balance in the momentum equations is

$$-v_0 = -\frac{\partial p_0}{\partial x} - \alpha u_0', \tag{6.8a}$$

$$u_0 = -\frac{\partial p_0}{\partial y} - \alpha v_0', \tag{6.8b}$$

$$0 = -\frac{\partial p_0}{\partial z} + b_0, \tag{6.8c}$$

$$0 = \frac{\partial u_0}{\partial x} + \frac{\partial v_0}{\partial y} + \frac{\partial w_0}{\partial z}, \tag{6.8d}$$

hence the pressure can be written $p_0 = z\, b_0 + \overline{p}_0$, and the horizontal momentum equations and mass conservation equation can be depth-averaged to give

$$-\overline{v}_0 = -\frac{\partial \overline{p}_0}{\partial x}, \tag{6.9a}$$

$$\overline{u}_0 = -\frac{\partial \overline{p}_0}{\partial y}, \tag{6.9b}$$

$$0 = \frac{\partial \overline{u}_0}{\partial x} + \frac{\partial \overline{v}_0}{\partial y}. \tag{6.9c}$$

Subtracting the depth-averaged horizontal momentum equations from Eq. (6.8) gives evolution equations for the horizontal velocity perturbations and vertical velocity

$$\alpha u_0' - v_0' = -z\frac{\partial b_0}{\partial x}, \tag{6.10a}$$

$$\alpha v_0' + u_0' = -z\frac{\partial b_0}{\partial y}, \tag{6.10b}$$

$$0 = \frac{\partial u_0'}{\partial x} + \frac{\partial v_0'}{\partial y} + \frac{\partial w_0}{\partial z}. \tag{6.10c}$$

Eq. (6.10) can be combined to give

$$\mathbf{u}_{H0}' = \gamma\left[-\alpha\,\nabla_H b_0 + \mathbf{k}\times\nabla_H b_0\right] z, \tag{6.11}$$

and

$$w_0 = \frac{\alpha\gamma(4z^2-1)}{8}\nabla_H^2 b_0, \tag{6.12}$$

where $\gamma = 1/(1+\alpha^2)$. From the depth-averaged mass conservation equation we can write $\overline{\mathbf{u}}_{H0} = -\nabla \times (\psi_0 \mathbf{k})$ for streamfunction ψ_0. From Eq. (6.9a) and Eq. (6.9b) we note that $\overline{p}_0 = \psi_0$. Hence

$$\mathbf{u}_{H0} = -\nabla \times (\psi_0 \mathbf{k}) + \gamma \left[-\alpha \nabla_H b_0 + \mathbf{k} \times \nabla_H b_0 \right] z. \tag{6.13}$$

As noted in Young (1994), the horizontal velocity has a non-zero vertical shear at leading order, unlike the buoyancy which is well-mixed at leading order. In the case of $\alpha = 0$, the equation for $\mathbf{u}_{H0}$ reduces to thermal wind balance. For nonzero α, vertical mixing acts to couple the cross-front and along-front flows, leading to a flow with a component in the direction of the buoyancy gradient. For $\alpha < 1$ stronger mixing results in a stronger cross-front shear, while the cross-front shear weakens with stronger mixing for $\alpha > 1$.

6.3.2 Order Ro Equations

We now consider the $O(\mathrm{Ro})$ terms in the buoyancy conservation equation. The advection of b_0 by the leading order velocity contributes to $O(\mathrm{Ro})$. Since $b_0 = b_0(x, y, t)$, the $O(\mathrm{Ro})$ buoyancy equation is

$$\frac{\partial b_0}{\partial t} + \mathbf{u}_{H0} \cdot \nabla_H b_0 + \mathcal{N}^2 w_0 = -\frac{\alpha}{\mathrm{Pr}_\alpha} b_1'. \tag{6.14}$$

Subtracting the depth average gives

$$\frac{\alpha}{\mathrm{Pr}_\alpha} b_1' = -\mathbf{u}_{H0}' \cdot \nabla_H b_0 - \mathcal{N}^2 w_0'. \tag{6.15}$$

Hence the solution for b_1' is

$$b_1' = \mathrm{Pr}_\alpha \gamma \left[z |\nabla_H b_0|^2 - \mathcal{N}^2 \frac{12z^2 - 1}{24} \nabla_H^2 b_0 \right]. \tag{6.16}$$

Solving for $\overline{b}_1$ requires the $O(\mathrm{Ro}^2)$ buoyancy equation. Note that even with $\mathcal{N} = 0$, there is a stable vertical stratification at this order, consistent with the finding from Tandon & Garrett (1994) that the vertical buoyancy gradient is proportional to the horizontal buoyancy gradient squared.

6.4 Evolution of the Background Fields

In order to determine the time dependence of the system on the slow timescale, t, we need to determine governing equations for the depth independent functions b_0 and ψ_0. These can be obtained by depth averaging the buoyancy and vertical vorticity equations. The vertical vorticity equation is

$$\mathrm{Ro}\left(\frac{\partial \zeta}{\partial t} + \mathbf{u}\cdot\nabla\zeta - \boldsymbol{\omega}\cdot\nabla w\right) + \nabla_H\cdot\mathbf{u}_H = \alpha(\overline{\zeta}-\zeta), \tag{6.17}$$

for vertical vorticity $\zeta = \boldsymbol{\omega}\cdot\mathbf{k}$, which can be depth-averaged to give

$$\frac{\partial \overline{\zeta}}{\partial t} + \nabla_H\cdot[\overline{\mathbf{u}_H\zeta - \boldsymbol{\omega}_H w}] = 0, \tag{6.18}$$

or using depth-averaged and perturbation quantities,

$$\frac{\partial \overline{\zeta}}{\partial t} + \nabla_H\cdot[\overline{\mathbf{u}}_H\overline{\zeta} - \overline{\boldsymbol{\omega}}_H\overline{w} + \overline{\boldsymbol{u}'_H\zeta'} - \overline{\boldsymbol{\omega}'_H w'}] = 0. \tag{6.19}$$

Similarly, the depth-averaged buoyancy equation is

$$\frac{\partial \overline{b}}{\partial t} + \overline{\mathbf{u}}_H\cdot\nabla_H\overline{b} + \nabla_H\cdot[\overline{\mathbf{u}'_H b'}] + \mathcal{N}^2\overline{w} = 0. \tag{6.20}$$

We now use the leading order solutions for the velocity and buoyancy fields (ψ_0 and b_0) to write the depth-averaged equations in terms of these fields.

6.4.1 Buoyancy

Substituting the expansions in Rossby number up to $O(\mathrm{Ro})$ into Eq. (6.20) gives

$$\begin{aligned}\frac{\partial b_0}{\partial t} + \overline{\mathbf{u}}_{H0}\cdot\nabla_H b_0 + \mathcal{N}^2\overline{w}_0 = \\ -\mathrm{Ro}\left[\frac{\partial \overline{b}_1}{\partial t} + \overline{\mathbf{u}}_{H1}\cdot\nabla_H b_0 + \overline{\mathbf{u}}_{H0}\cdot\nabla_H\overline{b}_1 + \mathcal{N}^2\overline{w}_1 + \nabla_H\cdot[\overline{\mathbf{u}'_{H0}b'_1}]\right].\end{aligned} \tag{6.21}$$

Using the definition of ψ_0, we can write $\overline{\mathbf{u}}_{H0}\cdot\nabla_H b_0 = J(\psi_0, b_0)$, where J is the Jacobian operator:

$$J(f,g) = \frac{\partial f}{\partial x}\frac{\partial g}{\partial y} - \frac{\partial f}{\partial y}\frac{\partial g}{\partial x}. \tag{6.22}$$

We can also write the flux term as

$$\overline{\mathbf{u}'_{H0}b'_1} = \frac{\mathrm{Pr}_\alpha\gamma^2}{12}(-\alpha\nabla_H b_0 + \mathbf{k}\times\nabla_H b_0)|\nabla_H b_0|^2, \tag{6.23}$$

and hence Eq. (6.21) can be written as

$$\begin{aligned}\frac{\partial b_0}{\partial t} + J(\psi_0, b_0) + \mathcal{N}^2\overline{w}_0 + \mathrm{Ro}\left[\frac{\partial \bar{b}_1}{\partial t} + \overline{\mathbf{u}}_{H1}\cdot\nabla_H b_0 + \overline{\mathbf{u}}_{H0}\cdot\nabla_H\bar{b}_1 + \mathcal{N}^2\overline{w}_1\right] \\ = \frac{\mathrm{Ro}\,\mathrm{Pr}_\alpha\gamma^2}{12}\nabla_H\cdot\left[(\alpha\nabla_H b_0 - \mathbf{k}\times\nabla_H b_0)|\nabla_H b_0|^2\right].\end{aligned} \tag{6.24}$$

In the limit where $\mathrm{Pr}_\alpha = \mathcal{P}/\sqrt{\mathrm{Ro}}$ for $\mathcal{P} = O(1)$, corresponding to momentum relaxation occurring on a faster scale than the buoyancy relaxation and in the absence of background stratification ($N^2 = 0$), the buoyancy evolution equation to order $O(\sqrt{\mathrm{Ro}})$ can be written as

$$\frac{\partial b_0}{\partial t} + J(\psi_0, b_0) = \frac{\sqrt{\mathrm{Ro}}\,\mathcal{P}\gamma^2}{12}\nabla_H\cdot\left[(\alpha\nabla_H b_0 - \mathbf{k}\times\nabla_H b_0)|\nabla_H b_0|^2\right]. \tag{6.25}$$

This result was obtained by Young (1994). The first term in brackets on the right hand side of Eq. (6.25) is a down-gradient buoyancy flux. The second term is a 'skew' flux directed perpendicular to the buoyancy gradient. The role of the skew flux will be discussed in more detail in Section 6.4.3. In the case of a two-dimensional front with no y dependence and $\mathcal{N}^2 = 0$, Eq. (6.24) reduces to

$$\frac{\partial b_0}{\partial t} = \frac{\mathrm{Ro}\,\mathrm{Pr}_\alpha\gamma^2\alpha}{12}\frac{\partial}{\partial x}\left(\frac{\partial b_0}{\partial x}\right)^3, \tag{6.26}$$

as $\bar{b}_1$ and $\overline{u}_{H1}$ can be assumed to be zero by symmetry. This equation describes frontal spreading on the timescale $T = \mathrm{Ro}\,t$ and can be solved with a similarity solution as in Chapter 3.

Here, we take a different approach from Young (1994) and assume that $\mathrm{Pr}_\alpha = O(1)$ while retaining a non-zero background stratification. The $O(1)$ terms in Eq. (6.24) are then

$$\frac{\partial b_0}{\partial t} + J(\psi_0, b_0) = \frac{\alpha\gamma\mathcal{N}^2}{12}\nabla_H^2 b_0, \tag{6.27}$$

where we have used $\overline{w}_0 = -\alpha\gamma\left(\nabla_H^2 b_0\right)/12$. Note that with this form for w_0, vertical advection acting on the background stratification ($\mathcal{N}^2 w_0$ in Eq. (6.24)) acts like horizontal diffusion on the leading order buoyancy.

6.4.2 Vorticity

We can formulate a closed system of two equations for the leading order buoyancy, b_0, and the leading order streamfunction, ψ_0, using conservation of vorticity. The leading order vorticity equation is

$$\frac{\partial \overline{\zeta}_0}{\partial t} + \nabla_H \cdot [\overline{\mathbf{u}}_{H0}\overline{\zeta}_0 - \overline{\boldsymbol{\omega}}_{H0}\overline{w}_0 + \overline{\boldsymbol{u}'_{H0}\zeta'_0} - \overline{\boldsymbol{\omega}'_{H0}w'_0}] = 0, \tag{6.28}$$

where each term can now be written in terms of b_0 and ψ_0. The leading order vertical vorticity is

$$\zeta_0 = \frac{\partial v_0}{\partial x} - \frac{\partial u_0}{\partial y} = \nabla_H^2\psi_0 + \gamma\, z\nabla_H^2 b_0. \tag{6.29}$$

Since b_0 is independent of z, and since z is antisymmetric about the midplane ($z = 0$), the final term does not contribute to the depth-average which leaves $\overline{\zeta}_0 = \nabla_H^2\psi_0$. Advection of vorticity by the depth-averaged horizontal velocity can be written as

$$\nabla_H \cdot [\overline{\mathbf{u}}_{H0}\overline{\zeta}_0] = \nabla_H \cdot [\overline{\mathbf{u}}_{H0}\nabla_H^2\psi_0] = J(\psi_0, \nabla_H^2\psi_0). \tag{6.30}$$

The horizontal vorticity is given by

$$\boldsymbol{\omega}_{H0} = \begin{pmatrix} \frac{\partial w_0}{\partial y} - \frac{\partial v_0}{\partial z} \\ \frac{\partial u_0}{\partial z} - \frac{\partial w_0}{\partial x} \end{pmatrix}, \tag{6.31}$$

and its depth-average is

$$\overline{\boldsymbol{\omega}}_{H0} = \begin{pmatrix} \frac{\partial \overline{w}_0}{\partial y} - \Delta v_0 \\ \Delta u_0 - \frac{\partial \overline{w}_0}{\partial x} \end{pmatrix}, \tag{6.32}$$

where Δu_0 and Δv_0 are the change in horizontal velocity between the top and bottom boundaries. The second flux term is

$$\nabla_H \cdot [\overline{\boldsymbol{\omega}}_{H0}\overline{w}_0] = \nabla_H \cdot \left[\frac{1}{2}\begin{pmatrix} \frac{\partial \overline{w}_0^2}{\partial y} \\ -\frac{\partial \overline{w}_0^2}{\partial x} \end{pmatrix} + \begin{pmatrix} -\Delta v_0\, \overline{w}_0 \\ \Delta u_0\, \overline{w}_0 \end{pmatrix}\right] = \nabla_H \cdot \begin{pmatrix} -\Delta v_0\, \overline{w}_0 \\ \Delta u_0\, \overline{w}_0 \end{pmatrix}, \tag{6.33}$$

or

$$\nabla_H \cdot [\overline{\boldsymbol{\omega}}_{H0}\overline{w}_0] = \frac{\alpha\gamma^2}{12}\nabla_H \cdot \left[(\nabla_H b_0 + \alpha\, \mathbf{k} \times \nabla_H b_0)\, \nabla_H^2 b_0\right]. \tag{6.34}$$

using the leading order velocities. The last two flux terms involving departures from the mean vorticity are

$$\nabla_H \cdot [\overline{\boldsymbol{u}'_{H0}\zeta'_0}] = -\frac{\gamma^2}{12}\nabla_H \cdot \left[(\alpha\nabla_H b_0 - \mathbf{k}\times\nabla_H b_0)\,\nabla_H^2 b_0\right], \tag{6.35}$$

and

$$\nabla_H \cdot [\overline{\boldsymbol{\omega}'_{H0}w'_0}] = \nabla_H \cdot \begin{pmatrix} \frac{1}{2}\frac{\partial}{\partial y}[\overline{w'^2_0}] - \overline{\frac{\partial v'_0}{\partial z}w'_0} \\ -\frac{1}{2}\frac{\partial}{\partial x}[\overline{w'^2_0}] + \overline{\frac{\partial u'_0}{\partial z}w'_0} \end{pmatrix} = \nabla_H \cdot \begin{pmatrix} -\frac{\partial v'_0}{\partial z}\overline{w'_0} \\ \frac{\partial u'_0}{\partial z}\overline{w'_0} \end{pmatrix} = \mathbf{0}, \tag{6.36}$$

since u'_0 and v'_0 are linear in z and $\overline{w'} = 0$. The terms in $\overline{w'^2_0}$ can be written as a curl and hence are divergence free.

Combining these results, the vertical vorticity equation can be written

$$\frac{\partial\nabla_H^2\psi_0}{\partial t} + J(\psi_0, \nabla_H^2\psi_0) = \frac{\gamma^2}{12}\nabla_H \cdot \left[\left(2\alpha\nabla_H b_0 + (\alpha^2-1)\,\mathbf{k}\times\nabla_H b_0\right)\nabla_H^2 b_0\right]. \tag{6.37}$$

6.4.3 The Skew Flux Term

As mentioned earlier, a skew flux term appears in the evolution equation for b_0 (the second term on the right hand side of Eq. (6.25)). This term, $\mathcal{J}_b = -\mathbf{k}\times\nabla_H b_0|\nabla_H b_0|^2$, represents a flux of buoyancy perpendicular to the buoyancy gradient. A skew flux also appears in the vertical vorticity Eq. (6.37) which we will denote $\mathcal{J}_v = (\mathbf{k}\times\nabla_H b_0)\nabla_H^2 b_0$.

The divergence of the skew flux terms in the buoyancy and vorticity equations can be re-expressed in terms of advection operators. First, note that the divergence of the skew flux terms can be written as

$$\nabla_H \cdot \mathcal{J}_b = -\nabla_H \cdot \left[\mathbf{k}\times\nabla_H b_0|\nabla_H b_0|^2\right] = -\nabla_H b_0 \cdot \left[-\mathbf{k}\times\nabla_H|\nabla_H b_0|^2\right], \tag{6.38}$$

and

$$\nabla_H \cdot \mathcal{J}_v = \nabla_H \cdot \left[(\mathbf{k}\times\nabla_H b_0)\nabla_H^2 b_0\right] = -\nabla_H b_0 \cdot \left[(\mathbf{k}\times\nabla_H)\nabla_H^2 b_0\right]. \tag{6.39}$$

Therefore, the terms in brackets can be written in the form of advection operators with velocities

$$\mathbf{u}_b = -\mathbf{k}\times\nabla_H|\nabla_H b_0|^2 = \nabla_H \times \left[|\nabla_H b_0|^2\mathbf{k}\right], \tag{6.40}$$

and

$$\mathbf{u}_v = (\mathbf{k} \times \nabla_H)\nabla_H^2 b_0 = \nabla_H \times \left[-\nabla_H^2 b_0 \mathbf{k}\right]. \tag{6.41}$$

The second equalities in the above equations show that $\mathbf{u}_b$ and $\mathbf{u}_v$ can be written in terms of streamfunctions, $\chi_b = -|\nabla_H b_0|^2$ and $\chi_v = \nabla_H^2 b_0$. In the buoyancy equation the skew flux term can be combined with the existing advection term, $J(\psi_0, b_0)$. From the form of the streamfunction, χ_b, we see that the effect of the skew flux term, $\mathcal{J}_b$, is to advect buoyancy along the contours of $|\nabla_H b_0|^2 = \text{const}$. Eq. (6.25) and Eq. (6.37) can then be written

$$\frac{\partial b_0}{\partial t} + J\left(\psi_0 - \frac{\sqrt{\text{Ro}}\,\mathcal{P}\gamma^2}{12}|\nabla_H b_0|^2, b_0\right) = \frac{\sqrt{\text{Ro}}\,\mathcal{P}\alpha\gamma^2}{12}\nabla_H \cdot \left[\nabla_H b_0 |\nabla_H b_0|^2\right], \tag{6.42}$$

and

$$\frac{\partial \nabla_H^2 \psi_0}{\partial t} + J(\psi_0, \nabla_H^2 \psi_0) + \frac{(\alpha^2 - 1)\gamma^2}{12} J(\nabla_H^2 b_0, b_0) = \frac{2\alpha\gamma^2}{12}\nabla_H \cdot \left[\nabla_H b_0 \nabla_H^2 b_0\right]. \tag{6.43}$$

Note that Eq. (6.42) corresponds to the Young (1994) case. In the $\text{Pr}_\alpha = O(1)$ limit that we consider, only the vorticity skew flux term, $\mathcal{J}_v$, enters the equations at leading order and the advection of buoyancy by the buoyancy skew flux term, $\mathcal{J}_b$, is small.

6.4.4 Horizontal Diffusion

The system described by Eq. (6.1a)-Eq. (6.1e) parametrises vertical mixing by relaxing the velocity and buoyancy fields towards their local depth average, but the equations do not include any parametrisation for horizontal mixing by small-scale turbulence. As will be shown below, the most unstable mode in this system has an infinite horizontal wavenumber or, equivalently, a vanishingly small wavelength. Fortunately, it is relatively straightforward to include a parametrisation of horizontal mixing using horizontal Laplacian viscous and diffusive terms, and the addition of these terms shifts the most unstable mode to a finite wavenumber. Note that this laplacian scheme differs from the relaxation parametrisation used to represent vertical mixing, this is for mathematical convenience as a similarly simple horizontal relaxation cannot be applied on an infinite domain. More complicated horizontal relaxation methods can be devised though these are unlikely to be analytically tractable.

With the addition of parametrised horizontal mixing, the terms $\epsilon^2 \text{E}\nabla_H^4 \psi_0$ and $\epsilon^2 \text{E}/\text{Pr}_E \nabla_H^2 b_0$ appear on the right hand sides of the depth-averaged vorticity and

buoyancy equations, respectively, where recall that $\epsilon = H/L$ is the aspect ratio, $\mathrm{E} = \nu/(fH^2)$ is the Ekman number and $\mathrm{Pr}_E = \nu/\kappa$ is the Prantl number. In most applications $\epsilon << 1$ and these terms will be small. However, for very small Ro these terms might contribute significantly. Writing $\mathcal{E} = \epsilon^2\mathrm{E}/\mathrm{Ro}$, the resulting equations are

$$\frac{\partial b_0}{\partial t} + J(\psi_0, b_0) = \left[\frac{\alpha\gamma\mathcal{N}^2}{12} + \frac{\mathcal{E}}{\mathrm{Pr}_E}\right]\nabla_H^2 b_0, \tag{6.44}$$

and

$$\frac{\partial \nabla_H^2\psi_0}{\partial t} + J(\psi_0, \nabla_H^2\psi_0) - \mathcal{E}\nabla_H^4\psi_0 = \frac{\gamma^2}{12}\nabla_H \cdot \left[\left(2\alpha\nabla_H b_0 + (\alpha^2 - 1)\,\mathbf{k}\times\nabla_H b_0\right)\nabla_H^2 b_0\right], \tag{6.45}$$

which are asymptotically valid if $\epsilon^2\mathrm{E} = O(\mathrm{Ro})$. For convenience, we will write the combined buoyancy diffusivity appearing in Eq. (6.44) as

$$\mathcal{D} = \left[\frac{\alpha\gamma\mathcal{N}^2}{12} + \frac{\mathcal{E}}{\mathrm{Pr}_E}\right]. \tag{6.46}$$

We note that these equations can be obtained from Young (1994) in the limit of fast buoyancy mixing ($1/\mu_b \ll L/U$). However this result would only strictly be valid for small α based on the analysis in Young (1994) due to the use of different asymptotic limits, while here no constraints have been placed on the size of α.

6.5 Instabilities of the Depth-Averaged Equations

Eq. (6.44) and Eq. (6.45) are a closed system of equations for the leading order buoyancy and vorticity. In this section, we will analyze the stability of these equations to small amplitude disturbances. For simplicity, we will consider perturbations about a basic state where buoyancy is a linear function of x, i.e. $b_0 = Bx$ for a constant B, and where the vertical vorticity is zero. Introducing normal mode perturbations of the form $\exp[i(kx + ly) + \sigma t]$, the total buoyancy and vorticity can be written using an eigenmode decomposition,

$$(b_0, \psi_0) = (\delta A \exp[i(kx + ly) + \sigma t] + Bx, \delta C \exp[i(kx + ly) + \sigma t])\,, \tag{6.47}$$

for wavevector (k, l), growth rate σ and small parameter δ. The vector (A, C) is the eigenvector of the resulting linear system.

To leading order in δ, the linearised buoyancy and vorticity equations can be written

$$\sigma A - ilBC = -(k^2 + l^2)\mathcal{D}A, \tag{6.48}$$

and

$$-\sigma(k^2 + l^2)C = \frac{\gamma^2}{12}\big[-2\alpha ik(k^2 + l^2) - (\alpha^2 - 1)il(k^2 + l^2)\big]BA + (k^2 + l^2)^2\mathcal{E}C, \tag{6.49}$$

or in the form of a single matrix equation,

$$\begin{pmatrix} \sigma + (k^2 + l^2)\mathcal{D} & -lB \\ \frac{\gamma^2}{12}\left[2\alpha k + (\alpha^2 - 1)l\right]B & \sigma + (k^2 + l^2)\mathcal{E} \end{pmatrix} \begin{pmatrix} A \\ iC \end{pmatrix} = \mathbf{0}. \tag{6.50}$$

For this equation to be valid for some vector (A, iC), the determinant of this matrix must vanish. Therefore

$$[\sigma + (k^2 + l^2)\mathcal{D}][\sigma + (k^2 + l^2)\mathcal{E}] + \frac{\gamma^2 B^2}{12}\left[2\alpha kl + (\alpha^2 - 1)l^2\right] = 0. \tag{6.51}$$

The solution to this equation for the growth rate, σ, is

$$\sigma_\pm = -\frac{\mathcal{D} + \mathcal{E}}{2}(k^2 + l^2) \pm \sqrt{\left[\frac{\mathcal{D} - \mathcal{E}}{2}\right]^2 (k^2 + l^2)^2 - \mathcal{B}^2\left[2\alpha kl + (\alpha^2 - 1)l^2\right]}, \tag{6.52}$$

where $\mathcal{B}^2 = \gamma^2 B^2/12$ is a re-scaled buoyancy gradient. The growth rate has a maximum at a finite wavevector (k, l). Note that in the case where $\mathcal{D} = \mathcal{E}$ (e.g. with $\mathcal{N}^2 = 0$ and $\mathrm{Pr}_E = 1$), the growth rate simplifies to

$$\sigma_\pm = -\mathcal{E}(k^2 + l^2) \pm \mathcal{B}\sqrt{-\left[2\alpha kl + (\alpha^2 - 1)l^2\right]}. \tag{6.53}$$

To find the maximum growth rate in the more general case, it is useful to define a rotated wavevector, $\mathbf{l}' = \mathbf{R}_\alpha \mathbf{l}$, where $\mathbf{l} = (k, l)$ and the rotation matrix,

$$\mathbf{R}_\alpha = \frac{1}{\sqrt{1 + \alpha^2}}\begin{pmatrix} 1 & \alpha \\ -\alpha & 1 \end{pmatrix}, \tag{6.54}$$

is orthogonal with determinant 1 corresponding to a rotation by $\theta = -\arctan\alpha$. The growth rate in rotated coordinates becomes

$$\sigma_\pm = -\frac{\mathcal{D}+\mathcal{E}}{2}(k'^2+l'^2) \pm \sqrt{\left[\frac{\mathcal{D}-\mathcal{E}}{2}\right]^2 (k'^2+l'^2)^2 + \mathcal{B}^2\left[l'^2 - \alpha^2 k'^2\right]}, \tag{6.55}$$

which, for fixed wavenumber, $|\mathbf{l}| = K$, is maximal for $(k', l') = (0, \pm K)$ corresponding to waves aligned at an angle of $\arctan\alpha$ to the down-front (y) direction. We note that the fastest growing modes therefore have a wavevector aligned with the horizontal velocity, similarly to the classical Eady instability (Eady, 1949; Vallis, 2006). The maximum growth rate over all directions as a function of the wavenumber is therefore

$$\sigma_{max}(K) = -\frac{\mathcal{D}+\mathcal{E}}{2}K^2 + \sqrt{\left[\frac{\mathcal{D}-\mathcal{E}}{2}\right]^2 K^4 + \mathcal{B}^2K^2}. \tag{6.56}$$

Maximising over K, the most unstable mode has a growth rate

$$\max_K[\sigma_{max}] = \frac{\mathcal{B}^2}{(\sqrt{\mathcal{D}}+\sqrt{\mathcal{E}})^2}, \tag{6.57}$$

which reduces to $\max_K[\sigma_{max}] = \mathcal{B}^2/(4\mathcal{D})$ in the case $\mathcal{D} = \mathcal{E}$. Therefore the most unstable wavenumber, K_{max} satisfies

$$K_{max}^2 = \frac{-2\mathcal{D}\mathcal{E} + \sqrt{\mathcal{D}\mathcal{E}(\mathcal{D}+\mathcal{E})^2}}{\mathcal{D}\mathcal{E}(\mathcal{D}-\mathcal{E})^2}\mathcal{B}^2, \tag{6.58}$$

which reduces to

$$K_{max}^2 = \frac{\mathcal{B}^2}{4\mathcal{D}^2}, \tag{6.59}$$

in the case $\mathcal{D} = \mathcal{E}$.

As noted above, the horizontal viscous/diffusion terms are necessary to produce a finite wavenumber maximum since $K_{max}^2 \to \infty$ as $\mathcal{E} \to 0$. Therefore, the system without horizontal viscosity and diffusion appears to produce an 'ultraviolet catastrophe'. However, the maximum growth rate in this case does remain bounded since σ_{max} asymptotes to $\mathcal{B}^2/\mathcal{D}$ for large K^2.

The case of $\mathcal{D} = 0$ and $\mathcal{E} \neq 0$ corresponds to no stratification and an infinite Prandtl number. By symmetry in $\mathcal{E}$ and $\mathcal{D}$ this case is the same as the $\mathcal{E} = 0$ case though with different eigenvectors. When both $\mathcal{E}$ and $\mathcal{D}$ are zero corresponding to no stratification

or horizontal diffusion, we have

$$\sigma_{max}(K) = \mathcal{B}K, \tag{6.60}$$

so the growth rate is unbounded and waves with infinite wavenumber will grow infinitely quickly.

As noted earlier, the direction of the most unstable modes described by Eq. (6.55) corresponds to $k' = 0$. In non-rotated coordinates this corresponds to $k = -\alpha l$, where k is the wavenumber in the cross-front direction and l is the wavenumber in the along-front direction. In contrast, the most unstable modes in the inviscid Eady problem have $k = 0$ and hence correspond to the limit of $\alpha \to 0$.

Instead, the modes perpendicular to the most unstable modes have $l = \alpha k$ in non-rotated coordinates. For these modes, the coefficient multiplying $\mathcal{B}^2$ inside the square root in Eq. (6.55) is negative. If $\mathcal{E} = \mathcal{D}$, $\sigma_\pm$ is purely imaginary for these modes, corresponding to traveling waves with a constant amplitude. Note, however, that the neglected higher order terms could add a real part to this growth rate and hence cause these perturbations to grow, while adding horizontal friction and diffusion will cause them to slowly decay with faster decay at higher wavenumbers.

Fig. 6.1 shows the real and imaginary parts of $\sigma_\pm$ in the case of no horizontal friction and diffusion or background stratification ($\mathcal{D} = \mathcal{E} = 0$). Only the σ_+ branch produces growing modes with the fastest growth occurring for large K along the line $k = -\alpha l$. Fig. 6.2 shows the real and imaginary parts of $\sigma_\pm$ with $\mathcal{E} = \mathcal{D} = 2.5 \times 10^{-3}$, corresponding to large horizontal friction and diffusivity or small Rossby number. A maximum in the growth rate can be seen on the plot of $Re[\sigma_+]$ for $K_{max} = 92.4$ along the line $k = -\alpha l$.

We anticipate that the 'ultraviolet catastrophe' above in the system without horizontal mixing will be cured by finite Rossby number effects. Eq. (6.42) and Eq. (6.43) contain terms that are $O(\mathrm{Ro})$ which were neglected in Eq. (6.44) and Eq. (6.45). These terms involve an extra power of the horizontal wavenumber magnitude, K, compared to the leading order terms. Therefore, the neglect of these terms is asymptotically valid when $K \ll O(1/\mathrm{Ro})$. For sufficiently large K the neglected $O(\mathrm{Ro})$ terms will become important and modify the growth rate, possibly resulting in a maximum growth rate at a lower wavenumber than predicted in Eq. (6.58) when the Rossby number is not infinitesimally small. This will be discussed further in Section 6.7.

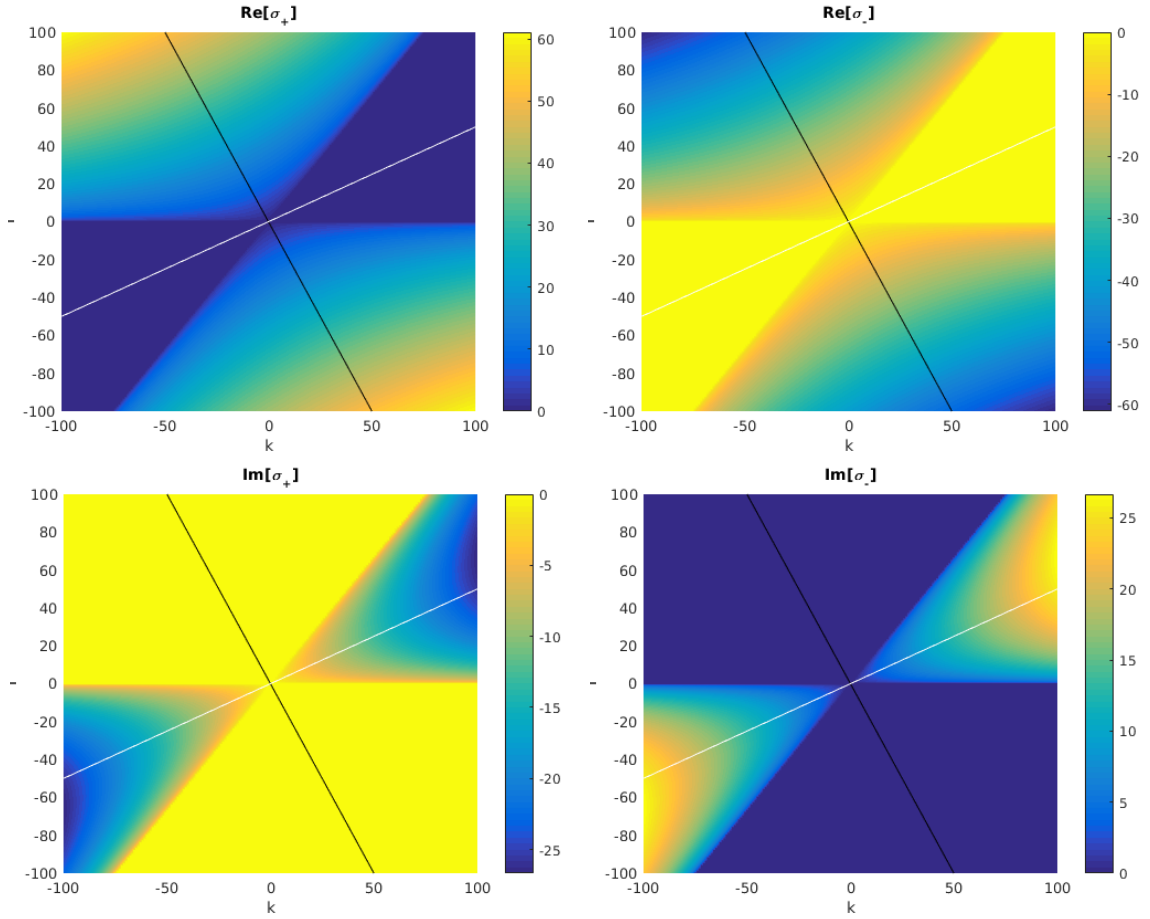

Fig. 6.1 Real and imaginary parts of the growth rate $\sigma_{\pm}$, predicted from the theory for $\mathcal{E} = \mathcal{D} = 0$ and $\mathcal{B}^2 = 0.213$ corresponding to $\alpha = 0.5$ and $B = 2$. The black lines are $k = -\alpha l$ and the white lines are $l = \alpha k$.

The case of $\alpha = 0$ corresponds to the small wavenumber (long wave) limit of the classical Eady problem, where the growth rate is

$$\sigma_{\text{Eady}} = \frac{Bl}{\mu}\left[\left(\coth\frac{\mu}{2} - \frac{\mu}{2}\right)\left(\frac{\mu}{2} - \tanh\frac{\mu}{2}\right)\right]^{1/2}, \tag{6.61}$$

for scaled wavenumber $\mu^2 = \text{Bu}\, l^2$ (Vallis, 2006). Since we consider $\text{Bu} = O(\text{Ro})$, the relevant limit is the small μ limit in which case σ_{Eady} reduces to

$$\sigma_{\text{Eady}} \sim \frac{Bl}{\sqrt{12}} = \mathcal{B}K, \tag{6.62}$$

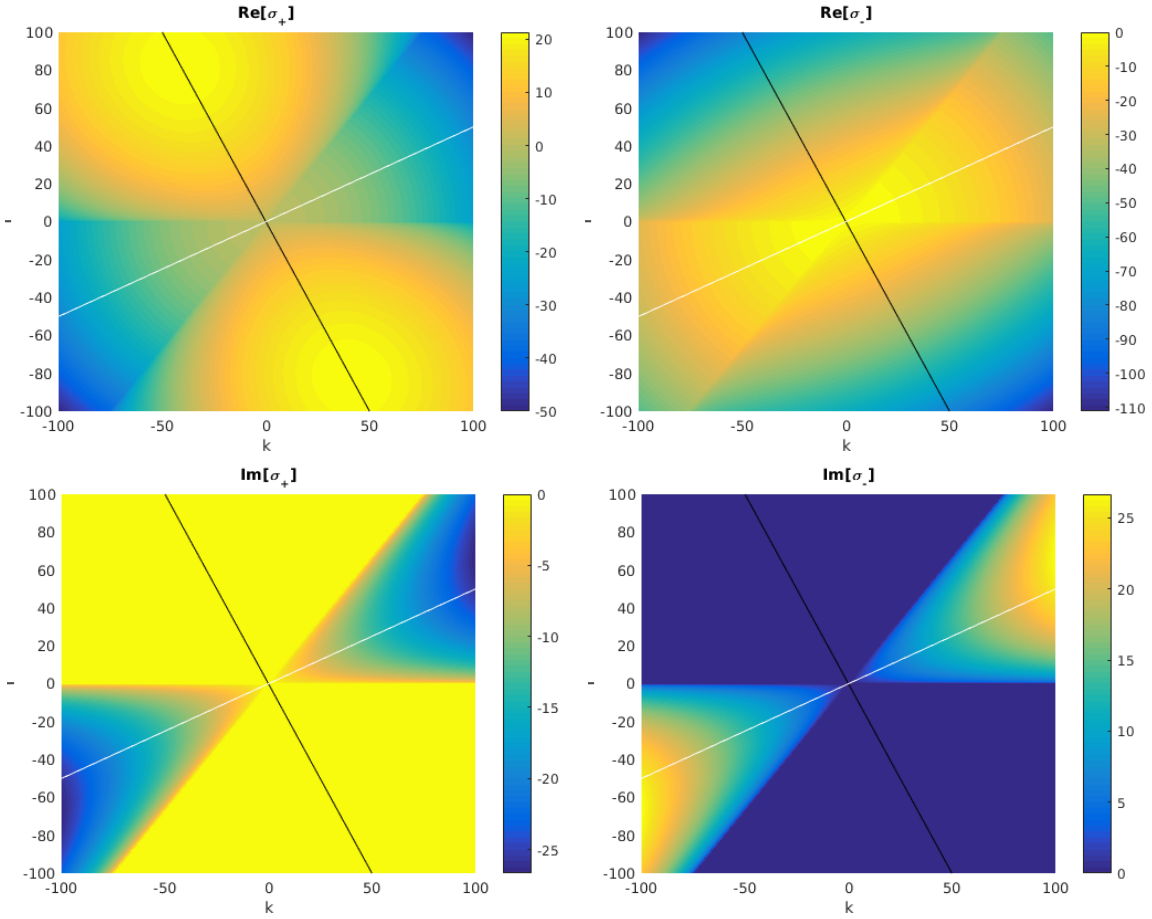

Fig. 6.2 The real and imaginary parts of the growth rate, $\sigma_{\pm}$, predicted from the theory for $\mathcal{E} = \mathcal{D} = 2.5 \times 10^{-3}$ and $\mathcal{B}^2 = 0.213$ corresponding to $\alpha = 0.5$ and $B = 2$. The black lines are $k = -\alpha l$ and the white lines are $l = \alpha k$.

consistent with Eq. (6.60). Note that this result is independent of the background buoyancy gradient represented by Bu. This result is also consistent with the small K limit of ageostrophic baroclinic instability considered by Stone (1966).

6.6 Numerical Simulations

To test the theory described above, we have conducted a series of fully nonlinear numerical simulations using the code DIABLO. The code solves the incompressible non-hydrostatic Boussinesq equations. Time stepping is performed with a combination of explicit third-order Runge-Kutta and implicit Crank Nicolson schemes while finite differences are used for derivatives in the vertical direction and discrete Fourier trans-

forms, using the pseudo-spectral method for non-linear terms, are used for derivatives in the horizontal direction (Taylor, 2008).

The simulations solve the non-dimensional equations where x, y, and z are normalised by the size of the computational domain such that the non-dimensional domain size is $L_x = L_y = L_z = 1$. The boundary conditions in the vertical direction are no stress, no buoyancy flux and no vertical velocity on the top and bottom surfaces. Periodic boundary conditions are applied to the velocity in both horizontal directions (see below for buoyancy).

For numerical stability, viscous terms of the form

$$D_{(u,v)} = \mathrm{E}\left(\frac{\partial^2}{\partial z^2} + \epsilon^2\nabla_H^2\right)(u, v), \tag{6.63}$$

$$D_w = \epsilon^2\mathrm{E}\left(\frac{\partial^2}{\partial z^2} + \epsilon^2\nabla_H^2\right)w, \tag{6.64}$$

and

$$D_b = \frac{\mathrm{E}}{\mathrm{Pr}_E}\left(\frac{\partial^2}{\partial z^2} + \epsilon^2\nabla_H^2\right)b, \tag{6.65}$$

are added to the horizontal momentum, vertical momentum and buoyancy equations respectively. We use a small Ekman number such that the dominant vertical mixing process is the relaxation to the depth-average. The simulations are initialised with the TTW solution given in Section C.2 so that the boundary layers are resolved. Away from the thin boundary layers the velocity and buoyancy fields correspond to the solution given in Section 6.3. The initial velocity field is set to the leading order solution while the initial buoyancy field is prescribed to be a linear horizontal background gradient plus the resulting $O(\mathrm{Ro})$ correction.

Periodic boundary conditions are inconsistent with the initial conditions for buoyancy which have a constant horizontal buoyancy gradient. To overcome this, we decompose the total buoyancy into a background term with a constant buoyancy gradient and departures from this gradient, i.e.

$$b = Bx + b_p, \tag{6.66}$$

where B is constant. This form is inserted into the buoyancy equation, and periodic boundary conditions are applied to b_p. This has the effect of fixing the change in buoyancy across the domain in the x direction. A similar approach has been used in a number of previous studies (e.g. Taylor & Ferrari (2011); Taylor (2016)).

Small amplitude normal mode perturbations are then added the buoyancy and streamfunction of the form

$$b_0' = \mathcal{R}\left[\sum_{(k,l)} A_{kl}\exp[i(kx+ly+\phi_{kl})]\right], \tag{6.67}$$

and

$$\psi_0' = \mathcal{R}\left[\sum_{(k,l)} C_{kl}\exp[i(kx+ly+\phi_{kl})]\right], \tag{6.68}$$

where ϕ_{kl} is a random phase, $\mathcal{R}[\phi]$ denotes the real part of ϕ and $(k,l) = 2\pi(n_k, n_l)$ for $n_{k,l} = 1, 2, \ldots$ and $n_k^2 + n_l^2 < N_{max}^2$ describing a disc in phase space of radius $2\pi N_{max}$.

Note that the leading order depth-dependent velocity depends on b_0 and hence the velocity perturbation can be found from b_0', while perturbations to the depth-independent velocity are introduced through ψ_0'. Similarly, the leading order depth-dependent buoyancy, b_1, depends on b_0 and therefore perturbations to b_1 are introduced through b_0'. In the simulations, we set the amplitudes $|A_{kl}| = |C_{kl}| = 10^{-12}$ which ensure an interval of linear perturbation growth, while the phase difference between A_{kl} and C_{kl} is randomised. We use a background buoyancy gradient of $B = 2$ such that $b = \pm 1$ at $x = \pm 0.5$.

There are several non-dimensional parameters in the system described here. For simplicity, the numerical simulations are conducted for fixed Burger number, Prandtl number, aspect ratio, and Ekman numbers, with $\mathrm{Bu} = 0$, $\mathrm{Pr}_\alpha = \mathrm{Pr}_E = 1$, $\epsilon = 0.05$ and $\mathrm{E} = 10^{-4}$. The Rossby number, Ro, and relaxation ratio, α, are varied over the set of values $\mathrm{Ro} \in \{10^{-4}, 10^{-3}, 10^{-2}, 10^{-1}\}$ and $\alpha \in \{0, 0.2, 0.4, 0.6, 0.8, 1\}$. Each simulation is run until growing modes develop and transition to a nonlinear state.

6.6.1 Description

First, we compare the linear instabilities captured by the numerical simulations with the predictions from the theory outlined above. We find that for sufficiently small Rossby numbers, the predicted angles of the instability and growth rates closely match the analytical predictions. This is perhaps not surprising since the theory is developed in the limit of asymptotically small Rossby number. However, by comparing the simulations and theory, we can quantify how large the Rossby number can be before the analytical theory breaks down.

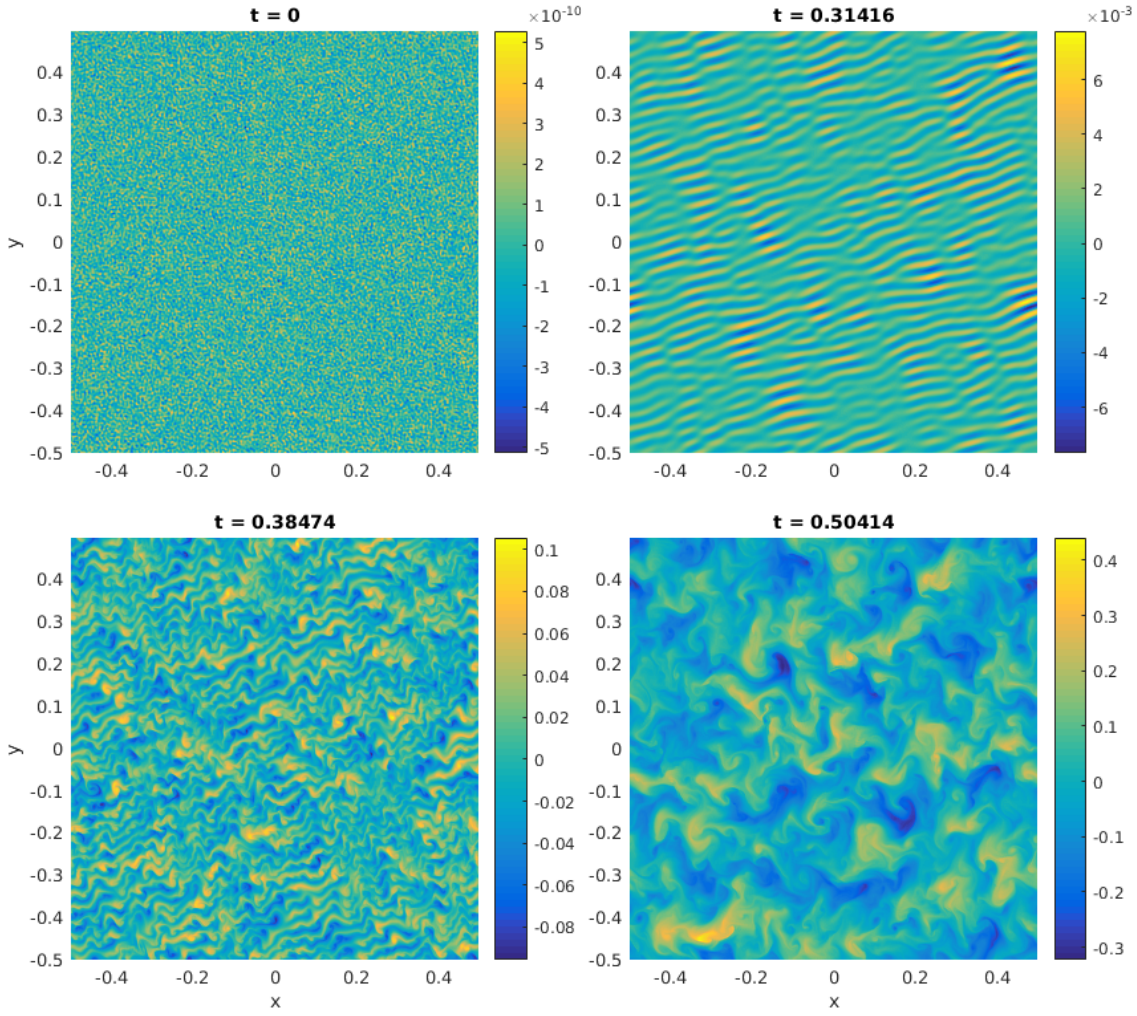

Fig. 6.3 Depth-averaged buoyancy perturbation, $\overline{b}(x,y) - Bx$ from a nonlinear numerical simulation with Ro $= 10^{-3}$ and $\alpha = 0.4$ and several times as indicated. The formation of the linear instability and the transition to nonlinear instability can be seen.

Fig. 6.3 illustrates the development and nonlinear breakdown of the unstable modes from a simulation with Ro $= 10^{-3}$ and $\alpha = 0.4$. Here, the depth-averaged buoyancy field is plotted, where the background buoyancy gradient, B, has been removed. For reference, the unperturbed basic state is $\overline{b} = Bx$, which would have vertical buoyancy contours in this figure. At a relatively early time ($t = 0.314$, upper right panel), growing perturbations develop with a distinctive angle with respect to the buoyancy gradient. Note that the fastest growing modes occur on a larger scale compared to the initial perturbations, suggesting a scale-selective process. By $t = 0.384$ (lower left panel) the flow transitions to a nonlinear regime and the growing perturbations roll up

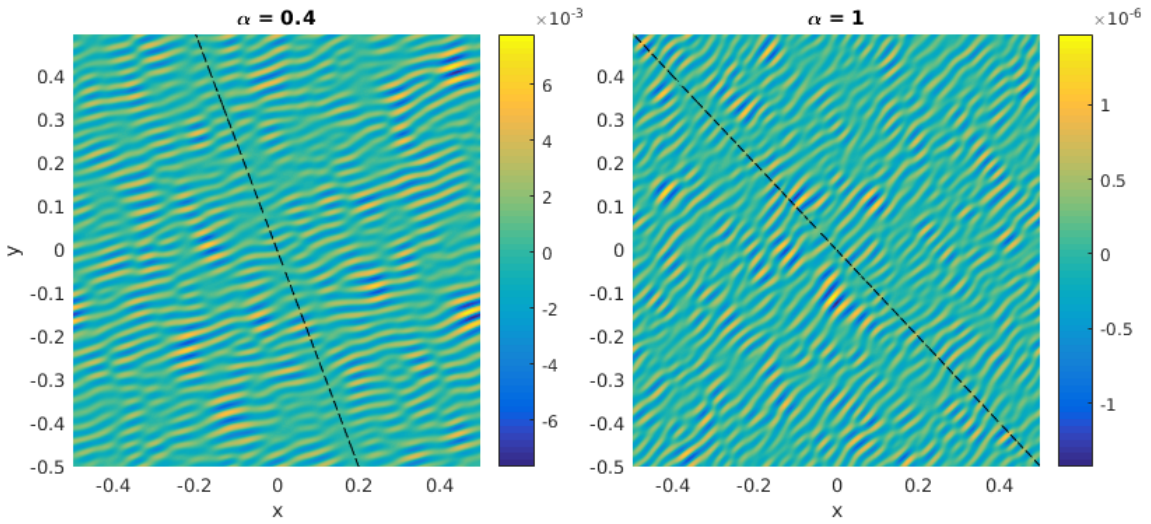

Fig. 6.4 Depth-averaged buoyancy perturbation, $\overline{b}(x,y)-Bx$ from numerical simulations with $\alpha = 0.4$ and $\alpha = 1$. In both cases $\mathrm{Ro} = 10^{-3}$ and the fields are shown at time $t = 0.314$. The black lines show the predicted wavevector direction, $k = -\alpha l$, which should be perpendicular to lines of constant phase.

into coherent vortices. These vortices then merge resulting in an energy cascade to larger scales (see lower right panel).

Fig. 6.4 shows two simulations with different values of α during the period when the perturbations are linear and the growth is exponential. The theoretical prediction for the direction of the fastest growing modes, $k = -\alpha l$, is plotted as a black dashed line. As predicted, the wave crests of the most unstable modes are nearly perpendicular to the predicted wavenumber vector.

Fig. 6.5 shows the buoyancy perturbation from four simulations with different values of the Rossby number. In all cases, $\alpha = 0.4$, and hence the predicted angle of the most unstable modes is the same. The wavelength of the most unstable modes changes with Ro, but interestingly the dependence is not monotonic. For the range of Ro tested, the shortest waves are observed for $\mathrm{Ro} = 10^{-3}$. For the cases of $\mathrm{Ro} = 10^{-4} - 10^{-2}$ we can see that the direction of the wavevector is independent of Ro and closely matches the theoretical prediction.

In the case with the largest Rossby number, $\mathrm{Ro} = 0.1$, the fastest growing mode does not fit in the domain, and instead a quantised mode with $(k,l) = (0, 2\pi)$ appears. There also appear to be growing perturbations at an angle nearly perpendicular to the analytical prediction of $k = -\alpha l$. These modes might be an indication of symmetric

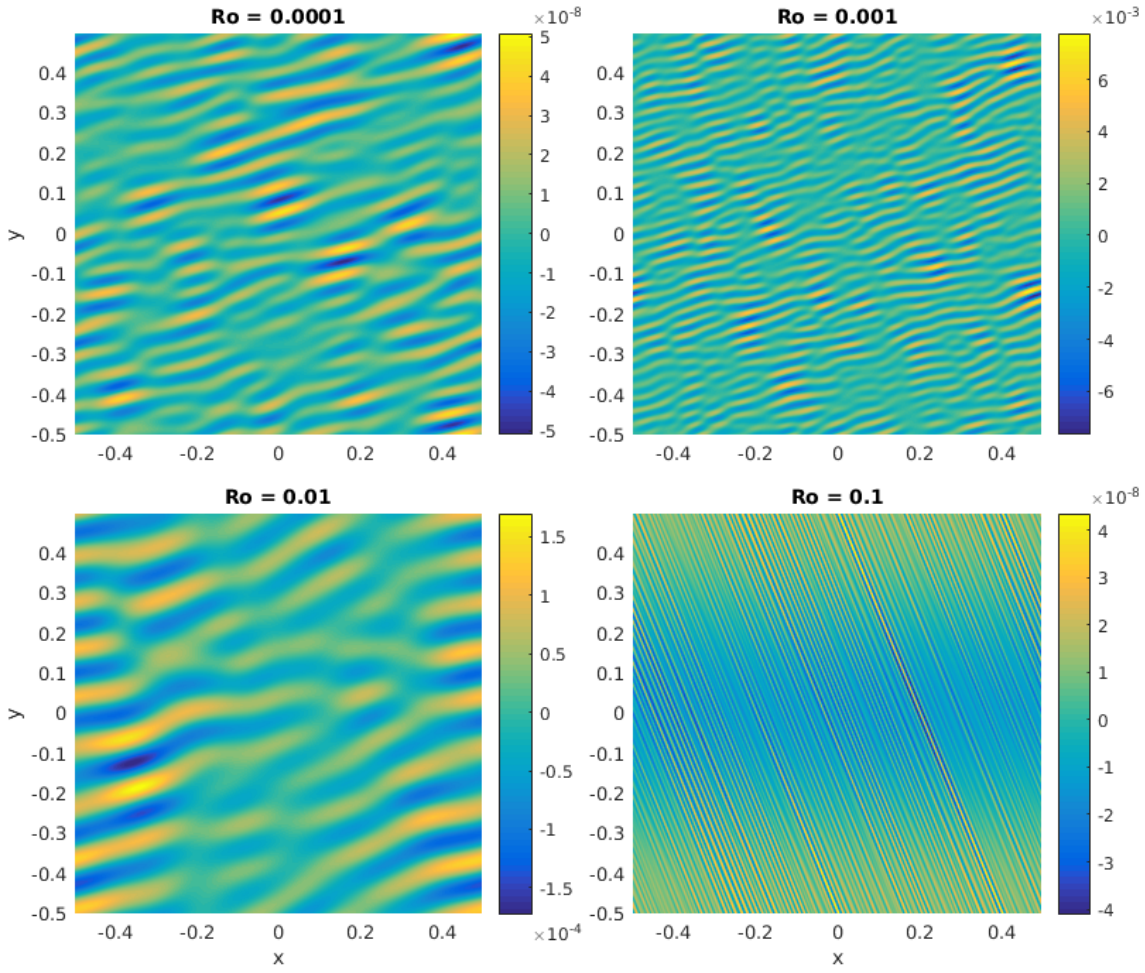

Fig. 6.5 Depth-averaged buoyancy perturbation, $\bar{b}(x, y) - Bx$ for $\alpha = 0.4$ and several Rossby numbers during the phase of linear perturbation growth in several numerical simulations. For Ro $= 0.1$ growing modes appear which are perpendicular to those predicted by the analytical theory, indicating a breakdown of the theory due to the relatively large Rossby number.

instability modified by vertical mixing, although this is not captured by our theory and we do not focus on it here.

6.6.2 Energetics

To describe the dynamics of the unstable modes, it is useful to diagnose the perturbation energy budgets. To start, we define the horizontal domain average to be

$$\langle \phi \rangle = \int_{-0.5}^{0.5} \int_{-0.5}^{0.5} \phi \, dx \, dy, \tag{6.69}$$

and let $\tilde{\phi} = \phi - \langle\phi\rangle$ denote the departure from the horizontal average. The nondimensional energy equation can be derived from the governing equations and written in conservative form as

$$\mathrm{Ro}\,\frac{\partial \mathcal{K}}{\partial t} + \nabla\cdot[(\mathrm{Ro}\,\mathcal{K} + p)\mathbf{u}] - b\,w = -\alpha\,(uu' + vv')\,, \tag{6.70}$$

for kinetic energy density

$$\mathcal{K} = \frac{1}{2}\left(u^2 + v^2 + \epsilon^2 w^2\right), \tag{6.71}$$

assuming that the diffusive terms are small. We now consider the perturbation kinetic energy,

$$e = \frac{1}{2}\left\langle \tilde{u}^2 + \tilde{v}^2 + \epsilon^2\tilde{w}^2\right\rangle, \tag{6.72}$$

and using Eq. (6.70) and the horizontally averaged governing equations, the perturbation energy budget can be written

$$\begin{aligned}\mathrm{Ro}\left[\frac{\partial e}{\partial t} + \langle w\rangle\frac{\partial e}{\partial z} + \underbrace{\langle\tilde{u}\tilde{w}\rangle\frac{\partial\langle u\rangle}{\partial z} + \langle\tilde{v}\tilde{w}\rangle\frac{\partial\langle v\rangle}{\partial z}}_{\mathcal{S}} + \underbrace{\frac{1}{2}\frac{\partial}{\partial z}\left\langle[\tilde{u}^2 + \tilde{v}^2 + \epsilon^2\tilde{w}^2]\tilde{w}\right\rangle}_{\mathcal{T}}\right] = \\ \underbrace{-\frac{\partial}{\partial z}\langle\tilde{p}\tilde{w}\rangle}_{\mathcal{P}} + \underbrace{\langle\tilde{b}\tilde{w}\rangle}_{\mathcal{F}}\underbrace{-\alpha\,\langle\tilde{u}'\tilde{u} + \tilde{v}'\tilde{v}\rangle}_{\mathcal{R}}.\end{aligned} \tag{6.73}$$

The terms in Eq. (6.73) can be interpreted as $\mathcal{S}$: production of perturbation kinetic energy by the mean shear, $\mathcal{T}$: turbulent transport, $\mathcal{P}$: pressure transport, $\mathcal{F}$: buoyancy flux, and $\mathcal{R}$: dissipation by the parametrised vertical mixing. From mass conservation $\partial\langle w\rangle/z = 0$ and hence $\langle w\rangle = \text{const.}$ and using the vertical boundary conditions we have that $\langle w\rangle = 0$. We can now vertically average Eq. (6.73) to remove the transport terms. The resulting equation for the domain averaged perturbation kinetic energy is

$$\mathrm{Ro}\,\frac{\partial\overline{e}}{\partial t} = \overline{\mathcal{S}} + \overline{\mathcal{F}} + \overline{\mathcal{R}}. \tag{6.74}$$

The depth-averaged dissipation associated with the vertical relaxation term is given by

$$\overline{\mathcal{R}} = -\alpha\left[\overline{\langle\tilde{u}'^2\rangle} + \overline{\langle\tilde{v}'^2\rangle}\right] = -\alpha\left[\overline{\langle\tilde{u}^2\rangle} + \overline{\langle\tilde{v}^2\rangle} - \left\langle\overline{\tilde{u}}^2\right\rangle - \left\langle\overline{\tilde{v}}^2\right\rangle\right], \tag{6.75}$$

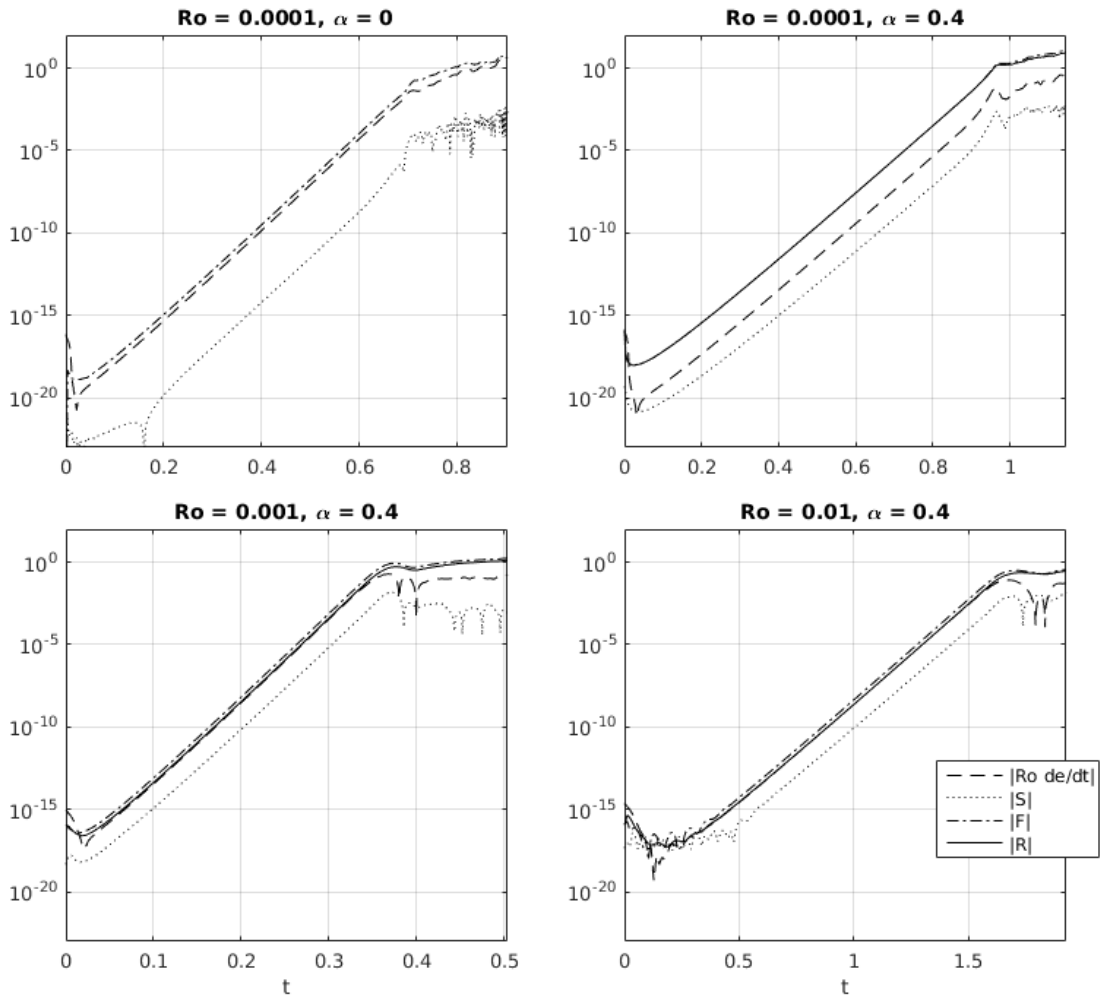

Fig. 6.6 Terms in the volume-averaged energy budget for numerical simulations with several values of Rossby numbers and α. The terms are as given in Eq. (6.73), specifically, the shear production is denoted S, buoyancy flux, F, and dissipation via vertical mixing (relaxation), R. The case of $\alpha = 0$ corresponds to the classical Eady model.

which is negative by the Cauchy-Schwarz inequality. We now calculate the four terms in Eq. (6.74) using our numerical data and consider the energy balance in order to determine the energy source and mechanism for the instability.

Fig. 6.6 shows the four terms in Eq. (6.74) for four different values of (Ro, α). Clear regions of exponential growth (with constant slope on the semi-log plot) develop in each case. When $\alpha = 0$, corresponding to the classical Eady model, we can see that the dominant energy balance is between the time rate of change in kinetic energy and the buoyancy flux, representing the transformation of perturbation potential energy

into perturbation kinetic energy and indicative of baroclinic instability. For nonzero α, the dominant balance is between the buoyancy flux and the relaxation dissipation with the residual corresponding to the time rate of change of kinetic energy. Therefore, in the presence of vertical mixing, the instability is driven by a transfer of potential energy from the buoyancy field consistent with baroclinic instability, although most of the energy extracted from the potential energy reservoir is dissipated through the vertical mixing (relaxation) term. We note that the balance between $\overline{\mathcal{F}}$ and $\overline{\mathcal{R}}$ is closer for smaller Ro which is consistent with the asymptotic theory. Once the instability reaches the nonlinear phase, the neglected viscous dissipation term becomes significant due to the appearance of small scale vortices.

6.6.3 Growth Rate

In this section, we diagnose the growth rate of the unstable perturbations from the numerical simulations and compare these with the prediction from the analytical theory. We define the growth rate of perturbations captured in the numerical simulations by

$$\sigma_N = \frac{1}{2\overline{e}} \frac{d\overline{e}}{dt}. \tag{6.76}$$

This can then be compared with the theoretical growth rate, σ, given by the eigenmode decomposition in Eq. (6.47). We now define $\sigma_{avg}(t_1, t_2)$ to be the average of σ_N in the time interval $[t_1, t_2]$ and $\sigma_{rms}(t_1, t_2)$ to be the RMS deviation from this average. Specifically,

$$\sigma_{avg}(t_1, t_2) = \frac{1}{t_2 - t_1} \int_{t_1}^{t_2} \sigma_N(t)\, dt, \tag{6.77}$$

and

$$\sigma_{rms}(t_1, t_1) = \left[\frac{1}{t_2 - t_1} \int_{t_1}^{t_2} \left[\sigma_N(t) - \sigma_{avg}(t_1, t_2)\right]^2 \, dt \right]^{1/2}. \tag{6.78}$$

We define the interval of exponential growth to be the largest time interval in which the ratio of σ_{rms} to σ_{avg} is below a specified tolerance, i.e. $\sigma_{rms}/\sigma_{avg} < \delta$. The value of the growth rate is then taken to be σ_{avg} within the region of exponential growth. We use a tolerance of $\delta = 0.01$ and do not define a growth rate if the region of exponential growth is small or σ_N is strongly oscillatory. We also use 2D discrete Fourier transforms to determine the wavevector of the fastest growing modes in each simulation.

Fig. 6.7 shows σ_N diagnosed from four simulations with different values of Ro and α. For large Ro, the small scale waves interfere with the mode 1 instability leading to

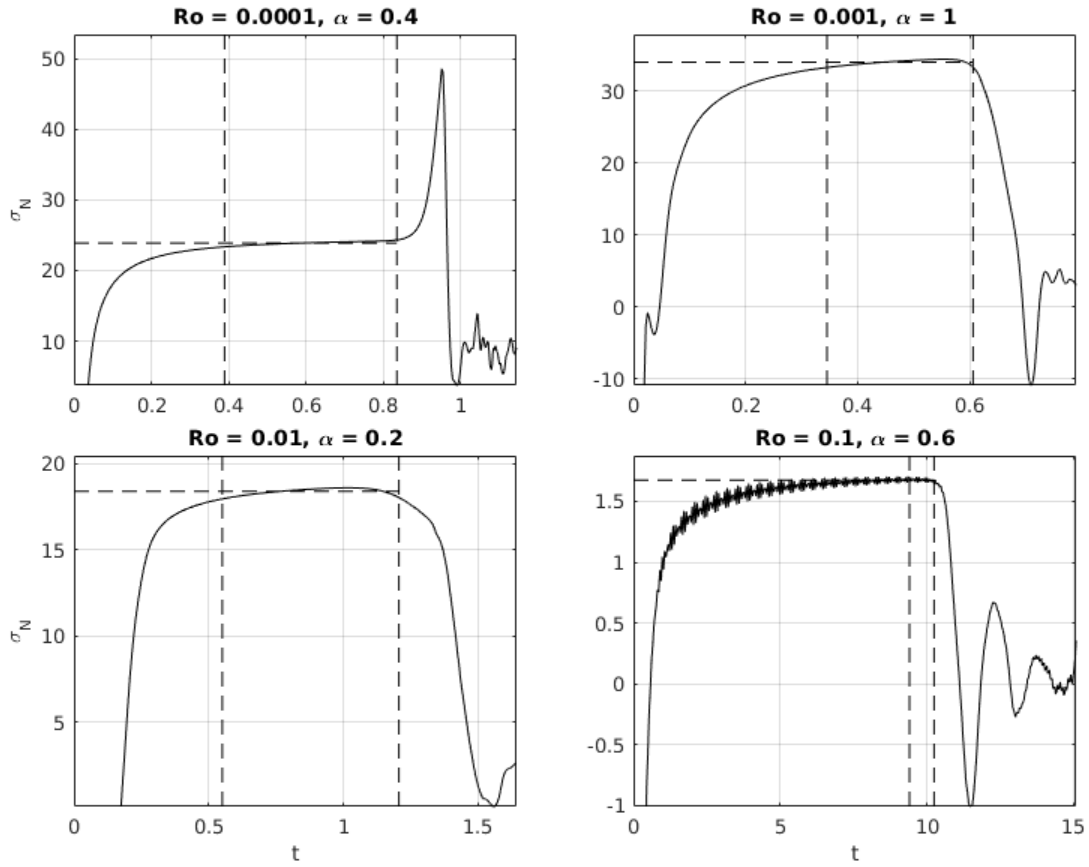

Fig. 6.7 Perturbation growth rate, σ_N, diagnosed from the numerical simulations for a range of Rossby numbers, Ro and relaxation ratios, α. The dashed lines show the interval of exponential growth and the average value of σ_N within this region.

strong oscillatory behaviour in σ_N and preventing us from accurately selecting a single growth rate for $\alpha > 0.6$.

Fig. 6.8 shows the growth rate and wavenumber of the fastest growing modes for each simulation. We exclude the results for $(\mathrm{Ro}, \alpha) = (0.01, 0.8)$, $(0.01, 1)$, $(0.1, 0.8)$ and $(0.1, 1)$ as there are not well-defined regions of exponential growth. We note that for $\mathrm{Ro} = 0.1$ the observed mode is $(k, l) = (0, 2\pi)$ which is likely not the fastest growing mode due to the restrictions of the domain size. For small Rossby number, the wavenumber of the fastest growing mode depends on α while for $\mathrm{Ro} \geq 10^{-3}$ it is independent of α. This is an indication that there are different processes controlling the most unstable modes for small and large Ro.

Fig. 6.9 shows the 2D Fourier transform of the depth-averaged buoyancy perturbation for several values of Ro and α. When viscous effects are included the wavenumber

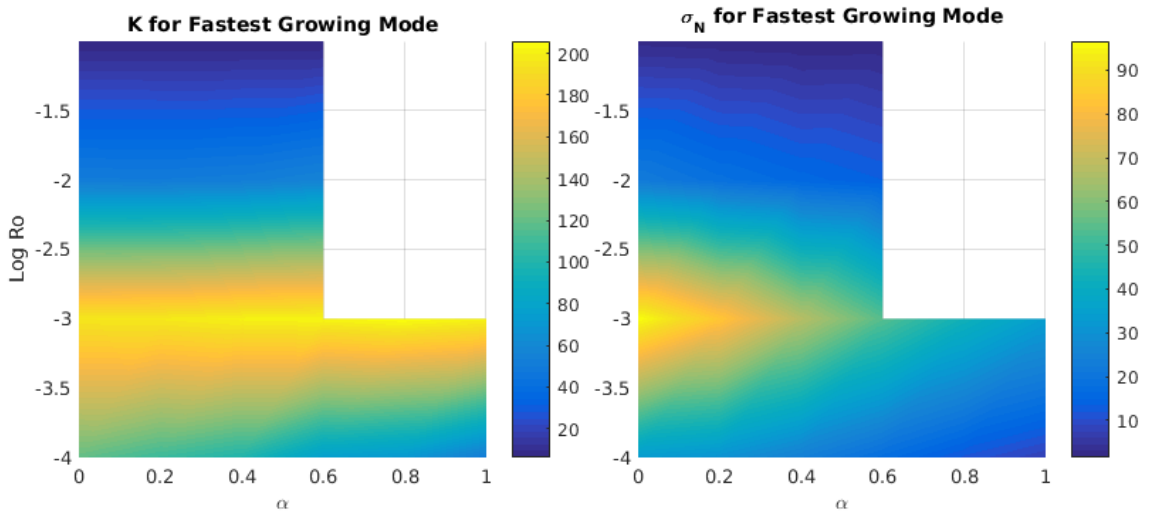

Fig. 6.8 Perturbation growth rate, σ_N, and the wavenumber, $K = \sqrt{k^2 + l^2}$, for the fastest growing mode inferred from the numerical simulations as functions of Ro and α.

associated with the most unstable mode is given by Eq. (6.59) and can be written as

$$K_{max} = \frac{\mathrm{Ro}\, B}{\sqrt{48}(1+\alpha^2)\epsilon^2 \mathrm{E}}. \tag{6.79}$$

The dependence of K_{max} on α matches that observed in Fig. 6.8 for $\mathrm{Ro} = 10^{-4}$. The circles on Fig. 6.9 have radius given by Eq. (6.79) and we can see that the numerical results match the predictions of fastest growing wavenumber for $\mathrm{Ro} = 10^{-4}$. For larger Ro the fastest growing wavenumber is too small to be due to viscous effects. It appears that there is a second, α independent effect which controls the fastest growing modes and is not captured by the theory, this will be examined further in Section 6.7. Note that K_{max} depends on the aspect ratio, ϵ, when viscous effects set the scale of the most unstable mode. However, for the larger Ro cases the scale of the most unstable mode is not influenced by viscosity and hence the value of ϵ has no effect on the instability.

Along the direction, $k = -\alpha l$, the growth rate is given by Eq. (6.56) and for $Bu = 0$ and $\mathrm{Pr}_E = 1$, can be written as

$$\sigma_{max} = \frac{BK}{\sqrt{12}(1+\alpha^2)} - \frac{\epsilon^2 \mathrm{E} K^2}{\mathrm{Ro}}. \tag{6.80}$$

Fig. 6.10 shows a comparison between the growth rates predicted by Eq. (6.80) (left panel) and the growth rates diagnosed from the numerical simulations (right panel) where the wavenumber corresponding to the most unstable mode as diagnosed in the

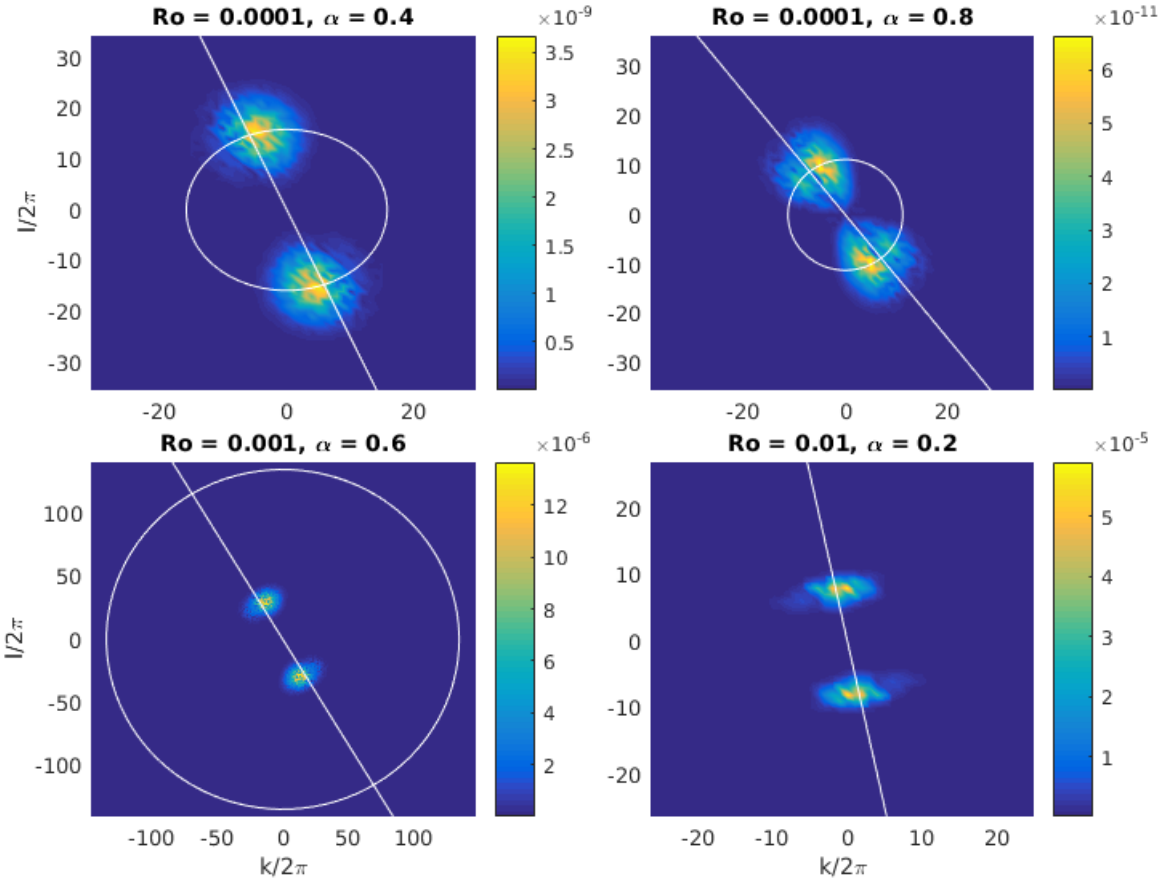

Fig. 6.9 Amplitudes of the horizontal Fourier coefficients from the depth-averaged buoyancy perturbation, $\overline{b}(x,y) - Bx$, calculated form the numerical simulations for a range of Ro and α. The line $k = -\alpha l$ is shown in white and the maximum wavenumber, K_{max}, is given by the white circle.

numerical simulations is used to set K in Eq. (6.80). There is very good agreement between the growth rates from the theory and simulations across a wide range of Rossby numbers and relaxation ratios. Interestingly, the growth rates match reasonably well even in cases where the most unstable wavenumber in the theory (Eq. (6.79)) doesn't match the most unstable wavenumber diagnosed in the simulations (e.g. the cases in the bottom panels of Fig. 6.9).

6.7 QG Predictions for the fastest growing mode

The numerical simulations described above indicate that the wavenumber of the most unstable mode is set by a process other than viscosity for the larger values of Ro.

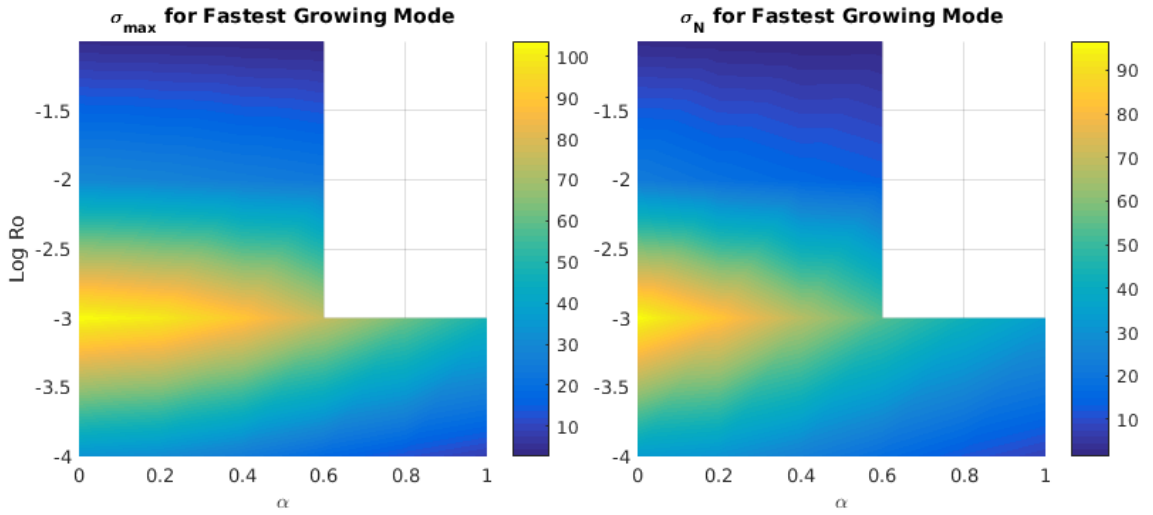

Fig. 6.10 Perturbation growth rate, σ, diagnosed from the numerical simulations (σ_N) and the maximum growth rate predicted from the theory (σ_{max}).

In this section we use the quasi-geostrophic (QG) equations to examine the stability of a depth-dependent basic state associated with vertical mixing of momentum and buoyancy. Specifically the velocity and buoyancy of the basic state will be given by Eq. (6.13) and Eq. (6.16). Importantly, here the stratification of the basic state is non-zero and is the result of a balance between cross-front advection and vertical mixing. Since the stratification in Eq. (6.16) appears at $O(\mathrm{Ro})$, it did not appear in the basic state analyzed in Section 6.5. Here, we also assume that departures from the basic state are not directly affected by vertical or horizontal mixing. This allows us to isolate the influence of vertical mixing on the background flow from its influence on the growing perturbations.

The total velocity and buoyancy fields can be written as

$$(u, v, w, b) = \left(U + \hat{u}, V + \hat{v}, \hat{w}, Bx + N^2 z + \hat{b}\right), \tag{6.81}$$

where capital letters denote the basic state and $\hat{\cdot}$ denotes a perturbation to the basic state. The nondimensional QG equation can be written

$$\left[\frac{\partial^2}{\partial x^2} + \frac{\partial^2}{\partial y^2} + \frac{1}{\mathrm{Ro}}\frac{\partial}{\partial z}\left(\frac{1}{N^2}\frac{\partial}{\partial z}\right)\right]\hat{\psi} = 0, \tag{6.82}$$

where the streamfunction satisfies $\hat{u} = -\partial\hat{\psi}/\partial y$ and $\hat{v} = \partial\hat{\psi}/\partial x$. Applying the boundary condition $w = 0$ at $z = \pm 1/2$ to the buoyancy equation gives

$$\left[\frac{\partial^2}{\partial t \partial z} + U\frac{\partial^2}{\partial x \partial z} + V\frac{\partial^2}{\partial y \partial z} - B\frac{\partial}{\partial y}\right]\hat{\psi} = 0, \tag{6.83}$$

where the nondimensional buoyancy perturbation is $\hat{b} = \partial\hat{\psi}/\partial z$ using the QG approximation. From Eq. (6.13) and Eq. (6.16) we now write

$$(U, V, N^2) = \left(-\alpha\gamma Bz,\ \gamma Bz,\ \mathrm{Ro}\,\mathrm{Pr}_\alpha \gamma B^2\right), \tag{6.84}$$

and note that N^2 describes the stratification that results from the balance between cross-front advection and vertical mixing. Eq. (6.82) has solutions of the form

$$\hat{\psi} = \left[A\sinh\kappa z + C\cosh\kappa z\right] e^{ikx+ily+\sigma t}, \tag{6.85}$$

for $\kappa = \sqrt{\mathrm{Ro}\,N^2(k^2+l^2)}$ and following Vallis (2006) we use Eq. (6.83) to determine a linear system for (A, C). The requirement that the determinant of this system vanishes determines the growth rate, which can be written

$$\sigma^2 = \frac{B^2}{\kappa^2}\left[\gamma(l-\alpha k)\frac{\kappa}{2} - l\tanh\frac{\kappa}{2}\right]\left[l\coth\frac{\kappa}{2} - \gamma(l-\alpha k)\frac{\kappa}{2}\right]. \tag{6.86}$$

We note that this result reduces to the classical Eady result (Eady, 1949) for $\alpha = 0$. Working in our rotated coordinate system (k', l'), we can show that σ is maximal for $k = -\alpha l$ where

$$\sigma^2 = \frac{\gamma B^2}{\mathrm{Ro}\,N^2}\left[\frac{\kappa}{2} - \tanh\frac{\kappa}{2}\right]\left[\coth\frac{\kappa}{2} - \frac{\kappa}{2}\right]. \tag{6.87}$$

Therefore, following Eady (1949) and Vallis (2006), we have maximum growth rate

$$\sigma_{max} = \frac{0.31B}{\sqrt{\mathrm{Ro}\,(1+\alpha^2)}\,N}, \tag{6.88}$$

for most unstable wavenumber

$$K_{max} = \frac{1.6}{\sqrt{\mathrm{Ro}}\,N}. \tag{6.89}$$

Using N^2 from Eq. (6.84) this result becomes

$$\sigma_{max} = \frac{0.31}{\mathrm{Ro}\sqrt{\mathrm{Pr}_\alpha}}, \tag{6.90}$$

and

$$K_{max} = \frac{1.6\sqrt{1+\alpha^2}}{\mathrm{Ro}\sqrt{\mathrm{Pr}_\alpha}\,B}. \tag{6.91}$$

Therefore the most unstable mode is set by the interaction of edge waves, moderated by the stratification that develops in response to vertical mixing of momentum. Since this stratification is an $O(\mathrm{Ro})$ term in the buoyancy equation, it does not appear in the leading order evolution equations for b_0 or ψ_0 (Eq. (6.44) and Eq. (6.45)), and hence its influence on the unstable modes is not captured by our asymptotic model.

These predictions can be compared with Fig. 6.8 and provide reasonably accurate predictions for the growth rate and wavenumber for $\mathrm{Ro} > 10^{-3}$ where the scale is not set by horizontal diffusion and the wavenumber of the most unstable mode decreases with increasing Ro. However, the growth rate from the QG analysis (Eq. (6.90)) is less accurate than the prediction from the asymptotic theory (Eq. (6.80)) when compared with the numerical simulations. For example, the growth rate in Eq. (6.90) is independent of α, while the prediction in Eq. (6.80) and the growth rate diagnosed from the simulations decrease with increasing α. This suggests that vertical mixing acts to damp the perturbations and reduces their growth rate. Nevertheless, the estimate from Eq. (6.90) still provides a reasonable approximation to the growth rate.

We expect the mixing-induced stratification to limit the size of the most unstable modes when it would give a smaller value of K_{max} than horizontal diffusion. This occurs when

$$\frac{\mathrm{Ro}\,B}{\sqrt{48}(1+\alpha^2)\epsilon^2\mathrm{E}} > \frac{1.6\sqrt{1+\alpha^2}}{\mathrm{Ro}\sqrt{\mathrm{Pr}_\alpha}\,B}. \tag{6.92}$$

Therefore the mixing-induced stratification will be important when

$$\mathrm{Ro} > \frac{3.3(1+\alpha^2)^{3/4}\,\epsilon\,\mathrm{E}^{1/2}}{B\,\mathrm{Pr}_\alpha^{1/4}}. \tag{6.93}$$

For the parameters used in our numerical simulations (specifically $\epsilon = 0.05$ and $\mathrm{E} = 10^{-4}$), this condition is satisfied for $\mathrm{Ro} \gtrsim 10^{-3}$, consistent with our observations that the fastest growing mode is not set by horizontal diffusion for this parameter range. We note that using a turbulent Ekman number scaling of $\mathrm{E} \sim u^*/fH$ for turbulent velocity u^* and mixed layer depth H can give values of E on the order of $10^{-2} - 1$.

Therefore in a highly turbulent mixed layer, a diffusive cutoff may be possible for Rossby numbers up to about $\mathrm{Ro} \sim 0.1$.

The angle of the most unstable mode from the QG analysis agrees with the theory in Section 6.5 and the simulations. Therefore, we can conclude that the orientation of the most unstable modes are primarily set by the background flow and is not strongly influenced by the effects of vertical mixing acting directly on the perturbations.

For small K the growth rate from the QG analysis (Eq. (6.86)) becomes

$$\sigma \sim \frac{BK}{\sqrt{12(1+\alpha^2)\mathrm{Bu}}}, \tag{6.94}$$

for $\mathrm{Bu} = \mathrm{Ro}\, N^2$. This does not have the same α dependence as Eq. (6.60), although we note that both expressions reduce to the classical Eady case for $\alpha = 0$. This discrepancy is likely because the QG approach does not consider the action of vertical mixing on the perturbations.

The analysis of the instability using the QG equations also provides insight into the relative accuracy of growth rate from the analytical theory. In the absence of horizontal mixing, the analytical theory predicted that the growth rate is a linearly proportional to the horizontal wavenumber (see Eq. (6.60)). As shown in Eq. (6.94), the growth rate in the QG analysis also increases linearly with K for small values of K, while stratification decouples the Eady edge waves and suppresses the growth rate for large K. However, the maximum growth rate in the QG analysis is relatively close to the value that would be obtained by using the wavenumber of the fastest growing mode in Eq. (6.94), which has the same form as the theory in Section 6.5. We expect that the true growth rate for the problem admits both a viscous cutoff and a decoupled edge wave cutoff and reduces to the analytical result for small K. If the maximum growth rate in the case of decoupled edge waves is close to the linear, small K region (as is the case in the QG model) then the analytical theory would well describe the growth rate even though it does not capture the cutoff mechanism. This may explain why our growth rate predictions in Fig. 6.10 closely match the numerical simulations.

Recall from Fig. 6.3 that modes with $l = \alpha k$ appeared in the simulation with $\mathrm{Ro} = 0.1$ which were perpendicular to the anticipated most unstable mode. Setting $l = \alpha k$ in the QG analysis gives

$$\sigma^2 = -\frac{B^2 l^2}{\kappa^2}. \tag{6.95}$$

These modes are stable and correspond to travelling waves. Therefore, the perpendicular modes observed in Fig. 6.5 do not appear to arise through QG dynamics, and are likely associated with finite Ro effects which we have not considered here.

Finally, we note that a similar QG analysis could be carried out for the TTW system with vertical mixing parameterised using a Laplacian viscosity and diffusivity, as described in Section C.3. However, in this case Eq. (6.82) would have to be solved numerically since N^2 depends on z.

6.8 Conclusions and Discussion

Here, we examined baroclinic instability in the presence of vertical mixing, where mixing is parametrised using a simple relaxation towards the local depth average. A theory was developed which is valid in the limit of small Rossby number, but arbitrary mixing rates. In the limit of no mixing we recover the long wave limit of baroclinic instability in the Eady model. The effect of the vertical mixing is to reduce the growth rate and tilt the unstable modes such that they are aligned with the horizontal velocity, with the angle determined by the relaxation timescale.

In the absence of horizontal mixing and a turbulent Prandtl number of 1, the growth rate associated with the fastest growing modes (from Eq. (6.57) with $B = 1$) is

$$\sigma = \frac{\mathrm{Ro}}{\alpha\,(1+\alpha^2)\,\mathrm{Bu}}, \tag{6.96}$$

where σ is nondimensionalised by $1/T = HM^2/(fL)$, H is the mixed layer depth, L is a characteristic horizontal length scale, M^2 is the horizontal buoyancy gradient, and f is the Coriolis parameter. The nondimensional parameters in Eq. (6.96) are the Rossby number, $\mathrm{Ro} = M^2H/(f^2L)$, the Burger number, $\mathrm{Bu} = N^2H^2/(f^2L^2)$, where N is the buoyancy frequency associated with a stable background stratification, and the mixing ratio, $\alpha = \mu/f$, where μ is the vertical mixing rate. Note that the horizontal length scale, L, characterises the width of the front and not necessarily the size of the unstable modes. Indeed, Fig. 6.8 shows that the non-dimensional wavenumber of the most unstable modes is $K >> 1$ and therefore the scale-dependent Rossby number associated with the growing perturbations will be significantly larger than Ro.

The theoretical growth rate in Eq. (6.96) decreases with decreasing Ro (e.g. for weak horizontal buoyancy gradients) and decreases with increasing vertical mixing rate. In the absence of a background stratification ($\mathrm{Bu} = 0$) the growth rate is

unbounded. However, when a horizontal Laplacian viscosity and diffusivity is included to parameterise horizontal mixing, the growth rate is bounded and equal to

$$\sigma = \frac{\mathrm{Ro}}{12\left(1+\alpha^2\right)^2\left[\sqrt{\epsilon^2\mathrm{E}}+\sqrt{\epsilon^2\mathrm{E}+\frac{\alpha\,\mathrm{Bu}}{12(1+\alpha^2)}}\right]^2}, \tag{6.97}$$

where $\mathrm{E} = \nu/(fH^2)$ is the Ekman number, ν is the horizontal viscosity (equal to the diffusivity since the Prandtl number is assumed to be 1) and H is the mixed layer depth.

The theory developed here is valid for asymptotically small Rossby numbers (although the vertical mixing rate can be large). To test the range of validity of the theory, we conducted a series of numerical simulations. The growth rate and wavenumbers predicted by the theory match those diagnosed from the simulations very closely for small Rossby numbers. The predicted growth rate matches the simulations for Rossby numbers up to $O(0.1)$. However for $\mathrm{Ro} > O(10^{-3})$, the most unstable modes in the simulations are significantly larger than those predicted from the theory. This implies that in this range of Ro and for the chosen values of E and ϵ, the neglected higher order terms become important and provide a scale selecting mechanism.

To investigate this further, we used the quasi-geostrophic (QG) equations to analyze the stability of a depth-dependent basic state. Here the density of the basic state was set through a balance between cross-front advection and vertical mixing. Since the stratification that results from this balance appears at $O(\mathrm{Ro})$ it was not included in the theory described earlier. We also neglected the direct influence of vertical mixing on the perturbations when applying the QG equations. Results from the QG analysis show that the horizontal orientation of the fastest growing modes is largely inherited from the orientation of the background flow. The QG analysis also shows that the stratification that develops from the cross-front flow can decouple the Eady edge waves, thereby providing a high wavenumber cutoff. Although this effect was not included in the theory presented in Section 6.5, the growth rate predicted from our theory agrees well with the growth rate diagnosed from the numerical simulations, even in parts of parameter space where the most unstable wavenumber is not set by a viscous cutoff.

Motivated by this, we can combine the predicted growth rate from our theory with the high wavenumber cutoff from the QG analysis. To put the results in the context of typical ocean conditions, it is useful to normalise the growth rate by f and write it as a function of $|\nabla b|/f^2$, which has the effect of eliminating the dependence of the growth

rate on the aspect ratio. In the case with $\mathrm{Bu} = 0$, $\mathrm{Pr}_E = 1$, and a non-dimensional horizontal buoyancy gradient $B = 1$, the growth rate given in Eq. (6.80) can be written

$$\frac{\sigma}{f} = \frac{K\mathrm{Ro}}{\sqrt{12}(1+\alpha^2)} - \frac{f^4}{|\nabla b|^2}\mathrm{E}K^2\mathrm{Ro}^2. \tag{6.98}$$

When the size of the most unstable mode is limited by horizontal mixing,

$$K\mathrm{Ro} = \frac{|\nabla b|^2}{\sqrt{48}f^4(1+\alpha^2)\mathrm{E}}, \tag{6.99}$$

and when it is limited by the influence of mixing-induced stratification on the interaction between Eady edge waves,

$$K\mathrm{Ro} = 1.6\sqrt{1+\alpha^2}. \tag{6.100}$$

When vertical and horizontal mixing are described using the same characteristic turbulent velocity u_* and length scale, l, we have $\alpha \sim \mathrm{E} \sim u_*/(fl)$ (see Eq. (6.4)).

Fig. 6.11 shows the growth rate prediction from Eq. (6.98) with $\mathrm{E} = \alpha$, and $K\mathrm{Ro}$ set by the minimum of Eq. (6.99) and Eq. (6.100). The dashed line separates regions where the most unstable mode is controlled by horizontal mixing through Eq. (6.99) (the region below the line) and mixing-induced stratification through Eq. (6.100) (the region above the line). The symbols show typical parameters corresponding to winter and summer conditions based on the observations reported in Thompson *et al.* (2016) (see Table 6.1). In the winter when submesoscale activity was clearly observed, the size of the most unstable mode is limited by mixing-induced stratification and the growth rate from Eq. (6.98) is close to the inviscid prediction from Stone (1966). However, for parameters more typical of conditions during summer, Fig. 6.11 suggests that mixing associated with small-scale turbulence can limit the size and dramatically reduce the growth rate of the unstable modes. This result might help explain the apparent absence of submesoscale activity in the summer months.

For the inviscid Eady problem (here with $\alpha = 0$), the dominant source of energy for the growing baroclinic modes is the buoyancy flux. Here, we find that for relatively large mixing rates, the dominant energy balance is between the buoyancy flux and the dissipation associated with vertical mixing, with the small residual corresponding to the kinetic energy growth. Therefore the instability is driven by a transfer of potential energy to the growing perturbations, consistent with baroclinic instability, although now most of the energy is dissipated by vertical mixing, which acts to reduce the growth rate of the unstable modes.

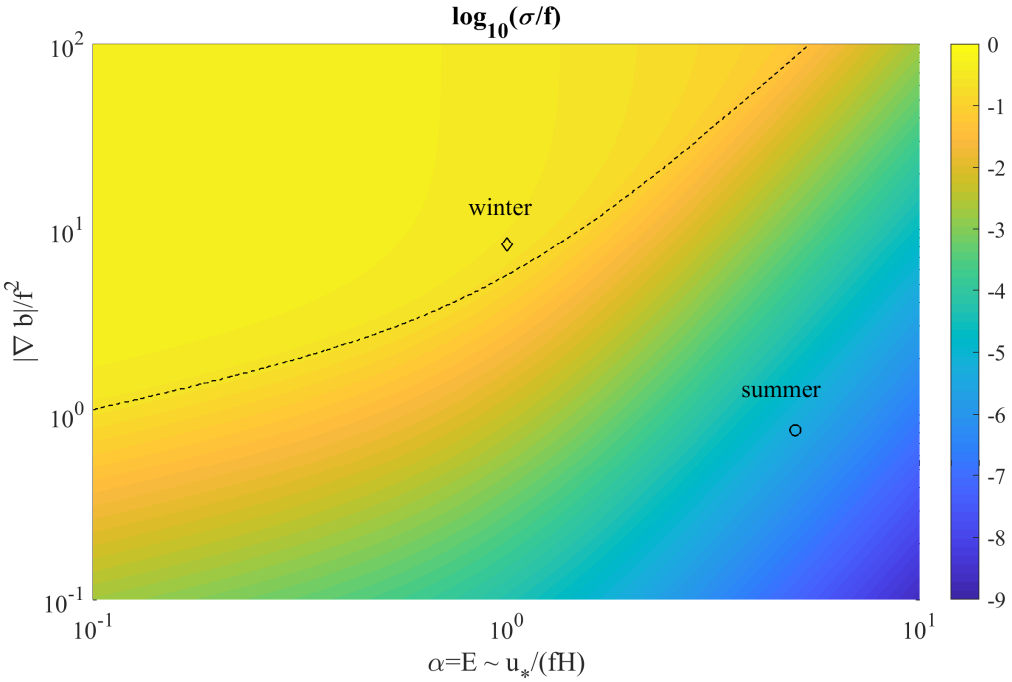

Fig. 6.11 Predicted growth rate of the most unstable modes from Eq. (6.98) where the wavenumber is set by the smaller of Eq. (6.99) and Eq. (6.100). The dashed line separates regions where the wavenumber is set by Eq. (6.99) (below the line) from regions where the wavenumber is set by Eq. (6.100) (above the line). The symbols indicate typical parameters from the OSMOSIS survey as reported in Thompson *et al.* (2016) in the winter and summer (see Table 6.1 for values).

For larger values of α and Ro, the numerical simulations show evidence of small scale modes with $l = \alpha k$ that are perpendicular to the predicted direction. These might be associated with the skew flux term in the leading order buoyancy equation (Eq. (6.24)) which cannot be neglected for large Ro and acts to destabilise modes with $l = \alpha k$. The energy budget suggests that these modes have a different energy source involving both the buoyancy flux and the shear production. These modes have not been studied in detail here since our theory is not valid for this range of parameters.

As noted above, the growth rate of the most unstable mode predicted from our theory matches the numerical simulations up to a Rossby number of about 0.1. This range includes many open ocean fronts. For example, based on a year-long timeseries from the OSMOSIS campaign, Thompson *et al.* (2016) found that the strongest fronts observed had $|\nabla b| \sim 10^{-7}\mathrm{s}^{-2}$. For mixed layer depths in the range $20 - 200$m and a horizontal scale between 20km, this corresponds to a Rossby number ranging from $0.01 - 0.1$. Stronger and/or sharper fronts such as the Gulf Stream (Thomas *et al.*,

Parameter	Symbol	Mahadevan *et al.* (N. Atl., spring)	Thompson *et al.* (N. Atl., summer)	Thompson *et al.* (N. Atl., winter)	Thomas *et al.* (Gulf Stream, winter)
Mixed layer depth	H (m)	300	20	200	100
Coriolis parameter	f (s^{-1})	1.3×10^{-4}	1.1×10^{-4}	1.1×10^{-4}	9.0×10^{-5}
Horiz. buoyancy grad.	$\lvert\nabla b\rvert$ (s^{-2})	7×10^{-9}	10^{-8}	10^{-7}	10^{-7}
Horizontal scale	L (km)	300	5	15	10
Turbulent velocity	u_* (m s^{-1})	10^{-2}	10^{-2}	2×10^{-2}	2×10^{-2}
Aspect ratio	ϵ	10^{-3}	4×10^{-3}	10^{-2}	10^{-2}
Rossby number	$\mathrm{Ro} = \frac{\lvert\nabla b\rvert}{f^2}\epsilon$	10^{-3}	4×10^{-3}	0.1	0.5
Relaxation ratio	$\alpha = \frac{u_*}{fH}$	0.3	5	1	1

Table 6.1 Estimates of physical scales and nondimensional parameters for three open ocean fronts as estimated based on observations reported in Mahadevan *et al.* (2012); Thompson *et al.* (2016); Thomas *et al.* (2013).

2013) are likely to be strongly influenced by the relatively large Rossby numbers characterising these fronts, and our results might not be applicable.

The turbulent thermal wind (TTW) model considered in Wenegrat & McPhaden (2016*a*); McWilliams (2017) and Chapter 3 used a large turbulent Ekman number instead of relaxation to represent mixed layer turbulence. As shown in Section C.3, the TTW model is also susceptible to the instability described here, and we expect that any turbulence parametrisation in which the leading order velocity is linear in the buoyancy gradient will exhibit the same instability.

Chapter 7

Conclusion

Fronts are ubiquitous features of the ocean mixed layer where they exist in the presence of an elevated level of small-scale turbulence due to surface forcing. Understanding the effects of turbulence on the evolution of mixed layer fronts will allow a better understanding of processes such as the vertical transport of biologically important nutrients and the transfer of tracers, such as heat and carbon, between the ocean and atmosphere.

An understanding of frontal dynamics will also allow an accurate prediction of frontal width, a parameter that is not currently well-understood, yet is important for parametrising processes including mixed layer instabilities and eddies (Fox-Kemper *et al.*, 2011; Bachman *et al.*, 2017). Due to the relatively low resolution required in climate models, the frontal width is typically not resolved, and hence an understanding of the scale-setting mechanisms will allow a more accurate parametrisation of mixed layer processes.

Instabilities in the surface mixed layer play a significant role in governing the formation and evolution of structures across a wide range of scales. For example, baroclinic instability can generate submesoscale eddies while restratifying the mixed layer (Fox-Kemper *et al.*, 2008). On the other hand, mixed layer instabilities can energise small-scale turbulence (Taylor & Ferrari, 2009; Taylor, 2016). Analytic studies of mixed layer instabilities have typically neglected the effects of small-scale turbulence; however, it is likely that the elevated levels of turbulence in the surface mixed layer act to modify the energy balance of these instabilities, leading to a growth rate that differs from previous predictions. Developing an understanding of the effects of turbulent processes on these instabilities will allow for better predictions of the energy budget in the upper ocean and hence in the global climate system.

Throughout this thesis we have used simple analytic models of mixed layer fronts with parametrised turbulence to address these questions. We now present a summary of our results and some areas for future work.

7.1 Summary of important results

7.1.1 Shear dispersive spreading a front by vertical mixing

In Chapter 3 we examined the effects of a large turbulent diffusivity on an isolated front. We found that the TTW secondary circulation drives a restratification of the mixed layer with the correlation between this restratification and the secondary circulation driving frontal spreading via shear dispersion. We derived a nonlinear diffusion equation for the depth-averaged buoyancy field which describes the spreading of the front and found similarity solutions that closely match our numerical solutions. The rate of frontal spreading is much larger than would result from even a large horizontal diffusivity so our results may allow more accurate predictions of the effective diffusivity required in ocean models that do not fully resolve frontal structures.

Near the edges of the front, the secondary circulation manifests as thin bands of intense vertical velocity corresponding to regions of high curvature in the cross-front buoyancy profile. The large vertical velocity within these bands could contribute to the vertical transport of biological nutrients and other important tracers.

In Chapter 4 we used numerical simulations of the full nonlinear equations to verify the theory presented in Chapter 3. We found that our predictions are valid for a much wider range of parameters than would be expected from the asymptotic regime. Remarkably, numerical results for order 1 Rossby numbers, well beyond the asymptotic regime, were found to agree with the predicted spreading rates and cross-front profiles. The largest discrepancies between the numerics and theory were found to occur for small E where the appearance of along-front jets modifies the absolute vorticity of the system. A modified solution was presented to account for this effect.

We observed some surface frontogenesis for large Rossby numbers and small Ekman numbers. However this did not significantly affect the evolution and was soon arrested as the front approached a balanced state and began to spread via shear dispersion. We predict that external forcing is required to maintain this phase of frontogenesis to the point of frontal collapse in an isolated front. It should be noted that spontaneous frontogenesis has been observed in the case of an unforced filament (Sullivan &

McWilliams, 2018) which may be viewed as the interaction of two fronts with opposing buoyancy gradients.

Using a scaling argument we estimated the magnitude of the vertical velocity and tested our predictions using the numerical simulations. Our scalings are found to be consistent with the numerics and give values similar to those found in observations and models; this suggests that the TTW secondary circulation significantly contributes to the frontal circulation and hence is important for the vertical transport of tracers in the surface mixed layer.

7.1.2 Spreading and sharpening of a front forced by surface wind stress and buoyancy flux

In Chapter 5 we considered the effects of a surface wind stress and buoyancy flux on an isolated front by including surface forcing terms in the turbulent diffusivity model. We found that wind stress can act to either spread or sharpen a front depending on the direction of the wind with respect to the front. If the wind-driven flow is able to oppose and overcome the cross-front TTW flow then it will drive an up-gradient flux of buoyancy which may lead to frontal sharpening. On the other hand, a wind stress-driven flow that reinforces the cross-front TTW flow will drive enhanced spreading. A positive surface buoyancy flux was shown to drive frontal spreading through the correlation between a stable stratification and large vertical velocity. The case of a negative buoyancy flux was not considered as we did not model the effects of convection. However, we predict that a negative buoyancy flux would act to enhance mixed layer turbulence and hence lead to an enhanced spreading through the mechanism described in Chapter 3.

By considering the form of the effective horizontal diffusivity we found that fronts cannot sharpen indefinitely and will approach a regime where the cross-front TTW velocity balances the wind stress driven flow; this process results in an equilibrium frontal width and may provide a mechanism for maintaining fronts over long times. Scalings for this frontal width are presented and may be useful for parametrising frontal strength in large-scale models that do not resolve submesoscale structures such as global ocean models.

7.1.3 Baroclinic instability in the presence of vertical mixing

In Chapter 6 we used a vertical relaxation scheme to examine baroclinic instability in a strongly turbulent layer. We found that the effect of vertical mixing is to tilt the modes at an angle to the cross front direction with the angle defined in terms of the relaxation ratio. Strong turbulent mixing also acts to reduce the growth rate by dissipating large amounts of potential energy.

To test our predictions we performed 3 dimensional numerical simulations of the full nonlinear equations. We found that our theory is accurate for small Rossby numbers. However for Rossby numbers greater than around Ro ~ 0.1, new modes appear that do not match the predicted growth rate, direction or energetics. It is likely that these modes result from the neglected $O(\mathrm{Ro})$ shear dispersive terms in the buoyancy evolution equation which become important for high wavenumbers.

In the case of very small Rossby number, we found that the most unstable mode is set by horizontal diffusion. For larger Rossby numbers this is not the case and the most unstable mode is set by the Eady mechanism of interacting edge waves (Eady, 1949). We found that our theory accurately predicts the growth rate for a wide range of Rossby numbers given the most unstable mode. This suggests that the process setting the most unstable mode does not significantly alter the growth rate.

Using physical parameters we determined that this model may be relevant to relatively weak ocean fronts where the Rossby number is small. Using our growth rate calculation for the North Atlantic fronts observed by Thompson *et al.* (2016), we predict much larger growth rates during the winter compared with the summer. This prediction may help explain the apparent absence of submesoscale activity during the summer months.

While the results in Chapter 6 are derived using a vertical relaxation scheme, the same conclusions hold for the viscous diffusivity model. Predictions for the growth rate and fastest growing mode using the viscous diffusivity parametrisation are shown in Section C.3.

7.2 General TTW solution

For completeness we have calculated the general solution to the model presented in Chapter 2 (see Eq. (3.1)); our results are shown in Section D.1. This solution is valid for any linear turbulence parametrisation that depends only on z as well as any surface

forcing consistent with that parametrisation. The solutions presented in Chapters 3 – 6 can be derived as special cases of this solution.

This model describes the evolution of a fluid layer in terms of 2 dimensional buoyancy and vorticity which describe the depth-averaged flow. The effects of vertical mixing and surface forcing are parametrised through flux terms. Once the solutions for the depth-averaged fields have been found, the full 3 dimensional solutions can be calculated using the expressions for the full velocity and buoyancy. As shown in Chapter 6 and Section C.3, this system is susceptible to baroclinic instability. However other frontal processes will need to be parametrised and included separately. For example symmetric instability will likely be suppressed or modified by the leading order turbulent effects but could be parametrised using additional flux terms in the momentum and buoyancy equations (Taylor & Ferrari, 2010). Similarly the effects of a nonlinear Ekman buoyancy flux (Thomas & Lee, 2005) are not included due to the assumption that the Rossby number associated with the background flow is not significantly larger than that associated with the TTW velocity. Inclusion of the background flow at a higher order would allow this effect to be considered.

Overall this system may prove useful for simulating a mixed layer in TTW balance. However, we do not necessarily expect it to be accurate for cases in which the Rossby number is large or there are significant contributions from effects that are not well described by our TTW model.

7.3 Future work

In our unforced model of a turbulent front, the only mechanism driving frontogenesis is the TTW circulation. Even for order 1 Rossby numbers this effect is not enough to drive significant frontal sharpening as shown in Chapter 4. This suggests that external processes are important for driving frontal sharpening so an area for future work is to study the effects of including these processes. One example of a process that can drive frontogenesis is deformation by an externally imposed strain flow. This background flow field has been used to study frontal systems in both analytic and numerical models (Hoskins & Bretherton, 1972; McWilliams, 2017; Shakespeare & Taylor, 2013) and could be incorporated into our TTW model. The inclusion of frontogenetic processes would allow us to study whether TTW shear dispersion could act to arrest frontogenesis.

In our model we have assumed that the turbulent mixing is independent of time and depends only on the depth, (z). Physically we expect the turbulence to have some

spatial dependence in the cross-front direction due to small-scale frontal processes. For example, recent observations have found that turbulence can be significantly enhanced at strong fronts (D'Asaro *et al.*, 2011; Thomas *et al.*, 2013; Johnston *et al.*, 2011). On the other hand, frontal restratification can act to suppress turbulent mixing (Taylor, 2016; Taylor & Ferrari, 2010). While these effects are not well understood, it is likely that the level of turbulence varies across a front and also evolves in time along with the front. This would lead to a coupled response between frontal dynamics and turbulence that cannot be described by our simple parametrisations. One area for future work would be to extend our TTW model to include turbulent parametrisations with temporal and spatial dependence though the resulting system would likely have to be solved numerically. The use of large eddy simulations (LES) would also allow a coupled response to be studied and would include the effects of small scale instabilities and surface forcing.

As well as providing a more realistic representation of turbulent processes, LES would allow us to test our predictions from Chapter 5 regarding the effects of surface processes. Additionally, LES would allow the effects of negative buoyancy flux and the resulting convective instability to be studied.

In Chapter 6, we examined the effects of turbulent mixing on baroclinic instability. While many of our predictions were supported by numerical simulations, there were some phenomenon that our model did not explain. These include the unknown mechanism setting the most unstable mode and the appearance of additional modes at higher Rossby numbers. Whilst we were able to make predictions that might explain these observations, an area of future work would be to study this system in more detail using either numerical simulations or a simple finite Rossby number model.

As described in Section 7.2, our model can be generalised to include processes such as symmetric instability (Taylor & Ferrari, 2010), nonlinear Ekman buoyancy flux (Thomas & Lee, 2005) and strain-induced frontogenesis (Hoskins & Bretherton, 1972). The development of a simple model unifying these processes would be an important step in understanding the formation, evolution and breakdown of ocean fronts.

References

Bachman, S.D., Fox-Kemper, B., Taylor, J.R. & Thomas, L.N. 2017 Parameterization of frontal symmetric instabilities. i: Theory for resolved fronts. *Ocean Modelling* **109**, 72 – 95.

Blumen, W. 2000 Inertial oscillations and frontogenesis in a zero potential vorticity model. *J. Phys. Oceanogr.* **30**, 31–39.

Boccaletti, Giulio, Ferrari, Raffaele & Fox-Kemper, Baylor 2007 Mixed layer instabilities and restratification. *J. Phys. Oceanogr.* **37** (9), 2228–2250.

de Boyer Montégut, C., Madec, G., Fischer, A. S., Lazar, A. & Iudicone, D. 2004 Mixed layer depth over the global ocean: An examination of profile data and a profile-based climatology. *J. Geophys. Res.* **109**.

Callies, Jörn & Ferrari, Raffaele 2013 Interpreting energy and tracer spectra of upper-ocean turbulence in the submesoscale range (1–200 km). *J. Phys. Oceanogr.* **43** (11), 2456–2474.

Callies, Jörn, Ferrari, Raffaele, Klymak, Jody M & Gula, Jonathan 2015 Seasonality in submesoscale turbulence. *Nature communications* **6**, 6862.

Callies, J., Flierl, G., Ferrari, R. & Fox-Kemper, B. 2016 The role of mixed-layer instabilities in submesoscale turbulence. *J. Fluid Mech.* **788**, 5–41.

Capet, X, Campos, EJ & Paiva, AM 2008*a* Submesoscale activity over the argentinian shelf. *Geophys. Res. Lett.* **35** (15).

Capet, X., McWilliams, J. C., Molemaker, M. J. & Shchepetkin, A. F. 2008*b* Mesoscale to submesoscale transition in the california current system. part ii: Frontal processes. *J. Phys. Oceanogr.* **38**, 44–64.

Charney, J. G. 1973 *Planetary Fluid Dynamics*, chap. Symmetric Circulations in Idealized Models, pp. 128–141. D. Reidel Publishing Company.

Cronin, Meghan F & Kessler, William S 2009 Near-surface shear flow in the tropical pacific cold tongue front. *J. Phys. Oceanogr.* **39** (5), 1200–1215.

D'Asaro, Eric, Lee, Craig, Rainville, Luc, Harcourt, Ramsey & Thomas, Leif 2011 Enhanced turbulence and energy dissipation at ocean fronts. *science* **332** (6027), 318–322.

Eady, E. T. 1949 Long waves and cyclone waves. *Tellus* **1**, 33–52.

Eliassen, A. 1962 On the vertical circulation in frontal zones. *Geofys. Publ.* **24** (4), 147–160.

Enriquez, R. M. & Taylor, J. R. 2015 Shutdown of turbulent convection as a new criterion for the onset of spring phytoplankton blooms. *ICES J. Mar. Sci.* Fsv071.

Erdogan, M. E. & Chatwin, P. C. 1967 The effects of curvature and buoyancy on the laminar dispersion of solute in a horizontal tube. *J. Fluid Mech.* **29**, 465–484.

Ferrari, R. 2011 A frontal challenge for climate models. *Science* **332** (6027), 316–317.

Ferrari, R. & Young, W. R. 1997 On the development of thermohaline correlations as a result of nonlinear diffusive parameterizations. *J. Mar. Res.* **55**, 1069–1101.

Fox-Kemper, Baylor, Danabasoglu, Gokhan, Ferrari, Raffaele, Griffies, SM, Hallberg, RW, Holland, MM, Maltrud, ME, Peacock, S & Samuels, BL 2011 Parameterization of mixed layer eddies. iii: Implementation and impact in global ocean climate simulations. *Ocean Modelling* **39** (1-2), 61–78.

Fox-Kemper, Baylor, Ferrari, Raffaele & Hallberg, Robert 2008 Parameterization of mixed layer eddies. part i: Theory and diagnosis. *J. Phys. Oceanogr.* **38** (6), 1145–1165.

Garrett, C. J. R. & Loder, J. W. 1981 Dynamical aspects of shallow sea fronts. *Phil. Trans. R. Soc. Lond. A* **302**, 563–581.

Gula, J., Molemaker, M. J. & McWilliams, J. C. 2014 Submesoscale cold filaments in the gulf stream. *J. Phys. Oceanogr.* **44**, 2617–2643.

Holton, J. R. & Hakim, G. J. 2012 *An introduction to dynamic meteorology: volume 88*, 5th edn. Academic press.

Hoskins, B. J. 1982 The mathematical theory of frontogenesis. *Annu. Rev. Fluid Mech.* **14**, 131–151.

Hoskins, B. J. & Bretherton, F. P. 1972 Atmospheric frontogenesis models: Mathematical formulation and solution. *J. Atmos. Sci.* **29**, 11–37.

Johnston, TM, Rudnick, Daniel L & Pallàs-Sanz, E 2011 Elevated mixing at a front. *J.Geophys. Res.: Oceans* **116** (C11).

Kato, H. & Phillips, O. M. 1969 On the penetration of a turbulent layer into stratified fluid. *J. Fluid Mech.* **37**, 643–655.

Large, W. G., McWilliams, J. C. & Doney, S. C. 2011 Oceanic vertical mixing: a review and a model with a nonlocal boundary layer parameterization. *Rev. Geophys.* **32**, 363–403.

Lorbacher, Katja, Dommenget, Dietmar, Niiler, PP & Köhl, A 2006 Ocean mixed layer depth: A subsurface proxy of ocean-atmosphere variability. *J. Geophys. Res.: Oceans* **111** (C7).

Mahadevan, Amala, D'asaro, Eric, Lee, Craig & Perry, Mary Jane 2012 Eddy-driven stratification initiates north atlantic spring phytoplankton blooms. *Science* **337** (6090), 54–58.

Mahadevan, Amala & Tandon, Amit 2006 An analysis of mechanisms for submesoscale vertical motion at ocean fronts. *Ocean Modelling* **14** (3-4), 241–256.

McWilliams, J. C. 2016 Submesoscale currents in the ocean. *Proc. R. Soc. A* **472**.

McWilliams, J. C. 2017 Submesoscale surface fronts and filaments: secondary circulation, buoyancy flux, and frontogenesis. *J. Fluid Mech.* **823**, 391–432.

McWilliams, J. C., Gula, J., Molemaker, M. J., Renault, L. & Shchepetkin, A. F. 2015 Filament frontogenesis by boundary layer turbulence. *J. Phys. Oceanogr.* **45**, 1988–2005.

Mensa, Jean Alberto, Garraffo, Zulema, Griffa, Annalisa, Özgökmen, Tamay Mehmet, Haza, Angelique & Veneziani, Milena 2013 Seasonality of the submesoscale dynamics in the gulf stream region. *Ocean Dynamics* **63** (8), 923–941.

NASA/Ocean Biology Processing Group, NASA Goddard Space Flight Center 2016 The turbulent north atlantic. https://www.nasa.gov/image-feature/the-turbulent-north-atlantic, [Online; accessed October 31, 2018].

Niiler, P. P. 1969 On the ekman divergence in an oceanic jet. *J. Geophys. Res.* **74** (28), 7048–7052.

Orlanski, I. & Ross, B. B. 1977 The circulation associated with a cold front: Part i: Dry case. *J. Atmos. Sci.* **34**, 1619–1633.

Ostdiek, V. & Blumen, W. 1997 A dynamic trio: Inertial oscillation, deformation frontogenesis, and the Ekman-Taylor boundary layer. *J. Atmos. Sci.* **54**, 1490–1502.

Rippeth, Tom P., Palmer, Matthew R., Simpson, John H., Fisher, Neil R. & Sharples, Jonathan 2005 Thermocline mixing in summer stratified continental shelf seas. *Geophys. Res. Lett.* **32** (5).

Rudnick, Daniel L & Ferrari, Raffaele 1999 Compensation of horizontal temperature and salinity gradients in the ocean mixed layer. *Science* **283** (5401), 526–529.

Rudnick, D. L. & Luyten, J. R. 1996 Intensive surveys of the azores front: 1. tracers and dynamics. *J. Geophys. Res.* **101**, 923–939.

Salmon, Rick 1998 *Lectures on geophysical fluid dynamics*. Oxford University Press.

Sasaki, Hideharu, Klein, Patrice, Qiu, Bo & Sasai, Yoshikazu 2014 Impact of oceanic-scale interactions on the seasonal modulation of ocean dynamics by the atmosphere. *Nature communications* **5**, ncomms6636.

Schumann, Ulrich & Gerz, Thomas 1995 Turbulent mixing in stably stratified shear flows. *J. App. Met.* **34** (1), 33–48.

Shakespeare, C. J. & Taylor, J.R. 2013 A generalized mathematical model of geostrophic adjustment and frontogenesis: uniform potential vorticity. *J. Fluid Mech.* **736**, 366–413.

Shay, T. J. & Gregg, M. C. 1986 Convectively driven turbulent mixing in the upper ocean. *J. Phys. Oceanogr.* **16**, 1777–1798.

Smith, R. 1982 Similarity solutions of a non-linear diffusion equation. *IMA J. App. Math.* **28** (2), 149–160.

Stern, M. E. 1965 Interaction of a uniform wind stress with a geostrophie vortex. *Deep-Sea Res.* **12**, 355–367.

Stone, P. H. 1966 On non-geostrophic baroclinic stability. *J. Atmos. Sci.* **23**, 390–400.

Sullivan, P. P. & McWilliams, J. C. 2018 Frontogenesis and frontal arrest of a dense filament in the oceanic surface boundary layer. *J. Fluid Mech.* **837**, 1341–1380.

Sverdrup, HU 1953 On vernal blooming of phytoplankton. *Conseil Exp. Mer* **18**, 287–295.

Tandon, Amit & Garrett, Chris 1994 Mixed layer restratification due to a horizontal density gradient. *J. Phys. Oceanogr.* **24** (6), 1419–1424.

Taylor, G. I. 1953 Dispersion of soluble matter in solvent flowing slowly through a tube. *Proc. Roy. Soc. A.* **219**, 186–203.

Taylor, J.R. & Ferrari, R. 2009 On the equilibration of a symmetrically unstable front via a secondary shear instability. *J. Fluid Mech.* **622**, 103–113.

Taylor, J. R. 2008 Numerical simulations of the stratified oceanic bottom boundary layer. PhD thesis, University of California, San Diego.

Taylor, J. R. 2016 The influence of submesoscale restratification and convection on light-limited phytoplankton growth. *Geophys. Res. Lett.* 2016GL069106.

Taylor, J. R. & Ferrari, R. 2010 Buoyancy and wind-driven convection at mixed layer density fronts. *J. Phys. Oceanogr.* **40**, 1222–1242.

Taylor, J. R. & Ferrari, R. 2011 Numerical simulations of the competition between wind-driven mixing and surface heating in triggering spring phytoplankton blooms. *Limnol. Oceanogr.* **56** (6), 2293–2307.

Thomas, L. N. & Ferrari, R. 2008 Friction, frontogenesis, and the stratification of the surface mixed layer. *J. Phys. Oceanogr.* **38**, 2501–2518.

Thomas, L. N. & Lee, C. M. 2005 Intensification of ocean fronts by down-front winds. *J. Phys. Oceanogr.* **35**, 1086–1102.

Thomas, Leif N, Tandon, Amit & Mahadevan, Amala 2008 Submesoscale processes and dynamics. *Ocean modeling in an Eddying Regime* **177**, 17–38.

Thomas, Leif N, Taylor, John R, Ferrari, Raffaele & Joyce, Terrence M 2013 Symmetric instability in the gulf stream. *Deep Sea Research Part II: Topical Studies in Oceanography* **91**, 96–110.

Thompson, Andrew F., Lazar, Ayah, Buckingham, Christian, Naveira Garabato, Alberto C., Damerell, Gillian M. & Heywood, Karen J. 2016 Open-ocean submesoscale motions: A full seasonal cycle of mixed layer instabilities from gliders. *J. Phys. Oceanogr.* **46** (4), 1285–1307.

Thompson, LuAnne 2000 Ekman layers and two-dimensional frontogenesis in the upper ocean. *J. Geophys. Res.: Oceans* **105** (C3), 6437–6451.

Thorpe, Steve A 2005 *The turbulent ocean*. Cambridge University Press.

Vallis, G. K. 2006 *Atmospheric and Oceanic Fluid Dynamics*. Cambridge University Press.

Venayagamoorthy, Subhas K & Stretch, Derek D 2010 On the turbulent prandtl number in homogeneous stably stratified turbulence. *J. Fluid Mech.* **644**, 359–369.

Wenegrat, J. O. & McPhaden, M. J. 2016*a* A simple analytical model of the diurnal ekman layer. *J. Phys. Oceanogr.* **46** (9), 2877–2894.

Wenegrat, J. O. & McPhaden, M. J. 2016*b* Wind, waves, and fronts: Frictional effects in a generalized ekman model. *J. Phys. Oceanogr.* **46** (2), 371–394.

Young, W. R. 1994 The subinertial mixed layer approximation. *J. Phys. Oceanogr.* **24**, 1812–1826.

Young, W. R. & Chen, L. 1995 Baroclinic instability and thermohaline gradient alignment in the mixed layer. *J. Phys. Oceanogr.* **25**, 3172–3185.

Young, W. R. & Jones, S. 1991 Shear dispersion. *Phys. Fluids A* **3** (5), 1087–1101.

Young, W. R., Rhines, P. B & Garrett, C. J. R. 1982 Shear-flow dispersion, internal waves and horizontal mixing in the ocean. *J. Phys. Oceanogr.* **12**, 515–527.

Appendix A

A.1 Analytic solution for the O(1) velocity for constant viscosity

Here we present the solution for the vertical structure functions K_0 and $\mathcal{Z}_n$ used in Chapters 3. We assume constant viscosity, $\nu = 1$, to find an analytic solution for the structure function K_0. Eq. (3.18) becomes

$$-K_0^{(4)} = K_0 + \zeta, \tag{A.1}$$

with boundary conditions $K_0' = K_0''' = 0$ at $\zeta = \pm\zeta_0$ where $\zeta_0 = 1/\sqrt{4\mathrm{E}}$. This is a fourth order ordinary differential equation which can be solved analytically. The exponents of the independent solutions are $(1 \pm i)/\sqrt{2}$ and $(-1 \pm i)/\sqrt{2}$ so, since the system is clearly odd in ζ, we use symmetry to obtain the solution

$$K_0 = -\zeta + C_+ \,\mathrm{cs}(\zeta) + C_- \,\mathrm{sc}(\zeta), \tag{A.2}$$

where

$$\begin{aligned} \mathrm{cc}(\zeta) &= \cosh\left(\zeta/\sqrt{2}\right)\cos\left(\zeta/\sqrt{2}\right), \\ \mathrm{cs}(\zeta) &= \cosh\left(\zeta/\sqrt{2}\right)\sin\left(\zeta/\sqrt{2}\right), \\ \mathrm{ss}(\zeta) &= \sinh\left(\zeta/\sqrt{2}\right)\sin\left(\zeta/\sqrt{2}\right), \\ \mathrm{sc}(\zeta) &= \sinh\left(\zeta/\sqrt{2}\right)\cos\left(\zeta/\sqrt{2}\right). \end{aligned} \tag{A.3}$$

From the boundary conditions, $K_0'(\zeta_0) = K_0'''(\zeta_0) = 0$, we get

$$\begin{pmatrix} \mathrm{cc}(\zeta_0) + \mathrm{ss}(\zeta_0) & \mathrm{cc}(\zeta_0) - \mathrm{ss}(\zeta_0) \\ \mathrm{cc}(\zeta_0) - \mathrm{ss}(\zeta_0) & -\mathrm{cc}(\zeta_0) - \mathrm{ss}(\zeta_0) \end{pmatrix} \begin{pmatrix} C_+ \\ C_- \end{pmatrix} = \begin{pmatrix} \sqrt{2} \\ 0 \end{pmatrix}, \tag{A.4}$$

which we invert to get

$$C_{\pm} = \frac{1}{\sqrt{2}} \frac{\mathrm{cc}(\zeta_0) \pm \mathrm{ss}(\zeta_0)}{\mathrm{cc}^2(\zeta_0) + \mathrm{ss}^2(\zeta_0)}. \tag{A.5}$$

We can also solve for $\mathcal{Z}_n$ analytically using Eq. (3.24) which reduces to

$$\frac{\partial^2 \mathcal{Z}_n}{\partial z^2} = -\lambda_n \mathcal{Z}_n. \tag{A.6}$$

We obtain solutions

$$\mathcal{Z}_n(z) = \begin{cases} 1, & n = 0, \\ (-1)^{(n-1)/2} \sin[n\pi z], & n \text{ odd}, \\ (-1)^{n/2} \cos[n\pi z], & n \text{ even}, \end{cases} \tag{A.7}$$

for

$$\lambda_n = n^2 \pi^2, \tag{A.8}$$

and

$$z_n^2 = \begin{cases} 1, & n = 0, \\ \frac{1}{2}, & n \in \mathbb{N}, \end{cases} \tag{A.9}$$

and integrate to get

$$\int_{-1/2}^{z} \mathcal{Z}_n(z')dz' = \begin{cases} z + \frac{1}{2}, & n = 0 \\ (-1)^{(n+1)/2} \frac{\cos[(1+2n)\pi z]}{n\pi}, & n \text{ odd}, \\ (-1)^{n/2} \frac{\sin[(1+2n)\pi z]}{n\pi}, & n \text{ even}. \end{cases} \tag{A.10}$$

We plot K_0 and $\mathcal{Z}_n$ in Section A.3 when considering the numerical solutions for general ν: see Fig. A.3 and Fig. A.4(a,b).

We now consider the Ekman number dependence of K_0 in the case of constant ν and κ, and Pr = 1. We find that there are regimes for small and large E where the maximum values of K_0 and its derivatives obey power law dependences on E. These are given in Table A.1 and can be calculated by expanding Eq. (A.2) for small and large E.

The maximum values for K_0 and K_0'' occur at the boundaries as the horizontal velocity is highest at the surface while the maximum for K_0' occurs in the interior of the vertical domain corresponding to the location of the maximum vertical velocity.

Function	$K_0(\zeta)$	$K_0'(\zeta)$	$K_0''(\zeta)$	$\sqrt{\mathrm{E}}K_0(\zeta)$	$\mathrm{E}K_0'(\zeta)$	$\sqrt{\mathrm{E}}K_0''(\zeta)$
Small E	$\mathrm{E}^{-1/2}$	1	1	1	E	$\mathrm{E}^{1/2}$
Large E	$\mathrm{E}^{-5/2}$	E^{-2}	$\mathrm{E}^{-3/2}$	E^{-2}	E^{-1}	E^{-1}

Table A.1 The Ekman number dependence of the maximum values of $K_0(\zeta)$, $K_0'(\zeta)$, $K_0''(\zeta)$, $\sqrt{\mathrm{E}}K_0(\zeta)$, $\mathrm{E}K_0'(\zeta)$ and $\sqrt{\mathrm{E}}K_0''(\zeta)$ for $\zeta = z/\sqrt{\mathrm{E}}$ in the case of small and large E. Here we ignore any constant coefficients.

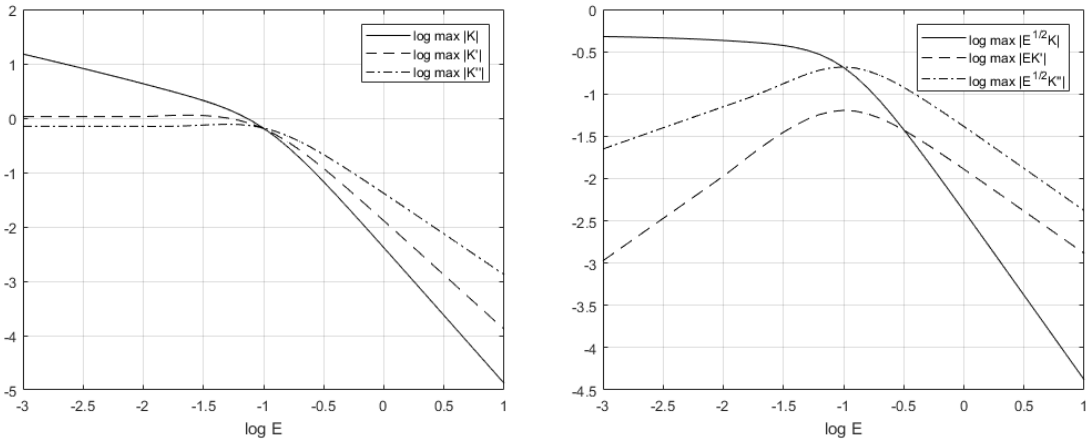

(a) (b)

Fig. A.1 Logarithmic plots of the maximum magnitude as a function of Ekman number of (a): $K_0(\zeta)$, $K_0'(\zeta)$ and $K_0''(\zeta)$ and (b): $\sqrt{\mathrm{E}}K_0(\zeta)$, $\mathrm{E}K_0'(\zeta)$ and $\sqrt{\mathrm{E}}K_0''(\zeta)$ for $\zeta = z/\sqrt{\mathrm{E}}$.

Fig. A.1 shows logarithmic plots of the maximum magnitude of $K_0(\zeta)$, $K_0'(\zeta)$, $K_0''(\zeta)$, $\sqrt{\mathrm{E}}K_0(\zeta)$, $\mathrm{E}K_0'(\zeta)$ and $\sqrt{\mathrm{E}}K_0''(\zeta)$ as functions of the Ekman number. We can see that for small E the along-front velocity, proportional to $\sqrt{\mathrm{E}}\,K_0$, approaches a constant value corresponding to the surface velocity from the thermal wind balance profile. The cross-front and vertical velocities tend to zero for small E in agreement with thermal wind balance. For large E all velocity components become small as motion is damped by the high viscosity. We note that there is a maximum for both the vertical and the cross-front velocities at $\mathrm{E} \approx 0.1$. Analytically, we can show that

$$K_0' \sim \begin{cases} -1, & \mathrm{E} \ll 1, \\ \frac{1}{\mathrm{E}^2}\left[\frac{z^2-1/4}{16} - \frac{z^4-1/16}{24}\right], & \mathrm{E} \gg 1, \end{cases} \tag{A.11}$$

hence,

$$Q(\mathrm{E}) \sim \begin{cases} \mathrm{E}, & \mathrm{E} \ll 1, \\ \frac{31}{362880}\mathrm{E}^{-3}, & \mathrm{E} \gg 1, \end{cases} \tag{A.12}$$

in agreement with Fig. 3.6.

A.2 Solution for M with arbitrary viscosity and diffusivity

To solve for M with arbitrary ν and κ, we take the Laplace transform of Eq. (3.39) to get

$$\left[s - \frac{\mathrm{E}}{\mathrm{Pr}}\frac{\partial}{\partial z}\left(\kappa\frac{\partial}{\partial z}\right)\right]\widetilde{M}(z,s) - M(z,0) = \widetilde{P}(z,s), \tag{A.13}$$

where we take $M(z,0) = \mathcal{M}(z)$ as our initial state. We usually take $\mathcal{M} = 0$ corresponding to a depth-independent front: if we were instead to consider a balanced initial setup, the solution would be given by the steady-state solution, M_0. The forcing term, $\widetilde{P}$ is given by

$$\widetilde{P}(z,s) = \left[s - \mathrm{E}\frac{\partial}{\partial z}\left(\nu\frac{\partial}{\partial z}\right)\right]\widetilde{K}(z,s) - \mathcal{K}(z), \tag{A.14}$$

where we can use Eq. (3.28) to write

$$\widetilde{K}(z,s) = \frac{1}{s}K_0\left(z/\sqrt{\mathrm{E}}\right) + \sum_{n=0}^{\infty} B_n\left[\frac{s+2\mathrm{E}\lambda_n}{(s+\mathrm{E}\lambda_n)^2+1}\right]\mathcal{Z}_n(z), \tag{A.15}$$

so

$$\widetilde{P}(z,s) = [K_0 - \mathcal{K}] - \frac{1}{s}\mathrm{E}\frac{\partial}{\partial z}\left(\nu\frac{\partial K_0}{\partial z}\right) + \sum_{n=0}^{\infty} B_n\left[\frac{(s+\mathrm{E}\lambda_n)(s+2\mathrm{E}\lambda_n)}{(s+\mathrm{E}\lambda_n)^2+1}\right]\mathcal{Z}_n(z). \tag{A.16}$$

We note that

$$K_0 - \mathcal{K} = -\sum_{n=0}^{\infty} B_n\mathcal{Z}_n(z), \tag{A.17}$$

hence,

$$\widetilde{P}(z,s) = -\frac{1}{s}\mathrm{E}\frac{\partial}{\partial z}\left(\nu\frac{\partial K_0}{\partial z}\right) + \sum_{n=0}^{\infty} B_n\left[\frac{\mathrm{E}\lambda_n(s+\mathrm{E}\lambda_n)-1}{(s+\mathrm{E}\lambda_n)^2+1}\right]\mathcal{Z}_n(z). \tag{A.18}$$

We now write

$$\widetilde{M} = \sum_{n=0}^{\infty}\widetilde{C}_n(s)\mathcal{Y}_n(z), \tag{A.19}$$

where the eigenfunctions, $\mathcal{Y}_n$, are given by

$$\frac{\partial}{\partial z}\left(\kappa\frac{\partial \mathcal{Y}_n}{\partial z}\right) = -\mu_n \mathcal{Y}_n, \tag{A.20}$$

for eigenvalues μ_n where $n = 0, 1, 2, \ldots$. We also define the orthogonality relation

$$\int_{-1/2}^{1/2} \mathcal{Y}_n \mathcal{Y}_m dz = y_n^2 \delta_{nm}, \tag{A.21}$$

for constant y_n representing the normalisation of $\mathcal{Y}_n$.

We can expand $\widetilde{P}$ and $\mathcal{M}$ in the basis $\mathcal{Y}_n$, so Eq. (A.13) becomes

$$\sum_{n=0}^{\infty}\left(s + \frac{\mathrm{E}}{\mathrm{Pr}}\mu_n\right)\widetilde{C}_n(s)\mathcal{Y}_n(z) = \sum_{n=0}^{\infty}\left(M_n + \widetilde{E}_n(s)\right)\mathcal{Y}_n(z), \tag{A.22}$$

where

$$\widetilde{E}_n(s) = \frac{1}{y_n^2}\int_{-1/2}^{1/2}\widetilde{P}(z,s)\mathcal{Y}_n(z)dz. \tag{A.23}$$

and

$$M_n = \frac{1}{y_n^2}\int_{-1/2}^{1/2}\mathcal{M}(z)\mathcal{Y}_n(z)dz. \tag{A.24}$$

Using the orthogonality relation, Eq. (A.21), we obtain

$$\widetilde{C}_n(s) = \frac{M_n + \widetilde{E}_n(s)}{s + \frac{\mathrm{E}}{\mathrm{Pr}}\mu_n}, \tag{A.25}$$

and hence

$$M = \sum_{n=0}^{\infty} C_n(\tau)\mathcal{Y}_n(z), \tag{A.26}$$

where the functions $C_n(\tau)$ are obtained as the inverse Laplace transforms of the functions $\widetilde{C}_n(s)$, i.e.

$$C_n(\tau) = \mathcal{L}^{-1}\widetilde{C}_n(s). \tag{A.27}$$

We can write $\widetilde{E}_n(s)$ as

$$\begin{aligned}\widetilde{E}_n(s) = \frac{\mathrm{E}\mu_n}{s}\frac{1}{y_n^2}\int_{-1/2}^{1/2}\left[\int_{-1/2}^{z}\frac{\nu}{\kappa}\frac{\partial K_0}{\partial z'}dz'\right]\mathcal{Y}_n dz \\ + \sum_{m=0}^{\infty} B_m\left[\frac{\mathrm{E}\lambda_m(s+\mathrm{E}\lambda_m)-1}{(s+\mathrm{E}\lambda_m)^2+1}\right]\frac{1}{y_n^2}\int_{-1/2}^{1/2}\mathcal{Z}_m\mathcal{Y}_n dz,\end{aligned} \tag{A.28}$$

where we have used integration by parts on the first term to write

$$\int_{-1/2}^{1/2} \frac{\partial}{\partial z}\left(\nu \frac{\partial K_0}{\partial z}\right) \mathcal{Y}_n dz = -\mu_n \int_{-1/2}^{1/2} \left[\int_{-1/2}^{z} \frac{\nu}{\kappa} \frac{\partial K_0}{\partial z'} dz'\right] \mathcal{Y}_n dz. \tag{A.29}$$

Hence,

$$\begin{aligned} \widetilde{C}_n(s) = {} & \frac{M_n}{s + \frac{\mathrm{E}}{\mathrm{Pr}}\mu_n} + \frac{\mathrm{E}\mu_n}{s\left(s + \frac{\mathrm{E}}{\mathrm{Pr}}\mu_n\right)} \frac{1}{y_n^2} \int_{-1/2}^{1/2} \left[\int_{-1/2}^{z} \frac{\nu}{\kappa} \frac{\partial K_0}{\partial z'} dz'\right] \mathcal{Y}_n dz \\ & + \sum_{m=0}^{\infty} B_m \left[\frac{\mathrm{E}\lambda_m(s + \mathrm{E}\lambda_m) - 1}{\left(s + \frac{\mathrm{E}}{\mathrm{Pr}}\mu_n\right)\left((s + \mathrm{E}\lambda_m)^2 + 1\right)}\right] \frac{1}{y_n^2} \int_{-1/2}^{1/2} \mathcal{Z}_m \mathcal{Y}_n dz, \end{aligned} \tag{A.30}$$

and so

$$\begin{aligned} C_n(\tau) = {} & M_n e^{-\frac{\mathrm{E}}{\mathrm{Pr}}\mu_n \tau} + \mathrm{Pr}\left[1 - e^{-\frac{\mathrm{E}}{\mathrm{Pr}}\mu_n \tau}\right] \frac{1}{y_n^2} \int_{-1/2}^{1/2} \left[\int_{-1/2}^{z} \frac{\nu}{\kappa} \frac{\partial K_0}{\partial z'} dz'\right] \mathcal{Y}_n dz \\ & + \sum_{m=0}^{\infty} B_m \left[\frac{1}{y_n^2} \int_{-1/2}^{1/2} \mathcal{Z}_m \mathcal{Y}_n dz\right] \left[\frac{\mathrm{E}^2 \lambda_m \left(\lambda_m - \frac{\mu_n}{\mathrm{Pr}}\right) - 1}{\mathrm{E}^2 \left(\lambda_m - \frac{\mu_n}{\mathrm{Pr}}\right)^2 + 1} e^{-\frac{\mathrm{E}}{\mathrm{Pr}}\mu_n \tau} \right. \\ & \left. + \frac{\left(1 - \mathrm{E}^2 \lambda_m \left(\lambda_m - \frac{\mu_n}{\mathrm{Pr}}\right)\right)\cos(\tau) + \mathrm{E}\left(2\lambda_m - \frac{\mu_n}{\mathrm{Pr}}\right)\sin(\tau)}{\mathrm{E}^2 \left(\lambda_m - \frac{\mu_n}{\mathrm{Pr}}\right)^2 + 1} e^{-\mathrm{E}\lambda_m \tau}\right]. \end{aligned} \tag{A.31}$$

The general solution for M can now be written as

$$\begin{aligned} M(z,\tau) = {} & \sum_{n=0}^{\infty} M_n \mathcal{Y}_n(z) e^{-\frac{\mathrm{E}}{\mathrm{Pr}}\mu_n \tau} + \mathrm{Pr} \int_{-1/2}^{z} \frac{\nu}{\kappa} \frac{\partial K_0}{\partial z'} dz' \\ & - \mathrm{Pr} \sum_{n=0}^{\infty} \left[\frac{1}{y_n^2} \int_{-1/2}^{1/2} \left(\int_{-1/2}^{z} \frac{\nu}{\kappa} \frac{\partial K_0}{\partial z'} dz'\right) \mathcal{Y}_n(z) dz\right] \mathcal{Y}_n(z) e^{-\frac{\mathrm{E}}{\mathrm{Pr}}\mu_n \tau} \\ & + \sum_{n=0}^{\infty} \sum_{m=0}^{\infty} B_m \left[\frac{1}{y_n^2} \int_{-1/2}^{1/2} \mathcal{Z}_m(z) \mathcal{Y}_n(z) dz\right] \left[\frac{\mathrm{E}^2 \lambda_m \left(\lambda_m - \frac{\mu_n}{\mathrm{Pr}}\right) - 1}{\mathrm{E}^2 \left(\lambda_m - \frac{\mu_n}{\mathrm{Pr}}\right)^2 + 1} e^{-\frac{\mathrm{E}}{\mathrm{Pr}}\mu_n \tau} \right. \\ & \left. + \frac{\left(1 - \mathrm{E}^2 \lambda_m \left(\lambda_m - \frac{\mu_n}{\mathrm{Pr}}\right)\right)\cos(\tau) + \mathrm{E}\left(2\lambda_m - \frac{\mu_n}{\mathrm{Pr}}\right)\sin(\tau)}{\mathrm{E}^2 \left(\lambda_m - \frac{\mu_n}{\mathrm{Pr}}\right)^2 + 1} e^{-\mathrm{E}\lambda_m \tau}\right] \mathcal{Y}_n(z). \end{aligned} \tag{A.32}$$

The first term of Eq. (A.32) corresponds to adjustment from the initial state, the second and third correspond to adjustment towards the final steady-state solution and the last double sum term represents the effects of the velocity adjustment with the $\cos\tau$ and $\sin\tau$ terms describing the inertial waves generated during the adjustment phase.

When $\nu = \kappa$, Eqs. (A.20) and (3.24) have the same form and hence $\mathcal{Z}_n = \mathcal{Y}_n$, $\lambda_n = \mu_n$ and $z_n = y_n$. Therefore, we can write

$$C_n(\tau) = \frac{\mathrm{Pr}}{z_n^2}\left[1 - e^{-\frac{\mathrm{E}}{\mathrm{Pr}}\lambda_n\tau}\right]\left[\int_{-1/2}^{1/2} K_0\mathcal{Z}_n dz\right] + B_n\left[\frac{\mathrm{E}^2\lambda_n^2\left(1-\frac{1}{\mathrm{Pr}}\right)-1}{\mathrm{E}^2\lambda_n^2\left(1-\frac{1}{\mathrm{Pr}}\right)^2+1}e^{-\frac{\mathrm{E}}{\mathrm{Pr}}\lambda_n\tau}\right.$$
$$\left. + \frac{\left(1-\mathrm{E}^2\lambda_n^2\left(1-\frac{1}{\mathrm{Pr}}\right)\right)\cos\tau + \mathrm{E}\lambda_n\left(2-\frac{1}{\mathrm{Pr}}\right)\sin\tau}{\mathrm{E}^2\lambda_n^2\left(1-\frac{1}{\mathrm{Pr}}\right)^2+1}e^{-\mathrm{E}\lambda_n\tau}\right] + M_n e^{-\frac{\mathrm{E}}{\mathrm{Pr}}\lambda_n\tau}. \tag{A.33}$$

For $\mathrm{Pr} = 1$, this becomes

$$C_n(\tau) = \frac{1}{z_n^2}\left[1 - e^{-\mathrm{E}\lambda_n\tau}\right]\left[\int_{-1/2}^{1/2} K_0\mathcal{Z}_n dz\right] + \left[(B_n\cos\tau + \mathrm{E}\lambda_n\sin\tau - 1) + M_n\right]e^{-\mathrm{E}\lambda_n\tau}. \tag{A.34}$$

A.3 Numerical solutions for the structure functions

For general ν and κ we need to solve for the functions K_0, $\mathcal{Z}_n$ and $\mathcal{Y}_n$ and eigenvalues λ_n and μ_n numerically. The equations and boundary conditions are

$$\begin{cases} \left(\nu\left(\nu K_0'\right)''\right)' = -K_0 - \zeta, & \zeta \in [-1/\sqrt{4\mathrm{E}}, 1/\sqrt{4\mathrm{E}}], \\ \left(\nu K_0'\right)'' = 0, & \zeta = \pm 1/\sqrt{4\mathrm{E}}, \\ K_0' = 0, & \zeta = \pm 1/\sqrt{4\mathrm{E}}, \end{cases} \tag{A.35}$$

for $K_0(\zeta)$ and

$$\begin{cases} \left(\nu\mathcal{Z}_n'\right)' = -\lambda_n\mathcal{Z}_n, & z \in [-1/2, 1/2], \\ \mathcal{Z}_n' = 0, & z = \pm 1/2, \\ \mathcal{Z}_n = 1, & z = 1/2, \end{cases} \tag{A.36}$$

and

$$\begin{cases} \left(\kappa\mathcal{Y}_n'\right)' = -\mu_n\mathcal{Y}_n, & z \in [-1/2, 1/2], \\ \mathcal{Y}_n' = 0, & z = \pm 1/2, \\ \mathcal{Y}_n = 1, & z = 1/2, \end{cases} \tag{A.37}$$

for $\mathcal{Z}_n(z)$ and $\mathcal{Y}_n(z)$. We choose the boundary conditions $\mathcal{Z}_n, \mathcal{Y}_n = 1$ at $z = 1/2$ to normalise our eigenfunctions. The constants z_n and y_n can be calculated by numerical integration using the solutions.

We now consider a function $\mathbf{g}(\boldsymbol{\sigma}) \in \mathbb{R}^m$, where $\boldsymbol{\sigma} \in \mathbb{R}^m$ for some positive integer m. We seek the roots of $\mathbf{g}$, i.e. the solutions $\boldsymbol{\sigma} = \boldsymbol{\sigma}^*$ satisfying $\mathbf{g}(\boldsymbol{\sigma}) = \mathbf{0}$. We can solve for

$\boldsymbol{\sigma}^*$ numerically using the Newton-Raphson iteration,

$$\boldsymbol{\sigma}_{n+1} = \boldsymbol{\sigma}_n - \left[\frac{\partial \mathbf{g}}{\partial \boldsymbol{\sigma}}(\boldsymbol{\sigma}_n)\right]^{-1} \cdot \mathbf{g}(\boldsymbol{\sigma}_n), \tag{A.38}$$

for some suitable chosen initial guess $\boldsymbol{\sigma}_0$. The Jacobian matrix, given by

$$\left[\frac{\partial \mathbf{g}}{\partial \boldsymbol{\sigma}}\right]_{ij} = \frac{\partial g_i}{\partial \sigma_j}, \tag{A.39}$$

can be approximated numerically to second order by

$$\left[\frac{\partial \mathbf{g}}{\partial \boldsymbol{\sigma}}\right]_{ij} \approx \frac{1}{2\delta}\left[g_i(\boldsymbol{\sigma} + \delta \mathbf{e}_j) - g_i(\boldsymbol{\sigma} - \delta \mathbf{e}_j)\right], \tag{A.40}$$

for some small δ requiring $2m$ evaluations of $\mathbf{g}$. We now iterate Eq. (A.38) until a suitable convergence condition is met; $\boldsymbol{\sigma}_0$ is chosen near the root such that the method converges. We say that the method has converged once

$$|\mathbf{g}(\boldsymbol{\sigma}_n)| < \epsilon^*, \tag{A.41}$$

for small parameter ϵ^*.

We now write Eqs. (A.35) to (A.37) as first order systems of the form

$$\mathbf{y}' = \mathbf{h}(\mathbf{y}, z), \tag{A.42}$$

for solution vector $\mathbf{y}$, function $\mathbf{h}$ and parameter z. We write Eq. (A.35) as

$$\begin{pmatrix} K_0 \\ \nu K_0' \\ (\nu K_0')' \\ \nu (\nu K_0')'' \end{pmatrix}' = \begin{pmatrix} [\nu K_0'] / \nu \\ (\nu K_0')' \\ \left[\nu (\nu K_0')''\right] / \nu \\ -K_0 - \zeta \end{pmatrix}, \tag{A.43}$$

with initial condition

$$\begin{pmatrix} K_0 \\ \nu K_0' \\ (\nu K_0')' \\ \nu (\nu K_0')'' \end{pmatrix} = \begin{pmatrix} \sigma_1 \\ 0 \\ \sigma_2 \\ 0 \end{pmatrix}, \tag{A.44}$$

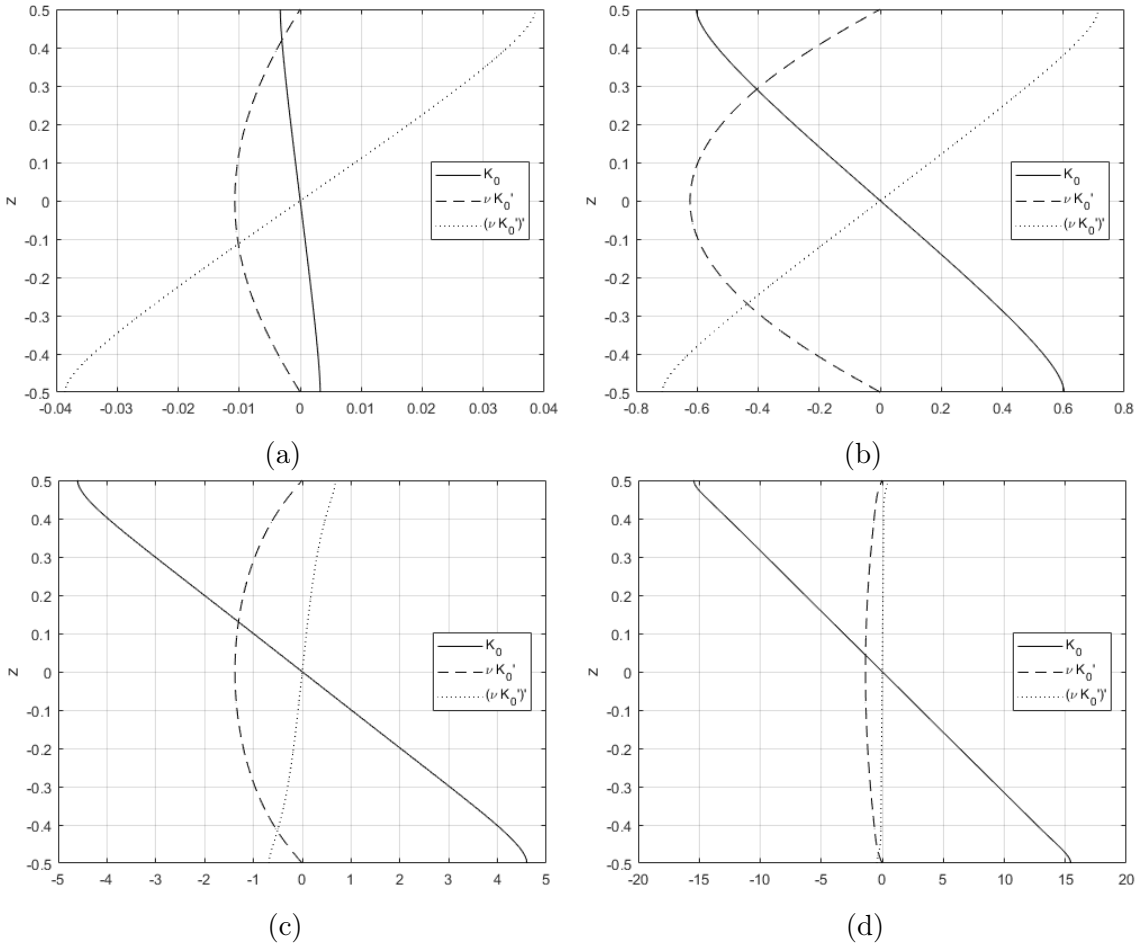

Fig. A.2 Vertical structure function, K_0 as a function of z for E = 1 (a), 0.1 (b), 0.01 (c) and 0.001 (d) and $\nu = 11/8 - 9/2z^2$.

at $\zeta = -1/\sqrt{4\mathrm{E}}$. We now integrate from $\zeta = -1/\sqrt{4\mathrm{E}}$ to $\zeta = 1/\sqrt{4\mathrm{E}}$ using a Runge-Kutta method and define

$$\mathbf{g}(\sigma_1, \sigma_2) = \begin{pmatrix} \nu K_0' \\ \nu(\nu K_0')'' \end{pmatrix}\Bigg|_{\zeta = 1/\sqrt{4\mathrm{E}}} . \tag{A.45}$$

We can see that finding a numerical solution for K_0 requires us to calculate the correct initial conditions (σ_1, σ_2) such that the boundary conditions at $\zeta = 1/\sqrt{4\mathrm{E}}$ are satisfied. These conditions correspond to $\mathbf{g} = \mathbf{0}$ so we can solve for (σ_1, σ_2) iteratively using Eq. (A.38). The solution for K_0 is given by the solution using the value of $\boldsymbol{\sigma}_n$ once the convergence condition has been met.

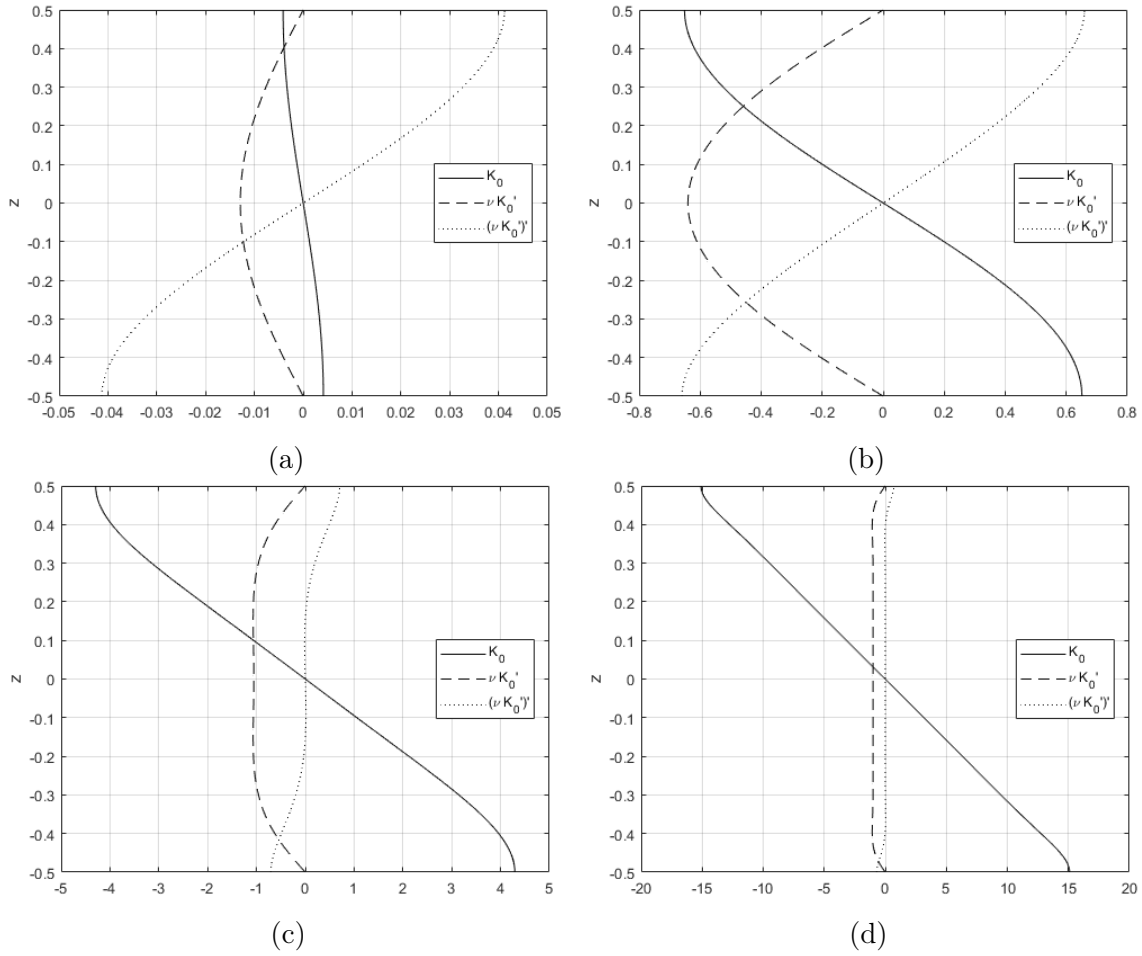

Fig. A.3 Vertical structure function, K_0 as a function of z for for E = 1 (a), 0.1 (b), 0.01 (c) and 0.001 (d) and $\nu = 1$.

We now write Eqs. (A.36) and (A.37) as

$$\begin{pmatrix} \mathcal{Z}_n \\ \nu\mathcal{Z}_n' \\ \mathcal{Y}_n \\ \kappa\mathcal{Y}_n' \end{pmatrix}' = \begin{pmatrix} \left[\nu\mathcal{Z}_n'\right]/\nu \\ -\lambda_n\mathcal{Z}_n \\ \left[\kappa\mathcal{Y}_n'\right]/\kappa \\ -\mu_n\mathcal{Y}_n \end{pmatrix}, \tag{A.46}$$

with initial condition

$$\begin{pmatrix} \mathcal{Z}_n \\ \nu\mathcal{Z}_n' \\ \mathcal{Y}_n \\ \kappa\mathcal{Y}_n' \end{pmatrix} = \begin{pmatrix} 1 \\ 0 \\ 1 \\ 0 \end{pmatrix}, \tag{A.47}$$

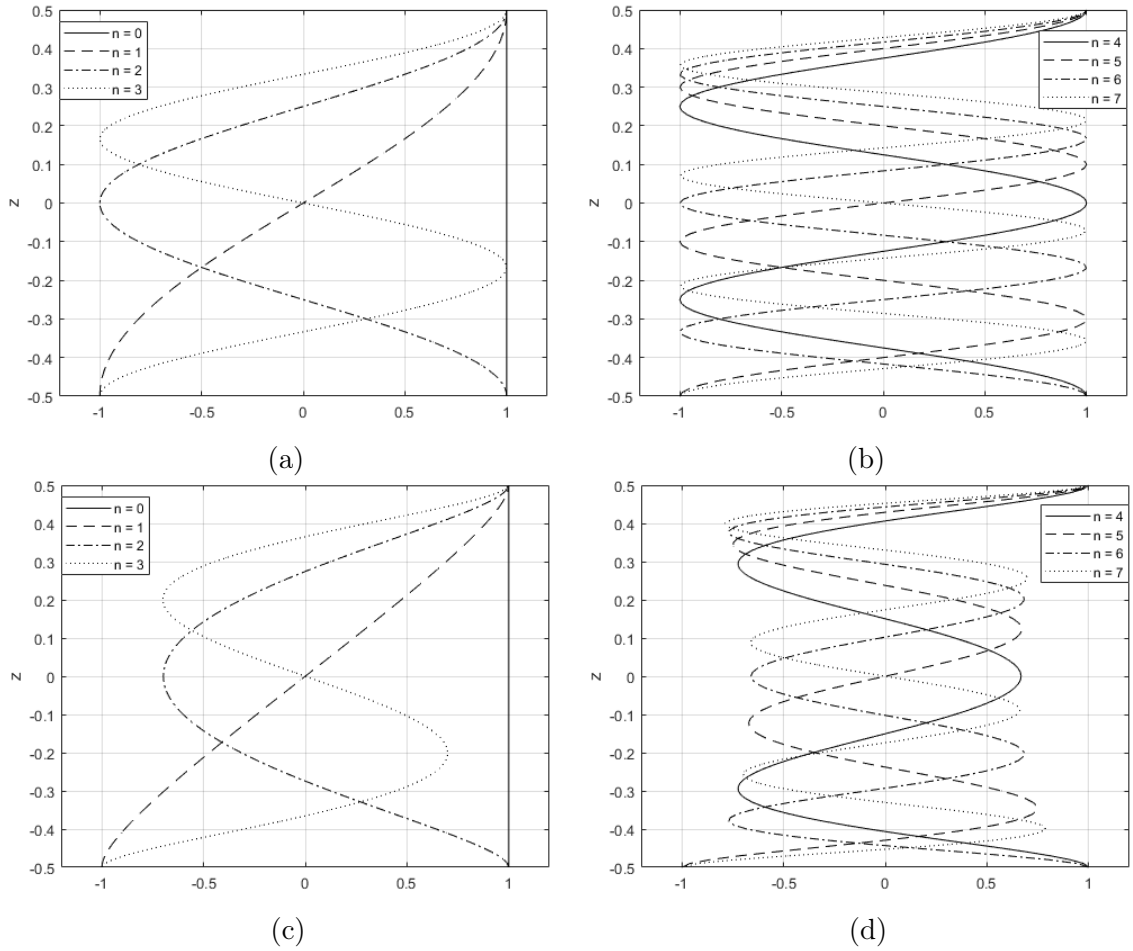

Fig. A.4 (a) $\mathcal{Z}_n$ for $\nu = 1$ and $n \in \{0, 1, 2, 3\}$. (b) $\mathcal{Z}_n$ for $\nu = 1$ and $n \in \{4, 5, 6, 7\}$. (c) $\mathcal{Z}_n$ for $\nu = 11/8 - 9/2z^2$ and $n \in \{0, 1, 2, 3\}$. (d) $\mathcal{Z}_n$ for $\nu = 11/8 - 9/2z^2$ and $n \in \{4, 5, 6, 7\}$. We note that if $\kappa = \nu$ then $\mathcal{Y}_n = \mathcal{Z}_n$.

at $z = 1/2$ and integrate backwards in z. In order to satisfy the boudary conditions at $z = -1/2$ we define

$$\mathbf{g}(\sigma_1, \sigma_2) = \begin{pmatrix} \nu \mathcal{Z}_n' \\ \kappa \mathcal{Y}_n' \end{pmatrix} \Bigg|_{z=-1/2}, \tag{A.48}$$

where $(\sigma_1, \sigma_2) = (\lambda_n, \mu_n)$ and take $\boldsymbol{\sigma}$ such that $\mathbf{g} = \mathbf{0}$. Therefore the solution $\boldsymbol{\sigma} = \boldsymbol{\sigma}^*$ determines the eigenvalues so we expect the components of $\mathbf{g}$ to be oscillatory with infinitely many positive roots. We note that the first component of $\mathbf{g}$ depends only on λ_n while the second depends only on μ_n. We can plot $g_1(\lambda_n)$ and $g_2(\mu_n)$ and use the plots to determine approximate values for the eigenvalues; these can be taken as starting values, $\boldsymbol{\sigma}_0$, in a Newton-Raphson iteration using Eq. (A.38). The solutions and eigenvalues are given once the method has converged.

We now consider a KPP-like profile for $\kappa = \nu$ where ν is given by

$$\nu = \frac{11}{8} - \frac{9}{2}z^2. \tag{A.49}$$

Numerical solutions for K_0 with E = 1, 0.1, 0.01 and 0.001 are shown in Fig. A.2. We can see that the upwelling, which is proportional to $\nu K_0'$, is stronger for smaller E, and, in the small-E limit, the along front velocity, which is proportional to K_0', approaches the linear thermal wind profile. The cross front velocity, proportional to $(\nu K_0')'$, is greatest at the surface and for small E is confined to thin boundary layers near the surfaces.

Fig. A.3 shows the solutions for K_0 with E = 1, 0.1, 0.01 and 0.001 in the case where $\nu = 1$. W can see that the form of the solutions is similar to the KPP case with a high horizontal surface velocity and strong upwelling in the centre of the vertical domain. For small E, the boundary layers are thicker for the constant case as the viscosity in this region is higher and the upwelling is approximately constant throughout the vertical domain. In both cases the along front velocity approaches the linear thermal wind profile for small E.

Fig. A.4 shows a comparison between the first eight vertical harmonics, $\mathcal{Z}_n$, for the constant and KPP viscosity profiles. We note that $\mathcal{Y}_n = \mathcal{Z}_n$ when $\kappa = \nu$. We can see that the magnitude of the osillations in the interior is smaller for the KPP case as the viscosity is higher here compared with the region near the boundary; we can think of this as stronger damping.

Appendix B

B.1 The leading order horizontal velocity for a forced front

In Chapter 5 the leading order horizontal velocity field for a forced front, $\mathbf{u}_{H0}$, satisfies the linear equation

$$\mathbf{k} \times \mathbf{u}_{H0} = -\nabla_H \overline{p}_0 - z\nabla_H b_0 + \mathrm{E}\frac{\partial^2 \mathbf{u}_{H0}}{\partial z^2}, \tag{B.1}$$

with boundary conditions

$$\mathrm{E}\frac{\partial \mathbf{u}_{H0}}{\partial z} = \boldsymbol{\tau}_0, \tag{B.2}$$

at $z = \pm 1/2$.

The general solution for $\mathbf{u}_{H0}$ can be written as

$$\mathbf{u}_{H0} = -\nabla_H \times (\overline{p}_0 \mathbf{k}) + \mathbf{v}(z) + A(z)\,\nabla_H b_0 + B(z)\,\mathbf{k} \times \nabla_H b_0, \tag{B.3}$$

where A and B respectively describe the cross-front and along-front buoyancy driven flows and $\mathbf{v}$ describes the stress driven flow. The functions A and B satisfy the equations

$$A = \mathrm{E}\frac{\partial^2 B}{\partial z^2}, \tag{B.4a}$$

$$-B = -z + \mathrm{E}\frac{\partial^2 A}{\partial z^2}, \tag{B.4b}$$

with boundary conditions

$$\frac{\partial A}{\partial z} = 0, \tag{B.5a}$$

$$\frac{\partial B}{\partial z} = 0, \tag{B.5b}$$

at $z = \pm 1/2$. Eq. (B.4) can be solved to obtain solution

$$A = -\sqrt{\mathrm{E}}\, K_0'' \left(z/\sqrt{\mathrm{E}} \right), \tag{B.6a}$$

$$B = -\sqrt{\mathrm{E}}\, K_0 \left(z/\sqrt{\mathrm{E}} \right), \tag{B.6b}$$

where K_0 is defined Section A.1. The stress driven flow, $\mathbf{v}$, satisfies

$$\mathbf{k} \times \mathbf{v} = \mathrm{E} \frac{\partial^2 \mathbf{v}}{\partial z^2}, \tag{B.7}$$

and

$$\mathrm{E} \frac{\partial \mathbf{v}}{\partial z} = \boldsymbol{\tau}_0, \tag{B.8}$$

at $z = \pm 1/2$. By linearity in $\boldsymbol{\tau}_0$ we can write

$$\mathbf{v} = C(z)\, \boldsymbol{\tau}_0 + D(z)\, \mathbf{k} \times \boldsymbol{\tau}_0, \tag{B.9}$$

hence

$$C = \mathrm{E} \frac{\partial^2 D}{\partial z^2}, \tag{B.10a}$$

$$-D = \mathrm{E} \frac{\partial^2 C}{\partial z^2}, \tag{B.10b}$$

with boundary conditions

$$\mathrm{E} \frac{\partial C}{\partial z} = 1, \tag{B.11a}$$

$$\mathrm{E} \frac{\partial D}{\partial z} = 0, \tag{B.11b}$$

at $z = \pm 1/2$. The solutions for C and D are given by

$$C = \frac{1}{\sqrt{\mathrm{E}}} K_0 \left(z/\sqrt{\mathrm{E}} \right) + \frac{z}{\mathrm{E}}, \tag{B.12a}$$

$$D = -\frac{1}{\sqrt{\mathrm{E}}} K_0'' \left(z/\sqrt{\mathrm{E}} \right). \tag{B.12b}$$

Combining our results the horizontal velocity can be written as

$$\begin{aligned} \mathbf{u}_{H0} = -\nabla_H \times (\overline{p}_0 \mathbf{k}) + \frac{1}{\sqrt{\mathrm{E}}} \left[\left(K_0 + \frac{z}{\sqrt{\mathrm{E}}} \right) \boldsymbol{\tau}_0 - K_0'' \, \mathbf{k} \times \boldsymbol{\tau}_0 \right] \\ -\sqrt{\mathrm{E}} \left[K_0'' \, \nabla_H b_0 + K_0 \, \mathbf{k} \times \nabla_H b_0 \right], \end{aligned} \tag{B.13}$$

which, by mass conservation, gives the vertical velocity

$$w_0 = \mathrm{E} \, K_0' \, \nabla_H^2 b_0. \tag{B.14}$$

B.2 Expressions for the Coefficients

The tensor coefficient in Eq. (5.33) are given by

$$[\mathbf{C}_{10}]_{ij} = -c_1 \delta_{ij} - c_2 k_m \varepsilon_{mij}, \tag{B.15}$$

$$[\mathbf{C}_{01}]_{ij} = (c_3 + c_6)\delta_{ij} + (c_4 + c_5) \, k_m \varepsilon_{mij}, \tag{B.16}$$

$$[\mathbf{C}_{21}]_{ijkl} = \frac{1}{\mathrm{E}} \big[c_6 \delta_{ij} \delta_{kl} - c_5 (\delta_{ij} k_m \varepsilon_{mkl} k_m \varepsilon_{mji} \delta_{kl}) + c_3 k_m k_n \varepsilon_{mji} \varepsilon_{nkl} \big], \tag{B.17}$$

$$\begin{aligned} [\mathbf{C}_{12}]_{ijkl} = -c_5 (\delta_{ij}\delta_{kl} + \delta_{ik}\delta_{jl}) \\ +c_3 \left(\delta_{ik} k_m \varepsilon_{mjl} + \delta_{jl} k_m \varepsilon_{mki} + \delta_{kl} k_m \varepsilon_{mji} \right) - c_4 k_m k_n \varepsilon_{mki} \varepsilon_{njl}, \end{aligned} \tag{B.18}$$

and

$$[\mathbf{C}_{03}]_{ij} = \mathrm{E} \left[c_3 \delta_{ij} + c_4 k_m \varepsilon_{mij} \right], \tag{B.19}$$

for positive constants, c_i, given in Table B.1. In the 2D case of a y independent front, the coefficients simplify to

$$C_0 = Q_1 \, \mathbf{i} \cdot \mathbf{C}_{10} \cdot \boldsymbol{\tau}_0 = -Q_0 [c_1 \tau_{0x} + c_2 \tau_{0y}], \tag{B.20}$$

$$C_1 = Q_1 [\mathbf{C}_{01}]_{11} + \mathbf{C}_{21} : [\mathbf{i} \, \boldsymbol{\tau}_0 \boldsymbol{\tau}_0 \mathbf{i}] = Q_1 (c_3 + c_6) + \frac{1}{\mathrm{E}} \big[c_6 \tau_{0x}^2 + 2 c_5 \tau_{0x} \tau_{0y} + c_3 \tau_{0y}^2 \big], \tag{B.21}$$

Constant	Definition	Small E	Large E
c_1	$2K_0''(\zeta_0)/\sqrt{\mathrm{E}}$	$\mathrm{E}^{-1/2}$	E^{-2}
c_2	$-2K_0(\zeta_0)/\sqrt{\mathrm{E}}$	E^{-1}	E^{-3}
c_3	$\overline{K_0'^2}$	1	E^{-4}
c_4	$\overline{K_0^2}$	E^{-1}	E^{-5}
c_5	$\overline{K_0''^2}$	$\mathrm{E}^{1/2}$	E^{-3}
c_6	$\overline{K_0'''^2}$	$\mathrm{E}^{1/2}$	E^{-2}

Table B.1 Definitions of positive constants, c_i. The asymptotic behaviour for small and large E is included. Note that $c_3+c_6 = \mathrm{E}c_2$ and $c_4+c_5 = 1/(12E)-\mathrm{E}c_1$. $\zeta_0 = 1/(2\sqrt{\mathrm{E}})$.

$$C_2 = \mathbf{C}_{12} : [\mathbf{i}\,\boldsymbol{\tau}_0\mathbf{i}\,\mathbf{i}] = -2c_5\tau_{0x} - 2c_3\tau_{0y}, \tag{B.22}$$

and

$$C_3 = \mathrm{E}c_3. \tag{B.23}$$

Here : denotes the contraction $\mathbf{A} : \mathbf{B} = A_{ijkl}B_{ijkl}$ and $\mathbf{i}$ is the unit vector in the x direction. Note that

$$\left[c_6\tau_{0x}^2 + 2c_5\tau_{0x}\tau_{0y} + c_3\tau_{0y}^2\right] = \overline{\left[K_0'''\tau_{0x} - K_0'\tau_{0y}\right]^2}, \tag{B.24}$$

hence the stress dependent part of C_1 is non-negative.

B.3 Similarity Solutions for Non-Linear Diffusion

We consider the equation

$$\frac{\partial F_n}{\partial T} = C_n \frac{\partial}{\partial x}\left[\left(\frac{\partial F_n}{\partial x}\right)^n\right], \tag{B.25}$$

for positive integer n and define similarity variable

$$\eta = \frac{x}{(\eta_n^{n+1} + k_n T)^{1/(n+1)}}, \tag{B.26}$$

where

$$k_n = \frac{2n(n+1)C_n\eta_n^{n-1}}{(n-1)}, \tag{B.27}$$

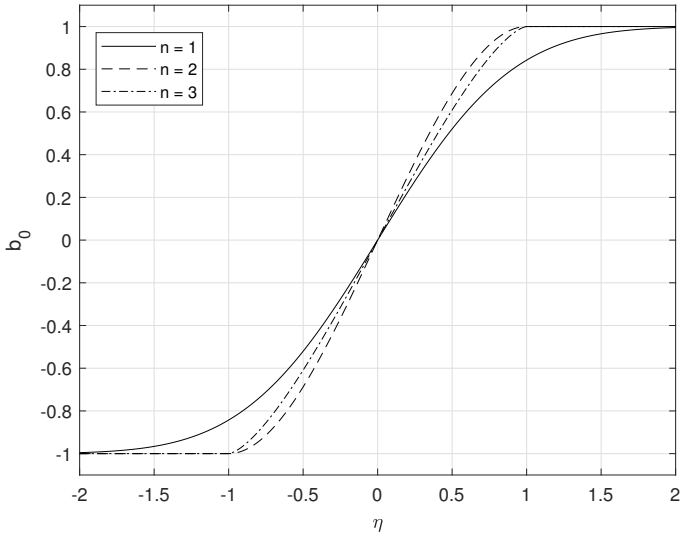

Fig. B.1 Similarity solution, $F_n(\eta)$, for $n = 1, 2$ and 3.

for constant η_n and k_n valid for $n \neq 1$. Transforming derivatives we obtain

$$-2\eta_n^{n-1}\eta\frac{\partial F_n}{\partial \eta} = (n-1)\frac{\partial^2 F_n}{\partial \eta^2}\left(\frac{\partial F_n}{\partial \eta}\right)^{n-1}, \tag{B.28}$$

with solution

$$F_n = \eta_n \int_0^{\eta} \left(1-\eta'^2\right)^{1/(n-1)} d\eta', \tag{B.29}$$

where we choose η_n such that $F_n|_{\eta=1} = 1$ i.e.

$$\eta_n = \left[\int_0^1 \left(1-\eta'^2\right)^{1/(n-1)} d\eta'\right]^{-1}. \tag{B.30}$$

Therefore we note that $\eta = \pm 1$ correspond to the edges of the front. Outside the frontal region we have the constant solution $F_n = \pm 1$. Note that at $T = 0$ we have

$$\left.\frac{\partial F_n}{\partial x}\right|_{x=0} = \left.\frac{\partial \eta}{\partial x}\frac{\partial F_n}{\partial \eta}\right|_{\eta=0} = \frac{1}{\eta_n} \times \eta_n = 1. \tag{B.31}$$

For $n = 1$ we instead have

$$k_1 = 4C_1, \tag{B.32}$$

and

$$\eta_1 = \frac{2}{\sqrt{\pi}}, \tag{B.33}$$

which gives solution

$$F_1 = \frac{2}{\sqrt{\pi}} \int_0^{\eta} e^{-\eta'^2} d\eta' = \mathrm{erf}(\eta). \tag{B.34}$$

Note that this is a smooth function for all η so there are no frontal edges. Plots of the similarity solutions for $n = 1$, $n = 2$ and $n = 3$ are shown in Fig. B.1.

Appendix C

C.1 Transient solution

In Section 6.3 we calculated the asymptotic solution for $\mathbf{u}_0$, b_0 and b_1' for the long time evolution. Here we include the transient evolution on the timescale τ for an initial flow with arbitrary vertical structure (e.g. thermal wind flow). Again the leading order buoyancy is assumed to be depth independent but we allow the buoyancy deviation, b_1', to have arbitrary initial vertical structure. This setup allows us to initialise the flow in thermal wind balance with a depth independent buoyancy, the transient evolution causes the front to slump over and the velocity to develop a cross-front component.

C.1.1 The O(1) equations

The leading order buoyancy balance is

$$\frac{\partial b_0}{\partial \tau} + \frac{\alpha}{\mathrm{Pr}_\alpha} b_0' = 0, \tag{C.1}$$

so we take solution with b_0 to be depth independent and hence independent of τ, therefore $b_0 = b_0(x, y, t)$.

The leading order velocity balance is given by

$$\frac{\partial u_0}{\partial \tau} - v_0 = -\frac{\partial p_0}{\partial x} - \alpha u_0', \tag{C.2a}$$

$$\frac{\partial v_0}{\partial \tau} + u_0 = -\frac{\partial p_0}{\partial y} - \alpha v_0', \tag{C.2b}$$

$$0 = -\frac{\partial p_0}{\partial z} + b_0, \tag{C.2c}$$

$$\frac{\partial u_0}{\partial x} + \frac{\partial v_0}{\partial y} + \frac{\partial w_0}{\partial z} = 0, \tag{C.2d}$$

hence the pressure can be written as

$$p_0 = z\, b_0 + \overline{p}_0, \tag{C.3}$$

and the horizontal momentum equations and mass conservation equation can be depth averaged to give

$$\frac{\partial \overline{u}_0}{\partial \tau} - \overline{v}_0 = -\frac{\partial \overline{p}_0}{\partial x}, \tag{C.4a}$$

$$\frac{\partial \overline{v}_0}{\partial \tau} + \overline{u}_0 = -\frac{\partial \overline{p}_0}{\partial y}, \tag{C.4b}$$

$$\frac{\partial \overline{u}_0}{\partial x} + \frac{\partial \overline{v}_0}{\partial y} = 0. \tag{C.4c}$$

Subtracting the depth averaged horizontal momentum equations from Eq. (C.2) gives evolution equations for the horizontal velocity perturbations and vertical velocity

$$\left[\frac{\partial}{\partial \tau} + \alpha\right] u_0' - v_0' = -z\frac{\partial b_0}{\partial x}, \tag{C.5a}$$

$$\left[\frac{\partial}{\partial \tau} + \alpha\right] v_0' + u_0' = -z\frac{\partial b_0}{\partial y}, \tag{C.5b}$$

$$\frac{\partial u_0'}{\partial x} + \frac{\partial v_0'}{\partial y} + \frac{\partial w_0}{\partial z} = 0. \tag{C.5c}$$

Eq. (C.5) can be solved to get

$$\mathbf{u}_{H0}' = A_1(z,\tau)\, \nabla_H b_0 + A_2(z,\tau)\, \mathbf{k} \times \nabla_H b_0, \tag{C.6}$$

and

$$w_0 = A_3(z,\tau) \nabla_H^2 b_0. \tag{C.7}$$

where

$$A_1 = \frac{-\alpha z}{1+\alpha^2} + \left[A_1^0(z) + \frac{\alpha z}{1+\alpha^2}\right] e^{-\alpha\tau}\cos\tau + \left[A_2^0(z) - \frac{z}{1+\alpha^2}\right] e^{-\alpha\tau}\sin\tau, \tag{C.8}$$

$$A_2 = \frac{z}{1+\alpha^2} + \left[A_2^0(z) - \frac{z}{1+\alpha^2}\right] e^{-\alpha\tau}\cos\tau - \left[A_1^0(z) + \frac{\alpha z}{1+\alpha^2}\right] e^{-\alpha\tau}\sin\tau, \tag{C.9}$$

$$A_3 = \frac{\alpha(z^2 - \frac{1}{4})}{2(1+\alpha^2)} - e^{-\alpha\tau}\cos\tau \int_{-1/2}^{z} A_1^0(z') + \frac{\alpha z'}{1+\alpha^2}\, dz' \\ -e^{-\alpha\tau}\sin\tau \int_{-1/2}^{z} A_2^0(z') - \frac{z'}{1+\alpha^2}\, dz', \tag{C.10}$$

and (A_1^0, A_2^0) describes the initial horizontal flow. Once the transients have decayed the balanced solutions are

$$\mathbf{u}'_{H0} = \gamma\left[-\alpha\,\nabla_H b_0 + \mathbf{k}\times\nabla_H b_0\right] z, \tag{C.11}$$

and

$$w_0 = \frac{\alpha\gamma(4z^2-1)}{8}\nabla_H^2 b_0, \tag{C.12}$$

for

$$\gamma = \frac{1}{1+\alpha^2}. \tag{C.13}$$

From the depth averaged mass conservation equation we can write

$$\overline{\mathbf{u}}_{H0} = -\nabla\times(\psi_0\mathbf{k}), \tag{C.14}$$

for streamfunction $\psi_0 = \overline{p}_0$. Hence

$$\mathbf{u}_{H0} = -\nabla\times(\psi_0\mathbf{k}) + A_1(z,\tau)\,\nabla_H b_0 + A_2(z,\tau)\,\mathbf{k}\times\nabla_H b_0. \tag{C.15}$$

C.1.2 The O(Ro) equations

The $O(\mathrm{Ro})$ buoyancy equation is

$$\frac{\partial b_1}{\partial\tau} + \frac{\partial b_0}{\partial t} + \mathbf{u}_{H0}\cdot\nabla_H b_0 + \mathcal{N}^2 w_0 = -\frac{\alpha}{\mathrm{Pr}_\alpha} b_1', \tag{C.16}$$

and subtracting the depth average gives

$$\left[\frac{\partial}{\partial\tau} + \frac{\alpha}{\mathrm{Pr}_\alpha}\right] b_1' = -\mathbf{u}'_{H0}\cdot\nabla_H b_0 - \mathcal{N}^2 w_0'. \tag{C.17}$$

When $\mathcal{N}^2 = 0$ the general solution is given by

$$b_1' = A_4(z,\tau)|\nabla_H b_0|^2, \tag{C.18}$$

where

$$A_4 = \frac{\mathrm{Pr}_\alpha z}{1+\alpha^2} + \left[A_4^0(z) - \frac{\mathrm{Pr} z}{1+\alpha^2} + \frac{\left[A_1^0(z) + \frac{\alpha z}{1+\alpha^2}\right]\alpha\left(1-\frac{1}{\mathrm{Pr}_\alpha}\right) + \left[A_2^0(z) - \frac{z}{1+\alpha^2}\right]}{1+\alpha^2\left(1-\frac{1}{\mathrm{Pr}_\alpha}\right)^2} \right] e^{-\frac{\alpha}{\mathrm{Pr}_\alpha}\tau}$$
$$+ \left[\frac{\left[A_1^0(z) + \frac{\alpha z}{1+\alpha^2}\right]\left(\sin\tau - \alpha\left(1-\frac{1}{\mathrm{Pr}_\alpha}\right)\cos\tau\right) - \left[A_2^0(z) - \frac{z}{1+\alpha^2}\right]\left(\cos\tau + \alpha\left(1-\frac{1}{\mathrm{Pr}_\alpha}\right)\sin\tau\right)}{1+\alpha^2\left(1-\frac{1}{\mathrm{Pr}_\alpha}\right)^2} \right] e^{-\alpha\tau}, \tag{C.19}$$

for initial vertical structure described by $A_4^0(z)$. The general steady state solution is given by

$$b_1' = \mathrm{Pr}_\alpha \gamma \left[z|\nabla_H b_0|^2 - \mathcal{N}^2 \frac{12z^2-1}{24} \nabla_H^2 b_0 \right], \tag{C.20}$$

and calculating $\bar{b}_1$ requires the $O(\mathrm{Ro}^2)$ buoyancy equation.

C.2 Analytic solution with relaxation and diffusion

If we include vertical diffusion with $\mathrm{E} = O(1)$ in the linear relaxation model, we can obtain the solution

$$\mathbf{u}_{H0}' = -\sqrt{\mathrm{E}}\left[B_1 \nabla_H b_0 + B_2\, \mathbf{k} \times \nabla_H b_0\right], \tag{C.21}$$

where

$$B_1 = \alpha\zeta/(1+\alpha^2) + iC_1 \sinh[\sqrt{\alpha+i}\zeta] - iC_2 \sinh[\sqrt{\alpha-i}\zeta], \tag{C.22a}$$
$$B_2 = -\zeta/(1+\alpha^2) + C_1 \sinh[\sqrt{\alpha+i}\zeta] + C_2 \sinh[\sqrt{\alpha-i}\zeta], \tag{C.22b}$$

and

$$\zeta = z/\sqrt{\mathrm{E}}. \tag{C.23}$$

Using boundary conditions of no vertical shear on the top and bottom surfaces gives that

$$\begin{bmatrix} i\sqrt{\alpha+i}\cosh\left[\sqrt{\frac{\alpha+i}{4\mathrm{E}}}\right] & -i\sqrt{\alpha-i}\cosh\left[\sqrt{\frac{\alpha-i}{4\mathrm{E}}}\right] \\ \sqrt{\alpha+i}\cosh\left[\sqrt{\frac{\alpha+i}{4\mathrm{E}}}\right] & \sqrt{\alpha-i}\cosh\left[\sqrt{\frac{\alpha-i}{4\mathrm{E}}}\right] \end{bmatrix} \begin{bmatrix} C_1 \\ C_2 \end{bmatrix} = \frac{1}{1+\alpha^2} \begin{bmatrix} -\alpha \\ 1 \end{bmatrix}, \tag{C.24}$$

which can be inverted to obtain solution

$$\begin{bmatrix} C_1 \\ C_2 \end{bmatrix} = \frac{1}{2(1+\alpha^2)} \begin{bmatrix} \frac{1+\alpha i}{\sqrt{\alpha+i}\cosh\zeta_{\alpha+}} \\ \frac{1-\alpha i}{\sqrt{\alpha-i}\cosh\zeta_{\alpha-}} \end{bmatrix}, \tag{C.25}$$

for

$$\zeta_{\alpha\pm} = \sqrt{\frac{\alpha \pm i}{4\mathrm{E}}} = \sqrt{\alpha \pm i}\,\zeta_0, \tag{C.26}$$

and $\sqrt{*}$ denoting the principle value of the square root with branch cut taken along the line $z \in -I\!R_0^+$. The leading order vertical velocity can be obtained by integrating the mass conservation equation as before which gives solution

$$w_0 = \mathrm{E}\left[\frac{\alpha^2-1}{(\alpha^2+1)^2} + \frac{\alpha(\zeta^2-\zeta_0^2)}{2(1+\alpha^2)} + \frac{iC_1}{\sqrt{\alpha+i}}\cosh[\sqrt{\alpha+i}\zeta] - \frac{iC_2}{\sqrt{\alpha-i}}\cosh[\sqrt{\alpha-i}\zeta]\right]\nabla_H^2 b_0, \tag{C.27}$$

for $\zeta_0 = 1/2\sqrt{\mathrm{E}}$.

We can now use this leading order solution for the velocity to calculate the $O(\mathrm{Ro})$ solution for the buoyancy perturbation, the governing equation is

$$\mathbf{u}'_{H0}\cdot\nabla_H b_0 = \frac{\mathrm{E}}{\mathrm{Pr}}\frac{\partial^2 b'_1}{\partial z^2} - \frac{\alpha}{\mathrm{Pr}}b'_1, \tag{C.28}$$

hence

$$\left[\frac{\partial^2}{\partial\zeta^2} - \alpha\right] b'_1 = -\sqrt{\mathrm{E}}\,\mathrm{Pr}\,B_1\,|\nabla_H b_0|^2, \tag{C.29}$$

which has solution

$$b'_1 = -\sqrt{\mathrm{E}}\,\mathrm{Pr}\,B_2\,|\nabla_H b_0|^2. \tag{C.30}$$

For small E this solution reduces to the solution given above in the region away from the boundaries. We use this solution to initialise the numerical simulations so that the initial state matches the no stress boundary conditions and hence will not produce inertial waves while adjusting to a balanced state.

C.3 Instability of the TTW model

Using the diffusive parametrisation model with a background streamfunction, ψ_0, we obtain steady state solution

$$\mathbf{u}_H = -\nabla\times(\psi_0\mathbf{k}) - \sqrt{\mathrm{E}}\,(K_0''\nabla_H b_0 + K_0\mathbf{k}\times\nabla_H b_0) + O(\mathrm{Ro}), \tag{C.31}$$

$$w = \mathrm{E}\, K_0' \nabla_H^2 b_0 + O(\mathrm{Ro}), \tag{C.32}$$

and

$$b = b_0 - \mathrm{Ro}\,\mathrm{Pr}\,\sqrt{\mathrm{E}}\, K_0 |\nabla_H b_0|^2 + O(\mathrm{Ro}^2), \tag{C.33}$$

where K_0 is given in Section A.1. Note that this model does not include a stratification so $\mathrm{Bu} = 0$ and we are using an order 1 Ekman number to describe the effects of turbulence. Here we have used a constant vertical turbulent viscosity and diffusivity profile, this is just for convenience and the resulting equations will be similar for arbitrary vertical profiles.

Using the depth averaged buoyancy and vorticity equations, Eqs. (6.20) and (6.37), and including horizontal diffusion we can write the governing equations for the background buoyancy and streamfunction as

$$\frac{\partial b_0}{\partial t} + J(\psi_0, b_0) = \frac{\epsilon^2 \mathrm{E}}{\mathrm{Ro}\,\mathrm{Pr}} \nabla_H^2 b_0, \tag{C.34}$$

and

$$\begin{gathered} \frac{\partial \nabla_H^2 \psi_0}{\partial t} + J(\psi_0, \nabla_H^2 \psi_0) - \frac{\epsilon^2 \mathrm{E}}{\mathrm{Ro}} \nabla_H^4 \psi_0 = \\ \mathrm{E}\, \nabla_H \cdot \left[\left(2\overline{K_0'^2} \nabla_H b_0 + \left[\overline{K_0''^2} - \overline{K_0^2} \right] \mathbf{k} \times \nabla_H b_0 \right) \nabla_H^2 b_0 \right]. \end{gathered} \tag{C.35}$$

These equations are of the same form as the governing equations for the relaxation model considered above hence we expect instabilities with the corresponding growth rate

$$\begin{gathered} \sigma_\pm = -\frac{\epsilon^2 \mathrm{E}}{2\mathrm{Ro}} \left[1 + \frac{1}{\mathrm{Pr}} \right] (k^2 + l^2) \pm \\ \sqrt{\left[\frac{1}{\mathrm{Pr}} - 1 \right]^2 \frac{\epsilon^4 \mathrm{E}^2}{4\mathrm{Ro}^2} (k^2 + l^2)^2 - \mathrm{E} B^2 \left[2\overline{K_0'^2} kl + (\overline{K_0''^2} - \overline{K_0^2}) l^2 \right]}, \end{gathered} \tag{C.36}$$

for frontal gradient B and horizontal wavevector (k, l). In the case $\mathrm{Pr} = 1$ this simplifies to

$$\sigma_\pm = -\frac{\epsilon^2 \mathrm{E}}{\mathrm{Ro}} (k^2 + l^2) \pm \sqrt{-\mathrm{E} B^2 \left[2\overline{K_0'^2} kl + (\overline{K_0''^2} - \overline{K_0^2}) l^2 \right]}. \tag{C.37}$$

The last term in square brackets in Eqs. (C.36) and (C.37) is a symmetric quadratic form so can be diagonalised by an orthogonal transformation. Therefore the fastest growing modes for a given wavenumber will be diagonal with angle dependent only on

a function of the Ekman number. The fastest growing mode for a given wavenumber, $K = \sqrt{k^2 + l^2}$, is

$$\sigma_{\pm} = -\frac{\epsilon^2 \mathrm{E}}{2\mathrm{Ro}} \left[1 + \frac{1}{\mathrm{Pr}}\right] K^2 + \sqrt{\left[\frac{1}{\mathrm{Pr}} - 1\right]^2 \frac{\epsilon^4 \mathrm{E}^2}{4\mathrm{Ro}^2} K^4 + \lambda \mathrm{E} B^2 K^2}, \tag{C.38}$$

for eigenvalue

$$\lambda = -\frac{1}{2}\left[\overline{K_0''^2} - \overline{K_0^2} - \sqrt{4\overline{K_0'^2}^2 + \left(\overline{K_0''^2} - \overline{K_0^2}\right)^2}\right], \tag{C.39}$$

with angle

$$\theta = \arctan\left[\frac{\overline{K_0''^2} - \overline{K_0^2} + \sqrt{4\overline{K_0'^2}^2 + \left(\overline{K_0''^2} - \overline{K_0^2}\right)^2}}{2\overline{K_0'^2}^2}\right], \tag{C.40}$$

from the down-front direction.

In the case $\mathrm{Pr} = 1$ the maximum growth rate reduces to

$$\sigma_{max} = \sqrt{\lambda \mathrm{E}} B K - \frac{\epsilon^2 \mathrm{E}\, K^2}{\mathrm{Ro}}, \tag{C.41}$$

which is the analogous result to Eq. (6.80) and has fastest growing mode

$$K_{max} = \frac{\sqrt{\lambda}\, B\, \mathrm{Ro}}{2\epsilon^2 \sqrt{\mathrm{E}}}, \tag{C.42}$$

with corresponding growth rate

$$\sigma(K_{max}) = \frac{\lambda B^2 \mathrm{Ro}}{4\epsilon^2}. \tag{C.43}$$

Fig. C.1 shows the formation of baroclinic instability for $\alpha = 0$, $\mathrm{E} = 0.1$ and $\mathrm{Ro} = 0.01$. We can see that the evolution and structure of the instability is similar to the case of the relaxation parametrisation with modes tilted by the angled TTW flow.

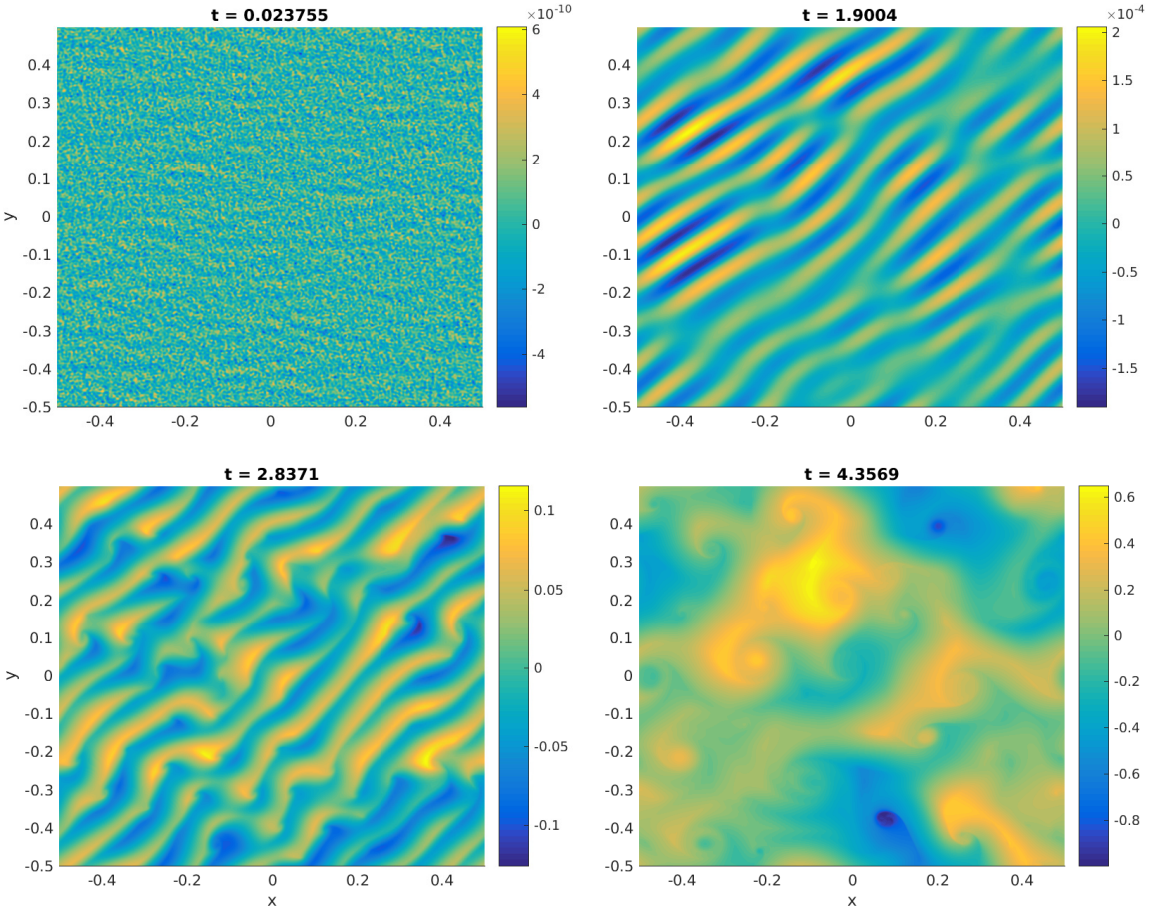

Fig. C.1 The formation of baroclinic instability for E = 0.1 and Ro = 0.01. We plot $b_0(x, y, z = 0) - Bx$ as a function of cross-front coordinate x and along-front coordinate y.

Appendix D

D.1 Introduction

Here we present a general solution to Eq. (3.1) in terms of the linear operators $\mathcal{L}_u$ and $\mathcal{L}_b$ which describe the effects of vertical mixing. As before we perform a multiple scale asymptotics and consider the different orders.

D.2 The O(1) equations

The $O(1)$ buoyancy equation is

$$\mathcal{L}_b b_0' = 0, \tag{D.1}$$

with solution

$$b_0' = 0 \quad \Longrightarrow \quad b_0 = b_0(x, y). \tag{D.2}$$

The $O(1)$ vertical momentum equation is

$$\frac{\partial p_0}{\partial z} = b_0, \tag{D.3}$$

hence

$$p_0 = \overline{p}_0 + b_0 z. \tag{D.4}$$

The horizontal momentum equations are

$$-v_0 = \frac{\partial p_0}{\partial x} + \mathcal{L}_u u_0', \tag{D.5a}$$

$$u_0 = \frac{\partial p_0}{\partial y} + \mathcal{L}_u v_0', \tag{D.5b}$$

and writing $\mathbf{u}_{H0} = \overline{\mathbf{u}}_{H0} + \mathbf{u}'_{H0}$ gives

$$\overline{\mathbf{u}}_{H0} = -\nabla_H \times (\overline{p}_0 \mathbf{k}), \tag{D.6}$$

hence $\overline{p}_0 = \psi_0$ where ψ_0 is the streamfunction for the depth-averaged vertical velocity. We now write

$$\mathbf{u}'_{H0} = \mathbf{u}_f + \mathbf{M} \cdot \nabla_H b_0, \tag{D.7}$$

for matrix M and substitute into equations D.5 to obtain solution

$$\mathbf{M} = \begin{pmatrix} \mathcal{L}_u M & -M \\ M & \mathcal{L}_u M \end{pmatrix}, \tag{D.8}$$

where $M(z)$ satisfies

$$\left(\mathcal{L}_u^2 + 1\right) M = z. \tag{D.9}$$

The vector $\mathbf{u}_f = (u_f, -\mathcal{L}_u u_f)$ is included to allow surface forcing (such as a surface stress) and satisfies

$$\left(\mathcal{L}_u^2 + 1\right) u_f = 0, \tag{D.10}$$

along with any surface forcing boundary conditions. In the case of no external forcing, $u_f = 0$. We can now write

$$\mathbf{u}_{H0} = -\nabla_H \times (\psi_0 \mathbf{k}) + \mathcal{L}_u M \, \nabla_H b_0 + M \, \mathbf{k} \times \nabla_H b_0 + \mathbf{u}_f, \tag{D.11}$$

which by mass conservation gives that

$$w_0 = R \, \nabla_H^2 b_0 + w_f, \tag{D.12}$$

where

$$R(z) = -\int_{-1/2}^{z} \mathcal{L}_u M \, dz', \tag{D.13}$$

and

$$w_f = -\int_{-1/2}^{z} \nabla_H \cdot \mathbf{u}_f \, dz'. \tag{D.14}$$

D.3 The O(Ro) Equations

The $O(Ro)$ buoyancy equation is

$$\frac{\partial b_0}{\partial t} + \mathbf{u}_{H0} \cdot \nabla_H b_0 = \mathcal{L}_b b_1', \tag{D.15}$$

which can be depth-averaged to get

$$\frac{\partial b_0}{\partial t} + \overline{\mathbf{u}}_{H0} \cdot \nabla_H b_0 = 0. \tag{D.16}$$

Subtracting gives

$$\mathbf{u}_{H0}' \cdot \nabla_H b_0 = \mathcal{L}_b b_1', \tag{D.17}$$

so

$$\mathcal{L}_b b_1' = \mathcal{L}_u M \left|\nabla_H b_0\right|^2 + \mathbf{u}_f \cdot \nabla_H b_0, \tag{D.18}$$

and we can write

$$b_1' = N \left|\nabla_H b_0\right|^2 + b_f, \tag{D.19}$$

where

$$N = \mathcal{L}_b^{-1} \mathcal{L}_u M, \tag{D.20}$$

and b_f satisfies

$$\mathcal{L}_b b_f = \mathbf{u}_f \cdot \nabla_H b_0, \tag{D.21}$$

as well as any surface forcing boundary conditions (such as a buoyancy flux). By symmetry we assume that $\overline{b}_1 = 0$.

D.4 The Depth-Averaged Buoyancy Equation

The $O(Ro^2)$ depth-averaged buoyancy equation is

$$\frac{\partial b_0}{\partial T} + J(\psi_1, b_0) + \nabla_H \cdot \left[\overline{\mathbf{u}_{H0}' b_1'}\right] = \frac{D}{Pr} \nabla_H^2 b_0, \tag{D.22}$$

where

$$D = \frac{\epsilon^2 E}{Ro^2}, \tag{D.23}$$

is the horizontal diffusivity. The flux term can be written as

$$\nabla_H \cdot \left[\overline{\mathbf{u}'_{H0} b'_1}\right] = \nabla_H \cdot \left[\left(\overline{N\mathcal{L}_u M}\,\nabla_H b_0 + \overline{MN}\,\mathbf{k}\times\nabla_H b_0\right)|\nabla_H b_0|^2 + \mathbf{F}\right], \tag{D.24}$$

where

$$\mathbf{F} = \overline{\mathbf{u}_f N}|\nabla_H b_0|^2 + \overline{b_f \mathcal{L}_u M}\nabla_H b_0 + \overline{b_f M}\mathbf{k}\times\nabla_H b_0 + \overline{\mathbf{u}_f b_f}, \tag{D.25}$$

contains the cross terms resulting from surface forcing. As shown in Chapter 5 these terms can lead to a negative effective diffusivity. We now assume that there is no background flow at $O(Ro)$ and that the only non-zero depth-averaged velocity term appears through ψ_0. Therefore $\psi_1 = 0$ and

$$\frac{\partial b_0}{\partial T} = \nabla_H \cdot \left[-\left(\overline{N\mathcal{L}_u M}\,\nabla_H b_0 + \overline{MN}\,\mathbf{k}\times\nabla_H b_0\right)|\nabla_H b_0|^2 - \mathbf{F}\right] + \frac{D}{Pr}\nabla_H^2 b_0. \tag{D.26}$$

The depth-averaged $O(Ro)$ buoyancy equation

$$\frac{\partial b_0}{\partial t} + \overline{\mathbf{u}}_{H0}\cdot\nabla_H b_0 = 0, \tag{D.27}$$

can be written as

$$\frac{\partial b_0}{\partial t} + J(\psi_0, b_0) = 0, \tag{D.28}$$

which describes the advection of buoyancy by the depth-averaged flow. Combining the evolution equations for b_0 at these two different orders gives an equation for b_0 that is valid up to $t = O(1/Ro)$

$$\begin{gathered}\frac{\partial b_0}{\partial t} + J(\psi_0, b_0) - \frac{RoD}{Pr}\nabla_H^2 b_0 = \\ Ro\,\nabla_H \cdot \left[-\left(\overline{N\mathcal{L}_u M}\,\nabla_H b_0 + \overline{MN}\,\mathbf{k}\times\nabla_H b_0\right)|\nabla_H b_0|^2 - \mathbf{F}\right].\end{gathered} \tag{D.29}$$

D.5 The Depth-Averaged Vorticity Equation

The $O(Ro)$ vertical vorticity equation can be depth-averaged to get

$$\frac{\partial \overline{\zeta}_0}{\partial t} + \nabla_H \cdot \left[\overline{\mathbf{u}_{H0}\zeta_0} - \overline{\boldsymbol{\omega}_{H0} w_0}\right] = Ro\,D\nabla_H^2 \overline{\zeta}_0, \tag{D.30}$$

where we have included the small horizontal diffusion term on the right-hand side. Here the vertical vorticity is

$$\zeta_0 = \mathbf{k} \cdot [\nabla_H \times \mathbf{u}_{H0}] = \nabla_H^2 \psi_0 + M\, \nabla_H^2 b_0 - \nabla_H \cdot (\mathbf{k} \times \mathbf{u}_f), \tag{D.31}$$

and the horizontal vorticity is

$$\boldsymbol{\omega}_{H0} = \mathbf{k} \times \frac{\partial \mathbf{u}_{H0}}{\partial z} + \nabla_H \times (w_0\, \mathbf{k}). \tag{D.32}$$

The divergence term in equation D.30 can be written

$$\nabla_H \cdot \left[\overline{\mathbf{u}_{H0}\zeta_0} - \overline{\boldsymbol{\omega}_{H0} w_0}\right] = J(\psi_0, \nabla_H^2 \psi_0) + \nabla_H \cdot \left[\overline{\mathbf{u}'_{H0}\zeta'_0} - \overline{\boldsymbol{\omega}_{H0} w_0}\right], \tag{D.33}$$

and now the second term on the right-hand side of equation D.33 can be written as

$$\nabla_H \cdot \left[\overline{\mathbf{u}'_{H0}\zeta'_0}\right] = \nabla_H \cdot \left[\left(\overline{M\mathcal{L}_u M}\, \nabla_H b_0 + \overline{M^2}\, \mathbf{k} \times \nabla_H b_0\right) \nabla_H^2 b_0 + \mathbf{G}_1\right]. \tag{D.34}$$

The final term on the RHS of equation D.33 can be written

$$\nabla_H \cdot [\overline{\boldsymbol{\omega}_{H0} w_0}] = \nabla_H \cdot \left[\overline{\left(\mathbf{k} \times \frac{\partial \mathbf{u}_{H0}}{\partial z}\right) w_0} + \frac{1}{2} \nabla_H \times (\overline{w_0^2}\, \mathbf{k})\right], \tag{D.35}$$

where the second term vanishes due to being the divergence of a curl. The first term can be re-written using integration by parts to obtain

$$\nabla_H \cdot [\overline{\boldsymbol{\omega}_{H0} w_0}] = -\nabla_H \cdot \left[\overline{(\mathbf{k} \times \mathbf{u}_{H0}) \frac{\partial w_0}{\partial z}}\right] = \nabla_H \cdot \left[\overline{(\mathbf{k} \times \mathbf{u}_{H0})\, \nabla_H \cdot \mathbf{u}_{H0}}\right], \tag{D.36}$$

so using

$$\nabla_H \cdot \mathbf{u}_{H0} = \mathcal{L}_u M\, \nabla_H^2 b_0 + \nabla_H \cdot \mathbf{u}_f, \tag{D.37}$$

we can write

$$\nabla_H \cdot [\overline{\boldsymbol{\omega}_{H0} w_0}] = \nabla_H \cdot \left[\left(-\overline{M\mathcal{L}_u M}\, \nabla_H b_0 + \overline{(\mathcal{L}_u M)^2}\, \mathbf{k} \times \nabla_H b_0\right) \nabla_H^2 b_0 - \mathbf{G}_2\right]. \tag{D.38}$$

Combining our results we have

$$\begin{aligned}\frac{\partial \nabla_H^2 \psi_0}{\partial t} + J(\psi_0, \nabla_H^2 \psi_0) - Ro\, D \nabla_H^4 \psi_0 = \\ \nabla_H \cdot \left[\left(-2\overline{M \mathcal{L}_u M}\, \nabla_H b_0 + \left(\overline{(\mathcal{L}_u M)^2} - \overline{M^2} \right) \mathbf{k} \times \nabla_H b_0 \right) \nabla_H^2 b_0 - \mathbf{G} \right].\end{aligned} \tag{D.39}$$

Together with the evolution equation for b_0, this gives a closed system that can be solved for (b_0, ψ_0). Both the self-similar spreading and Baroclinic instability papers are special cases of this general result. The term $\mathbf{G} = \mathbf{G}_1 + \mathbf{G}_2$ contains the cross terms resulting from surface forcing and is given by

$$\begin{aligned}\mathbf{G} = &- [\overline{\mathbf{k} \times \mathbf{u}_f \nabla_H \cdot \mathbf{u}_f + \mathbf{u}_f \nabla_H \cdot (\mathbf{k} \times \mathbf{u}_f)}] + [\overline{\nabla_H \cdot \mathbf{u}_f M - \nabla_H \cdot (\mathbf{k} \times \mathbf{u}_f) \mathcal{L}_u M}] \nabla_H b_0 \\ &- [\overline{\nabla_H \cdot \mathbf{u}_f \mathcal{L}_u M + \nabla_H \cdot (\mathbf{k} \times \mathbf{u}_f) M}] \mathbf{k} \times \nabla_H b_0 + [\overline{\mathbf{u}_f M - \mathbf{k} \times \mathbf{u}_f \mathcal{L}_u M}] \nabla_H^2 b_0.\end{aligned} \tag{D.40}$$

D.6 Summary of Results

Combining our results, we have buoyancy field

$$b = b_0 + Ro\, \left(b_f + N\, |\nabla_H b_0|^2 \right) + O(Ro^2), \tag{D.41}$$

horizontal velocity

$$\mathbf{u}_H = -\nabla_H \times (\psi_0 \mathbf{k}) + \mathbf{u}_f + \mathcal{L}_u M\, \nabla_H b_0 + M\, \mathbf{k} \times \nabla_H b_0 + O(Ro), \tag{D.42}$$

and vertical velocity

$$w = w_f + R\, \nabla_H^2 b_0 + O(Ro). \tag{D.43}$$

The vertical structure function M depends only on z and satisfies

$$\left(\mathcal{L}_u^2 + 1 \right) M = z, \tag{D.44}$$

N and R can be determined from M by

$$N = \mathcal{L}_b^{-1} \mathcal{L}_u M, \tag{D.45}$$

and

$$R(z) = -\int_{-1/2}^{z} \mathcal{L}_u M\, dz'. \tag{D.46}$$

The functions $(\mathbf{u}_f, w_f, b_f)$ are given above and are zero if the system is not forced through boundary conditions. The background fields b_0 and ψ_0 do not depend on z, and evolve according to

$$\begin{gathered}\frac{\partial b_0}{\partial t} + J(\psi_0, b_0) - \frac{\epsilon^2 E}{Ro\, Pr}\nabla_H^2 b_0 = \\ Ro\, \nabla_H \cdot \left[- \left(\overline{N\mathcal{L}_u M}\, \nabla_H b_0 + \overline{MN}\, \mathbf{k} \times \nabla_H b_0 \right) |\nabla_H b_0|^2 - \mathbf{F} \right],\end{gathered} \tag{D.47}$$

and

$$\begin{gathered}\frac{\partial \nabla_H^2 \psi_0}{\partial t} + J(\psi_0, \nabla_H^2 \psi_0) - \frac{\epsilon^2 E}{Ro}\nabla_H^4 \psi_0 = \\ \nabla_H \cdot \left[\left(-2\overline{M\mathcal{L}_u M}\, \nabla_H b_0 + \left(\overline{(\mathcal{L}_u M)^2} - \overline{M^2} \right) \mathbf{k} \times \nabla_H b_0 \right) \nabla_H^2 b_0 - \mathbf{G} \right].\end{gathered} \tag{D.48}$$

For a vertical relaxation parametrisation where momentum relaxation occurs on a faster scale than the buoyancy relaxation ($\mathcal{L}_b f \sim \sqrt{Ro}\, \mathcal{L}_u f$) we recover the result from Young (1994).